CVD synthesis of graphene

HERRON, CHRISTOPHER,ROBERT

CVD synthesis of Graphene

A thesis submitted for the partial fulfilment of the requirement for the Degree of

Doctor of Philosophy

In the faculty of Science of

Durham University

By

Christopher R. Herron

Durham University

Department of Chemistry

University Science Laboratories

South Road

Durham

2011

Copyright

Declaration

This work was conducted in the Department of Chemistry at Durham University between October 2007 and December 2010. The work has not been submitted for a degree in this, or any other university. It is my own work, unless otherwise indicated.

Dedication

This PhD thesis is dedicated to my Mum and Dad, without who I would not be here.

Acknowledgements

At this point I would like to take this opportunity to thank those people who have got me to this point. My family have to take much of the credit for getting me the position whereby I could get my Masters degree let alone my doctorate and I thank them for the support they have shown all the way through.

I must also thank Dr. Karl Coleman and the chemistry department for giving me the opportunity and funding to do this PhD in an area which is really still in its infancy and has given me many challenges, both welcomed and, more often that I would have liked, problematic. To Dr. Mustafa K. Bayazit who has worked with me every step of the way, I thank him for the support, knowledge, experience and maybe most important friendship, which at points I have found quite valuable. To doctors in training Ms. Rebecca Edwards who, as a project student, helped me refine the process for the film formation and Ms. Lucinda Clarke who have made my final few months so enjoyable both in and outside of work. Also to Maria Martin and Dr Dagou Zeze, Department of Engineering, who conducted the studies into the electronic applications of the spray pyrolysis product of sodium and ethanol, based on previous work with fullerenes and nanotubes.

I have to thank Mr Douglas Carswell to conducting all the DSC and TGA measurements of my samples. XRD measurements were performed by Gary Oswald using the department XRD service. I must thank Dr Graham Beamson (NCESS, Daresbury Laboratories, Warrington) for his assistance in performing and interpreting the XPS data. Also I'd like to thank Dr. Michael Fay (Nottingham Nanoscience and Nanotechnology Centre), Dr Budika Mendis and Mr Leon Bowen

Acknowledgements

(Durham GJ Russell Microscopy Facility, Department of Physics, Durham) for operation and technical assistance with the electron microscopes.

Collaborations

In this thesis collaborations were made with Maria Alba Martin and Dr. Dagou Zeze (Department of Engineering, University of Durham) investigate the electronic properties of the sodium ethoxide product in chapter 3. This work was carried out as a minor entry in Maria's final year Masters project focused on the application of carbon nanotube memory devices. Chapter 4 section 4.2 outlines the results of a memory storage device fabricated by his research group. I am grateful to them for allowing me to use the results in this thesis to demonstrate the application of the material.

In addition development of the thin film procedure in chapter 4 section 4.1 was undertaken with Miss. Rebecca Edwards (Department of Chemistry, University of Durham) as part of her final year Masters project. I thank her for allowing me to use results of this investigation for my thesis.

Abstract

The research into the subject of graphene has soared over the past few years. Due to the exceptional nature of some of its properties, it has become ever popular in the field of nanotechnology. The use of graphene for various electronics applications have been displayed using graphene that can be exfoliated or grown via several techniques. However, the scalability of these methods do not allow for bulk synthesis, known in the case of other graphitic nanomaterials like fullerenes and carbon nanotubes. For realistic applications, graphene has to be made in large quantities at a reasonable cost for use in, for example, solar cells, FETs, chemical sensors and engineering composites.

Here successful attempts have been made to synthesise few layer graphene via bulk methodologies commonly used in the manufacture of carbon nanotubes, using relatively inexpensive precursor materials. Spray pyrolysis, a simple and scalable technique for the manufacture of few layer graphene using ethanol and various sodium precursors was demonstrated, which showed polymer composite, electronic device and transparent thin film application.

Few layer graphene was grown using a bimetallic catalyst of sodium and cobalt. Addition of the sodium caused a visual decrease in the amount of carbon deposited from ethanol chemical vapour deposition. The product when observed using the scanning and transmission electron microscope was shown to be made up of turbostatic few layer graphene platelets.

Growth of single and few layer graphene was demonstrated using copper nanoribbons and cobalt nanosheets as catalyst templates. These when incorporated onto inert support material, produced single and few layer graphene in a process that is

deemed scalable and compatible with present industrial CVD reactors used for making carbon nanotubes.

Abbreviations

AFM	Atomic Force Microscopy
CNT	Carbon Nanotube
CVD	Chemical Vapour Deposition
DMA	Dynamic Mechanical Analysis
DMF	N, N'-Dimethylformamide
DSC	Differential scanning calorimetry
EDX	Energy Dispersive X-ray Spectroscopy
EELS	Electron Energy Loss Spectroscopy
EtOH	Ethanol
FTIR	Fourier Transform Infrared Spectroscopy
MIS	Metal-Insulator-Semiconductor
MWNT	Multi Walled Carbon Nanotube
PAA	Poly(acrylic acid)
PDMS	Poly(dimethylsiloxane)
PEI	Poly(ethyleneimine)
PMMA	Poly(methyl methacrylate)
SDS	Sodium Dodecylsulphonate
SEM	Scanning Electron Microscopy
SWNT	Single Walled Carbon Nanotube
TEM	Transmission Electron Microscopy
TGA	Thermogravimetric analysis
XPS	X-ray Photoelectron Spectroscopy

Table of Contents

Table of Contents

Table of Contents

Table of Contents

Table of Figures

Table of Figures

Table of Figures

Table of Figures

Table of Figures

Table of Figures

Table of Figures

Table of Figures

Table of Figures

Table of Figures

Table of Figures

Table of Figures

Schemes, Tables and Equations

1. INTRODUCTION

Graphene has become popular in the physical sciences due to its exceptional properties. This material, consisting of atomically thin sheets of hexagonally networked carbon atoms, forms the basis of all sp^2 carbon based systems (Figure 1). The various allotropes of carbon are composed of derivatives of this structure, whereby: graphite consists of stacked layers of graphene, carbon nanotubes have the structure of rolled up graphene and fullerenes are nanometre-sized spheres. These forms of carbon were isolated prior to the surge in interest of graphene, and have been used for various applications. However their electric, magnetic and elastic properties all originate from the parent structure. The number of publications and patents relating to graphene synthesis, properties and emerging technologies has flourished, more profoundly than that for CNTs and fullerenes in the 6 year period since its discovery. One major problem that exists for graphene is producing it in bulk quantities. This challenge must be met before graphene becomes a viable material for use in industrial applications. At present both fullerenes and carbon nanotubes can be grown by a number of different scalable methods. This has led to their dominance in application research despite the superior electrical and mechanical properties of graphene.

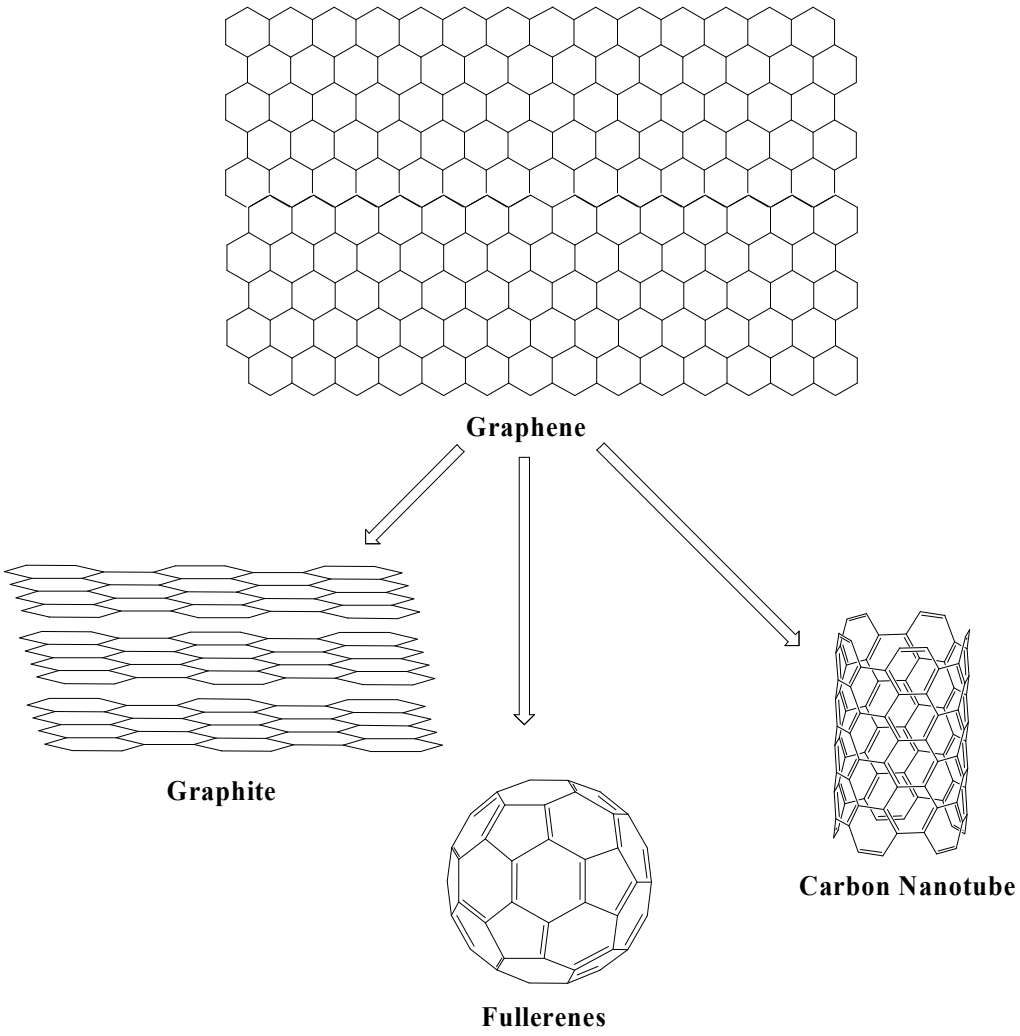

Figure 1 – Graphene and its relation to other carbon structures of fullerenes, carbon nanotubes and graphite

1.1 Discovery

Much of the literature points to the 2004 paper published in Science by Andre Geim of the University of Manchester as the first documented case of monolayer graphene observation.[1] This demonstrated the exceptional properties of the material, promoting the explosion in research on the subject, leading to the award of the 2010 Nobel Prize in

Physics, in partnership with Kostya Novoselov. The term graphene was first outlined in 1994,[2] however, before 1994 were a few instances in the literature that refer to the findings of atomically thin carbon films, describing them as: monolayer graphite,[3] single crystal plane graphite,[4] and 2D graphites.[5] Conversely, Geim confirmed the postulate[6] that graphene is a 2D crystal and further highlighted its exceptional properties that have promoted it to the forefront of the nanotechnology field.

1.2. Properties of Graphene

The hexagonal arrangement of carbon atoms in graphene enable electrons to travel through the material for thousands of interatomic distances without scattering. This aids the rapid dissipation of excess heat – making graphene a more suitable thermal conductor[7] ($5000 Wm^{-1}K^{-1}$) than carbon nanotubes[8] ($3500 Wm^{-1}K^{-1}$) and copper[9] ($401 Wm^{-1}K^{-1}$). An equally important reason for the interest in graphene is the unique nature of its charge carriers. In condensed matter physics, the Schrödinger equation is usually sufficient to describe electronic properties of materials. Graphene is an exception; its charge carriers mimic relativistic particles and therefore are more accurately described by the Dirac equation. Electrons in graphene are thought to behave like relativistic particles; they behave as if they have no rest mass and travel at 10^6 metres per second.[10,11] Although this value is three hundred times slower than the speed of light in a vacuum, it is still much faster than in an ordinary conductive material. Consequently, graphene has been shown to have a theoretical conductivity as high as $9.6 \times 10^5 Scm^{-1}$, greater than the measured value for copper[9] ($5.96 \times 10^5 Scm^{-1}$).

Mechanical investigations into the structure of graphene sheets using an AFM tip gave a Young's modulus of 0.5TPa (200 times stronger than steel on a nanoscale level).[12] This value suggests graphene has high strength and rigidity, providing potential applications in the field of nanoelectromechanical systems (NEMS) such as pressure sensors[13] and resonators.[14]

1.3. Applications of graphene

1.3.1 Electronics

We currently live in the age of silicon based nanotechnology, where silicon based transistors drive the present computing revolution. The size of transistors has consistently been decreasing allowing more transistors to be packed onto a single chip thereby increasing computer power. The rate at which this happens, approximately follows Moore's law:[15] the number of transistors on a integrated circuit is doubling approximately every two years. The $1 trillion computer market provides the economic drive for the worldwide demand for smaller and faster computers. There are two ways of achieving this; reducing the size of the device currently used for present silicon technology (45nm chips have recently become available) and increasing the speed at which charge moves inside the material. As silicon computer circuitry gets ever smaller, the miniaturised electronic devices become limited by the physics of the material. At this point, to further reduce the size of the circuitry, new technology will replace the silicon generation. Graphene has been suggested as a possible replacement of silicon. Unlike other known materials, graphene remains highly stable and conductive, even when it is cut into ribbons

a nanometre wide.[16] The smallest transistor created was in 2008, based on a monolayer of graphene 10 atoms wide.[17] Another major advantage of graphene is due to its high carrier mobility, which allows the creation of high speed and high performance transistors. Recently, the fastest graphene transistor ever created operated at 300GHz, double that measured for a silicon based device of similar size.[18] This was accomplished using a gate length of 140nm, but by reducing this value, graphene transistors are expected to be the first to achieve terahertz speeds.

Graphene is not only limited to use in transistor based devices but also high transparency electrodes for organic photovoltaics,[19,20] integrated circuitry[21] and chemical sensors.[13] Graphene films produced by both the chemical vapour deposition (CVD) routes on metal foils[22,23] and solution processing of graphene oxide (the oxidized form of graphene, highlighted in more detail later)[20,24,25] have been demonstrated as effective anode materials for OLEDs (Figure 2).

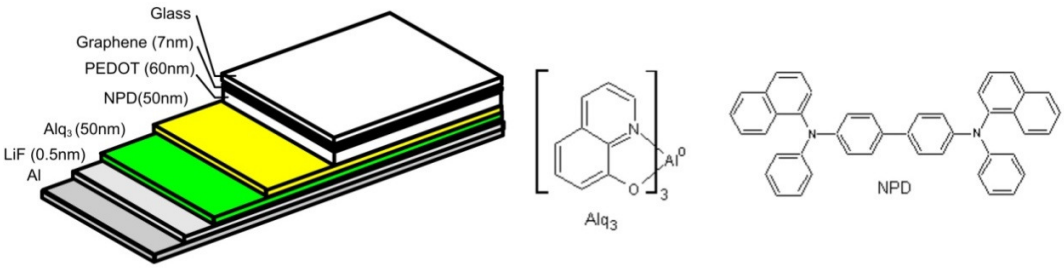

Figure 2 – Role of graphene as anode material in the OLED system prepared by Wu *et al.*(*redrawn from ref [20]*)

The foremost problems are the availability and cost of graphene. It is correct that from one small piece of highly order pyrolytic graphite (HOPG), thousands of graphene based devices could be constructed. However, as of late 2010, graphene is still priced at

£200 - £400 for single graphene flakes of a few hundred square micrometers.[26] Graphene oxide is more readily available in bulk quantities at ~£400 per gram for material <2nm in thickness,[27] however, few suppliers can guarantee this.

1.3.2 Composite Materials

Carbon nanotubes have demonstrated useful properties in the field of composite materials, improving both the mechanical properties and electrical properties of parent matrices of various polymer and inorganic media. Now graphene oxide is available in bulk quantities, graphene is seen as a material that could surpass the properties observed so far with CNTs.

Ramanathan et al[28] studied the behaviour and differences of poly(methyl methacrylate) (PMMA) composites containing functionalized graphene sheets (FGS), expanded graphite, and single walled carbon nanotubes (SWNT) at 1wt% content. The increase in mechanical strength for the FGS (>80%) exceeded that of SWNTs (52%) and expanded graphite (45%). This difference is suggested to be due to the interaction between the side chain groups of PMMA and the functionalised graphene surface. In addition, Rafiee et al[29] have also shown graphene to outperform carbon nanotubes, by 20 – 26%, in epoxy composites containing very small amount of material (0.1wt%). Similar studies with graphene and graphene oxide have been conducted with polyvinyl alcohol,[30] polystyrene,[31] poly(3,4-ethylenedioxythiophene)[32] and inorganic architectures like TiO_2,[33] [34]silica and clays.[35,36]

1.4 Graphene Synthesis

The general methods for graphene production can be separated into two categories; 'top down' and 'bottom-up' approaches. Obtaining graphene from 'top-down' methods involves separating the layers of graphitic structures, via mechanical or solution phase processing. Alternatively, 'bottom-up' approaches involve synthesising graphene from carbon sources other than graphite, using chemical methods. Generally, top-down methods produce highly crystalline material, however the methods are difficult to scale up, the products available can have large graphitic impurities and the ratio between single/few layer graphene can show wide variation between batches. 'Bottom-up' synthesises are generally considered to be more controllable and free of large graphitic impurities. Chemical vapour deposition (CVD), for example, is very sensitive to variations in specific parameters including source gas, flow rate, operating pressure and catalyst used. Most of these are controllable and so samples of few and single layer graphene have been shown to be reproducible. Detailed review articles on graphene synthesis exist in the literature, for example, by Rao[37] and Taghioskoui,[38] and the various types are discussed below.

1.4.1 Top-down methods

1.4.1.1 Micromechanical cleavage

Experimentally, graphene was first separated using the 'scotch tape' method, involving the use of adhesive tape to remove layers of carbon from the surface of highly ordered pyrolitic graphite (HOPG) (Figure 3).[1] This method produces an assortment of graphene nanosheets including mono- and few-layer graphene, in conjunction with much

thicker crystals. Due to such variation, initially this technique was quite labour intensive due to the search for single layers on the pieces of adhesive tape. However, the development of optical microscopy techniques, which utilize the fundamental properties of graphene, have made the identification and selection of monolayers much easier. The large difference in the refractive indices between graphene and 300nm SiO_2/Silicon allows graphene to be located and differentiated between mono and few layer sheets.[39,40] Using a standard optical microscope, fluorescence microscopy is a further method commonly used to identify graphene sheets on surfaces, exploiting their own characteristic quenching effects.[41,42] Kim *et al*[41] developed a method based on the fluorescein sodium salt in conjunction with polyvinylpyrrolidone (PVP), to deposit a continuous fluorescent layer over deposited samples. The authors showed that in addition to the location of the graphene sheets the degree of reduction of graphene oxide, could also be determined by sample quenching.

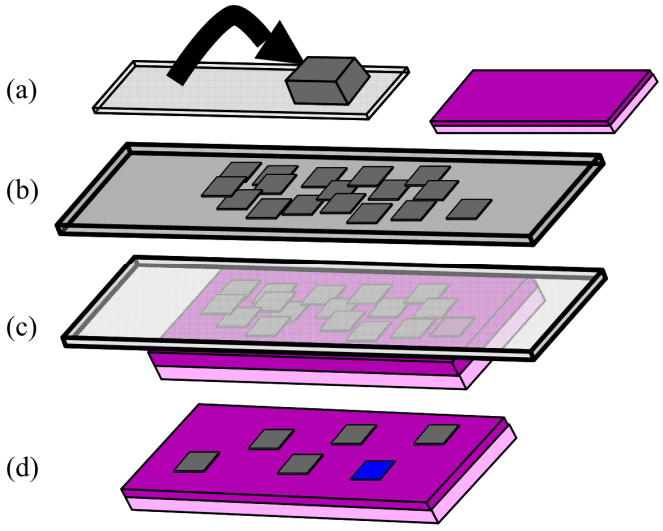

Figure 3 – (a) initial materials (HOPG, "scotch" tape, 300nm SiO_2/Si wafer) (b) repeated folding of tape produces small crystals on tape surface, (c) tape contacted with wafer, (d) graphite and graphene of various thicknesses deposited in wafer (many few layer and larger crystals (grey) and few single layers (blue)).

The samples obtained from this method display excellent quality, with high crystallinity and few defects.[43,44] For example, micromechanically cleaved samples of single layer graphene have shown the highest carrier mobility (μ) of any semi-metallic or semiconducting material at 200,000cm^2/Vs, when suspended without the use of a surface. Consquently, this is the material of choice for physicists studying the fundamental properties of graphene.

1.4.1.2 Graphite exfoliation in solution

Knowledge of the graphite intercalation compounds has been extended to develop methods to chemically separate the layers. This expansion occurs by intercalating species into the interlayer spacing, increasing the graphite interlayer spacing beyond 3.4Å. The exfoliation method involves infinitely expanding the interlayer spacing within the solution phase, so the layers are sufficiently separated, reducing the interlayer forces until layers cannot be held together.

Subsequently, these intercalated compounds can be exfoliated into discrete platelets. Such as example is the production of graphite nanoplatelets (GNPs) from alkali metal intercalated graphite in ethanol (Figure 4)).[45,46] The alkali metals donate electrons to the graphite layers forming intercalation compounds that can be expanded using solvent[45] or polymer reactions.[47] This route is not limited to inorganic intercalates; oleum and tetrabutylammonium hydroxide intercalates have produced monolayer graphene yields in excess of 90% in N, N-dimethylformamide (DMF), with a low concentration of defects or surface modifications.[48]

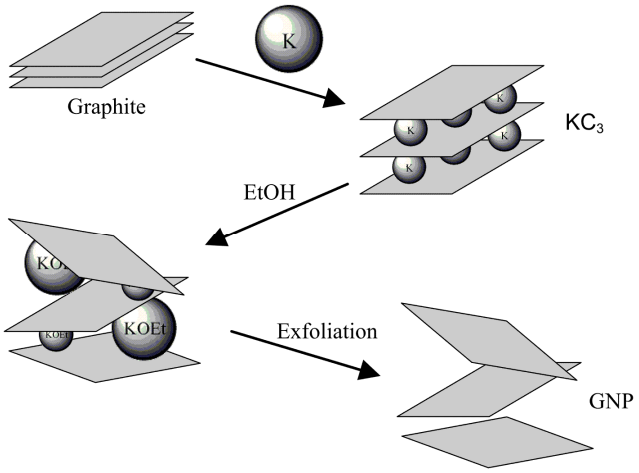

Figure 4 – Schematic representation of graphene nanoplatelet production (GNP) via exfoliation of KC_8. Hydrogen produced from the production of potassium ethoxide forces exfoliation of layers producing GNPs (redrawn from ref [45])

In addition, the supercritical phase of carbon dioxide has been used as a top down graphite exfoliant.[49] Supercritical CO_2 has both gas and liquid phase properties, allowing the molecules to migrate to the space in-between the graphene layers to behave as an intercalate. After removal of pressure, the graphite expands due to the rapid increase in volume of the CO_2 and subsequent mixing with aqueous sodium dodecylsulphate (SDS) preventing layer restacking, giving few layer graphene platelets with an average thickness less than 4nm.

Direct sonication in solution has been used for the formation of single layer graphene and has been demonstrated in various articles by the nanomaterials group at Trinity College, Dublin. They have used a number of specific solvents/solutions as exfoliation media for graphite. N-Methylpyrrolidone[50,51] (NMP) and surfactant water[52] have been shown to separate the parent structure into a mixture of mono, bi and few layer graphene, with yields (collected by centrifugation) of 1 – 3wt% respectively. However,

solvents including NMP and dimethylacetamide (DMA) are expensive and hazardous. In the case of sodium dodecylbenzenesulphonate (SDBS) the authors comment on the difficulty in removing the residual surfactant and a small degree of oxidation. As a consequence, the electrical conductivity of the resulting vacuum filtered films of graphene was reduced.[52] Hernandez *et al*[51] suggest using the same theory for the dispersal of carbon nanotubes in NMP; exfoliation occurs due to favourable interfacial interaction between the liquid phase and graphene layers, resulting in a small energy penalty for exfoliation. They further investigated the multiparameter components that govern this, for a range of solvents.[50]

1.4.1.3 Graphite oxide exfoliation

An encouraging method for graphene production is associated with the reduction of exfoliated oxidized graphite. This 'graphite oxide' can be produced by a variety of different processes including the Hummers,[53] Brodie[54] and Staudenmeier[55] methods, which all employ the use of strong acids and oxidants.[56,57] Various models for the structure of graphene oxide have been presented, and extensively reviewed.[57] One of these, the Lerf-Klinowski model (Figure 5), shows a layered structure with epoxy and hydroxyl functionalities on the surface in conjunction with carboxyl groups found at the edges. [58,59]

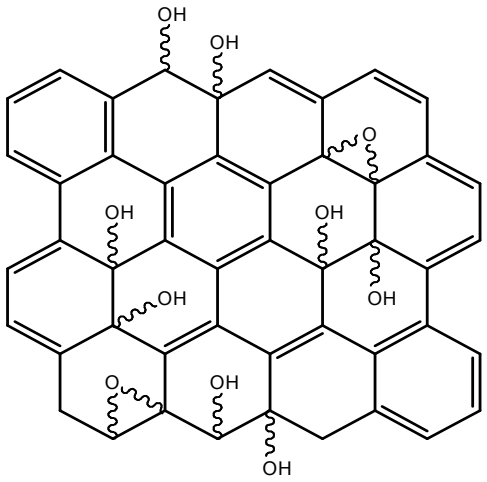

Figure 5 - The Lerf-Klinowski model graphite oxide displaying the alcohol and epoxide groups present on the surface. (redrawn from ref [58])

The presence of oxygen functionalities has a number of effects on the properties of graphene oxide. Firstly, they interfere with the sp^2 structure of the layers, producing a material which is electrically insulating, in contrast to the conductive nature of graphite. Further, the oxidation of the surface also increases the interlayer spacing (6 – 12Å, dependent on the amount of absorbed water) beyond that of graphite.[60] The hydrophilic character of the sheets allows them to be separated to thin plates by sonication or by thermal expansion at high temperature.[57,61,62] Upon exfoliation, chemical reduction has been achieved via a number of methods including hydrazine (both gas phase[63] and hydrate[64]), ascorbic acid/sodium borohydride mixtures[65] and hydroquinone.[66] The graphene structure produced by mechanical exfoliation and thermal reduction has been compared by Ju *et a*l.[61]

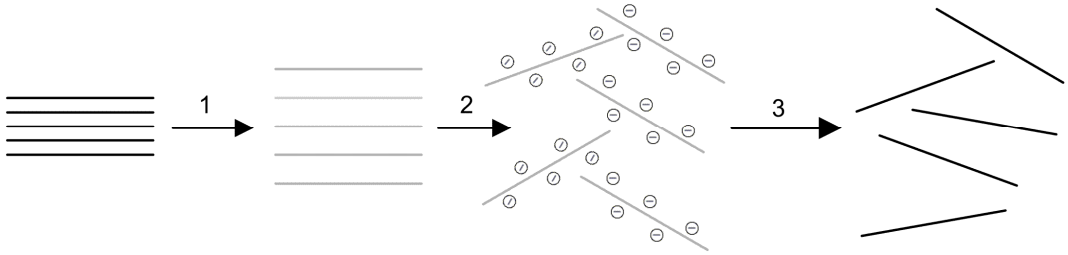

Figure 6 - General scheme showing the production of reduced graphene oxide dispersions from graphite using chemical methods. 1, Oxidation of graphite (black) to graphite oxide (grey). 2, Exfoliation of graphite oxide to graphene oxide. 3, Reduction of graphene oxide to graphene.

During reduction the hydrophilicity of the sheets decrease, promoting aggregation and precipitation.[64,67] As a result, full reduction cannot be accomplished and the presence of the remaining oxidation groups act as defect sites (electron traps) causing decreased conductivity and thermal stability.[63,66] Further investigations have been undertaken into milder synthetic methods to decrease the amount of defects incurred during oxidation.[68,69] Furthermore, the thickness distribution of exfoliated graphene oxide has been shown to be related to the variety of graphite starting material, and, in turn, the size of the precursor material.[70] Currently graphene oxide is the premier compound, now commercially available, for the large scale production of graphene.[71] It is commonly used to create graphene based composite materials and has been identified as a potential material to compete with thin films made from cleaved HOPG and CVD. [16,20,72]

1.4.2 Bottom-up methods for graphene synthesis

1.4.2.1 Epitaxial growth on silicon carbide

Growth of graphene has been achieved on silicon carbide (SiC) by heating to a high temperature (1300^{o}C) under ultra high vacuum (UHV) conditions (Figure 7), creating

high quality mono- and multi-layer graphene sheets via graphitization of a carbon rich surface induced by the sublimation of silicon.[73-75] Careful control of the sublimation process influences the coverage and uniformity over the entire SiC surface, in addition to the film thickness.[74,76] The process produces graphene with dimensions dependant on the size of the SiC precursors available. Additionally the patterning of graphene on SiC has been demonstrated using standard microelectronics techniques.[77] This ability allows the possibility of creating carbon based integrated circuitry first proposed in 2004[76] and patented for commercial use in 2006.[78] This has been extended by MIT researchers who have demonstrated the production of several hundred transistors per electronic chip[79] and recently gigahertz speed transistors have been documented on SiC by Hughes Research Labs.[80]

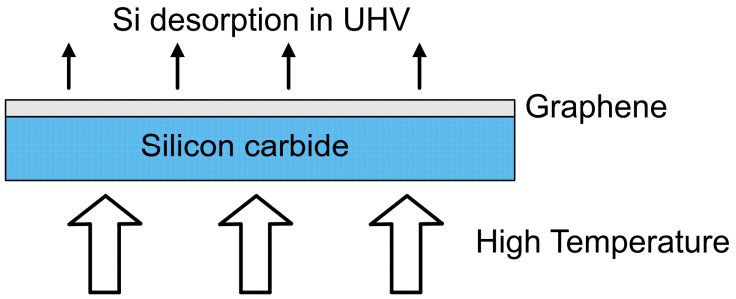

Figure 7 – Graphene films from silicon carbide decomposition in ultra high vacuum

However, there are many disadvantages to this procedure including: the expensive equipment required to achieve the ultra high vacuum conditions, the cost of suitable SiC, the strong interaction surface interaction and the stability of SiC, which restricts the transfer of graphene to other substrates. Recently, investigations have moved towards enhancing the process by developing a procedure of growing graphene on SiC coated with a thin layer of nickel, reducing the processing temperature to 750˚C.[81] The nickel layer

separating the graphene from the SiC can be etched away enabling graphene to be transferred more easily.

1.4.2.2 Chemical Vapour Deposition

Chemical vapour deposition (CVD) has been commonly used to synthesise carbon nanotubes, via high temperature decomposition of carbon containing gases over various metal catalysts. Various CVD methods including: atmospheric pressure, UHV, plasma enhanced, microwave assisted, are available, each using different metal substrates such as: nickel,[82-85] copper,[86] cobalt,[87] platinum,[88] iridium[89,90] and ruthenium[91] to synthesise thin films of graphene. It has been proposed that graphene films grow by either segregation/precipitation or surface absorption mechanisms. By employing isotope studies with methane, utilizing the difference in energy for the ^{12}C and ^{13}C Raman modes, nickel was found to proceed by the segregation/precipitation mechanism due to the significant solubility of carbon, (0.9 at% at 900^{o}C) consequently giving a uniform distribution of ^{12}C and ^{13}C within the graphene layers.[92] Due to the segregation/precipitation mechanism, the graphene films show an uneven thickness across the surface, particularly at the crystalline grain boundaries where the carbon prefers to precipitate from solution. This is rationalized by the temperature dependant solubility of carbon in metal melts,[93] where certain elements including nickel and cobalt form metastable carbides dissociating to graphitic carbon on cooling. In contrast, due to the negligible solubility of carbon in copper, (0.03at% at 1000^{o}C) (due to no carbide phase formation) carbon will only exist at the metal surface where it reorganises into graphitic carbon, growing as islands upon the substrate surface until total coverage occurs. This is

independent of any surface features.[94] Via isotope studies, Li *et al*[92] confirmed where pure domains of ^{12}C and ^{13}C were observed, in addition to domains containing both isotopes, which were suggested to be junction sites between two pure domains.

Nickel is one of the best working catalysts for carbon nanotubes and was one of the first to be adopted for use in the synthesis of graphene. Riena et al[85] have shown that polycrystalline nickel could be used as a deposition surface for templating the growth of graphene. The films showed variation in thickness across the surface between 1 – 10 layers, as a consequence of the segregation/precipitation growth method and the crystallite size. The use of nickel is advantageous in the semiconductor industry, due to the ease at which it can be patterned. As a result the authors were able to show intricate designs of graphene grown and transferred by acid etching to various substrates. In addition, CVD grown graphene on nickel show a carrier mobility of 4000 $cm^2V^{-1}s^{-1}$,[95] compared to 200,000$cm^2V^{-1}s^{-1}$ on mechanically cleaved samples.[96,97] Transfer of graphene from metal foils can be problematic, but progress has been made within the field using iron chloride etching (Figure 8) to the point where roll-to-roll transfer procedures have been used to create large (ca. 30 inch) display screens. Furthermore, conductivity analysis of these films displayed a sheet resistance 280Ω/□, analogous to that demonstrated by the OLED anode material ITO (40 Ω/□).

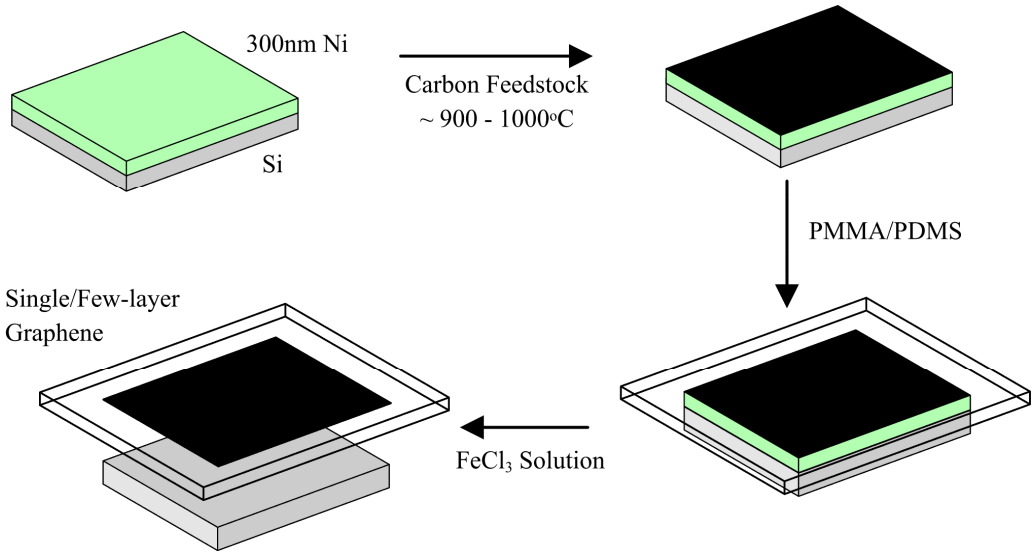

Figure 8 - A schematic illustrating the synthesis of graphene films grown on transition metal/SiO_2/Si substrates via CVD and layer separation as illustrated by Kim et al. Etching and transfer steps using PMMA/PDMS allow the transfer to several substrates (redrawn from ref [95])

Due to extensive processing associated with transition metal based methods, additional independent systems based on the CVD procedure have been developed. Dato *et al* have developed a method for graphene synthesis in a microwave plasma which needs no metal catalyst.[98] The process involves an ethanol aerosol into argon plasma at within a quartz tube at atmospheric pressure. The ethanol decomposes in the gas phase and deposits graphene sheets on a filter near the exhaust. The product was shown to consist of pure carbon via EELS analysis and observed to be single and bi-layer graphene using TEM. There are instances of support based bulk synthesises for graphene, using CVD in a similar fashion to those for CNTs.[99,100] The temperature dependant synthesis of graphene has been demonstrated using a mixed iron/cobalt catalyst supported on magnesium oxide (2.5:2.5:95 wt%) under radio frequency conditions with acetylene as the carbon

feedstock.[100] Graphene was found at temperatures above 1000^{o}C where nanotube geometries were found at temperatures between 700 – 950^{o}C.

1.4.2.3 Arc discharge

Arc discharge is widely known as the primary synthesis method of fullerenes[101,102] and to a lesser extent, CNTs.[103] Subrahmanyam et al[104] have shown a procedure involving the arc evaporation of pure graphite electrodes in a hydrogen/helium atmosphere produced a black deposit made of graphene sheets consisting of 2 – 4 layers. The rationalisation for the synthesis, was the presence of hydrogen terminating the graphene edges, preventing the synthesis of closed structures. More recently, a similar process incorporating air, demonstrated by Zhiyong et al,[105] which was able to produce gram scales of nanosheets in the range of 100 – 200 nm in lateral dimensions in conjunction with a narrow thickness range (2 – 10nm). Additionally, the authors showed the dependence of the synthesis on pressure, where nanosheets were favoured at higher pressure (in the region of 1000 Torr) whereas other geometries, such as nanohorns and spherical particles, were produced at lower pressure (400 – 500 Torr). The arc process may prove a useful way to introduce doping atoms of boron or nitrogen into a structure, modifying and allowing the exploration of graphene's properties.[104,106]

1.4.2.4 Precipitation from metal carbon melts

Additionally, metals have been used to template the growth of graphene from solid carbon precursors. The heating of copper above its melting point (~ 1100^{o}C) in a graphite crucible was shown to produce single layer graphene on the metal.[107] Carbon

sources such as PMMA, fluorene and sucrose were deposited on copper foils and heated to 800^{o}C in a H_2/Ar atmosphere, giving single layer graphene upon cooling.[108] In addition, by depositing metals on the surface of amorphous carbon films, graphene was found to be produced on nickel and cobalt surfaces after heating.[109]

1.4.2.4 Pyrolysis of solid species

The most effective gram scale, bottom-up method that has become available in recent years involves the flash pyrolysis of a sodium ethoxide clathrate produced by the reaction of sodium and ethanol under solvothermal conditions. On average this procedure synthesises half a gram of graphene and benefits over other methods due to the by-products being water soluble, in addition to the precursor materials being relatively inexpensive and readily available. However, a limitation of the system is the preparation of the solvothermal product, hence the total time scale for production is relatively long and the samples contain 17.35% oxygen, which the authors attribute to absorbed water.[110] Inert atmosphere camphor pyrolysis over nickel foils has produced thin graphitic platelets (20 – 50 layers). This route used environmentally friendly natural products as the precursor material and as one of the first documented routes to graphitic carbon films predating the studies of Reina[85] and Li[86] on nickel and copper using methane. Recently, Xu et al[111] have demonstrated that the number of graphene layers produced by the microwave decomposition of cobalt phthalocyanine at 450^{o}C can be controlled by the degree of rapid cooling. By using water, water/ice mixtures or liquid nitrogen as coolants, the average numbers of layers produced were 8, 4 and 1 – 2 respectively, in under half an hour. They

suggest that the layers of the fresh graphitised structure cleave due thermal stress induced by rapid cooling from high temperature.

1.4.2.5 Conversion of carbon nanomaterials

Carbon nanotubes are frequently described as rolled up graphene and conversion of these commercially available products to graphene nanoribbons has been demonstrated through selective "unzipping" (Figure 9). The plasma etching of nanotubes partially embedded in polymer films,[112] nanoparticle cutting[113] or by an oxidative process[114] has been used to uncurl nanotubes. The chemical reduction of these oxidized structures has provided 10 – 40nm wide nanoribbons with smooth edges. Conversely, ribbons defined from graphene sheets by lithographic methods generally give ribbons with very rough edges.[115] Platinum nanoparticles have recently been used in conjunction with oxygen for catalytic unzipping in the solution phase.[116] Despite this method producing 4 – 8% yield of few layer nanoribbons, the authors highlight the disadvantage of using environmentally damaging chemicals which are common in tube to ribbon conversion. Consequently, investigations into nanodiamond have been carried out; due to the sp^3 to sp^2 conversion at temperatures above 1600^{o}C, it was found that few layer graphene can be produced.[117,118] Comparisons between the graphitic products of the above method, the thermal expansion of GO, arc evaporation of SiC and reductive pyrolysis of camphor over nickel has been presented by Subrahmanyam *et al*.[62] They showed that although the nanodiamond product was the most thermally stable, it had the smallest in-plane crystallite size and showed 2 graphitic fractions showing a c-axis crystallite size of 2nm and 29nm.

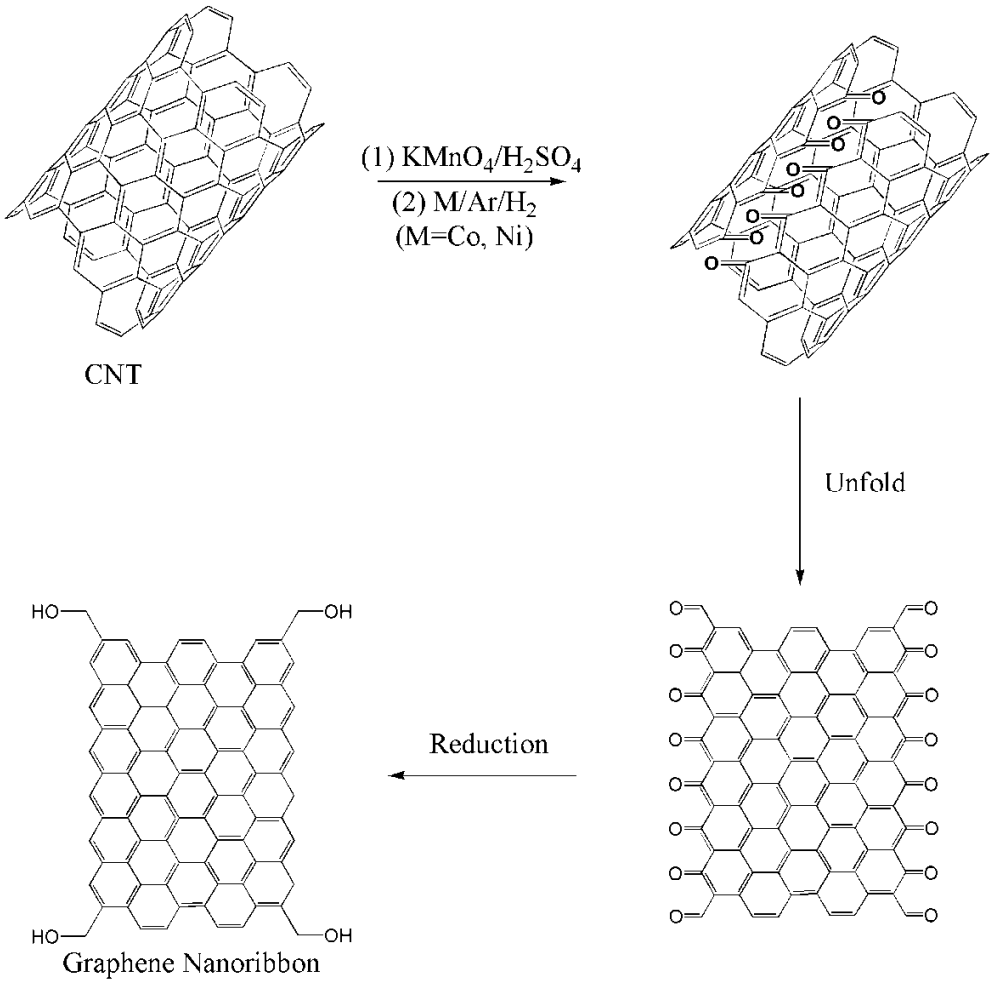

Figure 9 – Procedure for the "unzipping" of carbon nanotubes to make carbon nanoribbons using (1) oxidation or (2) nanoparticle etching methods

1.4.2.6 Bottom-up molecular synthesis

The bottom-up synthesis of ever larger aromatic molecule has been the goal of many organic chemists for over a century. This has culminated in many attempts to form long aromatic networks, using precursors with precise structures that allow the build up of graphene oligomers. One such example; the core structure of hexabenzocoronene consists of thirteen fused aromatic rings. Serial oxidative cyclodehydrogenation reactions of

substituted and branched derivatives build planar graphene discs, made up of ninety[119] to over two hundred[120] rings. In addition, the one dimension growth of graphene nanoribbons has been demonstrated by the use of other ringed systems with specific functional groups. Dehydrogenation of polyphenylene polymers, built from substituted polycyclic building blocks, has produced graphene nanoribbons, 8 – 12nm in length and 2.9nm in width.[121] Utilizing this procedure, variation in structure of the building blocks and the resulting polymer offer control over the edge configuration of nanoribbons defining metallic and semiconducting characteristics. Recently this has been extended further to produce armchair graphene nanoribbons using 10,10'-dibromo-9,9'-bianthryl precursor monomers.[122] The thermal sublimation of these molecules onto a solid surface promotes intermolecular radical addition, via the removal of the bromine substituents, creating the building blocks of a graphene nanoribbon. By varying the structure of the molecule the authors were able to demonstrate bolt linear, chevron and branched nanoribbons (Figure 10) by cyclodehydrogenation of the oligomers via further increase in the temperature.

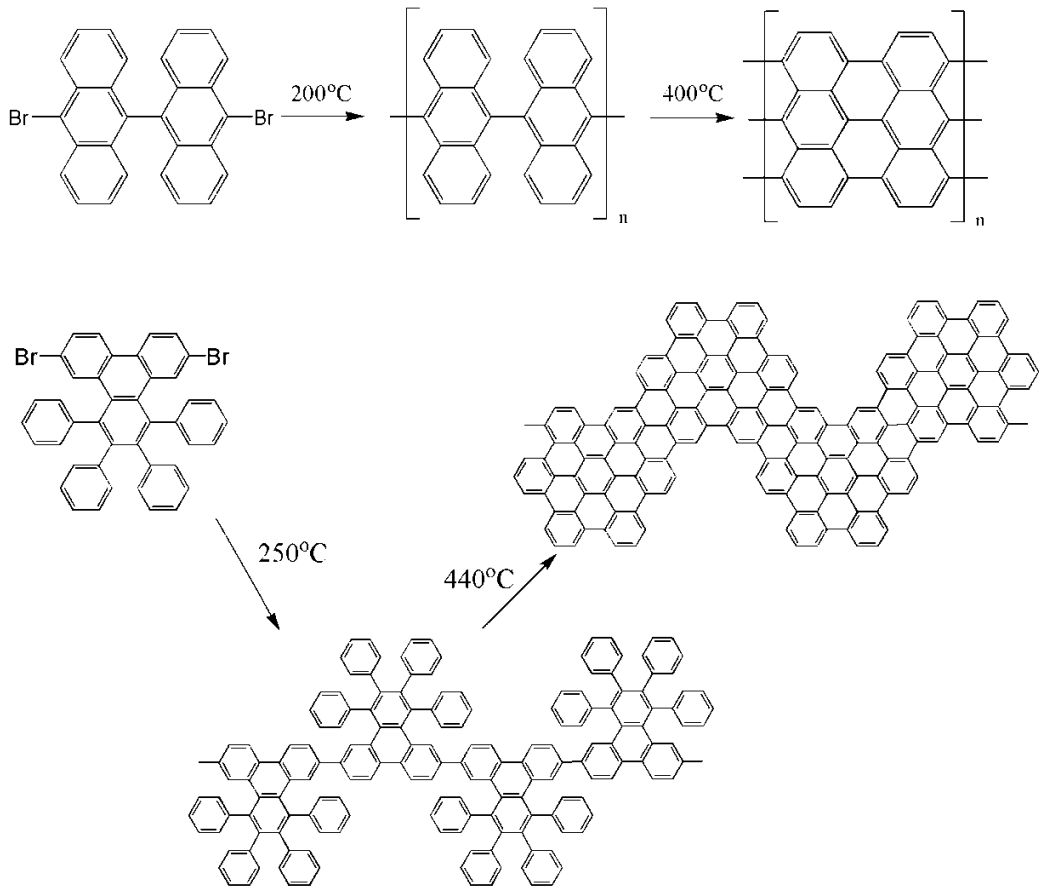

Figure 10 – Atomic building of graphene nanoribbons based on substituted polycyclic molecules. (redrawn from ref [122])

Introduction to thesis

Currently research into several applications of graphene is limited by the supply of material. This is especially true in academic and industrial composite research. Graphene oxide is an attractive route to bulk scale production as the starting material is graphite which is available in vast quantities. However, the process has disadvantages including the use of environmentally harmful chemicals, batch quality discrepancies, large thickness distribution and the presence of large graphitic impurities. Chemical vapour deposition is

an attractive route to synthesis of graphene and high quality films have been demonstrated in the literature. This method, in most aspects, avoid the issues related to graphene oxide but at this time very few bulk scale CVD methods have been published. This is due to the fine line between the production of carbon nanotubes, graphene and graphite.

In this thesis, attempts have been made to create procedures for graphene synthesis based on CVD techniques. Both non-transition and transition metal based routes have been utilized to produce single and few layer graphene with the aim of establishing scalable bulk syntheses. The structure of the graphene platelets has been characterised using various spectroscopic (Raman, FTIR, XPS), thermal (thermogravimetric analysis) and microscopic (Atomic force, Scanning and Transmission electron microscopy) techniques. The background to these techniques is highlighted in the next chapter.

2. INTRODUCTION TO EXPERIMENTAL TECHNIQUES

Raman Spectroscopy

Raman spectroscopy is a technique used to study vibrational, rotational, and other low-frequency modes within a system. It relies on inelastic scattering (Raman scattering) of monochromated light, usually from a laser ranging from the near infrared to the near ultraviolet wavelengths. Over the last four decades, Raman spectroscopy has played an important role in the study and characterization of graphitic materials such as; pyrolytic graphite, carbon fibers,[123] nanographite ribbons,[124] fullerenes,[125] carbon nanotubes,[126] and graphene.[127] The Raman spectra of the various carbon nanostructures are dominated by the signal corresponding to in-plane vibrations of sp^2-hybridised carbon commonly denoted as the "graphitic" or "G-band" at around 1580 cm^{-1}. Additionally, a band arises from defects or amorphous carbon corresponding to vibrations of sp^3-hybridised carbon and are denoted as the "disorder" or "D-band" at around 1350 cm^{-1}, with an overtone (G', sometimes referred to as the 2D) around 2700 cm^{-1} (Figure 11). In conjunction with these common bands, single walled carbon nanotubes also show signals below 500 cm^{-1} corresponding to low-energy radial breathing modes (RBM) of the tubular cages.

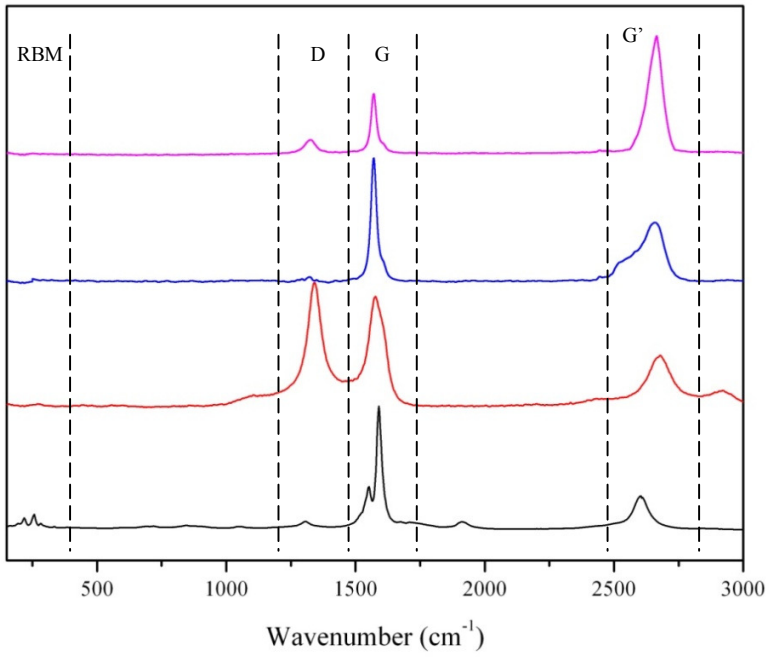

Figure 11 - Example Raman spectra of SWNT (black), MWNT (red), HOPG (blue) and HOPG cleaved graphene (magenta)

Furthermore, Raman spectroscopy can be utilized to give information about crystallite size, clustering of the sp^2 phase, the presence of sp^2-sp^3 hybridization and the introduction of chemical impurities, doping, defects and other crystal disorder, number of graphene layers, nanotube diameter, chirality, and the metallic versus semiconducting behavior.[128]

Raman spectroscopy has to be used in conjunction with imaging techniques due to the similarities between the peaks present and their line shapes. SWNTs can be confirmed/eliminated quickly because of the RBMs but all the others, multiwalled (MWNT), highly ordered pyrolytic graphite (HOPG) and graphene, have very similar spectra. For large area sheets of graphene under 1 nm in thickness, the G' has a much

higher intensity to that of the G-band, consequently this is commonly used in cleaved samples to detect single layers among the debris on “Scotch” tape.

X-ray Photoelectron Spectroscopy

X-ray photoelectron spectroscopy (XPS) is one of the most effective surface sensitive analysis techniques which has been used to give quantitative information about the chemical composition of nanostructures.

XPS is conducted by exposing a sample to x-rays of suitably high energies (Al Kα 1486.6eV used here) which excite emission of electrons from the core energy levels of atoms. The resulting ‘vacancies’ produced in the core electronic energy levels are filled by valence electrons from an higher electronic energy level falling to the lower energy core shell (accompanied by Auger emission, Figure 12).

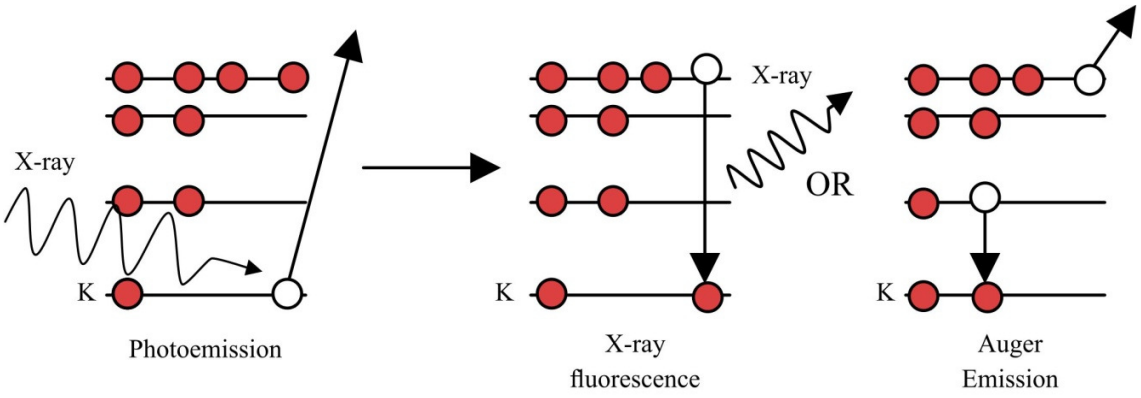

Figure 12 - Schematic diagram illustrating photoemission of a core shell electron from an atoms electronic structure stimulated by exposure of the sample to X-rays of high energy.

The kinetic energy distribution of the discharged photoelectrons can be measured using an appropriate electron energy analyser and a photoelectron spectrum plotted in terms of count intensity. Subsequently, the binding energies can be determined (Equation

1) from the relationship between the kinetic energy of ejected electrons and the input photon energy. Each element has characteristic binding energies, predetermined by the core orbitals, giving rise to a distinctive set of peaks in the photoelectron spectrum at kinetic energies governed by the photon energy and the particular binding energies. This technique also provides quantitative analysis, as both the presence and the concentration of a given element within the sample can be identified, via the existence of peaks and the integrated intensity of the peaks respectively. [129]

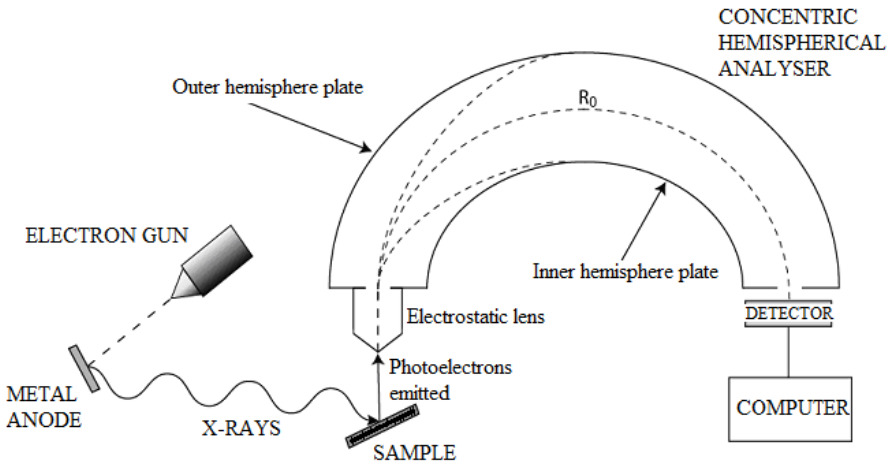

Figure 13 - Schematic diagram illustrating the basic design of an X-ray photoelectron spectrometer.

$$h\nu = BE + KE$$

Equation 1 – Derivative of binding energy (BE) from the photoelectric effect incorporating the initial X-ray energy (hυ) and the measured kinetic energy of emitted electrons (KE)

With respect to carbon nanostructured materials, XPS can be used to probe modifications to the graphitic structure. The characteristic binding energies for carbon materials are found in the binding energy range 280 – 295eV. Due to the specific nature of the various binding energies of carbon-carbon and carbon-heteroatom bonds, the signals

can be de-convoluted into so called "contributions" (Table 1).[130] Contributions can give information on the sp^2/sp^3 ratio, degree of oxidation and other carbon structures present.

Carbon Group	Binding Energy
Carbide	281.7 – 281.9
Sp^2/Graphitic Carbon	284.3 – 285.6
Sp^3/Saturated Hydrocarbons	285.3 – 285.6
Alcohol/Epoxide C-O	286.4 – 286.8
Ketone/Aldehyde C=O	287.4 – 287.9
Carboxylic Acid/Anhydride C(O)O	289.6 – 289.8
$\pi - \pi$ Plasmon	290.6 – 290.9

Table 1 – Table of characteristic C_{1s} binding energies[130]

XPS is commonly used to identify functionalised carbon surfaces. Broadening of the C_{1s} signal in carbon nanotubes has been used as evidence for surface functionalisation due to the increase in the contribution from the defect site carbon at 285.5eV with respect to that of graphitic carbon at 284.6eV.[131] Coleman *et al*[132] used XPS to identify the nature of the surface bonding in carbon nanotubes functionalised with phosphines. Further, various articles concerning the oxidation to graphene oxide and the subsequent reduction to graphene have been followed using XPS to confirm the removal of the oxygen functionalities from the carbon surface.[64] The carbon window for graphite oxide shows a very broad signal in the C_{1s} governing the inter-carbon bonding and the different carbon/oxygen surface functionalities (Figure 14). Reducing the graphene oxide with hydrazine reduced the carbon/oxygen contributions upon reinstating some of the original graphitic structure.

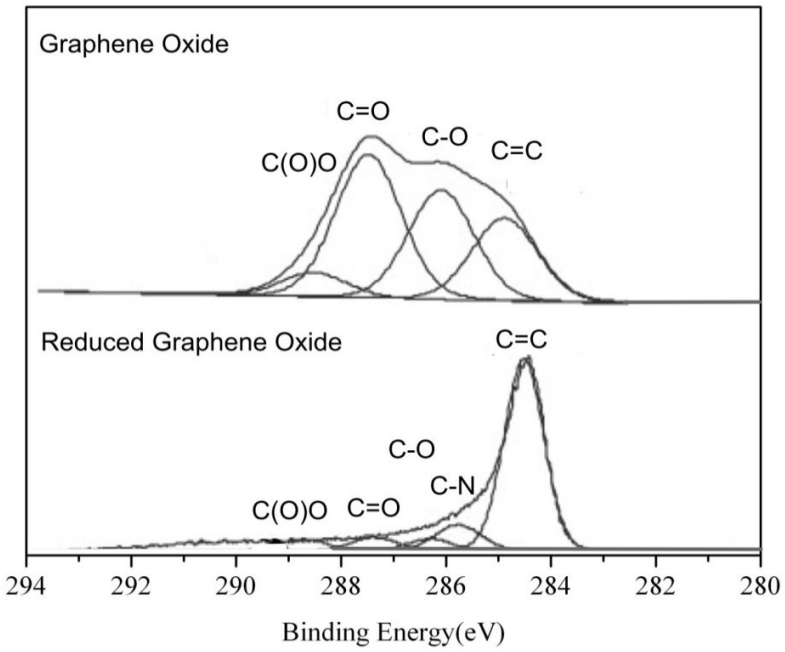

Figure 14 - XPS spectra showing C_{1s} signal for graphene oxide and the product of its reduction with hydrazine (redrawn from ref [64])

Electrical Measurement

Nanostructured carbon-based sp^2 networks are electrically conductive, as observed with the parent graphite. The four point probe method is commonly used for measuring the conductivity of metallic and semi-conducting thin films. These instruments use a long established technique to measure the average resistance of a thin layer or sheet, by passing current through the outer two points of the probe and measuring the voltage across the inner two points. The in-line probe setup used is illustrated in Figure 15. Details of the theory governing the relationship between the bulk resistivity *(ρ)*, and the voltage *(V)* and current *(I)* readings have been reported for various electrode geometries.[133,134] The bulk conductivity can be calculated as shown in Equation 2 where C' is the calibration constant

(dependant on probe separation s, dimensions a and d), the sheet resistance (R_s, Ω/□) and the film thickness, t are known.

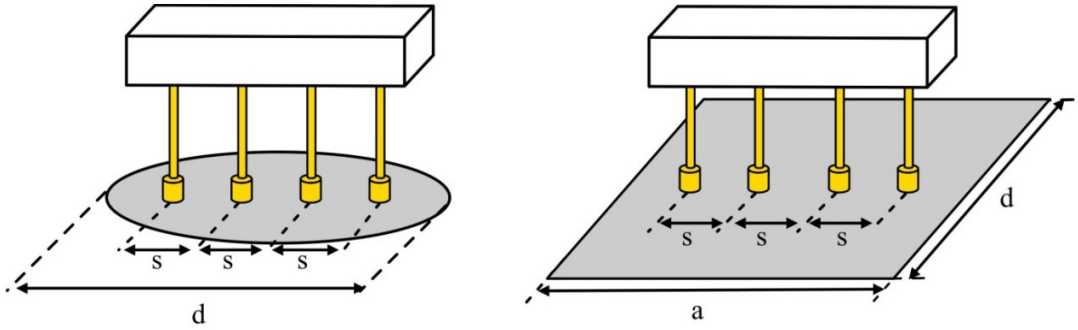

Figure 15 – Linear 4 point setup for electrical measurement (redrawn from ref [134])

$$R_s = \frac{V}{I} C'$$

$$\frac{d}{s} \to \infty, C' \to \frac{\pi}{ln2}$$

$$\sigma = \frac{1}{\rho} = \frac{1}{R_s t}$$

Equation 2 – Summary of bulk conductivity calculation

Standard four point probe measurements have been used to measure the conductivities of CNT[135] and graphene[85] thin films. Pang *et al*[136] have used the four point method to measure the effectiveness of graphene films prepared from graphene oxide as an anode in an organic field effect transistor. Graphene, formed on copper foil, has performed well as an anode material demonstrating a measured sheet resistance of 1.1742kΩ/□ in a field emission device.[137]

Atomic Force Microscopy

AFM is one of the most useful tools for imaging and controlling matter at the nanoscale. The information is gathered by following the contours of a surface with a mechanical probe. Scanning of the surface is facilitated using piezoelectric elements which produce accurate and precise movements. Deflections of the cantilever (in the z direction), caused by the probe encountering surface features during scanning, are followed using a laser, which is reflected from the top of the cantilever onto the detector (Figure 16). Changes in the position of the laser along the photodetector are used to build up a 3D picture of the sample. In TappingMode™, the cantilever is oscillated up and down at near its resonance. A tapping AFM image is therefore produced by following the height associated with periodic contact of the tip with the sample surface. "Tapping" lessens the damage to the surface and the tip, compared to use in contact mode and are useful for samples which are sensitive to mechanical force.

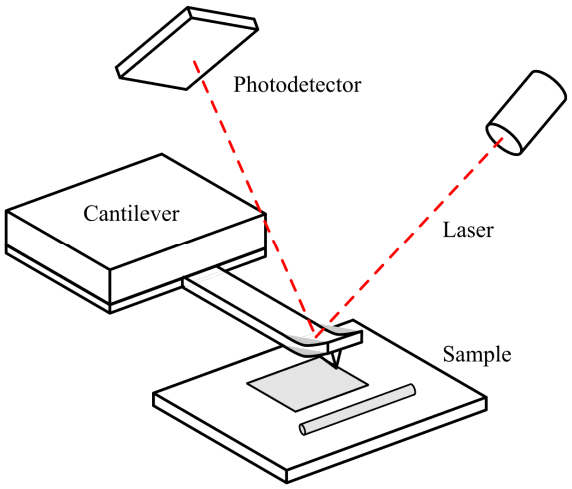

Figure 16 – Schematic diagram of AFM setup

AFM is also a common technique used to study the sheet-like nature of graphene and graphene oxide to characterise the average platelet size and thickness.[64] Additionally

the technique has been employed to measure the mechanical properties,[12,138] directly manipulate them on surfaces,[139] create nanoscale electronics through the use of heated tips to thermally reduce and pattern areas on single layer graphite oxide.[140] Some authors have reported inconsistencies associated with the height traces of single layer graphene. These have varied between the generally accepted 0.34nm[110,141] to heights of ≥1nm.[1,142] These discrepancies have been documented and reviewed in further literature.[143]

Electron Microscopy

Transmission electron microscopy (TEM) is the transmission of an electron beam through an ultra thin specimen, and as a result of interactions between the electron beam and the sample, an image is formed. Further, the image is magnified and focused onto an imaging device, such as a fluorescent screen or via a CCD camera (Figure 17). The TEM is used to characterize the structure of materials with very high spatial resolution. Information about the crystal structure and defects, morphology and composition can be obtained by a combination of imaging (2.4 Å point resolution) and selected area electron diffraction (SAED).

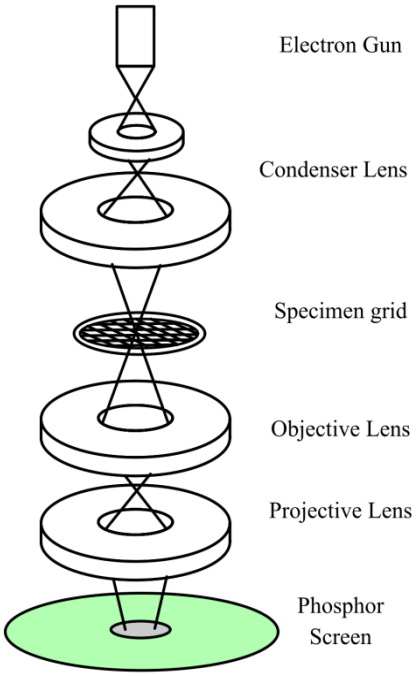

Figure 17 – Schematic diagram of transmission electron microscope

The problem associated with conducting TEM on carbon based materials is the effect that high accelerating voltages have on the materials themselves. Studies have shown the degradation that can be caused to CNTs by a TEM operating above 80keV, with 86keV being the energy at which carbon atoms can be displaced by ballistic ejection.[144-147]

TEM analysis of graphene sheets is also very common. Due to the 2D nature, TEM shows direct visualization of the graphene surface and, under high resolution, the poly-hexagonal structure can be directly observed by image filtering.[52] Furthermore, TEM is commonly used to probe the crystallinity of graphene through in-plane selective area electron diffraction (SAED) which displays two hexagonal sets of spots corresponding to the {1100} (2.13Å) and {2100} (1.24Å).[148,149] Due to the flexibility of graphene it has a

tendency to fold over which exposes the graphitic stacking where individual sheets can be observed displayed as dark lines. This method of layer counting has been used to investigate the thickness distribution in procedures where few layer graphene has been produced.

Due to the wide scope of structures carbon can take, TEM and especially electron energy loss spectroscopy (EELS) have been used to document and explore their natures. EELS involves the measurement of the energy distribution of electrons that have interacted with the atomic nuclei in a sample. The energy loss can be measured via an electron spectrometer. Many studies have explored the electron loss spectrum of different carbons, each with a distinctive fingerprint (Figure 18) allowing the identification of the structure and the confirmation of the presence of graphitic carbon and not free standing amorphous carbon films.[39,40] In carbon there is an increased number of electrons that pass out of the sample with 285eV - 300eV less energy compared to the initial energy. This energy loss is due to the promotion of core shell (1s) electrons to empty states above the Fermi level. The key components of the graphite spectrum are the $1s \rightarrow \pi^*$(285eV) and $1s \rightarrow \sigma^*$ (291-292eV) components in the carbon K edge, which are crucial in differentiating from diamond and the various amorphous carbons.[150,151] However, the similarities between graphene and graphite, allow the various contributions in the low and high loss regions to be assumed identical.[152] Consequently, this proves useful in the determination of the elemental composition, chemical bonding, valence/conduction band electronic properties and surface properties.

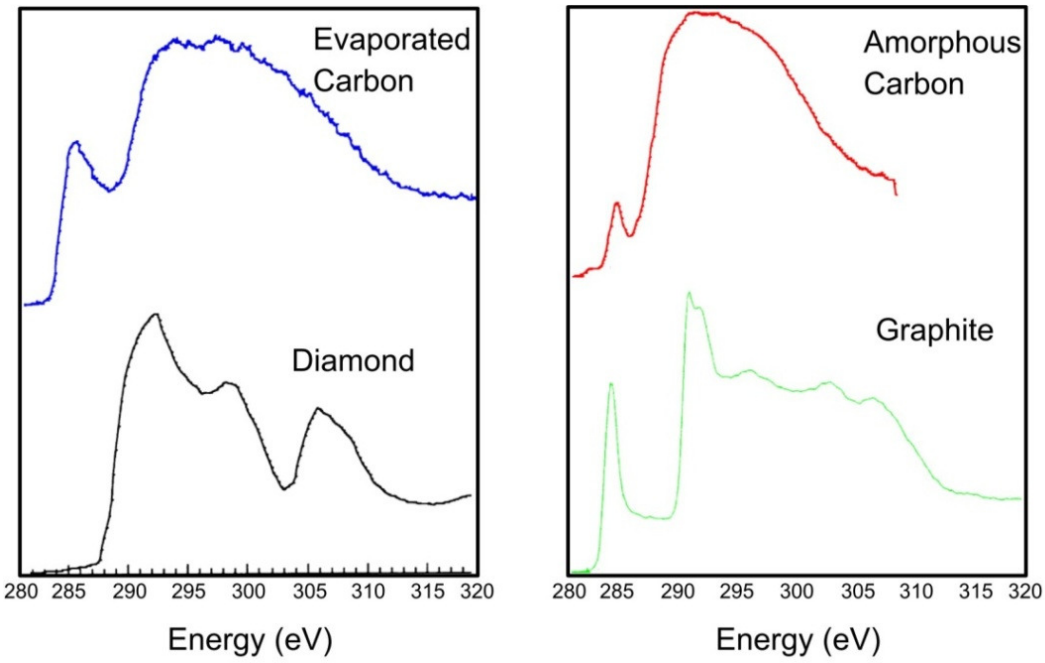

Figure 18 - Example K-edge EELS spectra of various varieties of carbon products.

The scanning electron microscope (SEM) images the sample surface by scanning it with a high-energy beam of electrons and detecting secondary (electrons produced as a result of ionisation) and backscattered electrons (primary electrons reflected back by elastic scattering). The electrons interact with the atoms within the sample, producing signals containing information about the sample's surface topography and composition. In general, the image resolution of an SEM is approximately one to two orders of magnitude poorer than that of a TEM, so it isn't as widely employed to image individual sheets of graphene. However, as SEM imaging relies on surface scattering processes in contrast to transmission, it is able to image and analyse large samples in the order of a centimetre in size and, depending on instrument settings and design, has a good depth of field compared to an optical microscope. Therefore, SEM can produce images that are good depictions of a bulk sample. Due to these advantages SEM has been exploited to analyse large sections

of graphene from fabricated devices or large area films, both via imaging and the EDX/WDX (energy dispersive/wavelength dispersive X-ray spectroscopy) for chemical analysis, to show their uniformity, coverage and intrinsic wrinkled nature before substrate transfer.[86]

Dynamic Mechanical Analysis

Dynamic mechanical analysis (DMA), is popular for studying the mechanical and thermal properties of polymer systems, polymer matrices and the effect nanoscale fillers, such as CNTs, graphene and nanoclays, can have on the parent polymer.

Upon application of a sinusoidal force (stress) to a material, deformation (strain) occurs, from which the magnitude and time lag (δ) of the frequency response can be measured. Hence, it is possible to calculate the energy stored in the system (storage modulus), the energy from heat dissipation (loss modulus) and the ratio of the two (tan δ). Below the glass transition, (T_g) polymer chains have relatively little mobility due to intermolecular interactions giving a strong frequency response under applied strain. When the temperature approaches the glass transition these chains gain energy from the increase in temperature, making them more mobile and as a result reduces the frequency response, resulting in a decrease in the storage modulus. This step behaviour is one method used in DMA to elucidate this position. Furthermore, there is a rise in the heat dissipation as the polymer softens due to the increased chain mobility causing an increase in the loss modulus to a maximum value. As the temperature travels through the T_g, a peak in the tan δ is observed due to the various energy changes during the transition. This tan δ maximum is often used as a measure of the change in the thermal properties of the polymer matrix

upon the inclusion of doped materials.[153] These glass transition shifts have been observed in several systems incorporating CNTs (both single[154] and multiwalled[155,156]), nanoclays[157-159] and graphene oxide.[28,160]

In addition, the accurate tracking of sample deformation under constant stress is beneficial. Under this applied stress (σ) the DMA technique is able to measure the change in the degree of strain (ε) incurred, which, at low applied stress, is linear as outlined by Hooke's law and the gradient, defined as the Young's modulus or stiffness of the material.

$$\sigma = \frac{3PL}{2bd^2} \qquad \varepsilon = \frac{6Dd}{L^2}$$

Equation 3 – Calculations of stress (σ) and strain (ε) based on the 3 point bend geometry. The given parameters are the load at a given point on the stress/strain curve (P, N), support span (L, mm), specimen width (b, mm), specimen depth (d, mm) and deflection length (D, mm).

X-ray powder diffraction

X-ray diffraction (XRD) is a versatile, non-destructive technique that reveals detailed information about the chemical composition and crystallographic structure of materials. The wavelength of some x-rays fall in the angstrom range and therefore their paths can be interfered with by interacting with atomic nuclei. Interaction of the x-rays with the sample produces diffracted beams which relate to the interplanar spacing in a crystalline system. The value of 2θ (defined as the angle between the incident and diffracted beams) is related to the interplanar spacing by Bragg's Law.[161] The peaks in the intensity versus 2θ can be used to identify a material, its morphology and crystalline size.

$$n\lambda = 2dsin\theta$$

Equation 4 – Relationship between d-spacing (d), X-ray wavelength (λ) and scattering angle (θ) as outlined by Bragg's law

XRD has been previously used to examine the crystalline structure of graphite[162] and graphene oxide.[163,164] Graphite has a characteristic peak with a d-spacing of 0.34nm (002) corresponding to the interlayer spacing. XRD is commonly used to examine the success of graphite oxidation methods. Upon oxidation the 002 peak shifts to a lower value of 2θ due to the increase in the interlayer spacing associated trapped water molecules.[164] Subrahmanyam et al[62] have used XRD to compare the graphene products of camphor decomposition on nickel, nanodiamond pyrolysis and expanded graphene oxide in terms of thickness. They used the Scherrer equation to compare c axis crystal size (assumed to be the thickness of the graphene materials) by analysis of the 2θ position and full width at half maximum of the 002 peaks. A single peak was observed for Camphor decomposition and gave an average layer thickness of 17nm. Graphene oxide and combusted nanodiamond had more complex 002 peaks and were deconvoluted. The thickness of graphene oxide was found to exist in 2 fractions, 1 and 5nm, whereas nanodiamond combustion produced thicknesses of 2 and 29nm.

3. SPRAY PYROLYSIS ROUTES TO FEW LAYER GRAPHENE

3.1 Spray pyrolysis of sodium ethoxide in ethanol

Spray pyrolysis or injection chemical vapour deposition is a commonly used technique for the deposition of thin films.[165,166] The precursor solution is forced into a fine mist by a carrier gas at high pressure and is instantly pyrolysed at elevated temperature and condenses on a surface. Using this technique the flow of the source and the speed at which the product forms can be closely controlled by variation of the flow of gas.

This technique was investigated as a way of creating a high yielding continuous process for the formation of graphene from ethanolic solutions of sodium ethoxide. Sodium ethoxide has been previously explored as a carbon source for graphene via the decomposition of a solvothermal precursor.[110] By reacting metallic sodium and ethanol under solvothermal conditions over the period of three days, a salt product was derived which when combusted in air gave a solid black product which was identified to be graphene by the authors by TEM and AFM. The authors comment that three days is required to make the precursor compound that gives 0.5g of graphene. This is a batch type procedure and is not ideally suited for mass production where more continuous approaches are preferred.

Spray pyrolysis was explored as a means to inject the precursor material, a solution of sodium ethoxide in ethanol, into a furnace using an aerosol nebulizer. The generated aerosol decomposed in the hot zone of the furnace and the product condensed onto the walls outside the hotzone of the reactor.

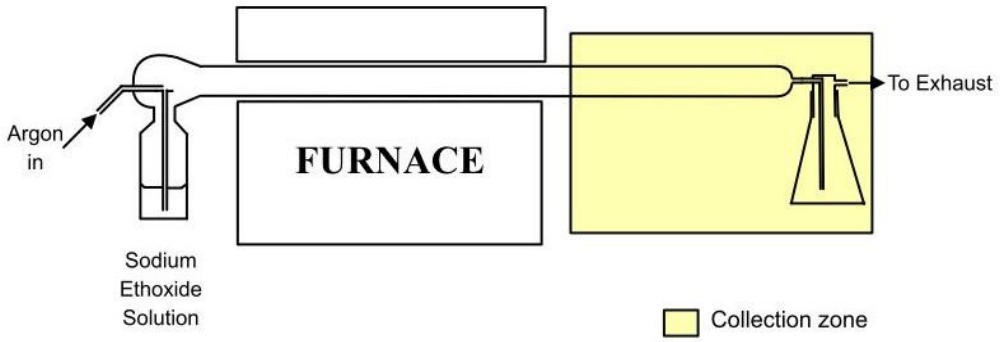

(a)

(b)

(c)

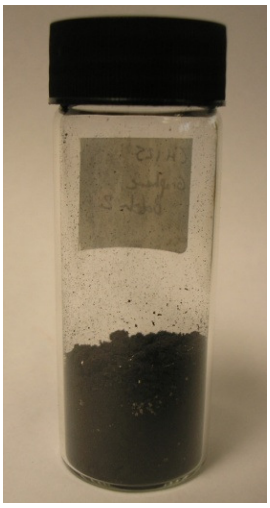

Figure 19 – (a) Diagram depicting typical experimental setup, (b) spray bottle and (c) raw graphene powder

$$EtOH_{(l)} + Na_{(s)} \longrightarrow NaOEt_{(aq)} + 1/2H_{2(g)}$$

Equation 5 – Synthesis of sodium ethoxide from ethanol and metallic sodium

XPS shows the presence of graphitic carbon, confirmed by its characteristic peak at 284.6eV, in both the raw and the purified samples.[167] Integration of the peak areas associated with the Na_{1s}, C_{1s} and O_{1s} (peak position shown in Figure 20a) showed sodium to be present at ~15at% and confirmed to be in the carbonate form from the intensity of the C_{1s} at 289.4eV.[168] The effectiveness of the purification with HCl is demonstrated by the large change in intensity associated with the Na_{1s} signal from 15 to 0.97at%.

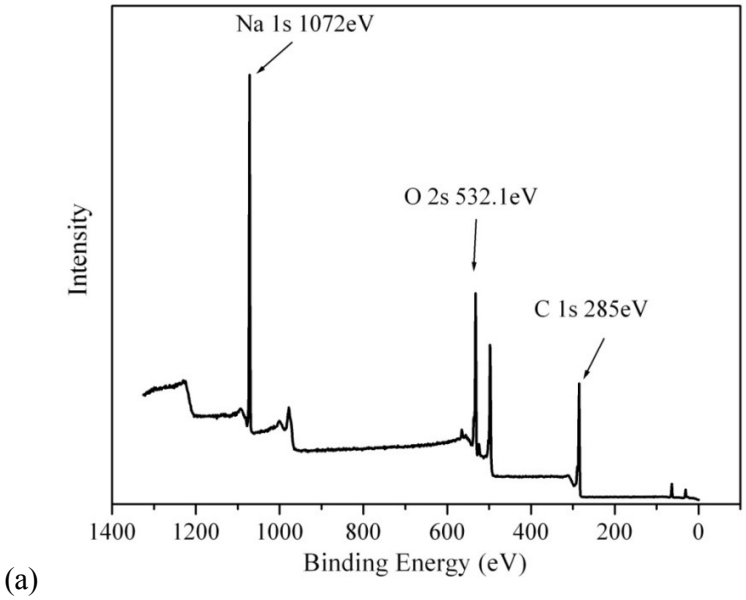

(a)

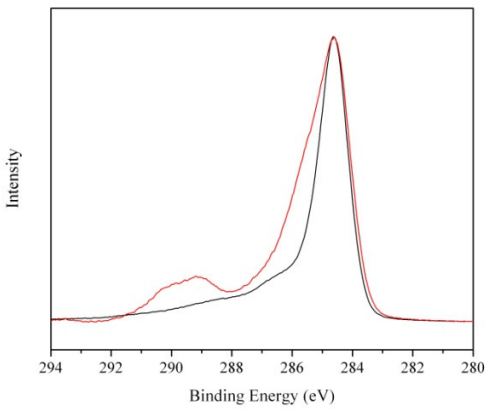

(b)

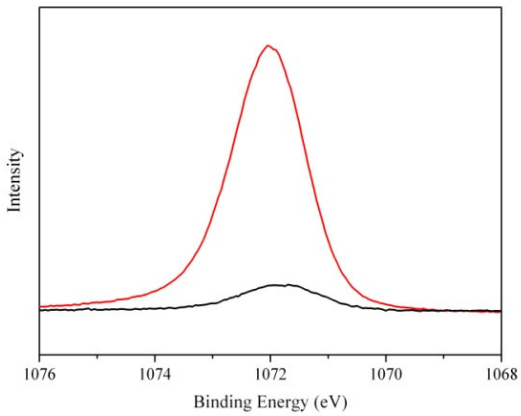

(c)

Figure 20 - (a) XPS survey scan of raw graphene powder, (b) high resolution C_{1s} spectrum and(c) high resolution Na_{1s} spectrum of raw (red) and purified (black) graphene product.

Deconvolution has been used in the literature to assess the quality of graphene samples from the reduction products of GO[64] and from liquid exfoliation.[51] The spectra were deconvoluted to show the contributions for the carbon-carbon and carbon oxygen functionalities as commonly used in the literature.[51,64,67,169] The nature and use of contributions in XPS were discussed in chapter 2 and can be used to identify the presence of oxidised graphene material. The backgrounds to the spectra were subtracted according to the Shirley line shape (the sigmoid line shape that best describes the background step associated with most XPS peaks),[170] the sp^2 contribution modelled asymmetrically as reported for HOPG,[171] and the carbon/oxygen functionalities using standard Gaussian line shape.

The C_{1s} spectra of the purified material (Figure 21) shows no large contribution in the region of 288-289eV which would indicate the identity of the sample to be graphene oxide. The contributions assigned to the purified C_{1s} peak showed graphitic carbon contribution of 79% and to only have 6% sp^3 carbon content. In comparison amorphous carbon show them to have much higher sp^3 contents in the region of 40 – 50%.[172,173] Graphene oxide reduced by hydrazine showed a increase in the sp^2 contribution from 21% to 75%.[169]

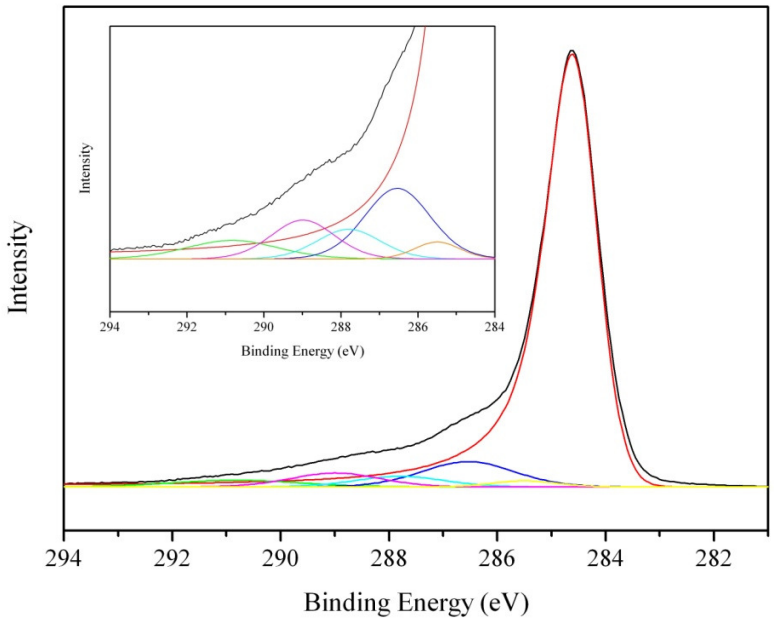

Figure 21 – Deconvoluted XPS spectrum of purified product using Shirley background subtraction. C=C (red) C-C (yellow), C-O (dark blue), C=O (light blue), C(O)O (pink) and π Plasmon (green) contributions to C1s peak are shown

The Raman spectrum of the graphene product (Figure 22) is similar to that for carbon nanotubes as described by Ferrari,[110,174] without the radial breathing mode which characterises the tubular structure of SWNTs. The as-produced material shows the characteristic G (graphitic carbon) band peak at 1592cm^{-1} and large D band as 1370cm^{-1}. The large D band could be due to the presence of oxygen defects on the sheet surface (as in graphene oxide) or small platelets with carboxylic acid and alcohol functional groups at the edges. This is further complicated by the fact that the carbon-carbon stretches in amorphous sp^3 hybridised carbon also lie within the D band window. The laser spot of a Raman microscope is typically a micron scale in size which causes additional problems in that, due a graphene sheet's tendency to overlap one another due to favourable π-π interactions, there is a high probability of exciting numerous edge sites within that micron

focal point. This may be why such a high intensity ratio between the two peaks is observed (I_D:I_G *ca* 1). The presence of graphene oxide can be ruled out due to the absence of significant intensity in the carbon/oxygen group area in the XPS C_{1s} spectrum.

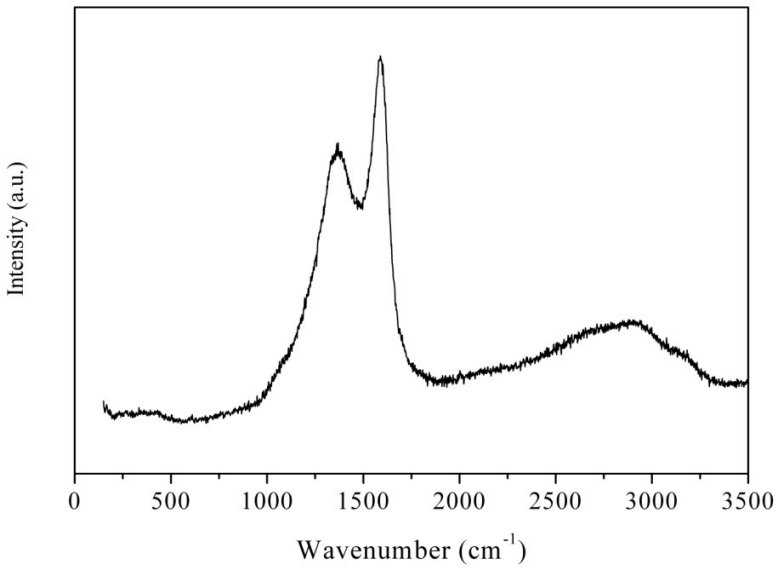

Figure 22 - The Raman spectrum of purified graphene powder displays the D, G and G' bands are displayed at 1370cm^{-1}, 1592cm^{-1} and 2678cm^{-1}.

Fourier transform infrared spectroscopy (FTIR) allows us to analyse the structure of the product that has been synthesised. There is no C=O peak suggesting that graphene has been made and not GO. The weak stretch at 1580 - 1600cm^{-1} in the FTIR has been observed in graphene samples produced from parent graphite and this has been suggested as the stretching vibration for the graphene backbone.[175] There is evidence for some C-O functionality on the surface (possibly hydroxyl or epoxide also seen in the XPS deconvolution) due to the stretches in the region 1100 – 1300cm^{-1}. The broad hydroxyl peak at 3500cm^{-1} is probably due to tightly bound water molecules and possibly a small amount of surface hydroxyl groups.

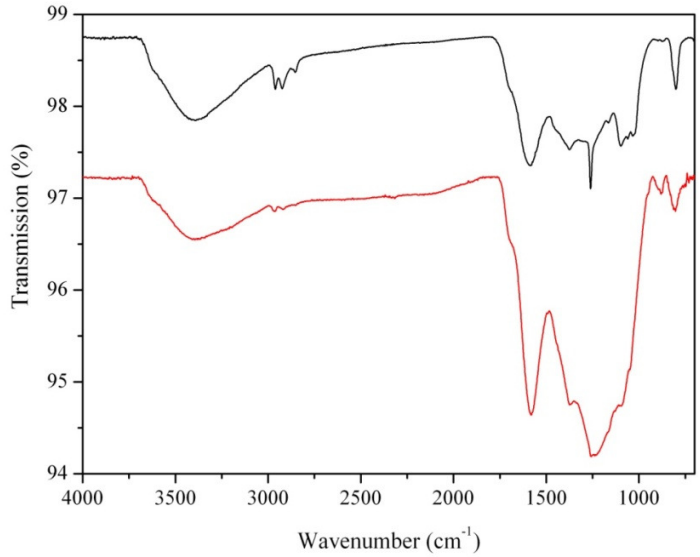

Figure 23 – FTIR spectra of raw (black) and purified (red) material. The peak at 1580 – 1600cm^{-1} has been suggested to be present in samples of graphene

By using scanning electron microscopy (SEM) the structure of the powder removed from the furnace could be studied. TGA and XPS have already shown that there is a high sodium salt content in the material and from the SEM of the material coated onto silicon substrate from diethyl ether, structures of various sizes could be defined (Figure 24a). Energy dispersive X-ray (EDX) spectroscopy showed these structures to be made up of mainly carbon with small amounts of sodium and oxygen. By enhancing the images, small bundled structures were observed in the surface indicating that these structures were agglomerations of the carbon platelet material encased within large particles of the metal salts (Figure 24c) after exposure to light sonication in water.

(a)

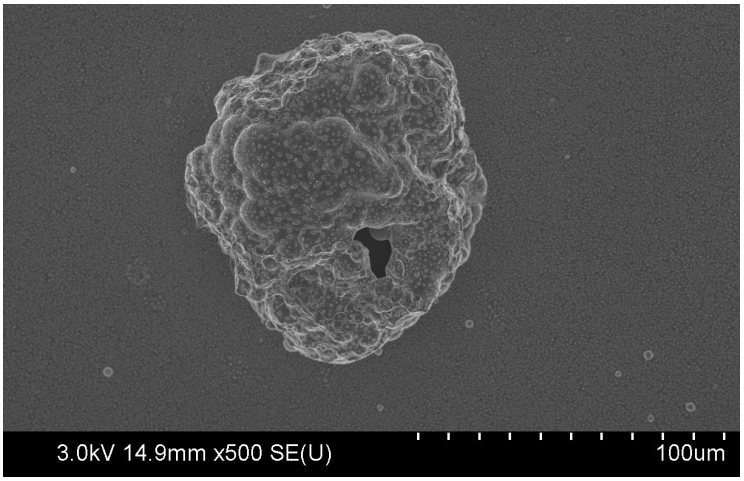

(b)

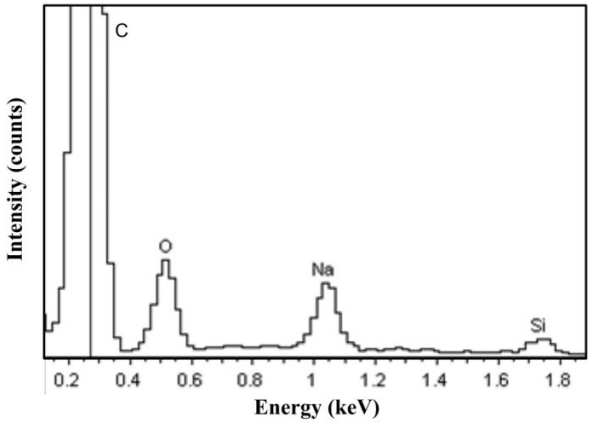

(c)

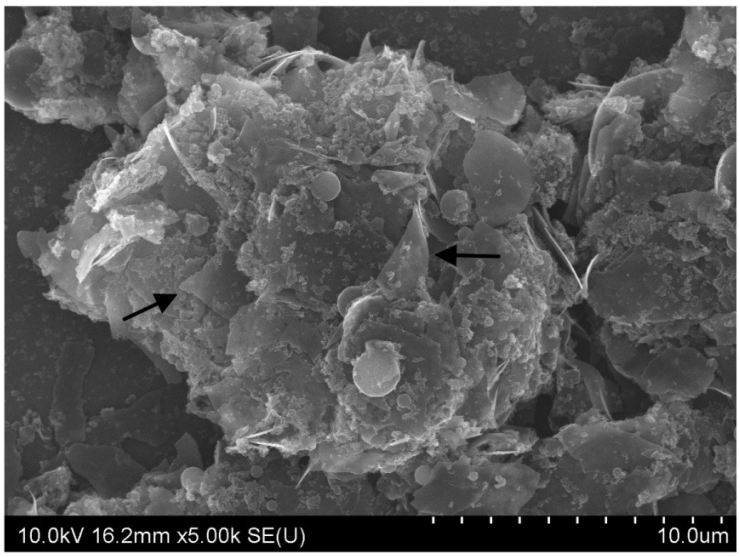

Figure 24 – SEM image of (a) large sodium carbonate particle from raw product, (b) SEM-EDX of the particle in (a) and (c) platelet agglomerations produced by light sonication in water. Black arrows show the presence of sheet like carbon deposits within the broken up structure.

After purification with acid in an attempt to remove the sodium carbonate salt, SEM of samples spin coated onto silicon show evidence of the flat platelets normally associated with exfoliated graphite products and the presence of smaller sodium impurities. Energy dispersive x-ray spectroscopy (EDX) of these platelets show that they are completely made of carbon with no traceable oxygen content. The platelets are semi-transparent to the electron beam suggesting that they are relatively thin. SEM relies on the detection of secondary electrons (electrons ejected from sample) which are generally low energy (<50eV). The penetration depth of electrons with accelerating voltage of less that 100eV (the smallest energy that can be modelled) in carbon is <5nm measured using Monte Carlo simulations in Casino software.[176] Therefore, to be observed by the secondary electron detector, the top graphene sheet is less than 5nm in thickness for the secondary electrons from sheets below to penetrate the surface.

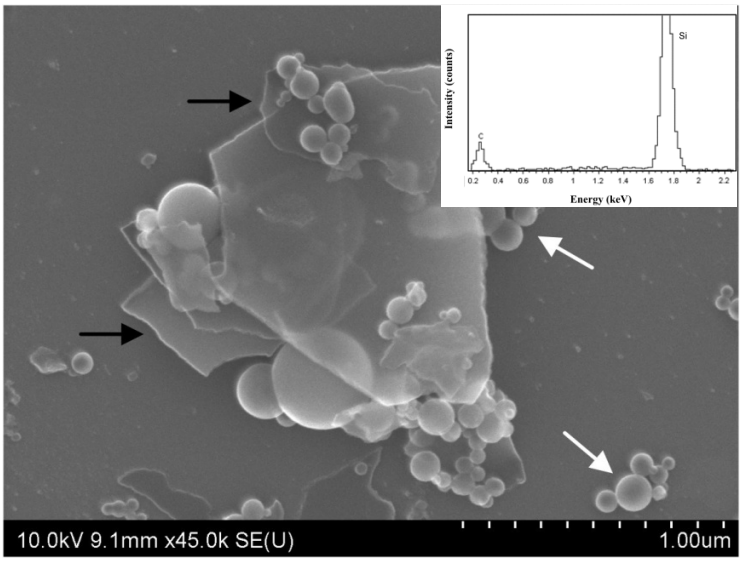

Figure 25 – SEM of exfoliated particles after purification with 5M HCl. Black arrows show places where carbon sheets lie and white arrows show the presence of remaining small sodium by-product (inset) EDX scan of purified carbon platelet.

Transmission Electron Microscopy (TEM) was used to further investigate the carbon structure. By depositing a dilute solution of the purified material in ethanol onto a lacey carbon TEM grid the structures can been seen as lying in sheets. This suggests that the structure that has been synthesised is flat layers of graphene and not other structures of graphite like nanoribbons or nanoscrolls. TEM also confirms the SEM observation of micron scale sheet size but the relative thickness of these sheets is difficult to determine, as few sheets showed any folds at the edges. It was however possible to observe some frayed edges which show multiple sheets underneath (Figure 26). Selected area electron diffraction (SAED) of these sheets shows the two rings corresponding to the expected diffraction planes.[149] These ring-like diffraction patterns suggest that the graphitic carbon synthesised has a turbostratic structure.[177] Turbostratic carbon is a graphitic material with AB stacking where the graphene layers are randomly rotated and translated relative to one another. Rotational faults in the AB stacking of few layer graphene prepared by micromechanical cleavage[148] and solvent exfoliation[178] have shown ring-like patterns in both the surface fast Fourier transform and the SAED. As turbostratic graphite is an extreme form of these stacking faults, the rotation and translation of many layers with respect to one another leads to the observation of the rings shown in the inset of Figure 26b. Even though thick platelets are observed it should be noted that the turbostratic nature of the material is important as studies have shown that the layers in turbostratic graphite have a similar Dirac-like spectrum as observed with free standing graphene[179] due to the rotation and translation of the layers resulting in electronic decoupling.[180,181]

(a)

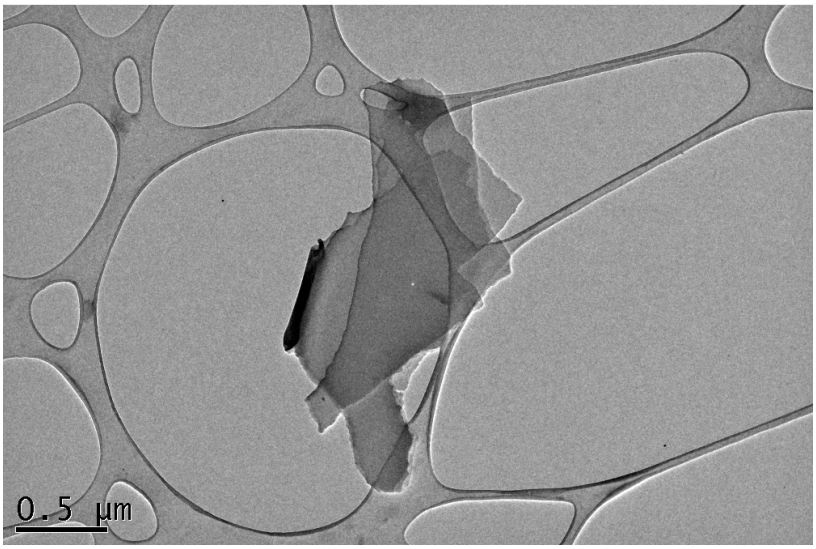

(b)

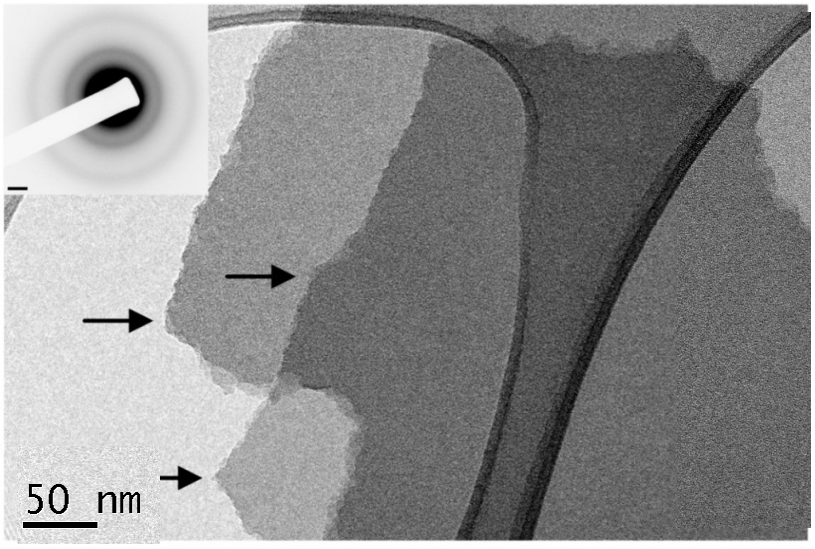

Figure 26 – (a) and (b) TEM images of deposited samples from probe sonicated ethanolic solutions on lacey carbon coated 300 mesh copper grids. Black arrows show areas of multilayer stacking. The SAED pattern (inset of b) of the platelets shown exhibits two concentric Debye rings which index as the in-plane *hki0* reflections {1100} (2.13 Å spacing) and {2110} (1.23 Å spacing)

The presence of the 001 reflection in addition to the hki0 in the transmission XRD spectrum (Figure 27) indicates the presence of the turbostratic structure. The {1100} at 2.13Å (2θ = 22.37º) and {2110} at 1.23Å (2θ = 39.26°) peaks are characteristic of graphite, whereas the 4.09 Å (002, 2θ = 11.6º) interlayer spacing is larger than the literature value of 3.4 Å. The interlayer distance is slightly larger than that found in graphite which it likely due to the turbostratic nature. Computational studies of the interlayer interactions in two-dimensional graphitic structures have shown that they are governed by both orbital and van der Waals interactions. Therefore, reduction of the orbital interaction causes the interlayer spacing to increase.[182,183] In the turbostratic graphite, there is less alignment among the carbon atoms between the layers, which reduces the orbital interactions and results in the wider interlayer spacing.

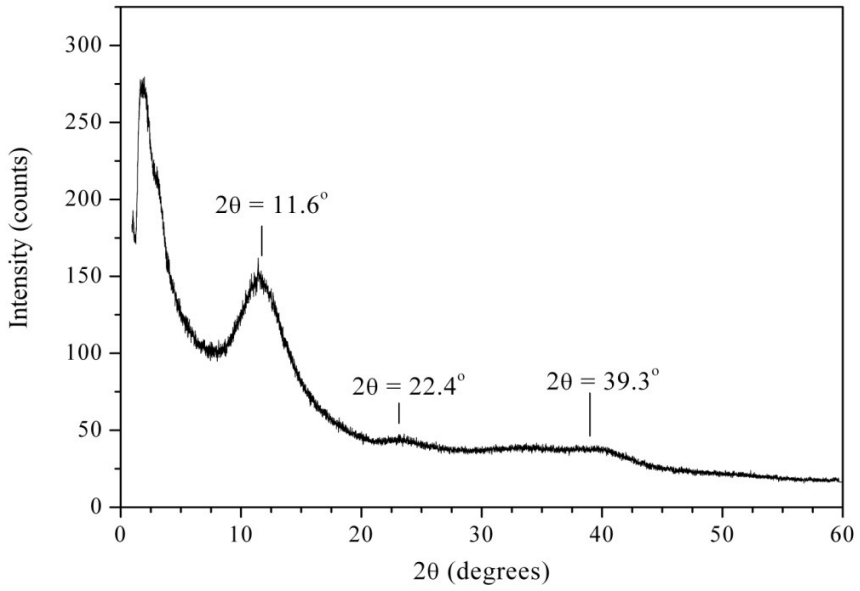

Figure 27 –product X-ray powder diffraction pattern of the graphene platelets (λ = 0.826Å). The 002 interlayer distance is at 4.09 Å spacing (2θ = 11.60°), {1100} at 2.13 Å spacing (2θ = 22.37°) and {2110}at 1.23 Å spacing (2θ = 39.26°). Spectrum taken at Diamond Beamline I11 (λ = 0.826Å)

Prolonged sonication of the graphene platelets can help separate the graphene sheets. Atomic force microscopy (AFM, Figure 28) of a sample of low concentration ($5\mu gmL^{-1}$) deposited on freshly cleaved mica shows the presence of thin graphene platelets, Sectional analyses of these flakes show them to be flat sheets with a height of approximately 1.4 nm (~ 4 layers). The surface of the sheet is shown to be rough, which could be due to the fluctuation of the AFM tip close to the limit of thicknesses it can probe. The AFM also confirms the presence of few-layer sheets in the sample that were difficult to observe by the TEM.

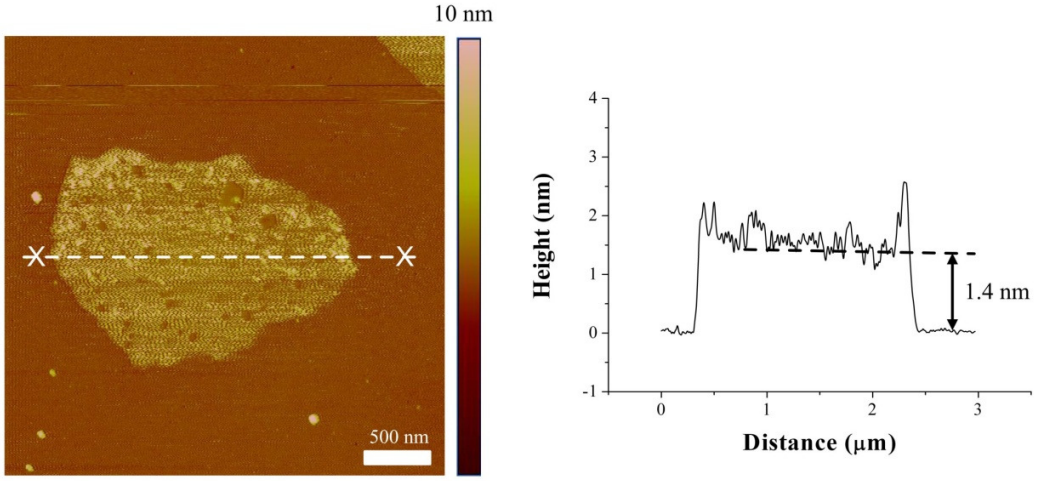

Figure 28 – AFM image (height mode, 3 x 3 μm, 10 nm height) of graphene flake on freshly cleaved mica surface, height topography along the mid regions

Electrical measurements were conducted on vacuum filtered suspensions of the spray pyrolysis products, assuming the product showed a similar density to graphite (d = 2-2.4 gcm^{-1}) to derive the film thickness. One milligram of the product was filtered over a Whatman mini filtration set (diameter = 1.75cm) from which a thickness of 2.4μm was calculated. Based on this measurement the sheet resistance ($4.4x10^7$ and $7.5x10^5$ Ω/□) was

measured using the 4 point method, and showed conductivities of 0.01 Sm^{-1} and 0.55 Sm^{-1} for the raw and purified spray pyrolysis products. This value was comparable to that found in the purified product from the solvothermal ethoxide product (0.05 Sm^{-1})[110] but lower than the value obtained for thin films prepared from graphene exfoliated from graphite with surfactant (35 – 1500 Sm^{-1})[52] and NMP (6500 Sm^{-1}).[51] This could be due to various factors including overestimation of the film thickness, ineffective exfoliation of the material (most films vacuum filtered from good solvents like NMP, DMA shown to disperse and exfoliate graphene from flake graphite[50]) and the remaining presence of insulating salt by-products. Also very rarely are the measurement conditions given for the measurement of these films and so variation in the methods may also account for differences. The films are not continuous and so achieving the low sheet resistances associated with continuous graphene films grown on metal foils aren't possible due to the numbers of junctions between platelets contributing to elevated contact resistance.

3.2 Variation in product using sodium hydroxide/ethanol

On an industrial scale the use of sodium as a precursor may make the route to the product problematic when scale up is taken into account due to the amount of hydrogen evolved by the procedure. An alternative way to make sodium ethoxide relatively cheaply would be to use the equilibrium between sodium hydroxide (NaOH) and sodium ethoxide in ethanolic solutions. It has been found that the equilibrium lies towards sodium ethoxide, even in solution with notable water content.[184]

$$NaOH_{(s)} + EtOH_{(l)} \rightleftharpoons NaOEt_{(aq)} + H_2O_{(l)}$$

Equation 6 – Synthesis of sodium ethoxide from sodium hydroxide and ethanol

Using the same procedure described in section 3.1 spray pyrolysis was carried out with sodium ethoxide synthesised by dissolving sodium hydroxide in ethanol at 40^{o}C and this produced few layer graphene. The presence of large plates as seen using the previous method were confirmed with the turbostratic structure (appendix Figure A 2a,b), but more interestingly platelets were also observed which showed a well ordered graphitised structure (Figure 29, appendix Figure A 2c and d). The selected area electron diffraction (Figure 29b) of these platelets shows the presence of hexagonal spots in the {1100} and {2110} planes. The intensity ratio between the spots in the {1100} and {2110} planes has been previously used by Hernandez et al[51] to discriminate between single and few layer graphene. Here, the intensity of the {2110} spots are greater than those of the {1100} and therefore are few layer. These platelets, which are much thinner than those observed in the graphene product from sodium/ethanol, may contribute to the turbostratic argument. These platelets showed no presence of polycrystalline domains, which can also give rise to ring diffraction patterns, suggests that the large platelets may be constructed of these much thinner sheets rotated and translated with respect to one another.

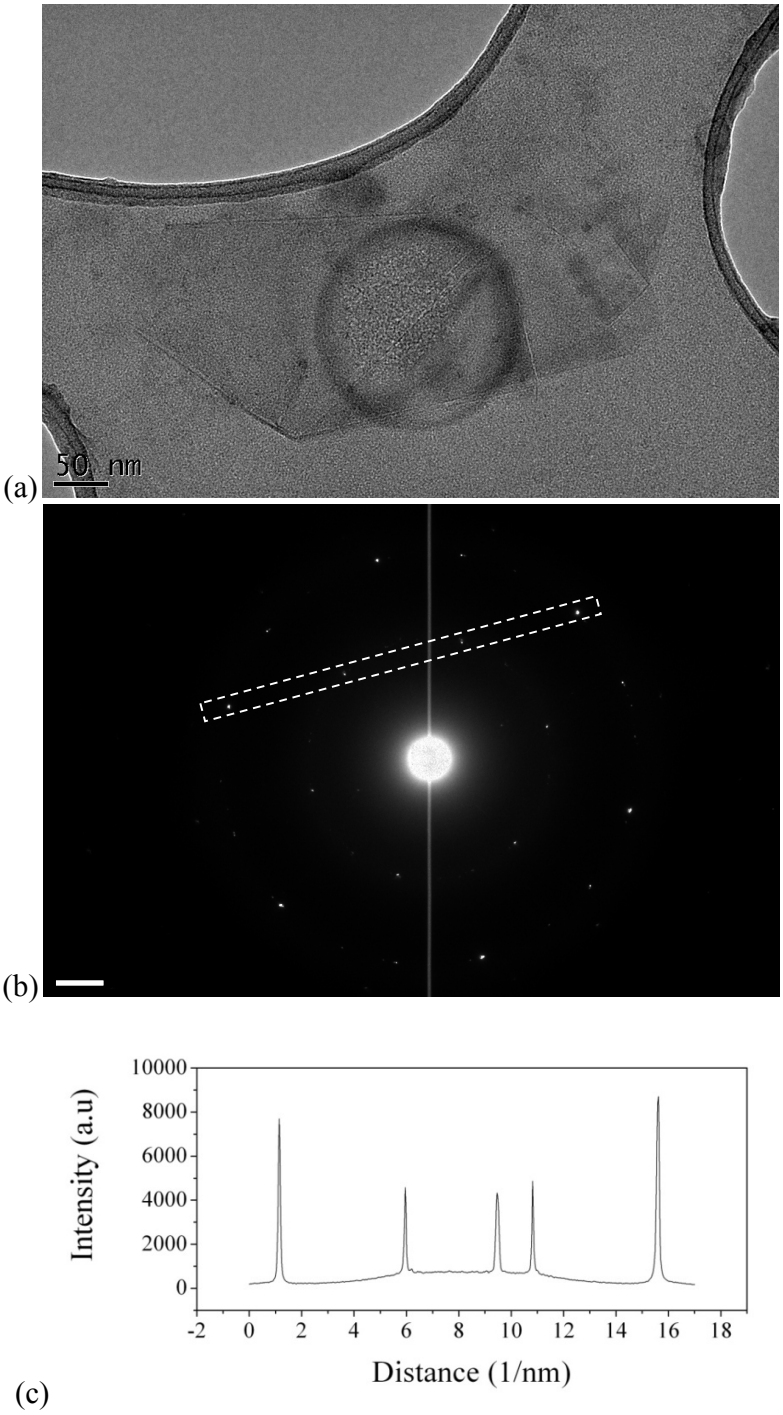

Figure 29 – (a) BF-TEM image showing well graphitized platelet of few layer graphene from the dispersion of EtOH/NaOH product in ethanol, and (b) electron diffraction pattern (scale bar 2 1/nm) associated with (a). (c) Plot of intensity versus distance for the area surround by white box.

The Raman spectrum (Figure 30a) of the few layer graphene produced from sodium hydroxide shows the characteristic peak of the D (1365cm^{-1}) and G (1590cm^{-1}). The I_D:I_G (*ca.* 1.1) is slightly higher than that measured in the few layer graphene produced from sodium/ethanol product (*ca.* 1) which may indicate a slight increase in oxidation. This appears to be in agreement with the appearance of the carboxyl stretch observed in the infrared spectrum (Figure 30b). In the XPS (Figure 30c) of the few layer graphene from sodium hydroxide/ethanol, a small ridge in the C_{1s} window is evident in the region where the carboxylic acid groups would be. This in turn shows a small increase in the contribution to the deconvoluted ketone/carboxyl signal *ca.* 289eV (10.35 compared to 9.03%) but in comparison to XPS studies of GO the level of oxidation is low.[185]

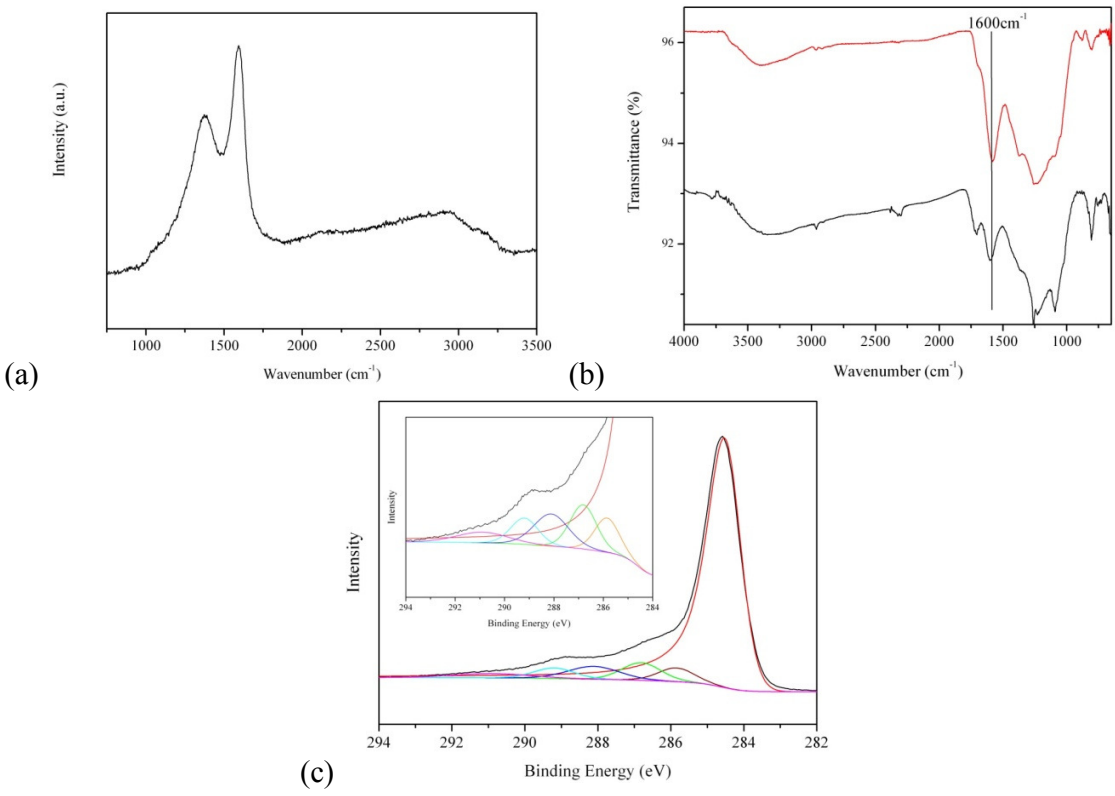

Figure 30 – (a) Raman spectrum (532nm) of sodium hydroxide/ethanol(b) FTIR spectrum comparing Na/EtOH product (red) and NaOH/EtOH product (black) (c) High Resolution C1s XPS of purified sodium hydroxide product. C=C (red) C-C(brown), C-O (green), C=O (dark blue), C(O)O (light blue) and π Plasmon (pink) contributions to C1s peak are shown

AFM conducted on few layer graphene synthesised from sodium hydroxide/ethanol product showed a wide variety of platelet sizes and thicknesses. Two main types of platelets were evident. Large platelets similar to those of few layer graphene using sodium metal/ethanol product having micron scale dimensions but are relatively thick compared to graphene (appendix Figure A 3). Centrifugation in DMF was used to remove the majority of the larger platelets in the attempt to isolate and visualise the smaller graphene platelets. Even though they were very difficult to find, a few small area platelets were found to show thicknesses in the range of 1 nm. These platelets seem to show similar scale and morphology to those indentified from the filtrate of oxidized arc discharge material.[104,186]

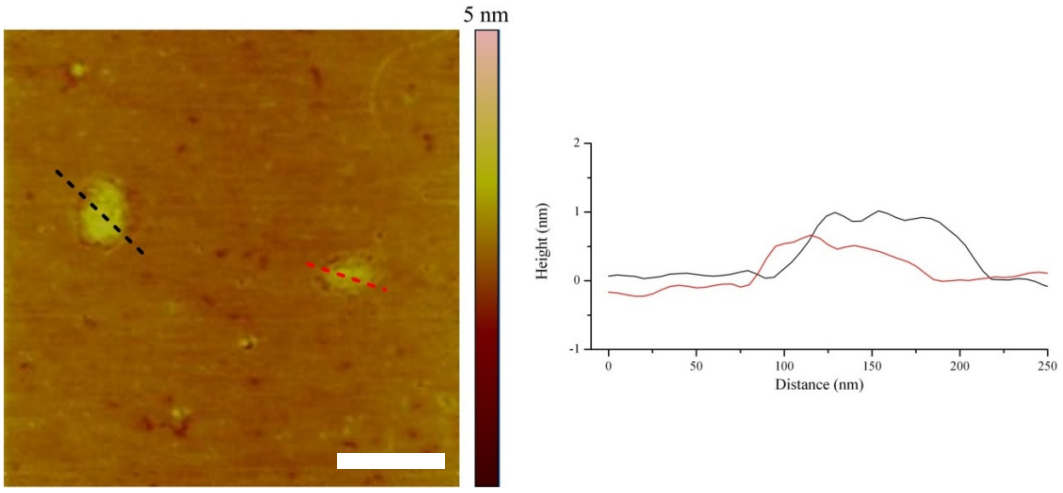

Figure 31 – AFM image (1x1µm, scale bar 250nm) of centrifuged solution of sodium hydroxide product in DMF spin-coated onto mica surface

3.3 Platelet production using chemical vapour deposition over sodium carbonate

It has been noted that sodium carbonate is a by-product of the injection pyrolysis in the process described in section 3.1. Due to the basic nature of sodium carbonate it will react with acids to form a sodium salt, carbon dioxide and water (Equation 7). As a result sodium ethoxide is formed when sodium carbonate is added.[187] Unfortunately, sodium carbonate is only slightly soluble in ethanol and so is unfit for the injection CVD process. The process devised is similar to the injection method but to promote the reaction between the carbonate and ethanol, the carbonate was held at 800°C (below its decomposition point) in the furnace in an ethanol atmosphere, with a similar set up used for CVD synthesis of carbon nanotubes.[188] It was noted that a run conducted without an ethanol atmosphere produced no change in the carbonate as would be expected.

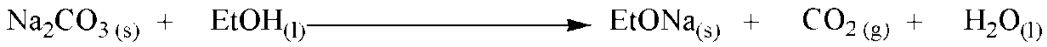

Equation 7 – Synthesis of sodium ethoxide from sodium carbonate using ethanol

One consequence of the change in synthesis method is that the carbon product spends much longer in the furnace that the previous materials. The purified product is dark grey rather than black, much in the way that graphite is dark grey whereas CNTs are black (appendix Figure A 4). It also behaves more like graphite in such a way that it is difficult to disperse in aqueous or organic phases. Raman spectroscopy (Figure 32) of the material displayed the D (1378cm^{-1}) and G (1592cm^{-1}) band (I_D:I_G ratio *ca.*1). Effective purification of the product is evident by the absence of the band associated with sodium carbonate at 1066cm^{-1}.[189]

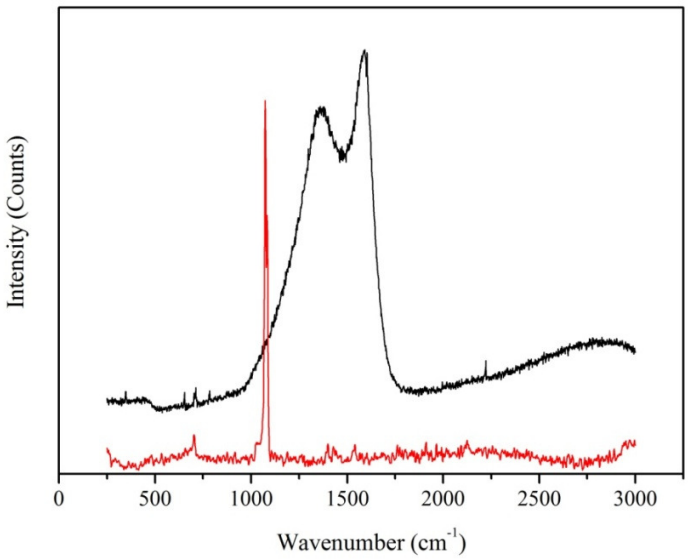

Figure 32 – Raman spectra of the sodium carbonate/ethanol product synthesised at 800°C (black) shows characteristic D (1378cm^{-1}) and G (1592cm^{-1}) bands. Raman spectrum of sodium carbonate (red) is displayed as a comparison

The microscopy of the graphene produced from sodium carbonate/ethanol shows the sheets to be much thicker than that of the spray pyrolysed methods. Very few of these platelets were found to be semi-transparent in comparison to those from the few layer graphene synthesised from the spray pyrolysis of sodium/ethanol. This may account for the difficulty in dispersing the material. Due to the large differences between the methodologies employed it is possible that the products could be remarkably different. The other difference is that the SEM (Figure 33) shows the lateral dimensions of the platelets to be much larger than that of the injection products. Platelets up to 8μm in length were observed, which may be due to the extended time period the sodium carbonate spent in the furnace exposed to ethanol. The perimeter of these plates show uneven textures associated with the presence of multilayer edges confirming a graphitic structure.

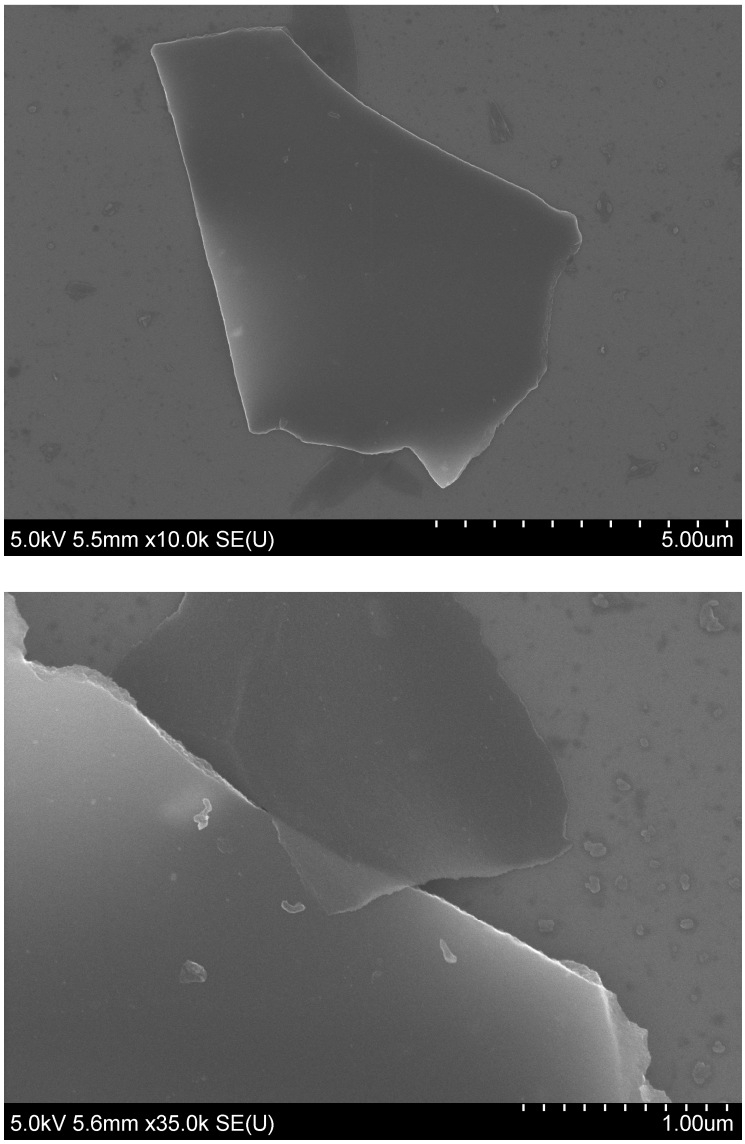

Figure 33 – SEM images of sodium carbonate/ethanol product deposited from N'N Dimethylformamide on silicon.

The multilayered structure is apparent from the TEM images (Figure 34b). SAED (insert Figure 34a) of the surfaces of these sheets exhibit the ring pattern associated with turbostratic graphite, observed in samples of the Na/EtOH product) and the EELS measurements (appendix Figure A 5) display the characteristic π* and σ* peaks present in the EELS spectrum of graphitic carbon.

(a)

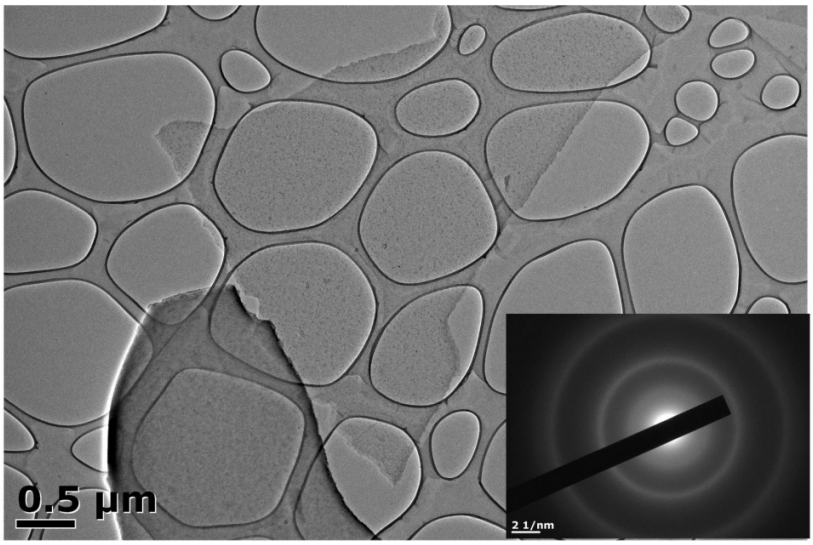

(b)

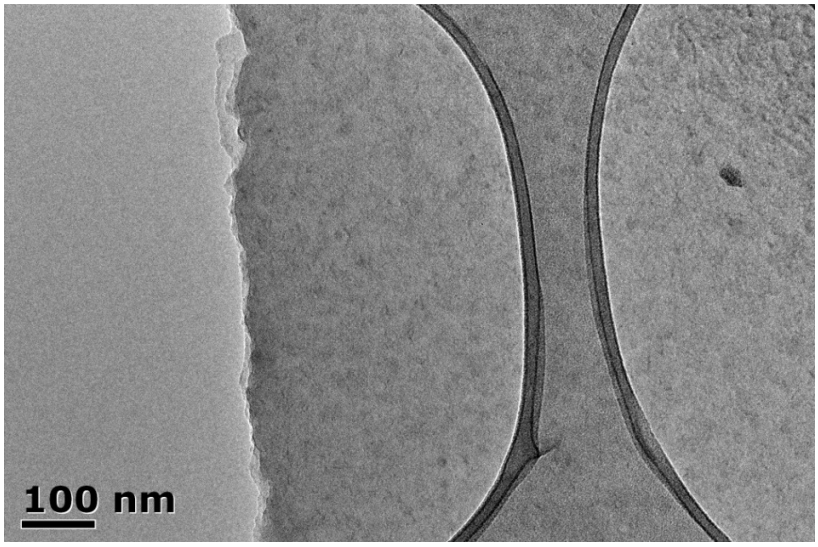

Figure 34 – TEM showing one of the thinner flakes associate with the sodium carbonate/ethanol product and its associated electron diffraction and (b) multilayer edge. Samples were deposited from N, N-Dimethylformamide suspensions allowed to settle overnight, onto TEM grids.

3.4 Discussion

Due to the problems of following the progress of CVD syntheses in-situ it is difficult to postulate an exact mechanism for platelet formation. Even in the field of CNT growth there are varied opinions governing how the feedstock is utilized and grown in the tube architecture. Introducing ethanol into the hot zone of the furnace without any dissolved sodium ethoxide showed no carbon deposition on the walls of the reactor. This suggests that the presence sodium ethoxide is important for the formation of the platelets Chandran and co-workers have studied the gaseous products of the thermal decomposition of various sodium alkoxides in inert atmosphere producing sodium carbonate and carbon.[190] However they do not elaborate on the structure of the produced carbon and so the two procedures cannot be compared. In addition ethanol is known to act as an in-situ reduction medium and has been previously used to create carbon nanostructures without the need of hydrogen pre-reduction.[191] Therefore the carbon source for the synthesis of these carbon platelets is most likely to be from the sodium ethoxide with the ethanol providing a reducing atmosphere which prevents the formation of amorphous carbon, commonly seen from hydrocarbon decomposition when forming carbon nanotubes.

Spray pyrolysis was also attempted using other precursors including titanium *iso*propoxide/*iso*propanol and sodium methoxide/methanol. These precursors produced no carbon as a result of spray pyrolysis, depositing white powders on the quartz reactor found to be titanium dioxide (TiO_2) and sodium oxide (Na_2O). Sodium isopropoxide and other transition metal ethoxides couldn't be used due to insolubility in the precursor solutions and therefore were not suitable for spray pyrolysis.

3.6 Conclusion

The issue that is restricting the use of graphene in many applications is efficient production. For several areas, composite materials for example require a few milligrams per gram of host material to enhance mechanical, thermal and electrical properties. In this chapter several routes to the synthesis of few layer graphene has been demonstrated based on the spray pyrolysis of sodium ethoxide as a method that is both simple and scalable for bulk production. The product of this was shown to be made up of turbostratic graphitic platelets under electron microscopy and, with further dispersion in ethanol or N, N'-dimethylformamide, the presence of few layer graphene could be seen by AFM measurements. XRD showed the presence of the graphitic 002 peak shifted to a lower value of 2θ, indicating an increased interlayer spacing previously shown with turbostratic graphite. XPS showed the C_{1s} maximum to be centred at 284.6eV. The material could be synthesized in bulk quantities, at rates of *ca* one gram per hour, providing an advantage to the composite market where large quantities of material are required. The use of sodium hydroxide produced a similar material and interestingly showed the presence of few layer graphene platelets, shown by the intensity ratio from the selected area electron diffraction. The absence of crystalline domains in these few layer platelets indicated that the ring diffraction patterns was likely to be a result of translated and rotated stacks of these few layer platelets. The use of sodium carbonate in an alternate procedure yielded material shown to be thicker indicated in the SEM, displaying rings in the electron diffraction patterns in addition to multilayered edges.

In the next chapter the properties of these materials are investigated in view of applications envisioned for graphene.

4. APPLICATIONS OF FEW LAYER GRAPHENE SYNTHESISED BY SPRAY PYROLYSIS OF SODIUM/ETHANOL SOLUTIONS

4.1 Thin transparent graphene films synthesised by spray pyrolysis of sodium ethoxide solutions

Graphene films are seen as an important step towards the development of devices that may supersede current silicon and indium tin oxide (ITO) based structures. At present, the largest graphene sheets commercially available for purchase are around 1000μm^2 produced using the "Scotch tape" method.[1] These are suitable for small scale electronic applications but are still quite expensive to purchase. CVD methods provide a route to much larger scale and patternable thin films for several electronic applications. Recently, sheets exceeding lengths of 1cm have been grown via CVD on thin nickel coated silicon wafers,[95] and 30 inches on copper foils[22] which have found use as transparent electrode materials under development at Samsung in Korea. There are several problems with using metal foils including metal etching, transfer and processing. Therefore synthetic methods that do not involve heavy metals for graphene production either on silicon for device manufacture or directly on transparent material are desired to negate the need for additional processing.

Direct synthesis of few layer graphene without the need for transition metals was introduced in chapter three. Inserting a substrate (quartz or silicon oxide/silicon) into the furnace prior to pyrolysis allows the deposition of graphene onto the substrate surface

forming large area films. Such films, when detached from the substrate support, showed a high reflectivity and metallic shine as observed by optical microscopy (Figure 35a). SEM was used to investigate the thickness and relative smoothness of the graphene films through analysis of film shards, which had adventitiously peeled away from the quartz support. SEM images revealed the defined edges of these to have an associated thickness of 300 – 350nm. In addition, SEM-EDX (Figure 35d) showed the film composition to be primarily carbon with trace amounts of oxygen only detectable at the very limits of the technique. This suggests that the film coverage is largely continuous with only a low number of oxygen defects present. It should also be noted that despite evidence of particles of sodium salts being observed in the surface images (see Figure 35c, white arrow), these are very small in comparison to the scale of the film. It should be noted that these films on quartz and silicon substrates required no preparatory coatings or electron filtering during SEM analysis, indicating good levels of conductivity within the films.

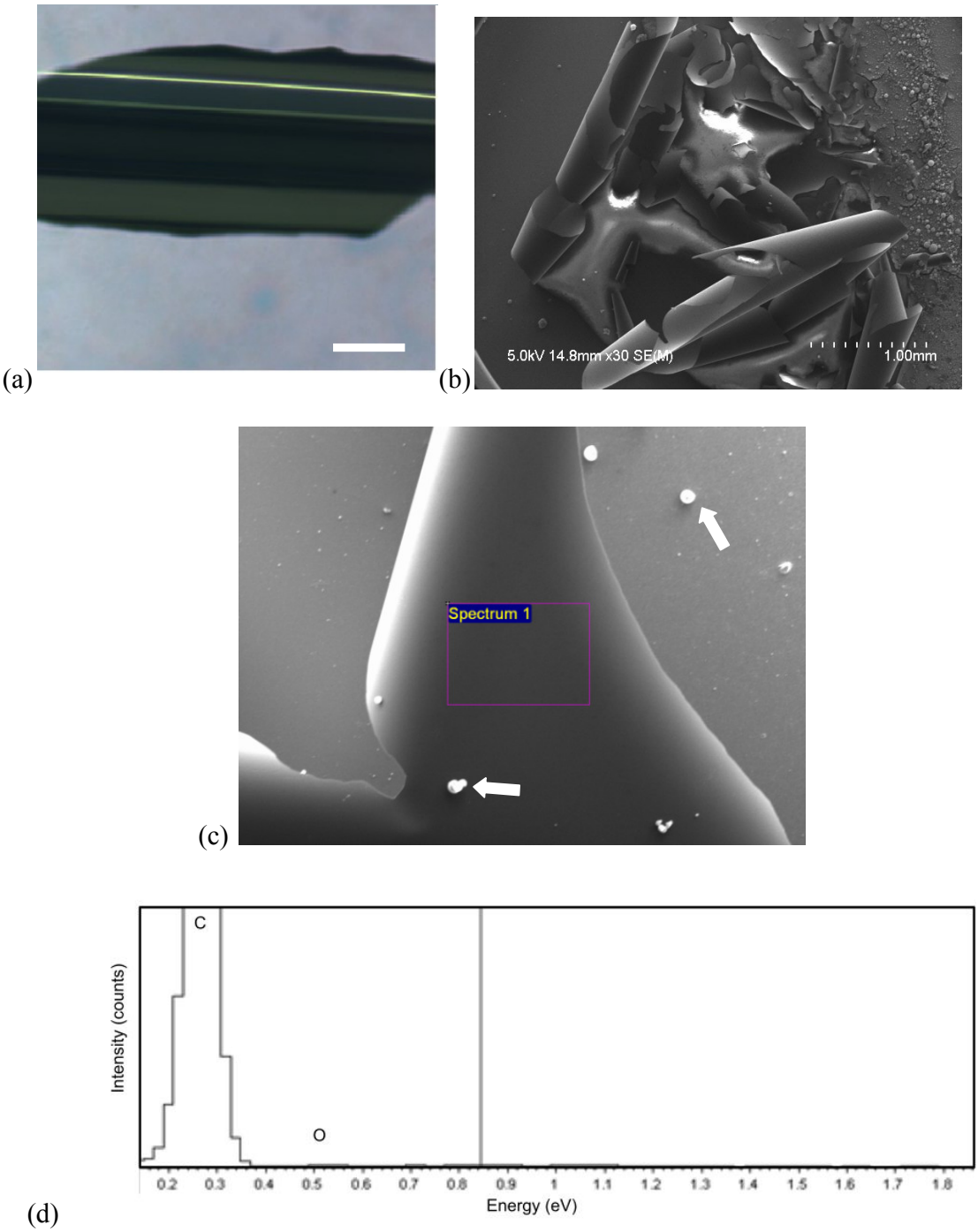

Figure 35 - (a) Optical microscope image of film flake removed from quartz surface (scale bar 100µm), (b) SEM image of flakes at film edge, (c) SEM image (200µm) showing peeled film surface and (d) EDX spectrum of (c).

Previously, XPS studies conducted by Filik[172] and Taki[173] on amorphous carbon films have shown the carbon C_{1s} signal to be very broad (full width at half maximum is 1.5 – 1.6eV) due to a large contribution from sp^3 carbon, and the peak maximum shifted above 285eV. In comparison, XPS analysis of graphene films (Figure 36) prepared using the spray pyrolysis approach shows a significantly narrower peak width (fwhm = 0.63eV) associated with the C_{1s} signal/peak/band, indicating a large sp^2 contribution (peak maximum at 284.6eV) which suggests a high degree of graphitization. Absence of any large intensity in the carbon/oxygen region (low contributions in region 287-290eV) indicates a low degree of oxidation which would severely affect the conductivity. Characterisation of the film surface using XPS showed the presence of sodium (in a small amount, 0.23at%), which is likely due to sodium salts on the surface, as observed by SEM (denoted by the white arrows in Figure 35c).

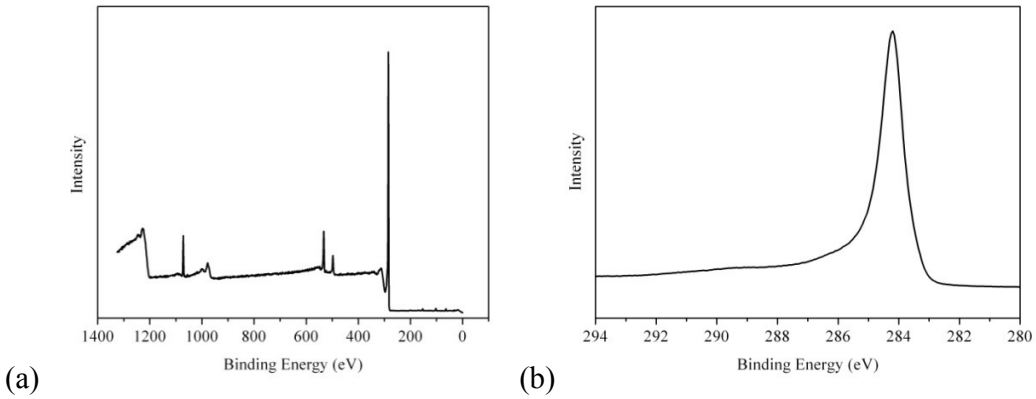

Figure 36 – X-ray photoelectron spectroscopy of film surface including (a) survey scan showing Na_{1s} (1025eV), O_{1s} (532ev) and C_{1s} (285eV) peak positions and (b) high resolution scan of the C1s region displays peak maximum at 284.6eV

The work in this section was conducted in conjunction with Ms. Rebecca Edwards as part of her Masters Degree research project. For device applications envisaged with

these types of films, thinner films are often desired which are able to make use of other properties such as transparency, useful for electrodes in organic light emitting devices (OLED). Control of the film thickness using this method is possible based on the variation of spray time and concentration of sodium ethoxide solution. A concentration of 1.7M, used to give the few layer graphene platelets in chapter three, produced very thick films over the course of 1h which also had a tendency to peel from the substrate. To derive thinner films a lower concentration of sodium ethoxide was investigated over the same period. The result of this produced semi-transparent thin graphitic films (Figure 37a) from concentrations reduced from 1.7M to 10^{-2} M over a fixed spray time period of 1 hour. Raman spectroscopy of these films showed the presence of the three peaks that are expected from graphitic carbon. The high D band: G band ratio in the Raman spectrum (*ca.* 1) suggests the film either has a defective structure or may exist as platelets on the surface much like a vacuum filtered film. The G' band was more pronounced which could be a consequence of a more ordered material. Indeed the Raman spectrum bears some resemblance to that shown by high temperature annealed graphene oxide films.[72,192] Importantly, the graphene film was optically transparent between 300 – 1100 nm include transmittance of 76% at 550 nm. In comparison, Reina *et al*[85] have demonstrated graphene films grown using the transition metal CVD technique on nickel had a transparency of 90% at 550nm for a film with an average thickness of 3nm as measured by AFM. Transparency at 550nm is a standard adopted by many researchers when few-layer graphene films are compared.[16,193] Commercial ITO films presently have transparencies greater than 85% even at thicknesses well in excess of 1μm, and it is only very thin continuous films that can surpass this value. However, there are advantages of using

transparent graphene films to replace ITO. Indium is a finite resource and there is expected to be a shortage of ITO supply in less than 10 years, therefore graphene which can be made from abundant resources could be an ideal replacement. In addition ITO films are very fragile and inflexible and therefore cannot be used to make flexible electrodes. In contrast, due to the high Young's modus and breaking stress of graphene, it has a higher flexibility and shows little change in conductivity when bent and stretched to large degrees.[95] Generally films grown on metal foils have shown transparencies >85% when transferred to poly(ethylene terephthalate) (PET) due to their high crystallinity and low defect content. In contrast vacuum filtered films of reduced graphene oxide have transparencies comparable to or lower than ITO. This rise is normally explained by the difficulty in transferring thin films from the filter membranes, and the presence of thick flakes. Thicker films (10 – 50nm) are generally created so that the extra thickness stabilizes the film upon removal of the underlying membranes.[52,192,194]

(a)

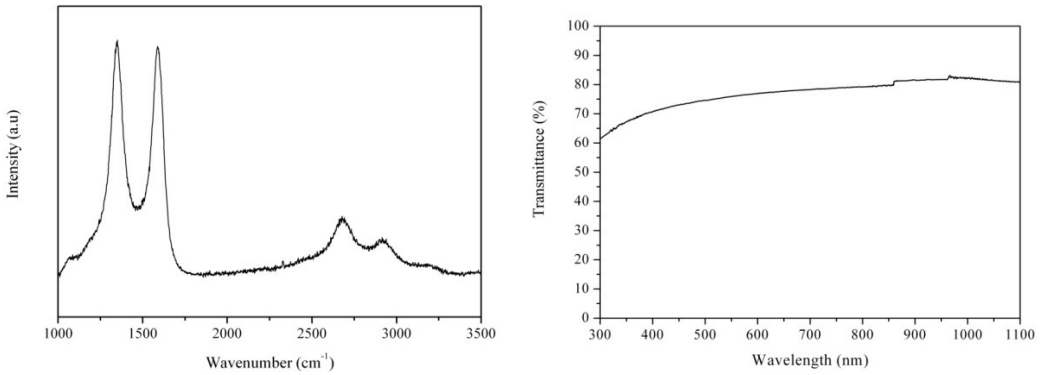

(b)

Figure 37 – (a) Optical photograph showing film produced quartz surface from sodium ethoxide concentration of $5.6x10^{-2}$M (quartz surface is exposed in top right corner removed using adhesive tape), (b) corresponding Raman (532nm) and transmission UV/NIR (300 – 1100nm) of film

Much work has been conducted into the development of various methodologies for the production of graphene films, with significant variations in the resulting film thickness depending upon the method used. Graphene films grown on copper substrates[22,86] for example, are reported to provide films of a single layer thickness, whilst those grown on nickel foils[85] result in films between 3-5 nm thickness. Various methods exist for determining the thickness of film samples including AFM,[85] reflection and contrast spectroscopy[195] and TEM. AFM was used to determine the thickness of the films grown here, prepared by mechanically cleaving a small area with adhesive tape. Consequently, an average height of 16 ± 2 nm was observed at the cleaved edges. Although this value is

significantly larger than the reported for thickness of films produced through metal foil CVD techniques, this method is based only on carbon deposition and not on the carbon absorption and precipitation. In the latter the thicknesses are influenced by the degree of carbon solubility and metal thickness. Early evidence from the findings suggests that it is possible to exert some control over the film thickness by varying the concentration of sodium ethoxide in ethanol. However, further work is needed to elucidate the exact influence of this parameters on the film thickness obtained. Although it should be possible to reduce the thickness even further.

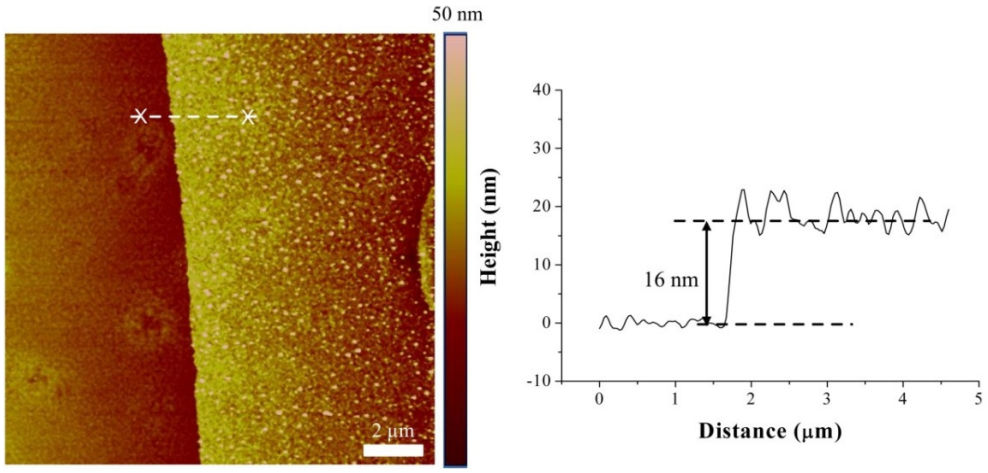

Figure 38 - Thickness measurement of graphene film. (a) TappingMode™ AFM height image (15 µm × 15 µm, scale bar 2 µm) of an optically transparent graphene film grown on quartz substrate. (b) The height profile, following the white line on the image, shows the height of the graphene film to be *ca.* 16 nm.

The conducting properties of the film were measured using the four point probe method. The average 4 – point resistance and sheet resistivity of the surface was found to be 4.7kΩ□$^{-1}$, corresponding to a conductivity of ~13,200 Sm^{-1}. Metal contacts were not used in these measurements, and as a result mechanical damage may have occurred when contacting the film surface. Therefore, the sheet resistance may be lower than what has

been stated above. Previously reported values for the sheet resistance of graphene vary between the methods of production as summarised in Table 2. The value obtained here, exceeds the conductivity values of several previous studies that reduce graphene oxide to graphene but is still far below the values observed from the CVD synthesis of graphene films on metal foils. Wang et al[192] have demonstrated thin films of reduced graphene oxide via vacuum filtration and conductivities of these have been measured in the range of 1 - 10Sm^{-1}. As highlighted in chapter one, reduction of graphene oxide rarely produces fully reduced material, and as a result, to achieve higher levels of conductivity prolonged annealing steps under ultra dry conditions are needed. In comparison, non-destructive solvent exfoliation of flake graphite with NMP[51] and SDS/water[52] have displayed conductivities of 1500 and 6500Sm^{-1} respectively in vacuum filtered films of 30nm thickness. These films were produced using no oxidation techniques and so are more likely to show the properties associated with platelet graphene films which have been produced here.

Method	Preparation	Transparency (%)	Sheet Resistance (Ω/□)	Reference
ITO		90	15	196
Vacuum filtration	GO/Hydrazine	98 – 60	10^5 – $4.3x10^4$	16
Vacuum filtration	GO/Hydrazine	35	$1x10^6$	192
CVD	CH_4/H_2/Ar, Ni/SiO_2/Si	76	350	95
CVD	CH_4/H_2, Cu foil	94.7	125	22
Spin Coating	GO/Hydrazine	70	$2x10^4$	197
Vacuum filtration	Graphite/SDS	62	$9.7x10^5$ – $2.25x10^4$	52
Dip coating	Graphene/$CHCl_3/H_2O$	70	100	198
Langmuir Blodgett	EG, Oleum, Tetrabutylammonium Fluoride, DMF	94	$1.5x10^5$	199
Spray Pyrolysis	Sodium Ethoxide, Quartz substrate	76	$4.7x10^3$	This work

Table 2 – Comparison of transparency and sheet resistance to various reported fabrication methods

4.2 Memory storage device fabrication using sodium/ethanol spray pyrolysis product

In the past, development of electronic devices has been focused on the further development of silicon based technology. However this is not always suitable for use in new and envisioned applications such as plastic electronics and organoelectronics. Intense studies of such devices have led to application in solid state lighting,[200] organic solar cells,[201] light emitting displays[202] and organic thin film transistors (OTFTs).[203,204] Due to the advantages of organic devices over their inorganic counterparts such as low manufacture costs, lightweight, large area fabrication and suitability for flexible substrates, they have potential for the next generation of devices. However, the

development of these has not yet overcome the supremacy of silicon. For example current silicon/silicon oxide based field effect transistors display greater electron mobility ($500cm^2V^{-1}s^{-1}$)[205] than fabricated organic field effect transistors ($0.33cm^2V^{-1}s^{-1}$).[203]

In the future, plastic electronic components will require organic based memory devices. Currently there is a significant interest in the development of non volatile memory devices based on organic storage and semiconducting molecules. Such devices have been fabricated using metal–insulator–semiconductor (MIS) device architecture by the integration of nanoparticulate materials as the charge-storage elements have received considerable attention in the literature. Various storage materials have been illustrated, including fullerenes (C_{60}),[206] SWNTs,[207] gold nanoparticles,[208,209] aluminium,[210] germanium,[211] and gold nanocrystals.[212]

Memory devices of this nature are based on capacitors which store charge under the influence of an electric field. The structure of a MIS capacitor is shown in Figure 39, where the gate (top electrode) and back electrode (bulk contact) are metal contacts.

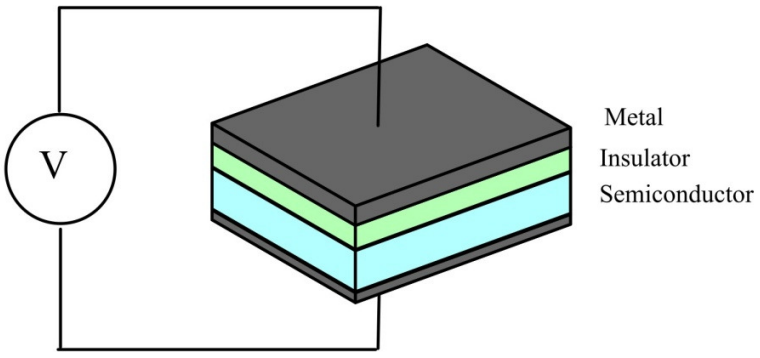

Figure 39 – Metal – Insulator - semiconductor (MIS) capacitor structure

The variation of capacitance with voltage of a typical MIS capacitor is shown in Figure 40a. From this, four main regions are apparent from the S shaped C-V curve; inversion, flatband, accumulation and depletion. Within the flatband region the semiconductor has no charge, and therefore, there is no electric field across the insulator layer. The flatband voltage (V_{FB}) is defined as that which separates the accumulation and depletion regions. Accumulation in p-type devices (demonstrated in this section), occurs at an applied voltage less than the flatband voltage (typically negative). The negative charge at the gate attracts positive charge carriers (holes) to the semiconductor/insulator interface where they accumulate (hole density at semiconductor surface greater than in the bulk). Above the flatband voltage, depletion occurs where the holes are pushed from the interface due to the increasing positive charge at the gate electrode. At this point no charge carriers exist at the semiconductor/insulator interface producing a further insulating layer. Further positive bias induces a small number of negative charge carriers to build at the interface. Here the semiconductor has n-type (negative) character opposite to the initial p-type and so is called inversion.

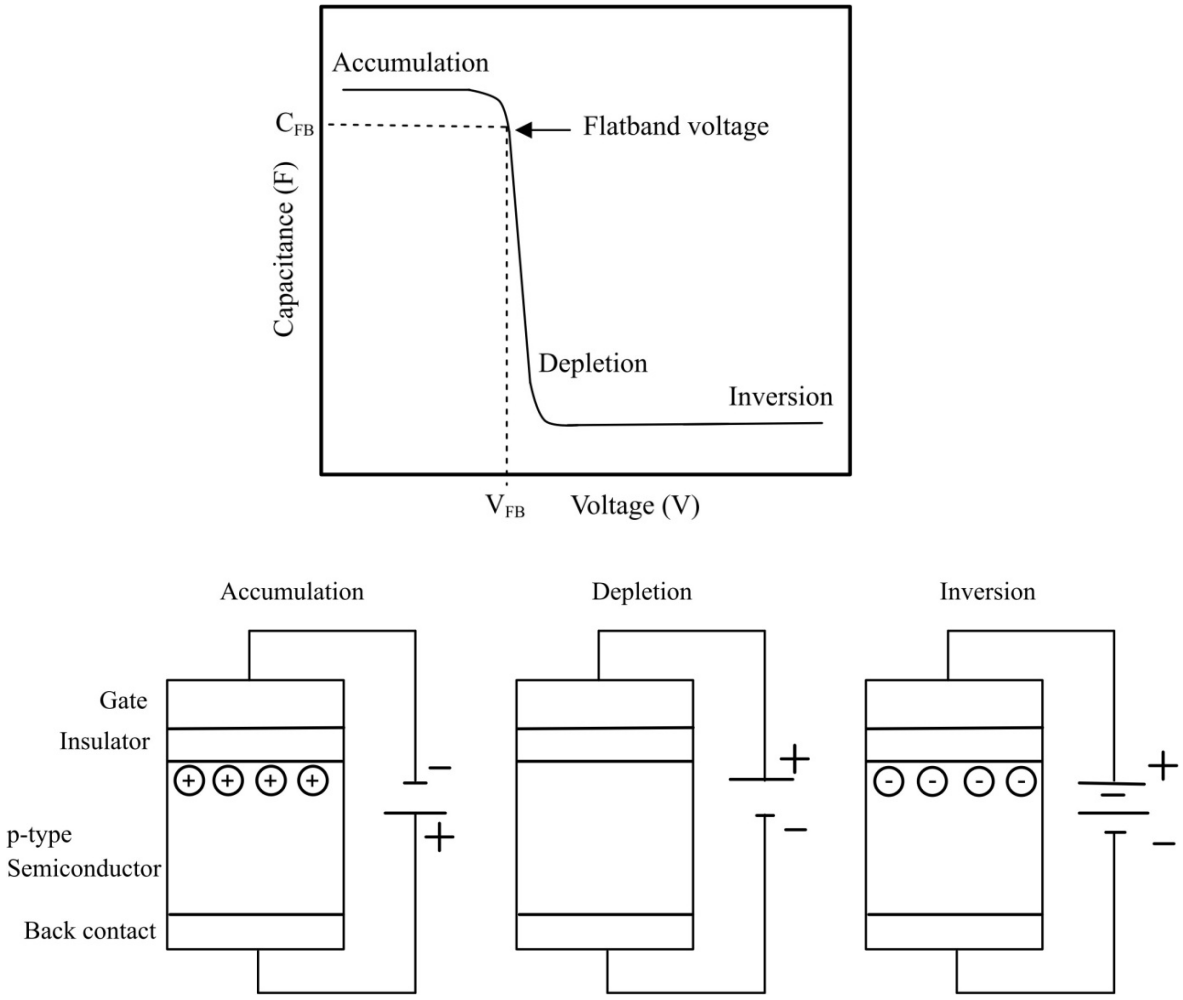

Figure 40 – (top) typical MIS accumulation/depletion/inversion behaviour (bottom) an MIS capacitor in accumulation, depletion and inversion modes

The inclusion of charge storage sites causes slight variations in the C-V curves because the trapping of charge from the gate influences the position of the flatband voltage. These sites act as a "nano floating gate" electrode electrically isolated from the main gate, which in-turn affect the charge at the semiconductor/insulator interface. Accumulation occurs as stated before but now charge has been added to the sites from the gate. The charges on these sites then affect the position of the flatband voltage upon applying a positive bias, causing a shift in the curve during depletion (Figure 41b). The

nature of the charge storage can be derived from the position of the flatband voltage shift. Negative charge storage will cause the flatband voltage to shift positively (increasing V_{FB}). Positive charge storage will induce a negative shift in the flatband voltage. This shift induces hysteresis behaviour and is the basis of all capacitor based memory devices, the width of which is commonly referred to as the memory window.

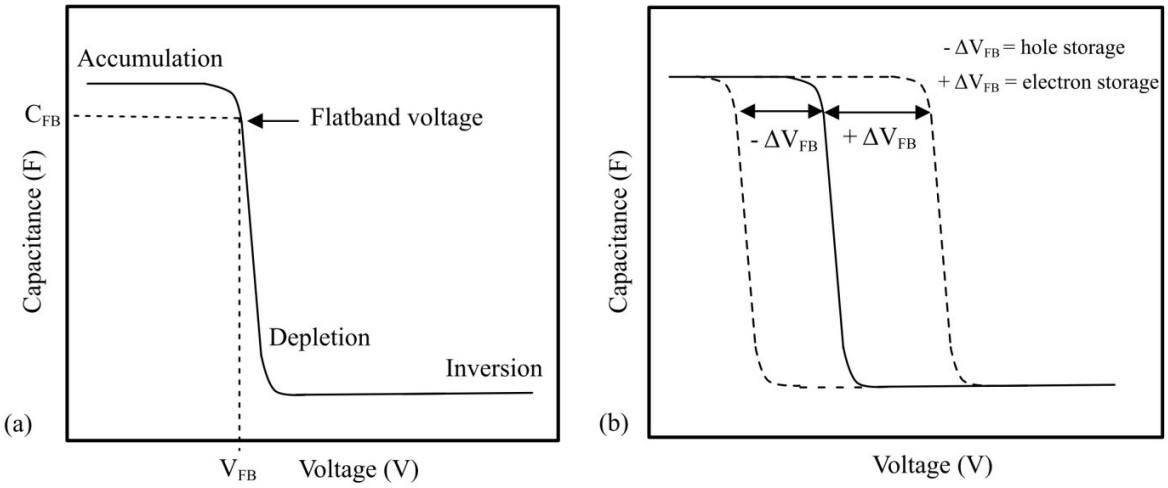

Figure 41 - Typical MIS accumulation/depletion/inversion behaviour in (a) p-type silicon devices and (b) with addition charge storage sites

The work in this section was a result of collaboration with Maria Alba Martin and Dr Dagou Zeze, a member of the Centre for Molecular and Nanoscale Electronics, Engineering Department, Durham University. A MIS device based on the few layer graphene produced by the spray pyrolysis of sodium ethoxide (sodium/ethanol) were fabricated to form devices with non-volatile memory storage properties. The arrangement of layers in the MIS device is given in Figure 42. This work follows earlier studies, in Durham, using a similar architecture to investigate the charge storage properties of gold nanoparticles, buckminsterfullerene (C_{60}) and single walled carbon nanotubes SWNTs.[213] The graphene layers were deposited on silicon substrates (p-type, 4.5nm SiO_2 thickness)

using the layer by layer deposition technique. Initially a poly(ethyleneimine) (PEI)/poly(acrylic acid) (PAA) bilayer was deposited to enhance the adhesion of the graphene layers to the oxide surface. An aqueous solution (0.1 $mgmL^{-1}$) of few layer graphene was produced by non covalent modification with sodium dodecylsulfonate (SDS) by sonication for 30 minutes. The film was built by first immersing the substrate in aqueous graphene/SDS and aqueous PEI each for 10 minutes. Layer by layer deposition was repeated to give a film two bilayers in thickness. Poly(methyl methacrylate) (PMMA) was then spin coated onto the surface to provide an insulating layer between the graphene and the gate electrode.

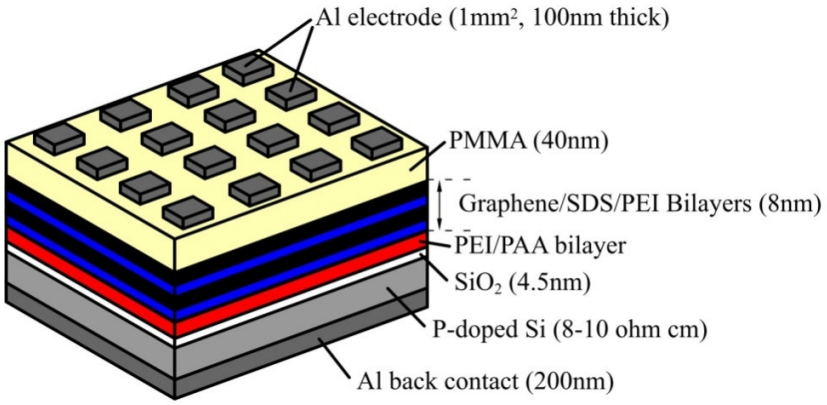

Figure 42 - MIS capacitor architecture incorporating few layer graphene as a charge storage layer.

The C-V curve for $Al/SiO_2/Si$ reference devices showed the usual accumulation-depletion-inversion characteristics of the MIS structure, with a flat band voltage of -1.8V. No hysteresis was observed by sweeping the voltage. The addition of PMMA to the reference structure showed a small negative shift in the flat band voltage indicating a small degree of incorporated charge (appendix Figure B 1).

Addition of the few layer graphene bilayers resulted in a large positive shift in the flat band voltage (memory window *ca.* 4.6V for a bias scan width of 14V, Figure 43a)

during the positive C-V sweep. In comparison, the negligible hysteresis in the PMMA reference device in comparison indicates the graphene layers are the cause of the hysteresis, acting as a charge storage layer. The observation of clockwise hysteresis in a device based on p doped silicon suggests that during accumulation, electrons are injected from the top electrode.[213] The opposite effect occurs upon application of a positive bias where, during inversion, electrons are extracted through the top electrode. In comparison to the reference device, there is a positive shift in the flatband voltage which infers the storage of negative charge due to the addition of few layer graphene. The accumulation (writing) and depletion (erasing) voltages were measured to be *ca.* -4 and 5V respectively. Therefore application of a voltage inbetween these can be used for reading. The memory window of the C-V curves increases in an approximately linear fashion, ranging between 2 - 5 V for sweep ranges of 8 - 16V (Figure 43b). This linear behaviour of hysteresis window was also seen with the addition of gold particles as the charge-storage element.[213] However, the hysteresis widths were lower in value (1.6V at 8V sweep) than those observed for the few layer graphene sheets (2.3V). There are very few instances of graphene based non volatile memory devices. The largest memory window observed in these studies was 7.5V for a sweep range of 19V based on an architecture constructed of tantalum nitride/aluminium oxide/graphene oxide/SiO_2/p-Si.[214] The linear dependence is attributed to an increase in stored charge in the graphene layers as the magnitude of the gate voltage increases. The amount of charge stored can be calculated using the equation $Q = C_{MAX}\Delta V_{FB}$ where C_{MAX} and ΔV_{FB} are the maximum capacitance and the flat band voltage shift. This gives a figure of $7.04 \times 10^{11} cm^{-2}$ for the charge carrier concentration at a

sweep range of 8V and is one order of magnitude lower than the value of $5.7x10^{12}$ cm^{-2} calculated for gold nanoparticles.[213]

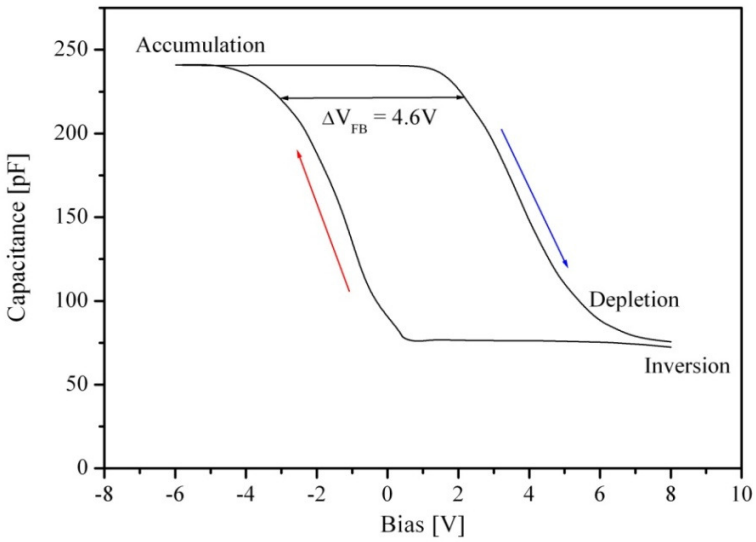

(a)

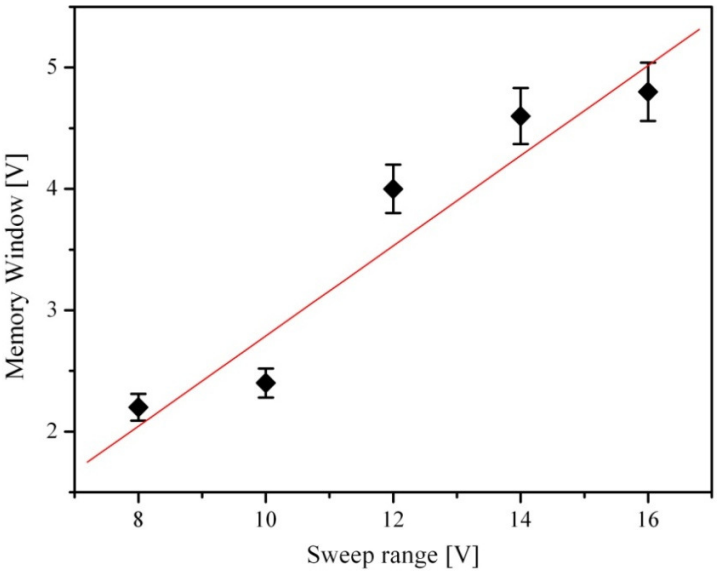

(b)

Figure 43 – (a) C-V characteristics at 400kHz for the MIS memory structure containing 2 bilayers consisting of a few layer graphene/SDS/PEI combinations, (b) Memory window (ΔV) as a function of sweep voltage

The charge retention capabilities of all devices were studied by charging the MIS structures with a voltage in the accumulation region for a few seconds, followed by the application of a stress bias voltage, in this instance 6.2V. From this, the charge retention on the graphitic sheets was calculated to be 41% in comparison to gold nanoparticles at 76% (Figure 44).[213] The retention of charge in the graphitic sheets is similar to that shown for C_{60}, and *ca.* 10% higher than for SWNTs.[213] A possible reason for the low charge retention may be due to ineffective insulation from the gate electrode. Due to the lateral dimensions of graphene (micrometre scale), any platelets that lie at an angle on the substrate surface may protrude from the PMMA layer (60nm) creating a path for charge to escape to the gate electrode.

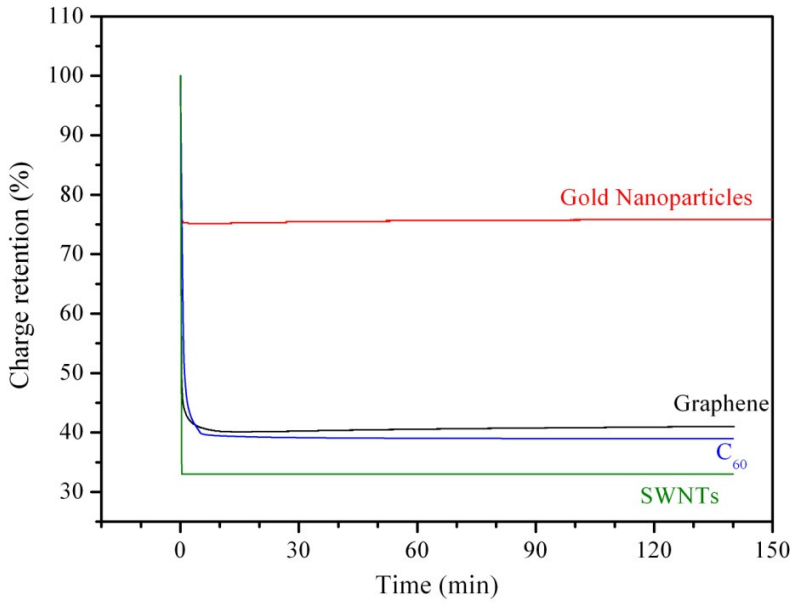

Figure 44 – Charge retention characteristics of MIS device with gold nanoparticles (red) and graphitic sheets/SDS (black) as charge-storage elements. Comparative data for C_{60} (blue) and SWNT/DTAB (green) using are also provided.

4.3 Few layer graphene polymer composites

Fillers such as carbon nanotubes, fullerenes, silica and various clays have shown some promising results as supporting materials in composite matrices. Also now that graphene and graphitic nanoplatelets (made by oxidative acid intercalation) are now commercially available, these nanostructured materials are also becoming the focus of much research due to a wide combination of properties associated with nano-clays and other graphitic carbon structures. The closest comparison in structure to these nanosheets is that of layered nano-clays. These materials can show considerable improvements in mechanical properties such as strength, modulus, and toughness with very low weight percent of the plate-like nanofiller.[215,216]

Graphite and its expanded forms have also attracted interest in terms of its composites. Unfortunately effective increases in properties have only been documented when the loading of expanded graphite was above 2%,[217,218] with unexpanded graphite often showing property degradation.[219] Due to the low solubility of graphite in various solvents, inhomogeneous composites are formed at low weight percentage and in-turn produce ineffective or detrimental changes. However, many researchers have commented that only by fully oxidizing graphite to graphite oxide, do composites get the necessary dispersion and surface area required and thus outperform carbon nanotubes at low filler loadings.[28,220] The large elastic modulus value for graphene (1.1TPa), in conjunction with the large platelet surface area, allow graphene and graphene oxide derived materials to be the main supporting component of a nanocomposite. There have been reports of Young' moduli increases over 100% in graphene and graphene oxide filled polymer composites of poly(vinyl alcohol),[221] poly(acrylonitrile),[218] and polycaprolactone.[222] The added

advantage to graphene over other filler materials like nano-clays and glass fibers is that it is a conductive material and therefore composite materials have the potential to be used in device and other electronic applications. The incorporation of reduced graphene oxide into insulating polymer matrices has increased bulk conductivity by several orders of magnitude.[31,223]

4.3.1 Composites of poly(methyl methacrylate) and few layer graphene from sodium ethoxide/ethanol as filler material

Poly(methyl methacrylate) (PMMA) is a transparent thermoplastic, often used as a light or shatter-resistant alternative to glass. It is a strong, highly transparent, lightweight material which has found applications in various engineering disciplines. At the present time, the automotive and aerospace sectors are moving towards the development of composite based technology to replace the external shells of their vehicles. This gives added benefit to speed and fuel consumption as composite materials are generally a lightweight alternative to metals and the alloys.

Here we report the addition of the few layer graphene platelet material synthesized by the spray pyrolysis of sodium and ethanol to a PMMA matrix. A solution processing method similar to that used by Ramanathan *et al*[28] to prepare PMMA composites of graphene oxide, SWNTs and expanded graphite, was employed to mix the few layer graphene into the PMMA matrix via dispersion and shear mixing of the two components in DMF. Following mixing, the composite was precipitated from solution by drop-wise addition into water and dried. It was then pressed into a suitable sample mould for three

point bend geometry dynamic mechanical analysis (DMA). By measuring the deformation of the molded polymers with respect to the applied stress, the Young's modulus (stiffness) of the material was calculated according to the linear behavior related to Hooke's Law. In matrices which are effectively reinforced by the filler, the gradient in the associated stress/strain measurement increases indicating a rise in stiffness.

The gradual increase in Young's modulus with increased filler content is shown in Figure 45. The same trend has been observed with carbon nanotube[224] and reduced graphene oxide[225] composites. From the results, addition of low amounts of material (0.2wt%) to the polymer matrix is enough to cause an increase in stiffness by 28% to 2.2GPa from 1.72GPa. This Young's modulus enhancement was observed up to 63% at 1% filler content, illustrating good correlation between the percentage filler and the increase in stiffness. In the literature, comparable increases in the Young's modulus have been measured in graphene composites using different graphene materials, including a 57% increase in polystyrene composites (1%) formed by in-situ polymerization of styrene in the presence of alcohol modified graphene oxide[226] and an 80% increase from the composite synthesized by solution processing of graphene oxide in PMMA with THF.[28] Although the results of this study shows a lower mechanical enhancement compared to that of Ramanathan, a direct comparison cannot be made. The graphene oxide/PMMA study was carried out using a much higher molecular weight (350,000 g/mol) and experiments were conducted in film tension. A summary of results for the Young's modulus for several other polymers is shown in Table 3.

.

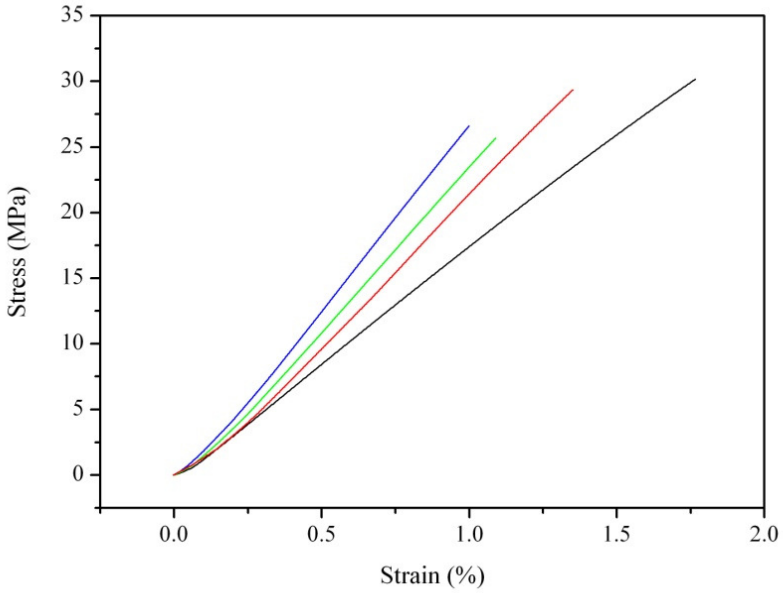

Figure 45 – 3 point bend stress/strain measurement for composites of ethanol/Na product in PMMA at various weight percentages 0%(black), 0.2%(red), 0.5% (green) and 1% (blue)

Polymer	Reinforcement Material	Processing Method	E_{matrix} (MPa)	Graphene concentration (wt%)	Modulus Increase (%)	Ref
PVA	GO	solution	2100	2.5	128	[221]
PDMS	TRG	In-situ polymerization	0.6	2.2	1100	[227]
PCL	GO	solvent	340	2.4	108	[222]
PMMA	TRG	solution	2100	1	80	[28]
PS	RGO	solution	1450	0.4	57	[226]
Epoxy	TRG	In-situ polymerization	2850	0.05	31	[29]
PAN	KC_6 exfoliation	solution, in-situ polymerization	2450	2.1	100	[218]
PMMA	Sodium Ethoxide product	solution	1720	1	63	This Study

Table 3 – Young's modulus data for selected polymer matrices showing mechanical enhancement. TRG = thermally reduced graphene oxide, PVA = poly(vinyl alcohol), PCL = poly(caprolactone), PAN = poly(acrylonitrile)

For a range of polymers, the glass transition and decomposition point have been observed to migrate significantly to higher temperatures.[28,228-231] Due to the nature of the nanostructures good dispersions of the material are thought to interfere with the mobility of the polymer phase due to strong interaction at the interfaces increasing the amount of thermal energy needed in the system to pass from a more elastic material to a more viscous one (glass transition temperature, T_g). Ramanathan *et al*[28] suggest that the oxygen groups on the graphene oxide surface give added electrostatic interactions at the interface, which explain such a large change in the properties of their PMMA composites. For the composites prepared here, the multi-frequency data for the various weight percent composites (Figure 46) show an increase in the glass transition temperature associated with the storage modulus drop. In unmodified PMMA this point occurs between 95 – 102^{o}C and the resulting peak in the tan δ (ratio between storage and loss moduli) at 112^{o}C. Even at 0.2wt% an increase in this thermal property by *ca* 25^{o}C is observed. The study conducted by Ramanathan *et al*[28] involving surface functionalized graphene material showed a maximum glass transition increase in the region of 30% even at filler content as low at 0.01%. As in their study, no further increase in the glass transition temperature was observed beyond the lowest percentage composite. These glass transition shifts have been observed previously on other composites with graphene,[232] CNTs,[233-235] metal particles[236] and nanoclays.[237]

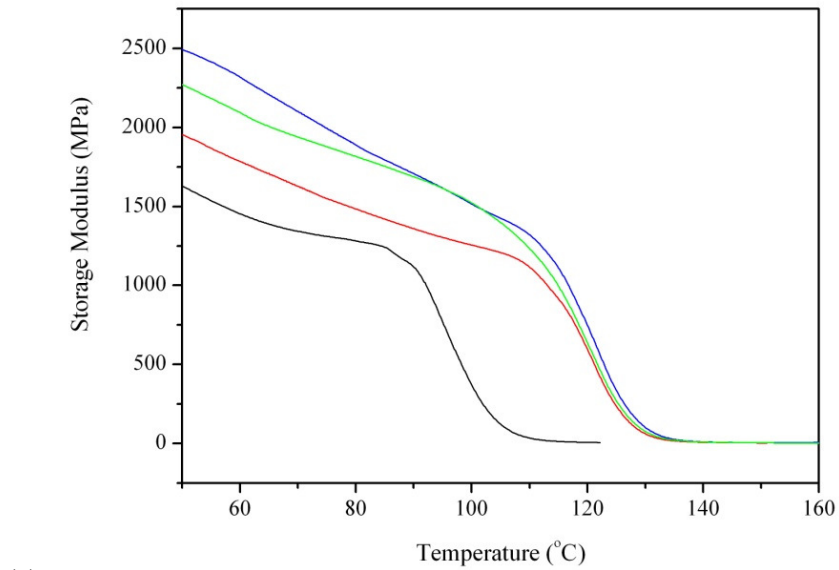

(a)

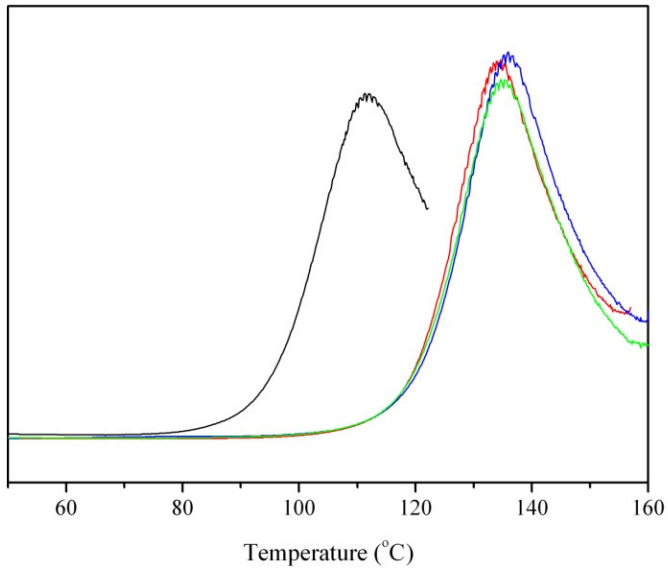

(b)

Figure 46 - Multi-frequency data showing (a) storage modulus and (b) tan delta for PMMA (black), 0.2% ethanol/Na (red), 0.5% (green) and 1% (blue)

	Young's Modulus (GPa)	Glass Transition (^{o}C, DMA)	Grass Transition (^{o}C, DSC)
PMMA	1.72 ± 0.08	112 ± 1	113 ± 1
0.2 wt%	2.2 ± 0.2 (+ 28%)	138 ± 3	123 ± 2
0.5 wt%	2.5 ± 0.3 (+ 45%)	138 ± 4	125 ± 1
1 wt%	2.8 ± 0.2 (+63%)	140 ± 2	126 ± 2

Table 4 – Mechanical and thermal properties of graphene produced from Na/EtOH product/PMMA composites at differ weight percentages

The fracture region in the 0.5% PMMA composite is shown in an ESEM image (Figure 47). No large agglomerations of sheets were observed and, in places, thin plates could be observed protruding from the fracture surface. This indicates that the few layer graphene sheets have achieved a good dispersion using the shear mixing method and as a consequence, large enhancements are observed in the thermal and mechanical properties. Dispersion is regarded as the most basic issue for composite processing. Nanostructures must be uniformly dispersed to the level of isolated structures individually coated with polymer. This is imperative in order to achieve efficient load transfer to the network. This also results in a more uniform stress distribution and minimises the presence of stress sites. The effects of poor dispersion are seen in a number of nanotube systems when the loading level is increased beyond the point where aggregation begins. This is generally accompanied by a decrease in strength and modulus.[238]

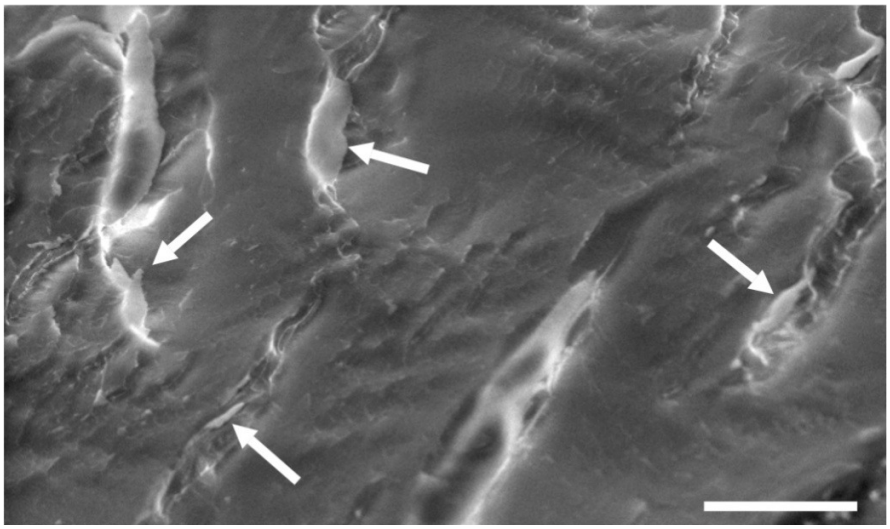

Figure 47 – Environmental SEM image (scale bar 10μm) showing fracture surface of 0.5% composite. White arrows denote areas where platelets have been pulled out during sample failure

The outcome of the incorporation of the few layer graphene is a large enhancement in properties between the composites and the parent matrix. But are these composites better than those combining SWNTs and PMMA which are available commercially? From the results of composites using HiPCO™ nanotubes prepared by a similar method, which included an extra sonication stage after the shear mixing step, the few layer graphene composites still outperform the SWNT composites by ~ 15% (Figure 48). This observation is similar to conducted by Ramanathan[28] (PMMA) and Rafiee[29,220] (Epoxy resin) who showed that graphene composites outperform other nanostructures by 18% and 20 - 26% respectively with respect to the Young's modulus. In addition increases in the thermal properties measured by differential scanning calorimetry (DSC) and DMA multi-frequency (Figure 49a,b) of 1% few-layer graphene and SWNT PMMA composites are comparable suggesting that both materials show good filler dispersion and it is the difference in structure that is the reason for further performance of the graphitic platelets.

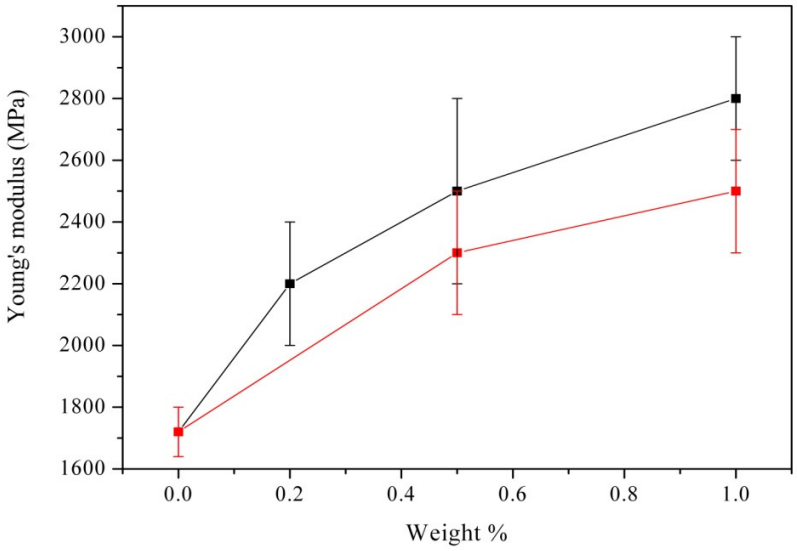

Figure 48 – Plot of Young's modulus against weight percentage content of few layer graphene (black) and SWNT (red) composites of PMMA

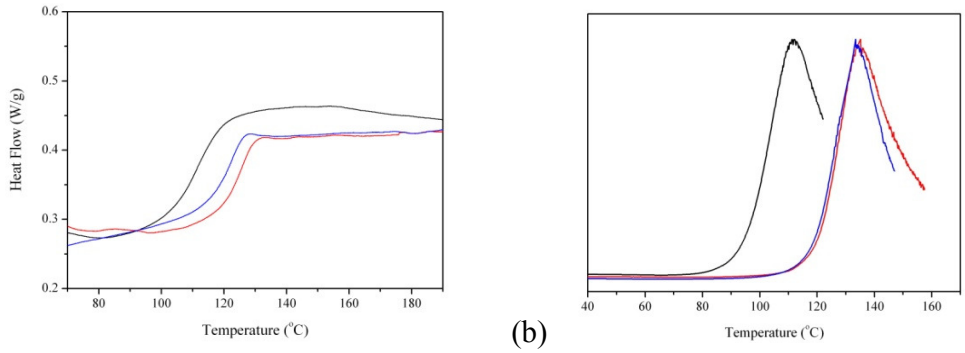

(a) (b)

Figure 49 – (a) DSC heat trace and (b) multi-frequency tan delta for PMMA (black), 1% SWNT (blue) and 1% Ethanol/Na product (red)

4.3.2 Comparison of composite properties produced with different filler materials

In section 6.3.1, few layer graphene from the spray pyrolysis of sodium and ethanol has shown some exciting physical properties and application for composite materials. In this section the spray pyrolysis product of NaOH/EtOH, CVD product of

sodium carbonate/ethanol (Na_2CO_3/EtOH) and graphite were tested for comparison to highlight any differences in their performance.

As discussed previously the most important system requirement for effective reinforcement is the dispersion of the material in the matrix. This is imperative in order to achieve efficient load transfer to the filler network. This also results in a more uniform stress distribution and minimises the presence of stress concentration centres. The effects of poor dispersion can be seen in a number of systems using carbon nanotubes at high loading levels where they have a tendency to aggregate.[238] Graphite is not a popular choice for use as a composite material due to its difficult dispersion for solution processing and weak exfoliation in melts associated with the strong inter-sheet interactions. Zheng *et al*[239] demonstrated the difference in properties between graphite before and after expansion. They found that graphite actually had a detrimental effect on the mechanical properties of the PMMA reducing its Young's modulus below that shown for the parent matrix. The difference in the stability of the different filler materials in DMF is evident from Figure 50. The SWNTs and the graphitic nanosheet materials show a greater stability in solution to that of graphite and the sodium carbonate product which are reflected in the mechanical and thermal results.

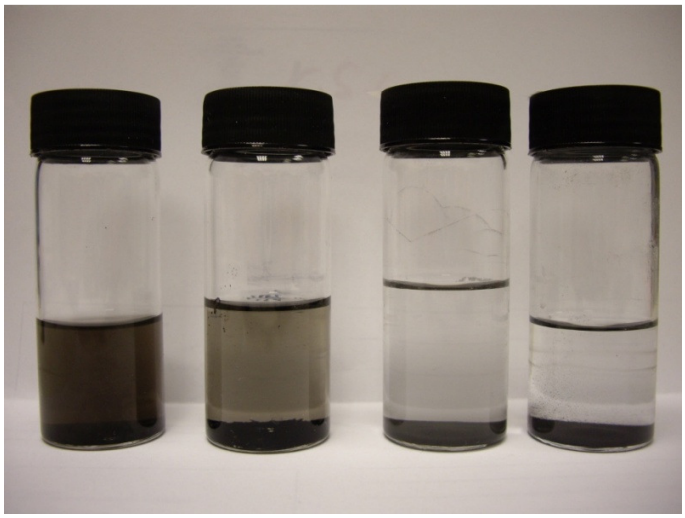

Figure 50 – Optical photograph showing the difference in stable solubility in DMF of (from left to right) the Na/EtOH graphene product, HiPCo™ SWNT, Na_2CO_3/EtOH graphene product and graphite.

From the mechanical and multi-frequency data there is a large difference in the performance of the sodium/ethanol (Na/EtOH) and sodium hydroxide/ethanol (NaOH/EtOH) spray pyrolysis products to that of graphite and CVD decomposition of ethanol over sodium carbonate. Graphene from Na_2CO_3/EtOH and graphite had low solubility and were difficult to disperse and this is reflected in the mechanical and multi-frequency results. Over the course of the processing, the Na/EtOH and NaOH/EtOH spray pyrolysed materials maintained their exfoliation whereas the Na_2CO_3/EtOH product and graphite had a tendency to fall out of solution during the process of precipitating the polymer. This affects the strength of the composites as inhomogeneous composites have large agglomerations that don't provide the surface area to evenly distribute the applied stress and can often be points of failure. Graphite showed a negative effect on the stiffness of the PMMA composite. This has been observed in other composites of graphite[217] and CNTs[238] where the authors have observed very poor dispersions. This was observed as an

average 7% decrease in the Young's modulus during testing. The graphene product from sodium carbonate product results in a small increase in Young's modulus (11%) almost certainly due to the presence of thinner platelets observed in the TEM, see section 3.3, which are able to weakly reinforce the matrix. However, due to aggregation during precipitation, it does not compare favorably to the graphene product from the Na/EtOH and NaOH/EtOH which showed increases in Young's modulus of 60 – 65%.

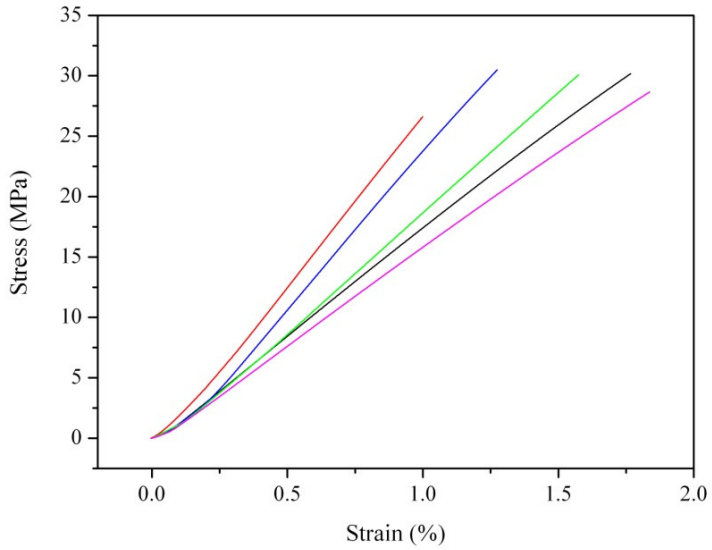

Figure 51 – Comparison mechanical testing data for PMMA (black) and 1wt% composites of Na/EtOH (red) NaOH/EtOH (blue), Na_2CO_3/EtOH (green) and graphite (magenta)

	Young's Modulus (GPa)	Increase
PMMA	1.72 ± 0.08	
Na/EtOH graphene /PMMA	2.8 ± 0.2	63%
NaOH/EtOH graphene/PMMA	2.8 ± 0.2	63%
Na_2CO_3/EtOH graphene/PMMA	1.9 ± 0.1	11%
Graphite/PMMA	1.6 ± 0.2	-7%

Table 5 – Tabulated Young's modulus values for PMMA and composites filled with graphene products from spray pyrolysis of Na/EtOH and NaOH/EtOH, ethanol CVD over sodium carbonate and graphite

With the effect that the dispersions have on the mechanical properties, it can be observed that the graphite and sodium carbonate products make little impression on the surrounding matrix. The dispersion also explains the observation of only small changes in the glass transition temperature. In contrast to the changes of *ca* 30°C in the Na/EtOH and NaOH/EtOH spray pyrolysis product composites, the positive shift of the sodium carbonate product is only 7°C and the composite of graphite shows minimal change to the position of the tan δ maximum (Figure 52).

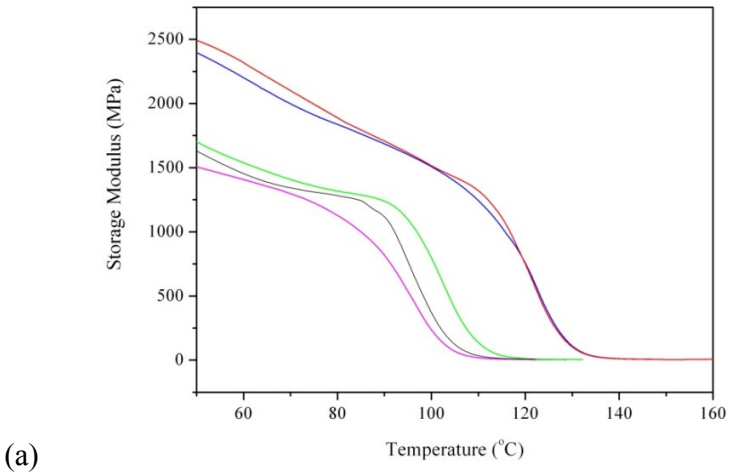

(a)

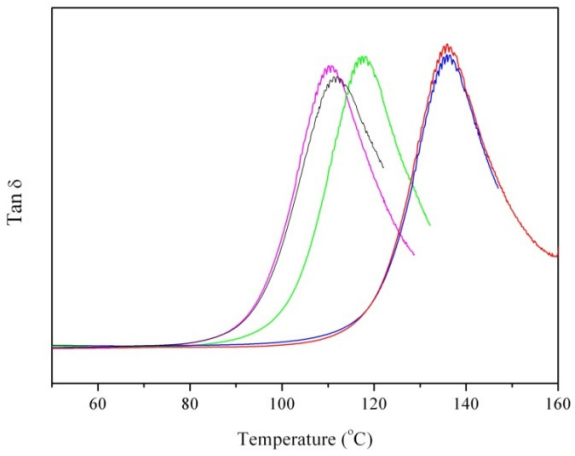

(b)

Figure 52 – Multi-frequency data showing (a) storage modulus and (b) tan delta curves for PMMA (black) and the 1% composite with Na/EtOH (red), NaOH/EtOH (blue), Na_2CO_3/EtOH (green) and graphite (magenta)

4.4 Conclusion

Here, applications of the graphene produced by the spray pyrolysis methodology have been demonstrated in three of the most common areas of graphene development (thin film, electronic devices and nanofiller composites) which demonstrates the adaptability of the spray pyrolysis method and the material.

Nanoscale thickness films of graphene were prepared on quartz using an adapted version of the procedure demonstrated in chapter 3. Films of 16 nm thickness, as determined by AFM measurements, grown using a sodium ethoxide/ethanol concentration of $5x10^{-2}$ M, demonstrated a conductivity of ~13,000 Sm^{-1} in conjunction with a film transparency above 70%. Although this value is lower than other reported synthetic routes, it has been grown without the use of heavy transition metals, negating the need for film processing and transfer; it exceeds the values demonstrated by films made using top down methods. The advantage of these films lies in their use as transparent electrode materials. The films are grown directly onto quartz, as opposed to silicon where film transfer steps are required. Therefore it is an economically sound route for the fabrication of electrically conducting thin graphene films, which may offer application in next generation solar cells and display screen technologies.

Application of the material to the electronics industry was demonstrated by the fabrication of MIS memory storage devices which were able to show data storage higher than that shown for SWNTs. These results support the development of memory devices based on charge storage in nanoparticle materials, although further device development is needed to further improve storage lifetimes. These results are promising due to the expected need for graphene as silicon replacements in areas of the semiconductor industry.

Chapter IV

Carbon nanotubes have been widely used as filler materials in polymer composites with some success. The arrival on the scene of graphene has excited the composite community due to studies demonstrating the ability to outperform single and multi walled CNTs in terms of mechanical properties. With the new product created in the scalable pyrolysis reaction from chapter three, application to composite materials has been demonstrated through its incorporation at various weight percentages into a PMMA matrix via solution processing. Not only do they give enhancement of mechanical properties at low content (28% increase in Young's modulus at 0.2wt%) and enhance the thermal properties, but they outperform SWNTs composites. Now that bulk synthesis of graphene is possible, application in composites is a very realistic and exciting prospect.

5. SYNTHESIS OF FEW LAYER GRAPHENE USING BIMETALLIC CATALYST

Bimetallic catalysts have been found to be effective in the preferential synthesis of SWNT over multi-walled carbon nanotubes, including mixtures of cobalt/molybdenum,[240,241] iron/molybdenum,[242,243] and iron/ruthenium.[244] The amount of carbon available for growth is affected by the presence of a secondary metal within the system. Instances in the literature indicate that the introduction of non transition metal salts to catalyst systems have a negative effect on the desired carbon products of chemical vapour deposition (CVD) reactions. For example, a study by Liu *et al*[245] showed that CVD on a sodium chloride supported cobalt catalyst, with a methane carbon source at 600ºC failed to produce carbon nanotubes. However, carbon encapsulated nanoparticles were produced instead, drawing the conclusion that the salt had a deactivating effect on the longitudinal growth. Furthermore, the addition of sodium salts to iron magnesium oxide catalyst support systems at very low percentages (< 0.5wt%) quantitatively inhibited growth which the authors postulate could be used to give more control over the CVD growth of carbon nanotubes.[246] The reasoning behind their results suggests that the presence of sodium reduces the solubility of carbon in the metallic phase, creating less carbon on cooling.

5.1 Synthesis of sodium cobalt carbonate

Bimetallic catalysts have been shown as effective systems for the controlled synthesis of carbon nanotubes. This, in conjunction with the observation that sodium can inhibit growth in carbon CVD, poses an interesting question. Can sodium be used to influence the nature of the graphitic carbon produced from CVD over a transition metal catalyst? The simplest way to incorporate sodium into the catalyst is to form a mixed sodium/transition metal structure, one of which is Kambaldaite ($Na_2Ni_8(CO_3)_6(OH)_6.6H_2O$). Kambaldaite cannot be made synthetically but analogues using cobalt have been reported by Petrov[247] and Ohnishi.[248] The cobalt analogue was chosen as the bimetallic catalyst, adapting the method using sodium carbonate in section 3.3. Sodium cobalt carbonate was prepared using a method similar to that of Ohnishi *et al,*[248] where the analogue was precipitated from cobalt nitrate in aqueous sodium hydrogen carbonate over a period of two hours. During the synthesis the purple cobalt carbonate was observed to change to light pink indicating the reaction was complete. Elemental analysis (ICP-AES) of the compound revealed the sodium content to be in the region of 1.3 – 1.6wt%. However, for the Kambaldaite analogue, a value of 4.2 - 4.7wt% (dependant on water content) was expected. The XRD spectrum (Figure 53) of the product from the synthesis shows the expected peaks for sodium cobalt carbonate (red circles) as described by Ohnishi, however the sample additionally contains cobalt carbonate (blue squares). The presence of cobalt carbonate in the sample explains the reduced percentage of sodium measured.

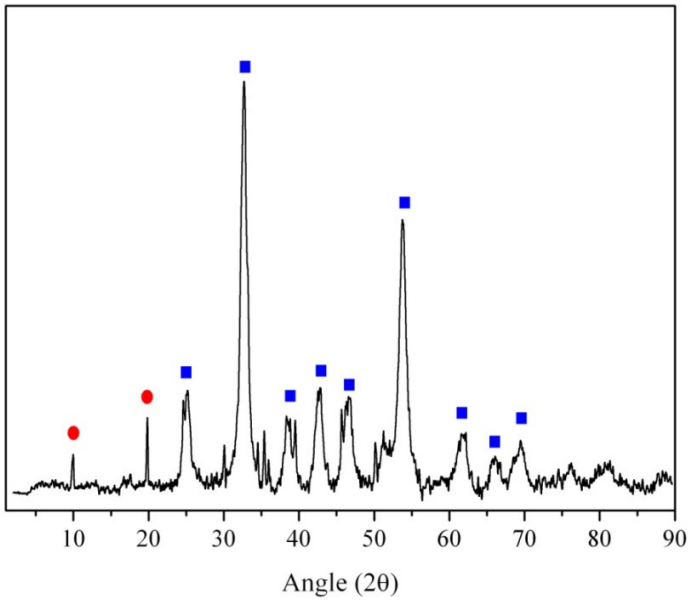

Figure 53 - XRD spectrum of sodium cobalt carbonate synthesised using a variation of the Ohnishi synthesis. Peaks for the kambaltite structure of sodium cobalt carbonate shown in red and cobalt carbonate in blue

SEM images of the catalyst precursor particles are shown in Figure 54. A mixture of morphologies were evident including rough particles, platelets and cubes. The sodium Kambaldaite structure was shown to exist as cubes by Ohnishi[248] and rough spheres by Petrov et al.[247] EDX analysis of particle agglomerate areas did show the presence of sodium. Nanoplatelets and nanocubes have been reported for cobalt carbonate, shown to be present from the XRD.[249,250]

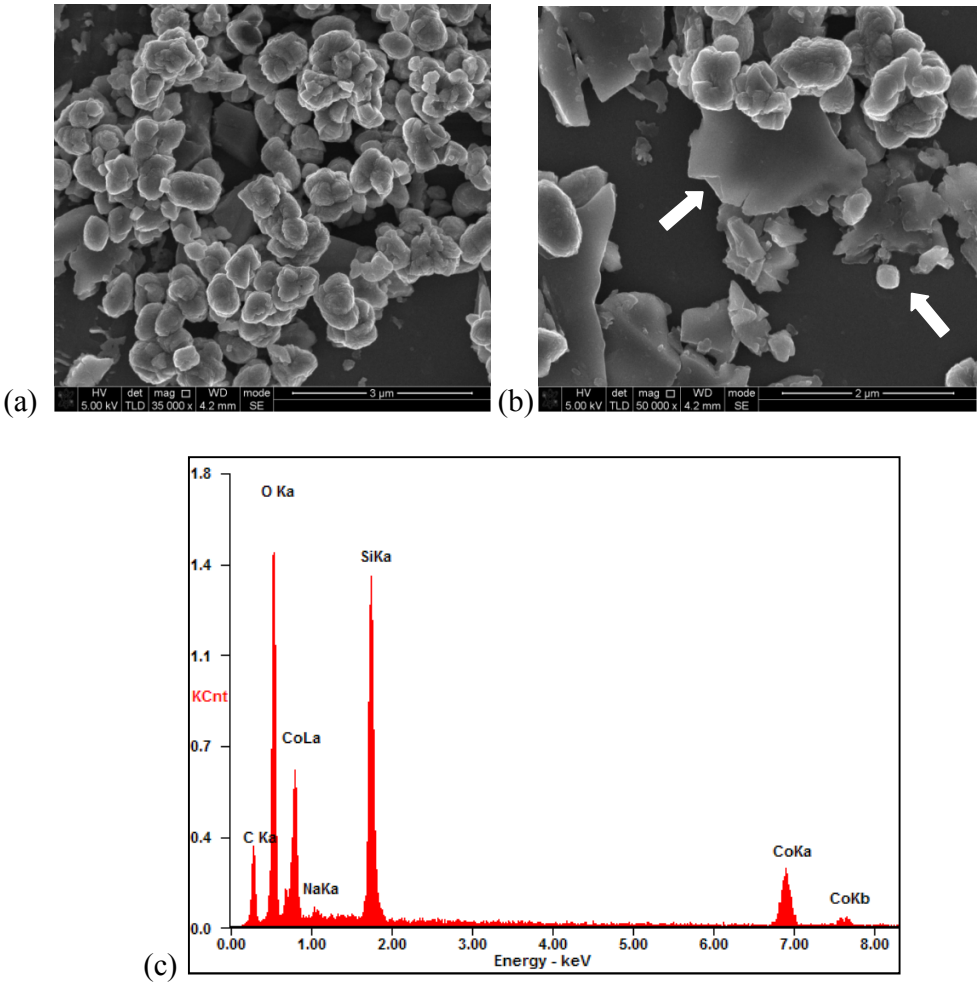

Figure 54 – (a) SEM image of particle resembling those reported previously for Kambaldaite. (b) Sheet and cube particle previously reported for cobalt carbonate. (c) EDX spectrum of particle shown by white arrow in (a)

5.2 CVD synthesis using bulk sodium cobalt carbonate

The synthesis of few layer graphene was achieved by heating the bimetallic precursor to 800^{o}C in argon, after which ethanol was introduced as a vapour. After 50 mL of ethanol had been passed through the system the catalyst was held at temperature for a further 3 hours and cooled. Sodium and cobalt were removed by an acid wash with 6M

HCl. The solution was filtered, then repeatedly dispersed in and filtered from water to neutral pH and dried under reduced pressure.

Raman analysis of the black powder exhibits the characteristic bands for graphitic carbon (D 1350cm^{-1}, G 1580cm^{-1} and G' at 2695cm^{-1}). The behaviour of the G' band with increasing numbers of layers has previously been reported[251] suggesting only single layer graphene shows a symmetrical lineshape with much greater intensity than the G band. Upon increasing the number of layers the intensity of the band decreases with respect to the G band and shifts above 2700cm^{-1}, developing a shoulder at a lower wavenumber present in HOPG.[174] Further, the G' intensity is relatively high compared to that of the G (ca 1.4). Reina *et al*[85] have showed that mono, bi and trilayer graphene sheets (measured by AFM) synthesised by CVD on nickel have a I_g:$I_{g'}$ ratio of 0.18, 0.35 and 1.3 respectively. Comparison of these values could suggest that few-layer graphene may be present within the sample (supported by TEM images, Figure 59). Further analysis of the G' peak shows it to be symmetrical in nature suggesting, that if the sample is multilayer, these platelets may be made of the turbostratic structure highlighted in chapter 3.[252]

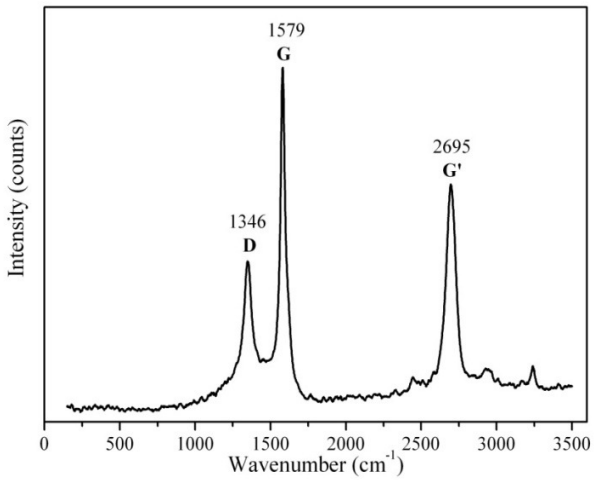

Figure 55 – Raman analysis of purified carbon product synthesised from the sodium cobalt carbonate catalyst and ethanol through CVD

Figure 56 shows the thermal degradation profile of the black deposit with respect to other graphitic materials. The decomposition peak for the product is between that of HiPCO™ SWNTs, (an excellent quality and high purity variety of single walled tube) and graphite, suggesting a closer relation to single and few layer nanostructures. Kitiyanan *et al*[240] have previously used TGA to characterise mixtures of SWNT, MWNT and graphite from the decomposition of carbon monoxide over cobalt/molybdenum mixed catalysts. The results indicated the total thermal decomposition of SWNT, MWNTs and graphite in air had a positive correlation to the number of layers produced, (from TEM images) based on the surface area available for oxidation. The similarity in the total decomposition point of the SWNTs, in comparison to that of graphite, suggests that the product could be few-layer graphene.

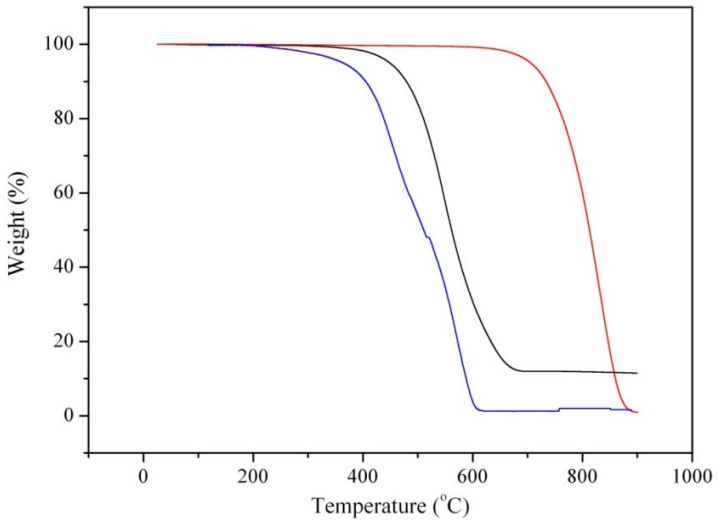

Figure 56 –Thermal decomposition of carbon deposit in air post purification (black). Comparative thermograms in air are shown for graphite (red) and HiPCO™ SWNTs (blue)

SEM images of the raw product taken directly from the process are shown in Figure 57. Flower like morphologies, consisting of a metal core surrounded by thin

graphitic platelets are revealed. The images also showed little evidence of large graphite crystals. The presence of these few lay platelets therefore should not need extensive solution processing to get graphene in comparison to natural flake graphite, commonly used in solution phase exfoliation.[51,52]

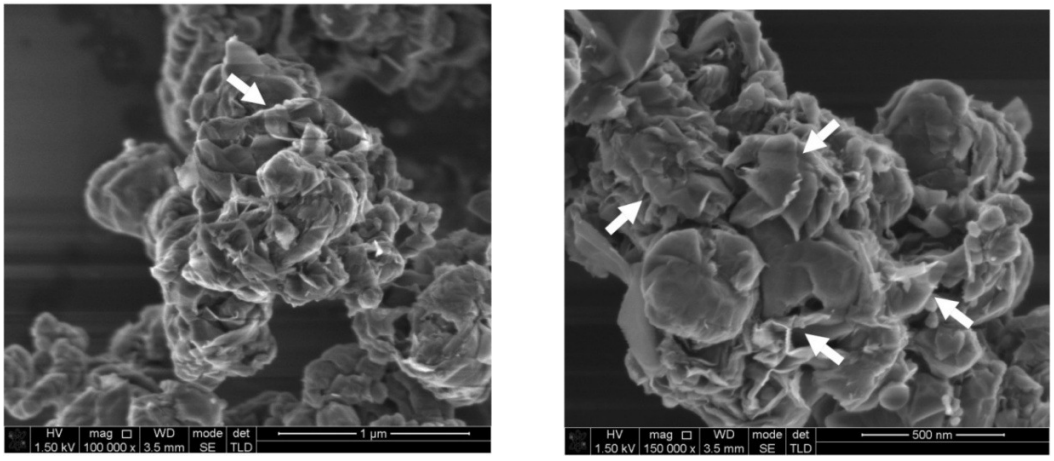

Figure 57 – SEM images of raw product of CVD where the precursor compound has been spin coated into silicon surfaces. White arrows depict areas where sheets are shown protruding from the surface.

To investigate the mechanism of formation for the carbon product, XRD was utilised to follow the heating of the precursor to 800^{o}C. At this temperature the peaks visible (black) correspond to a mixed CoO/Co_3O_4 phase. This observation indicates that the growth does not occur through a special sodium cobalt oxide phase and therefore exists as cobalt oxide plus a sodium salt, most likely sodium carbonate. After flowing ethanol over the surface of the oxide, XRD (Figure 58) shows the raw product (red) is a mixture of graphitic carbon ($2\theta = 26°$) and metallic cobalt[253] ($2\theta =$ 44 (111), 51.5(200) and 75.7 (220)). The most striking aspect of the XRD of the raw product is the magnitude of the graphitic 00l peak compared to the cobalt indicating the small degree of carbon deposition using the bimetallic catalyst. Following purification with hydrochloric acid, the

00l peak (2θ = 26.48, full width at half maximum = 0.73) became more prominent indicating the removal of cobalt.

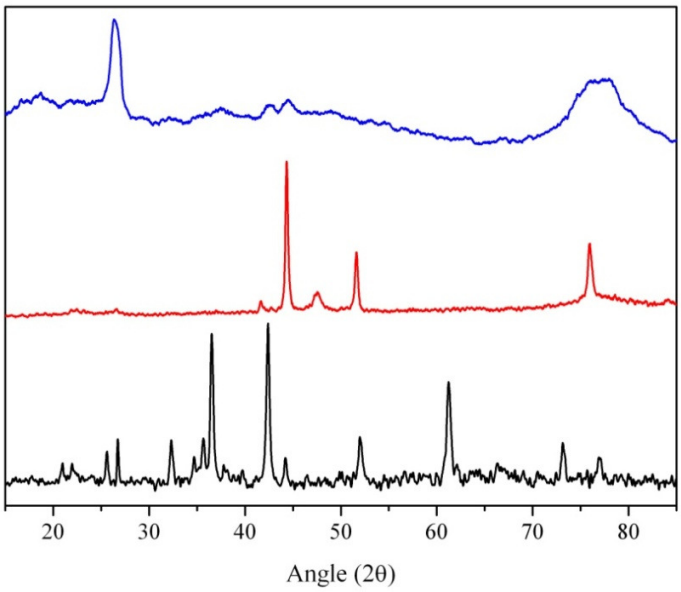

Figure 58 – XRD of the decomposed catalyst precursor at 800ºC (black), raw product after CVD run (red) and purified carbon product (blue)

The structure of the product is clearly demonstrated upon combining scanning and transmission electron microscopy (SEM and TEM). The samples were prepared with ethanol (SEM) and N, N'- dimethylformamide (TEM) as solvents, via mild sonication after which they were deposited on cleaned silicon surfaces and copper TEM grids by spin coating (SEM) or by drop casting (TEM). Collections of free sheets are observed in both the SEM and TEM. Under high resolution TEM the edges of these free sheets are shown to be made up primarily of few layer platelets (Figure 59, additional images shown in appendix Figure C 2). In general, when measured by layer counting, these platelets were in the region of 1 – 10nm. In areas where the platelets are folded, the individual graphene sheets are displayed with a separation of 0.35nm.

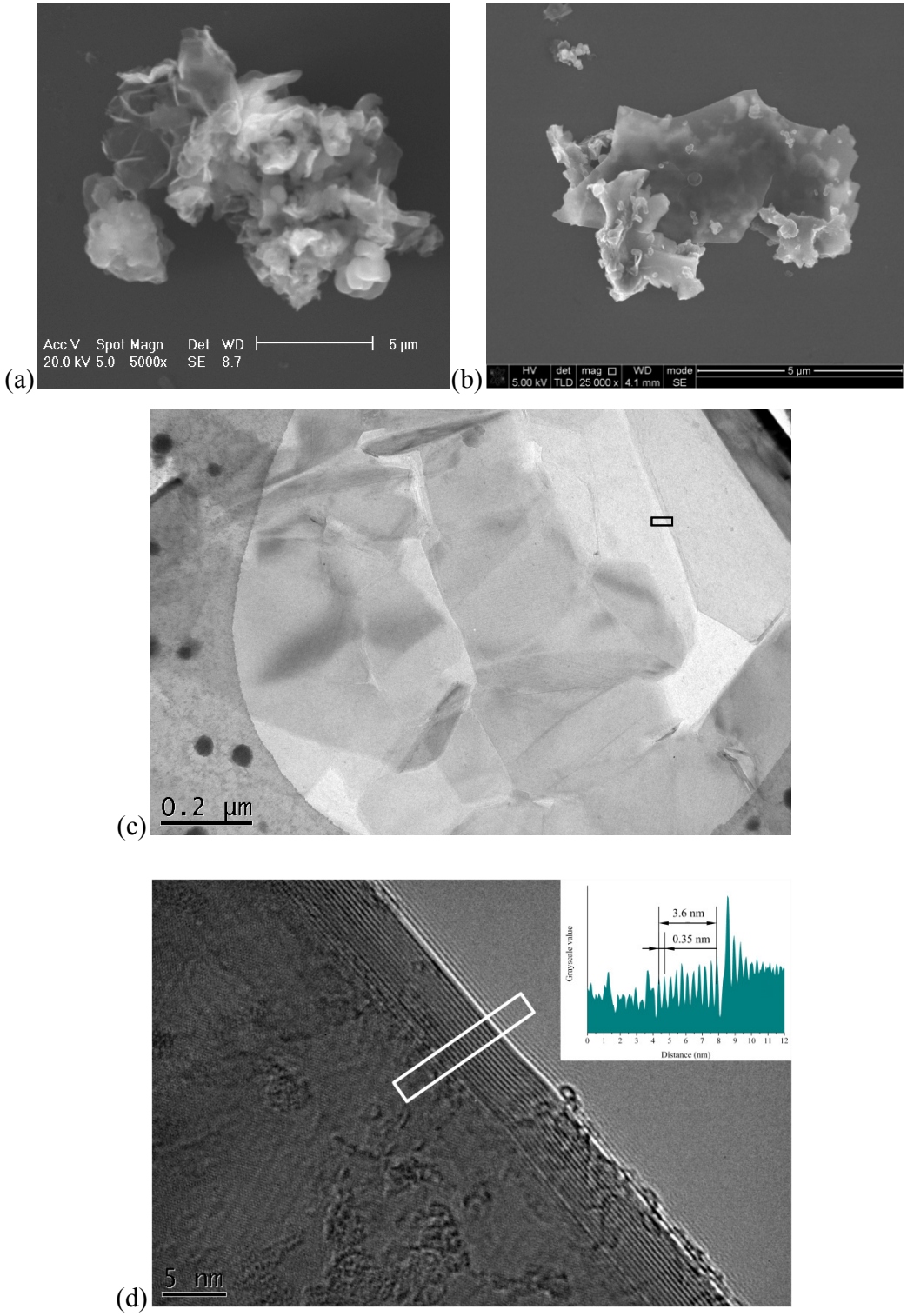

Figure 59 – (a,b) SEM images of free sheets agglomerated on silicon surface deposited from bath sonicated ethanol suspensions. (c) Bright field of purified product deposited in TEM grids from DMF and (d) HREM of area denoted by black rectangle in (c)

Interestingly, fast Fourier transform (FFT) of the platelets highlights more than one hexagonal pattern, expected for graphene or graphite, in some of the images, suggesting that more than one orientation of the sheets is present. From this observation two possibilities can be reasoned; either the platelets have turbostratic structure or there exists multiple thinner layered sheets at different orientations. From the various FFTs, the disappearance of hexagonal sets suggests that a different number of rotated sheets exist in the various areas. Image FFTs have been used previously to investigate rotational stacking faults in few layer graphene by Warner *et al*.[148] It was shown that by applying a circular mask filter to the FFT and reconstructing the image, (using the inverse FFT function) they were able to show the Moiré pattern associated with the selected stacking faults.

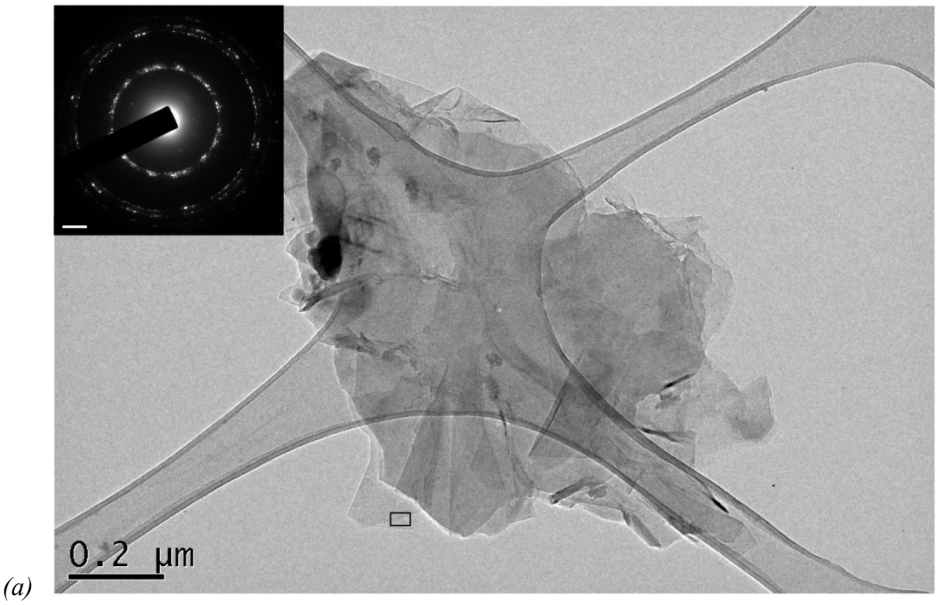

(a)

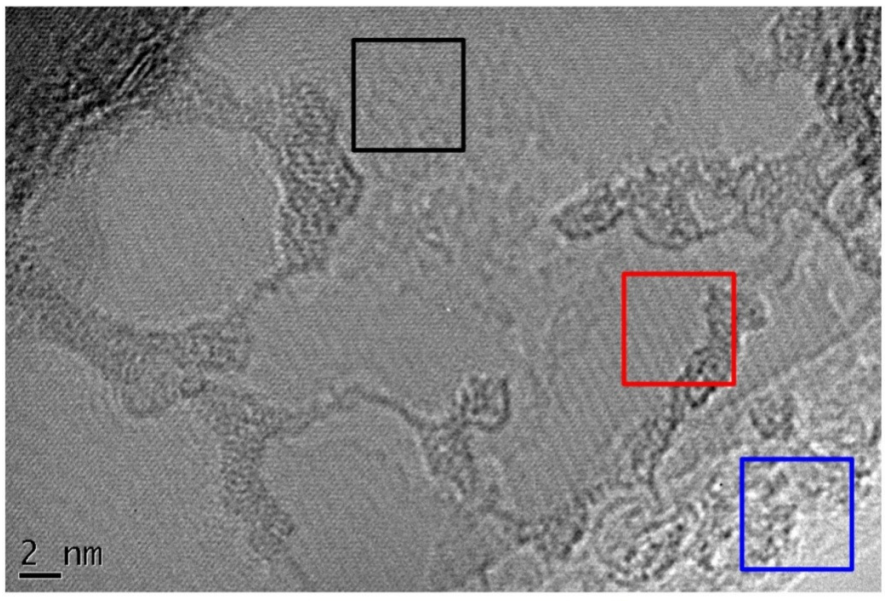

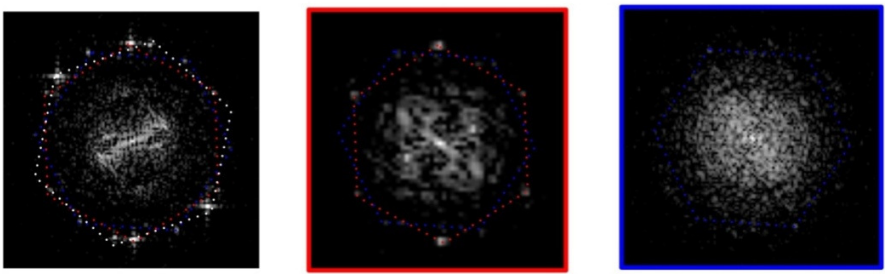

(b)

Figure 60 - (a) Bright field image of sheet agglomeration with associated diffraction pattern (scale bar 2 1/nm), (b) image of area shown by square with associated FFTs taken from highlighted areas.

Figure 61a shows the revelation of a similar Moiré pattern from the reconstructed image associated with applying a circular mask to the FFT of the region within the black box in Figure 60b. By masking only one hexagonal set from the image, (Figure 61b) the reconstruction shows the hexagonal makeup of graphitic carbon, which is similar to that shown in the surface FFTs from graphene dispersed in SDS.[52] Measurements from the reconstituted images show values analogous to the expected values for a hexagon size and sp^2 bond lengths (2.5Å and 1.42Å respectively). No evidence of any tubular, onion-like deposits or metal encapsulated carbons was evident in the microscopy, indicating a selective technique to sheet formation.

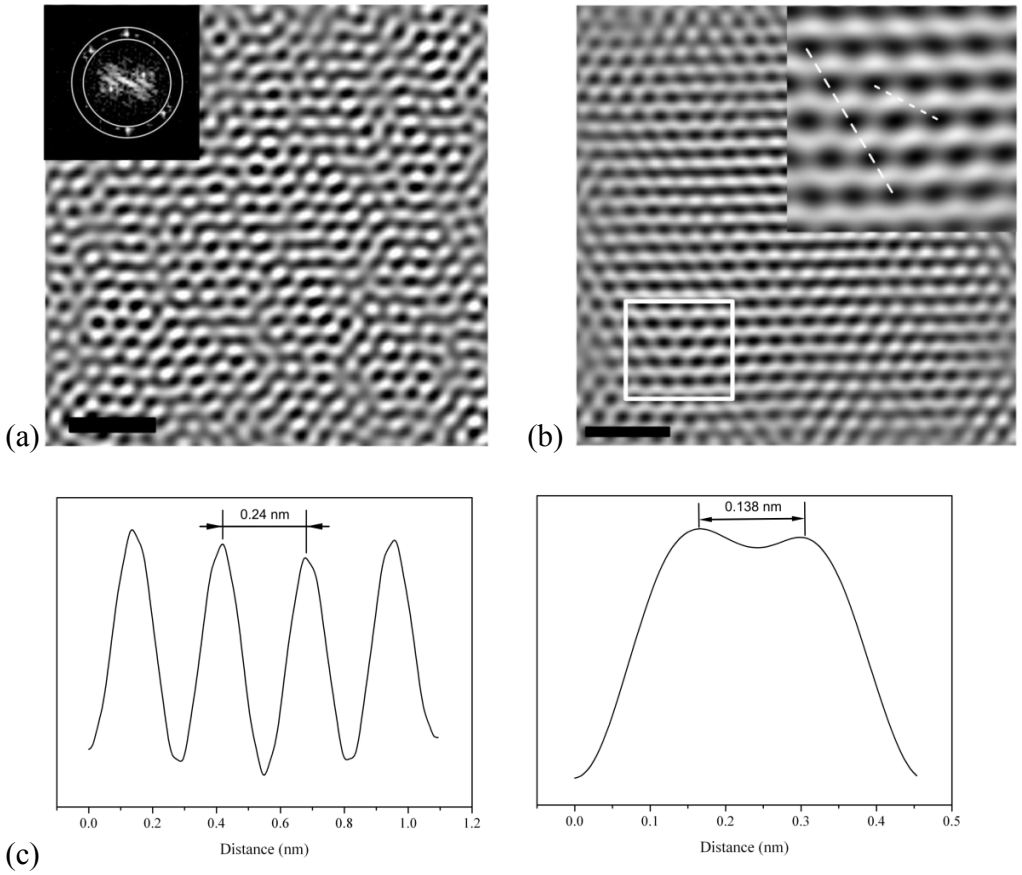

Figure 61 – (a) circular mask filter inverse FFT of the area shown in black in Figure 60b, (b) spot mask filter inverse FFT of one hexagon taken from FFT of area in black, (c) measurements take over highlighted area in (b)

5.3 Discussion

In addition to sodium cobalt carbonate, various other cobalt precursors were investigated, including cobalt carbonate, oxide (Co_3O_4) and nitrate to observe any variation in the products. In vast contrast to the product from the 1.5% sodium cobalt carbonate precursor, a marked increase in the amount of carbon was observed. On average the amount of carbon produced from the sodium cobalt carbonate was 45 mg (12 mg/mmol Co). In comparison, when using cobalt carbonate (no sodium present) and the oxide, a large weight of carbon was produced (*ca.* 300 mg, 75 mg/mmol Co) based on the same amount of precursor material. The large discrepancy indicates a noticeable difference in the contents of the products. Various explanations exist; the formation of metal encapsulated graphite contributing to the increased weight post purification or the presence of much larger graphite crystals. In the case of cobalt hexahydrate there was further evidence for MWNT and onion-like structures (Figure 64).

XRD, Figure 62, illustrates the difference between the raw products of the two carbonates (0% and 1.5% sodium content). By normalising the intensities of the largest peak of metallic cobalt, the difference in the size of the 00l graphite peak is apparent. This suggests large differences in the size of the graphitic fractions between the samples, indicating that those formed from the sodium cobalt carbonate product are considerably smaller/thinner (supported by the TEM images of the various carbon products). In addition to the intensity reduction shown in the raw products, there is an increase in the full width at half maximum for the purified deposit from the Kambaldaite analogue (fwhm = 0.73) compared to cobalt carbonate (fwhm = 0.51) and has been used previously to compare

several graphene production methods.[62,254] When these values are used in conjunction with the Scherrer equation, the c-axis grain sizes (perpendicular direction) are 11.18 nm and 16.31 nm respectively. However, the Scherrer equation cannot be used to give the finite thickness of the graphitic material, and has only been used in this case to show that the product of the Kambaldaite analogue is generally smaller/thinner than made from using cobalt carbonate.

$$D(nm) = \frac{K\lambda}{\beta cos\theta}$$

Equation 8 – Calculation of grain size, D, using Scherrer equation. K≈0.9, λ = 0.154 (Cu Kα), B = fwhm (rads) and θ = the Bragg angle.

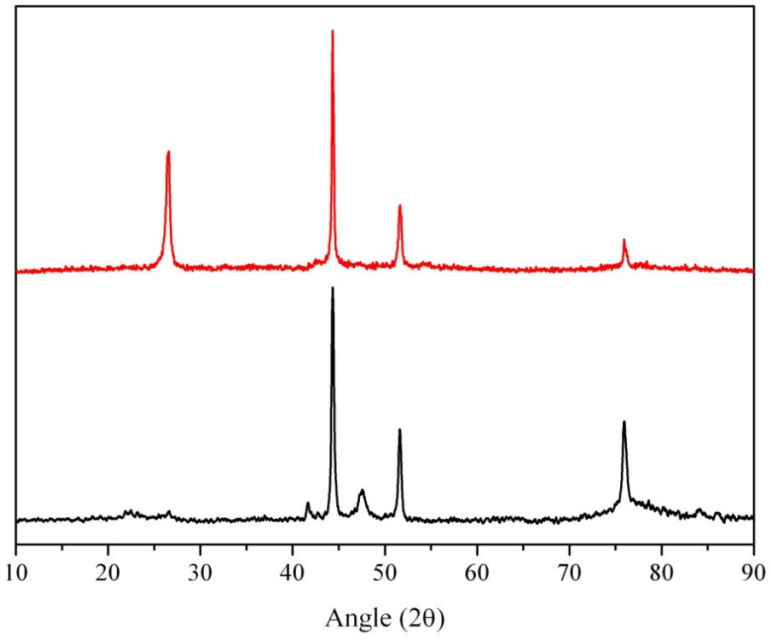

Figure 62 – XRD comparison of the raw products of the 1.5wt% sodium cobalt carbonate (black) and the pure cobalt carbonate

The increased amount of carbon is evident by visual observation in addition to the presence of large opaque graphite crystallites under electron microscopy, (Figure 64) in samples where elemental analysis indicates no trace of sodium content These samples did show some few layer platelets but, in general most were found emerging from larger crystals which constituted most of the sample on the grid (Figure 63a further images displayed in appendix Figure C 3). This is contrary to the images seen from samples containing 1.5wt% sodium, where images primarily show a higher percentage of few layer platelets. CVD procedures with cobalt oxide bought from external suppliers displayed only large graphite crystals with no free lying platelets (Figure 63b). In the case of cobalt nitrate hexahydrate there was further evidence for MWNT and onion-like structures (Figure 64a,b).

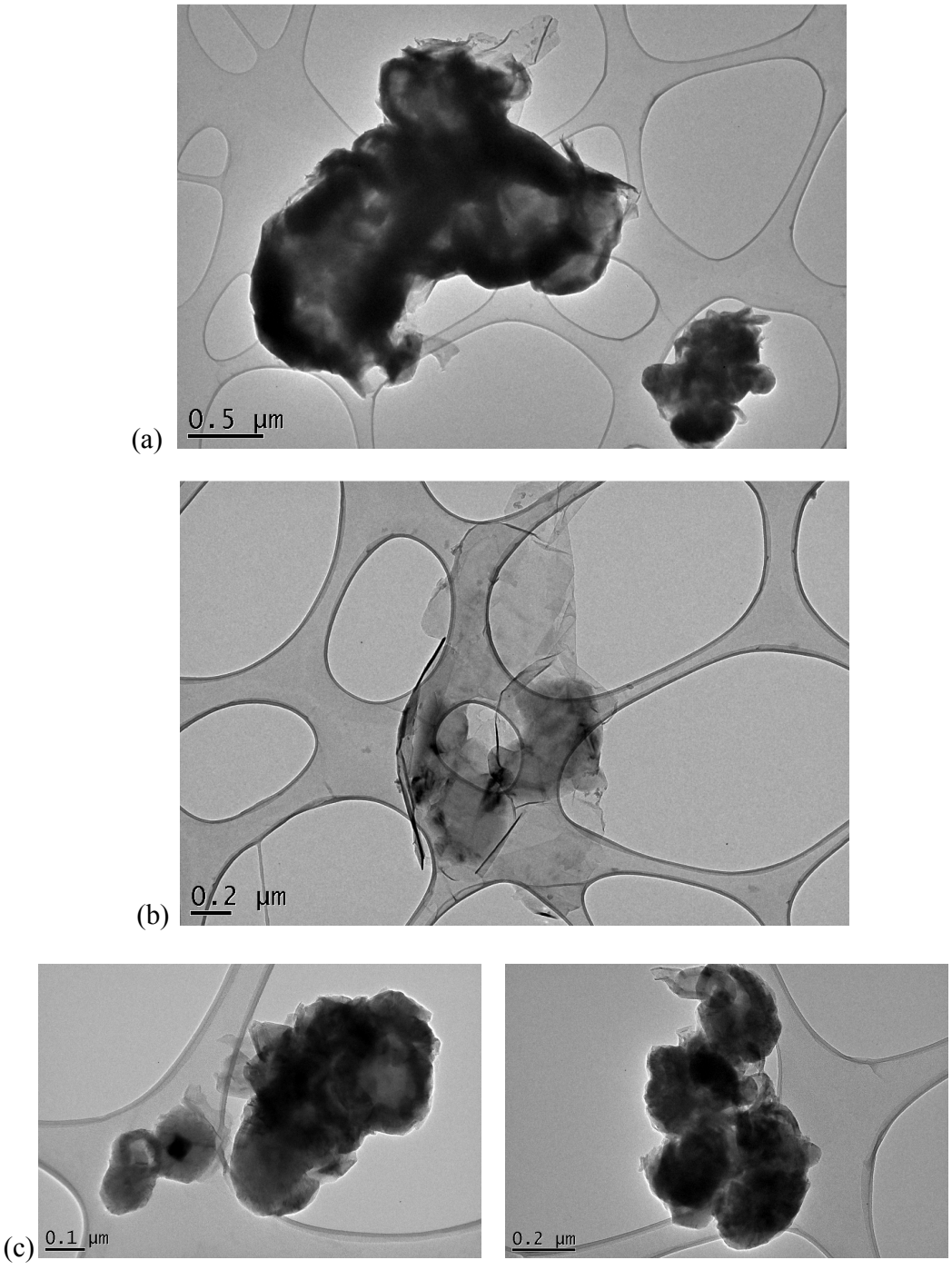

Figure 63 – TEM images displaying the various products of the CVD synthesis run with $CoCO_3$ (a) large crystals with exposed few layer sheets, (b) free standing few layer sheets and (c) Co_3O_4 as catalysts.

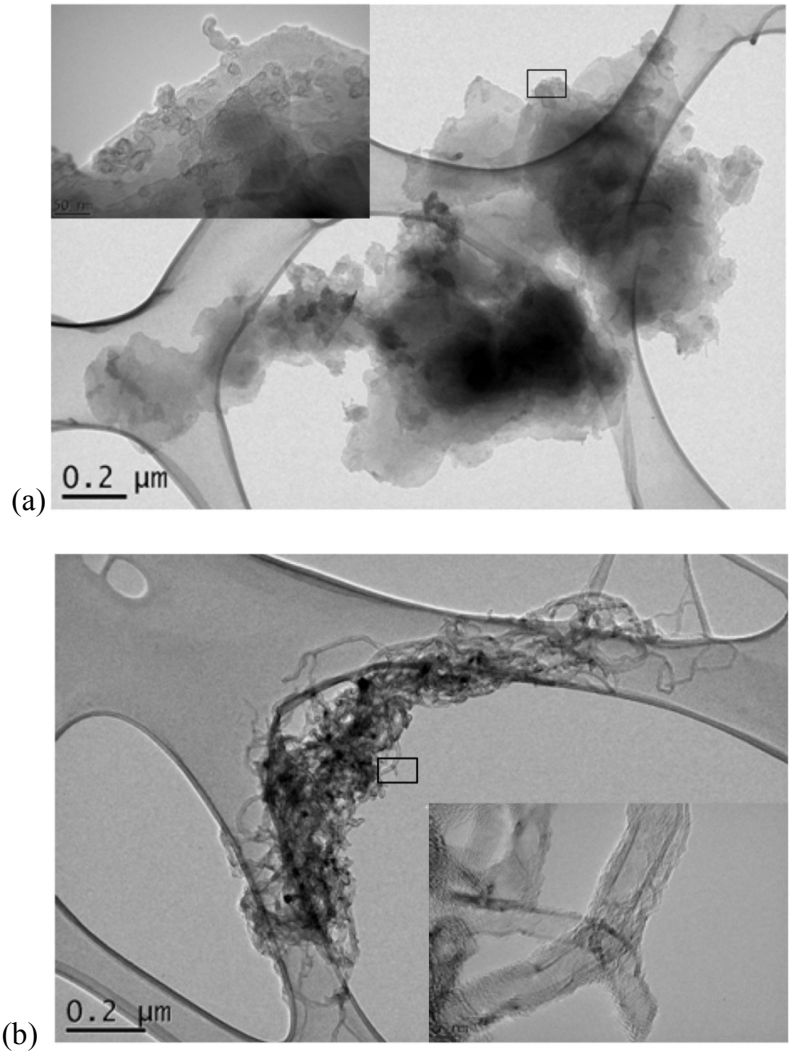

Figure 64 – TEM images of ethanol CVD over $Co(NO_3)_2.6H_2O$ showing (a) plates covered in nano-onions (inset, HREM) and (b) nanotubes (HREM inset)

5.4 Conclusion

It has been demonstrated that the presence of a non transition metal element, (in this instance sodium) can influence the amount of carbon that is produced by CVD and so the thickness of the graphitic material. Previously, this has been established to suppress the growth of carbon nanotubes by CVD synthesis, and subsequently has been used here

to suppress the growth of large graphite plates. In samples containing 1.5wt% sodium, electron microscopy showed the carbon product to primarily consist of few layer graphene platelets. In comparison samples containing no sodium gave products of a larger thicknesses (by comparing the XRD of the raw products of the two different precursors), reinforced by the appearance of mainly large graphite crystals in TEM. Analysis of the XRD pattern of the Kambaldaite analogue product shows a decrease in intensity in comparison to the product of cobalt carbonate reflecting the difference in yields. In addition modelling of the 002 peak using the Scherrer equation shows that there is a reduction in the c-axis crystallite size when sodium is present. In comparison when using other cobalt catalysts ($CoCO_3$, Co_3O_4 and $Co(NO_3)_2.6H_2O$) without the presence of sodium, products were primarily thicker or showed the additional presence of carbon nanotubes and nano-onions.

6. TEMPLATED SYNTHESIS OF GRAPHENE USING STRUCTURED TRANSITION METAL NANOPARTICLES

Nanoparticle templating has been previously used to synthesise CNTs in bulk quantities, with a range of studies describing how the choice of metal and spherical particle size can affect the CNT structure and properties.[188,197] This has been extended to other templates to produce selective structures. For example, large diameter (70 – 75nm) few layer (2 – 6) carbon nanotubes have been synthesised by CVD synthesis using nickel nanowires as templates.[255] This cannot be achieved using conventional CNT synthesis single and few layer nanotubes are typically 2 – 5nm in diameter due to the nanoparticles size. Furthermore, the use of atomic layer deposition of zinc sulfide nanoribbons on silicon substrates have provided an effective surface for the synthesis of few layer graphene nanoribbons from the decomposition of methane/hydrogen mixtures.[256] Using the same templating principle, bottom up synthesis of graphene should be possible by using flat nanoparticles as nanoscale metal foils, which facilitates the synthesis of many small size films/platelets instead of one large continuous film. The morphology of the flat particle is used to template of graphene layers is determined by the shape of the surface, as is observed in previous studies documenting the metal foil growth of graphene.[85,257]

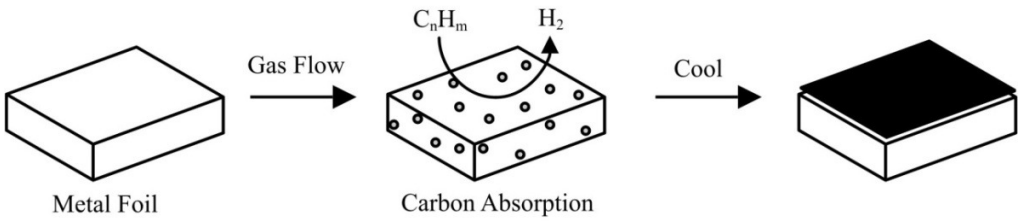

Scheme 1 – Mechanism of graphene formation on metal foil from high temperature CVD decomposition of carbon feedstock gases.

6.1 Synthesis of few layer graphene sheets using cobalt nanoplatelets

6.1.1 Synthesis of cobalt hydroxide nanosheets

Various designs of nanoplatelet structure were used to produce platelets large enough to maximize the size of the resultant carbon sheets. One of the most commonly reported methods of synthesising such structures is under hydrothermal conditions in Teflon lined autoclaves[258-261] or by exfoliation.[262] However, their products rarely show lateral dimensions greater than a few hundred nanometres. Liu *et al*[263] have shown platelets with dimensions in the range of micrometers can be made without using hydrothermal conditions at low concentration. This was achieved by heating a low concentration of cobalt chloride hexahydrate ($CoCl_2.6H_2O$) in the presence of sodium chloride (NaCl) and hexamethylenetetramine (HMT) within a water/ethanol mixture (Scheme 2), with cobalt hydroxide platelets beginning to precipitate after an hour under reflux. The product, purified of NaCl, forms the basis of the catalyst discussed in this section.

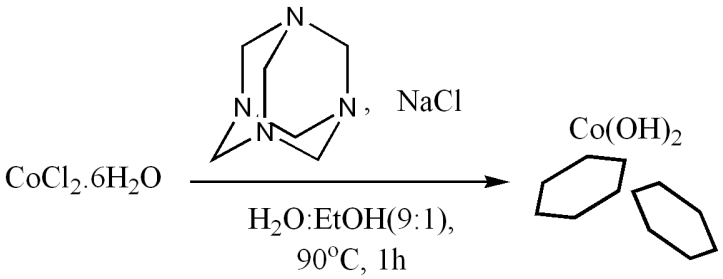

Scheme 2 – Synthesis of cobalt hydroxide nanosheets via precipitation as detailed by Liu et al[263]

XRD shows the diffraction spectrum of the green product prepared in the $CoCl_2$-NaCl-HMT system as shown in Figure 65. The presence and position of the 2θ values for

the 003 (7.95Å) and 006 (3.98Å) reflections confirm the presence of the layered hexagonally closed packed structure of α-$Co(OH)_2$ with intercalated chloride ions as presented in the original paper.[263]

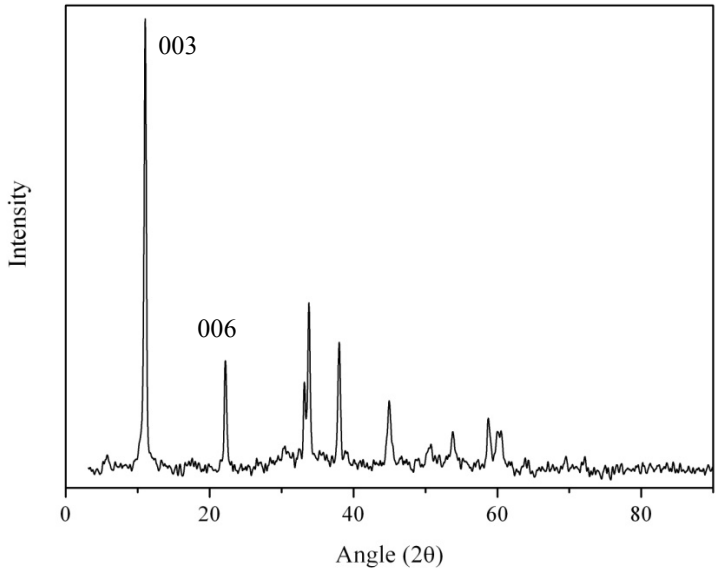

Figure 65 – XRD (CuK_α λ=1.54eV) spectrum of $Co(OH)_2$ platelets created through precipitation synthesis from $CoCl_2.6H_2O$, HMT and NaCl.

The size and morphology of the particles was confirmed by SEM. The lateral dimensions were found to be in the micrometer size, (1 – 5μm) with the average thickness of the platelets being in the region of 40 – 60nm. The particles were present as either platelets or with a flower-like morphology (Figure 66a). TEM analysis showed individual crystalline hexagonal plates distributed across the surface of the grid (Figure 66b). The corresponding SAED pattern (Figure 66b, inset) revealed hexagonally arranged diffraction spots, which could be indexed to the in-plane reflections (110) and (100) at 1.59Å and 2.72Å respectively for α-$Co(OH)_2$ (literature values 1.57Å and 2.71Å).[263] In addition, the presence of cobalt and chlorine were confirmed using EDX analysis.

(a)

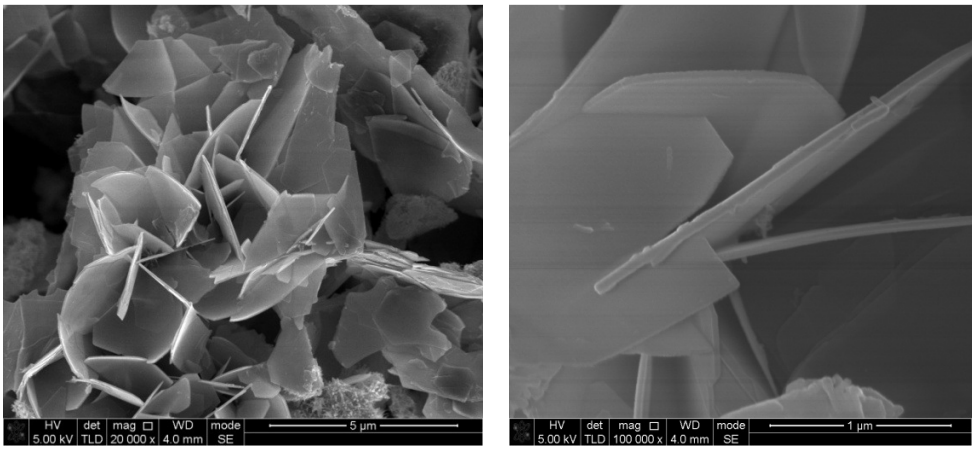

(b)

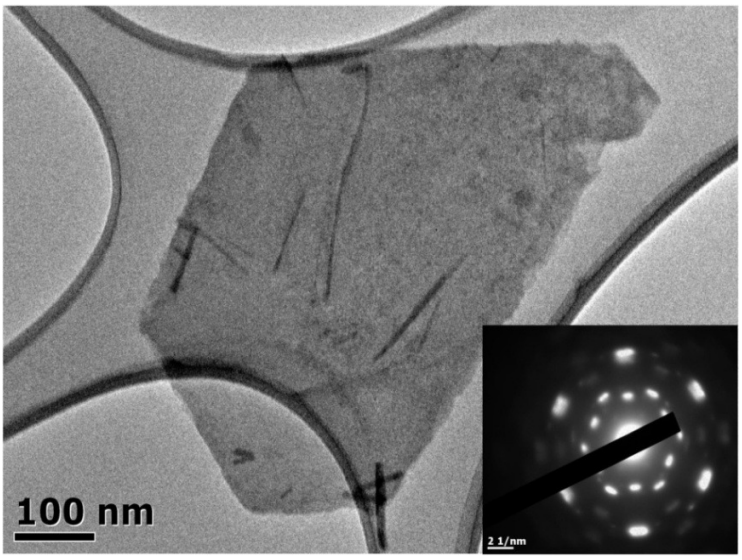

(c)

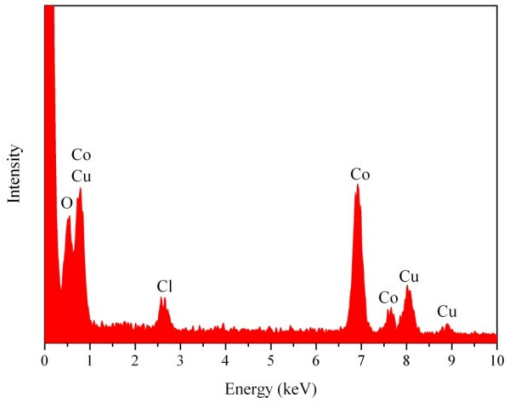

Figure 66 – (a) SEM images of $Co(OH)_2$ nanoplatelets spin-coated on Si/SiO_2 surfaces from ethanol suspension. (b) TEM image showing $Co(OH)_2$ nanoplatelet and associated SAED, (c) associated EDX analysis.

6.1.2 CVD synthesis of few layer graphene using cobalt nanosheets on silicon substrates

One of the key principles of this current CVD method, which is critical to its success, is the observation that the catalyst particles remain in the flat platelet morphology at high temperature and following reduction. This is of fundamental importance in order to enable the carbon to precipitate out with the architecture to give single/few-layer graphene on its surface. Hou *et al*[260] have shown that metal oxide nanoplatelets can be produced from hydroxide precursors after heating whilst the morphology remains intact. From these observations one would expect the cobalt hydroxide platelets used in this synthesis to behave similarly.

To investigate the growth of carbon on the cobalt nanoplatelet surface, a procedure was devised whereby the synthesised cobalt platelets were dispersed at low concentration in ethanol (ca 5 μgmL^{-1}) and spin-coated onto clean silicon substrates. Hence, a surface which could be imaged by both Raman spectroscopy and SEM was obtained. These silicon wafers were exposed to flowing ethanol at 800^{o}C, introducing carbon to the CVD system and then cooled to room temperature. As the cobalt hydroxide platelets are 1 - 5μm in size, confocal Raman spectroscopy can be utilized to detect carbon growth on the catalyst. The presence of the D, G and G' bands confirm the growth of graphitic carbon on the cobalt surface. The high intensity of the D band with respect to the G is apparent from the spectra (*ca.* 0.67, Figure 67), similarly to other graphene samples prepared on cobalt

by Ago *et al*.[87] Large area films of single layer graphene derived from CVD synthesis on cobalt foils were observed to give a high I_D:I_G ratio while attached to the cobalt surface.

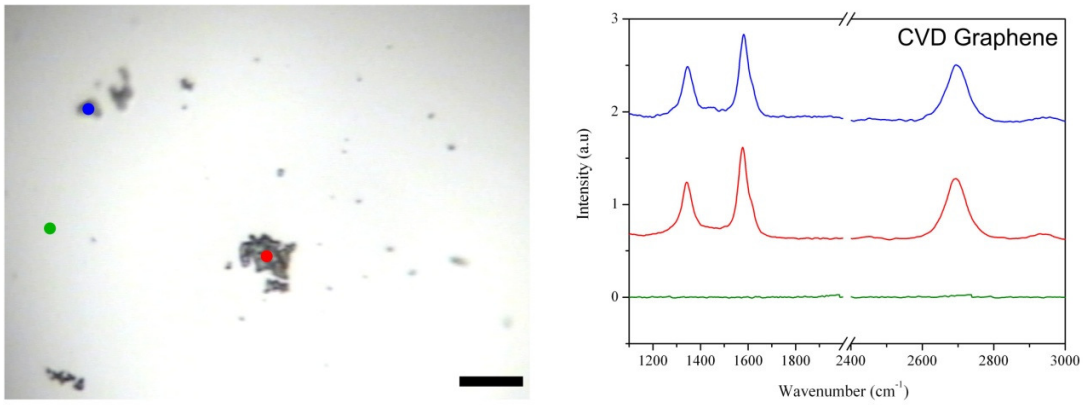

Figure 67 - Raman microscope image (x50WA lens, scale bar 8μm) showing silicon surface after CVD reaction of $Co(OH)_2$ nanosheets (left), Raman spectrum taken at different points shown in optical image

SEM images of the silicon surface show retention of the platelet morphology after CVD growth of graphene (Figure 68). The surfaces of the plates appear smooth, with observed ripples or wrinkles (white arrows). Meyer *et al*[14] observed, during investigations into suspended micromechanically cleaved graphene, that they do not lie perfectly flat; both when self suspended and when mounted. As a consequence, these features have been observed on several metal foils, such as nickel[5] and iridium[90] after CVD synthesis. This is thought to be as a result of the difference in the thermal expansion coefficients for graphene and metal substrate.[264,265] As a consequence mechanical stress is applied to graphene during cooling, inducing the structure to ripple in areas of weak adhesion in order to counteract such an effect.

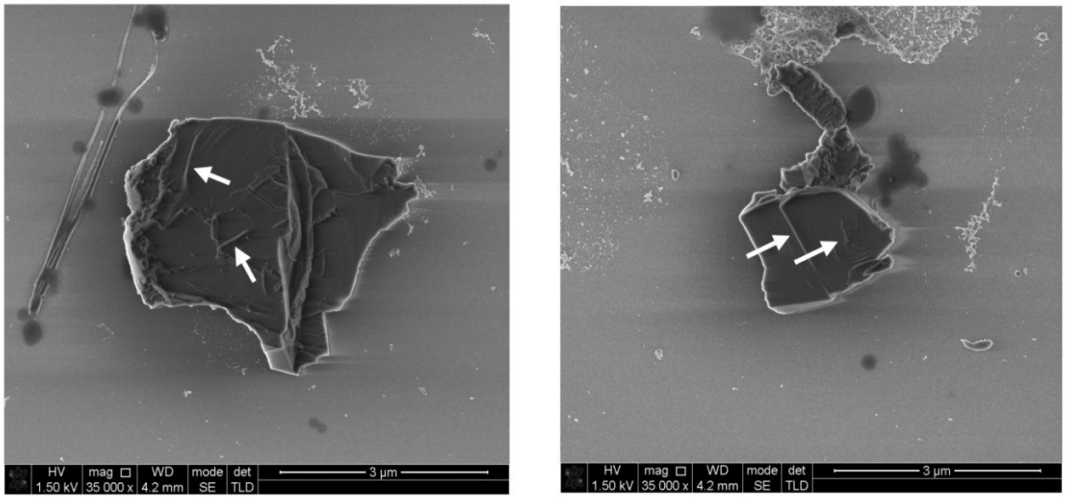

Figure 68 – Cobalt/carbon nanoplatelets post CVD procedure. White arrows depict regions where rippled natures are observed.

Reina *et al*[266] have previously shown films of graphene can be removed from the surface of nickel foils by acid etching in dilute hydrochloric acid, therefore these films can be transferred to various substrates for analysis. Similarly, dilute acid was used to remove the cobalt between the graphene and the silicon surface, enabling few layer graphene platelet transfer to carbon coated TEM grids. TEM analysis showed agglomerations of platelets, made of individual few layer graphene platelets (Figure 5a). The presence of spots in the {1100} and {2110} planes from the SAED illustrate good crystallinity in the graphene platelets, which exist in ring patterns due to the various orientations present. In addition, the FFT of surface features in Figure 69b show the hexagonal pattern associated with the {1100} graphene plane, previously illustrated in graphene synthesis, via the surfactant exfoliation of graphite.[52] High resolution TEM of platelet boundaries show long straight edges, characteristic of well crystallised graphene, ranging from bi and trilayers (white arrows in Figure 69c) up to *ca.* 3 nm.

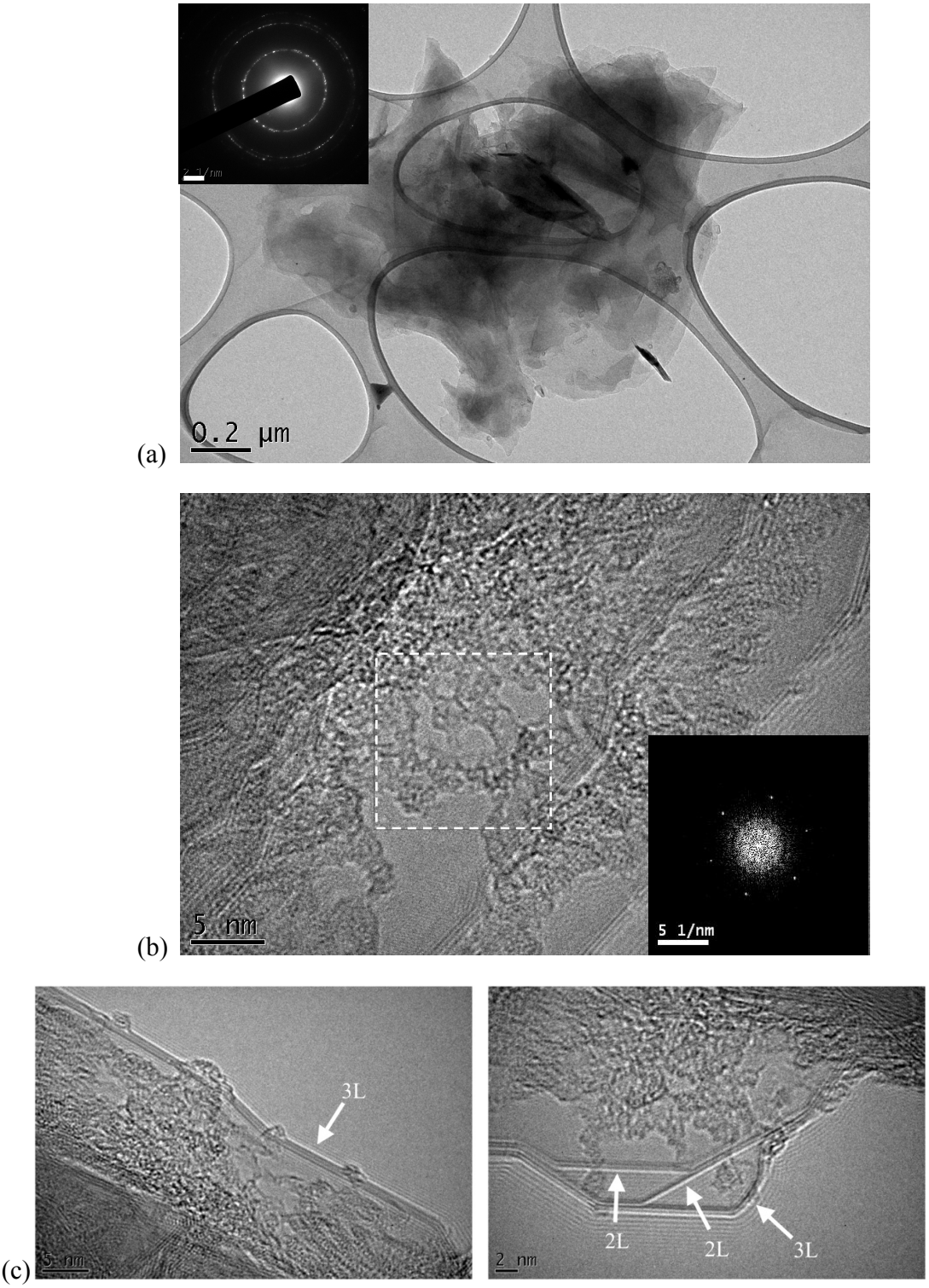

Figure 69 – (a) BF-TEM of agglomeration of material on grid (inset SAED, scale bar 2 1/nm), (b) HREM of surface and edge with attached FFT of area shown in white and (c) HREM of platelet edges

6.1.3 CVD synthesis of few layer graphene using magnesium oxide supported cobalt hydroxide nanoplatelets

Few layer graphene growth has been demonstrated on the surface of metal nanoplatelets. However the limited surface of the silicon hinders scalability. To increase the yield of graphene from the cobalt hydroxide catalyst and enhance the growth potential of this catalyst, the nanoparticles can be incorporated into inert supports which are commonly used for CNT synthesis: magnesium, aluminium and silicon oxides (MgO, Al_2O_3, SiO_2 respectively). Hence, assuming the growth of the graphene is identical to that shown in section 6.1.2, the dispersion of these platelets in the inert support should improve the surface area and in turn yield.

The MgO supported catalyst was prepared using wet impregnation in ethanol with 1 – 5 wt% used. The appropriate mass of $Co(OH)_2$ nanoplatelets were weakly sonicated in ethanol exfoliating the cobalt platelets in solution to which mechanically ground MgO was added and sonicated for a further hour. Removal of the ethanol under reduced pressure gave a visually homogeneous catalyst. The MgO serves as a buffer material, increasing the surface area of activity and negates the possibility of the cobalt particles sintering at high temperature. CVD growth of graphene using the supported catalyst was achieved using ethanol at 800^{o}C under argon atmosphere. The argon flow rates used were identical to chapter 5; however ethanol input was discontinued after thirty minutes and cooled to room temperature. Removal of the catalyst and support yielded *ca.* 30 mg per gram of 1% cobalt nanoplatelet/magnesium oxide catalyst (0.12 g/mmol Co).

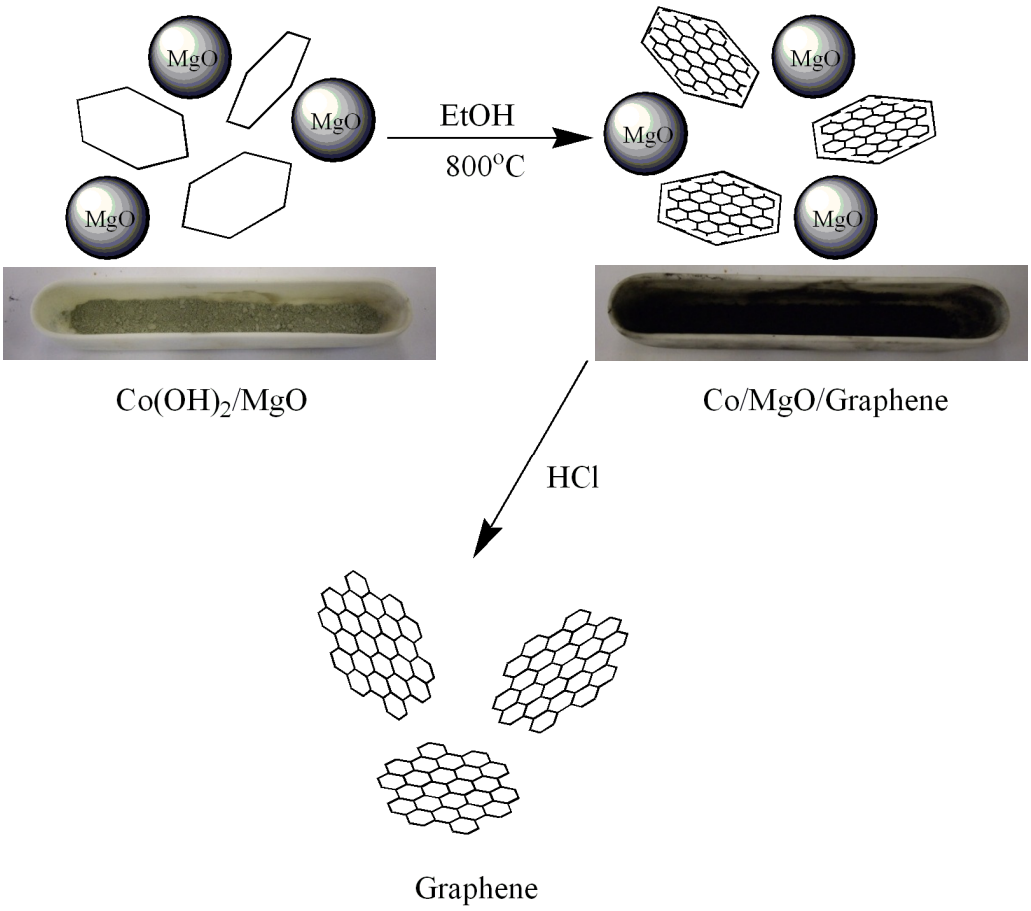

Scheme 3– (main) Schematic description of the bulk synthesis of graphene based on the cobalt hydroxide/magnesium oxide synthesis methodology (inset) above shows catalyst before and after synthesis.

Further, Raman analysis, Figure 70 shows the expected three peaks associated with graphene. In comparison to the graphene produced from the silicon supported cobalt nanosheets, the I_D:I_G ratio of the MgO graphene is much higher in this case (1.1 compared to 0.67), possibly due to smaller crystallite size. The thermal stability of the few layer graphene synthesised, measured by TGA in air, illustrates the point at which all the carbon has been burnt off (660°C) being similar to that of HiPCO™ nanotubes (600°C) suggesting that the product is few layer. A small weight loss (4wt%) is observed in the

region 300 – 400ºC which may be due to a small amount of amorphous carbon produced.[240,267] XPS analysis (appendix Figure D2) of the material showed minimal contamination from the catalyst and support, suggesting clean removal using the simple acid cleaning procedure. The C_{1s} window (Figure 70c) shows the major contribution is from the C=C at 284.6eV (71.44%) in addition to only limited signs of oxidation, with peaks allocated to C-O, C=O and carboxyl groups with relative intensities of 8.2%, 4% and 2.2% respectively.

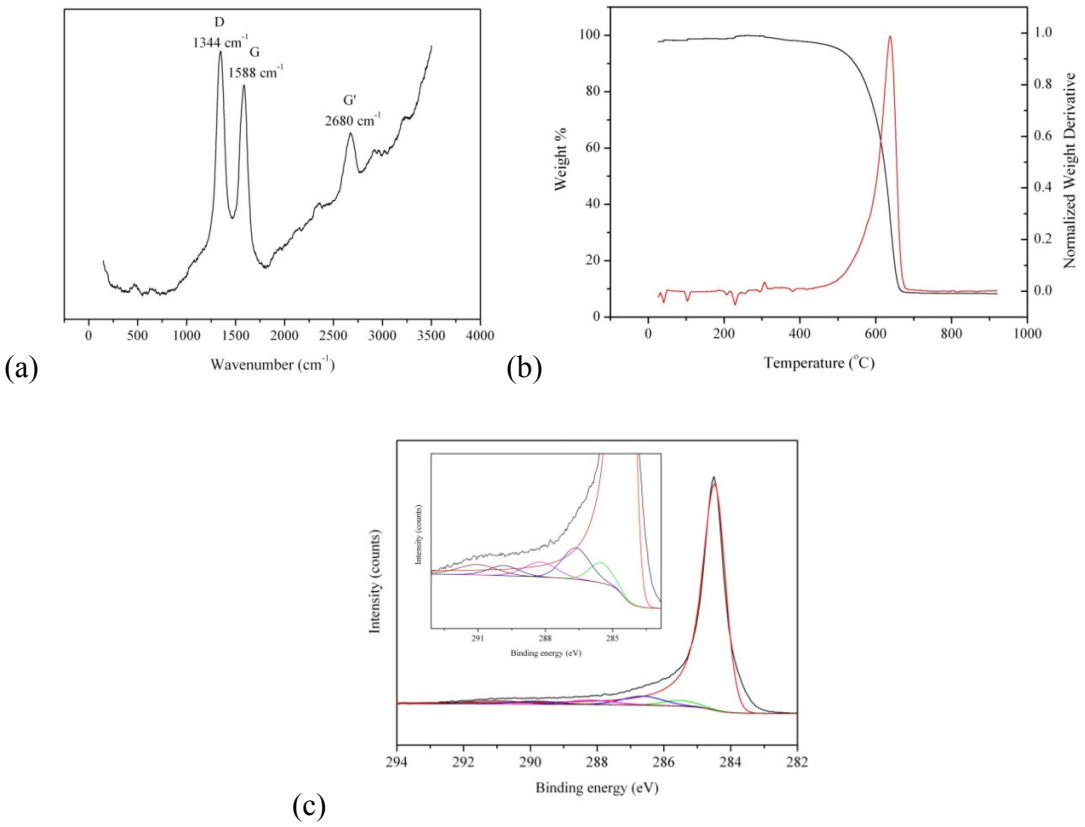

Figure 70 – (a) Raman, (b) TGA and (c) XPS analysis of product from ethanol decomposition over 1% $Co(OH)_2$/MgO

Following purification and removal of the MgO support/residual metal, SEM shows multiple agglomerations of material made up of carbon deposit (as shown by EDX,

Figure 71c). Upon closer examination, the agglomerated sheet like carbon structures are shown protruding from the surface (identified by white arrows Figure 71b). In addition, the SEM does show evidence of possible nanotube/nanoribbon deposits. This is most likely due to nanoparticles/nanoribbons of $Co(OH)_2$, which did not grow into sheets during the precipitation synthesis.

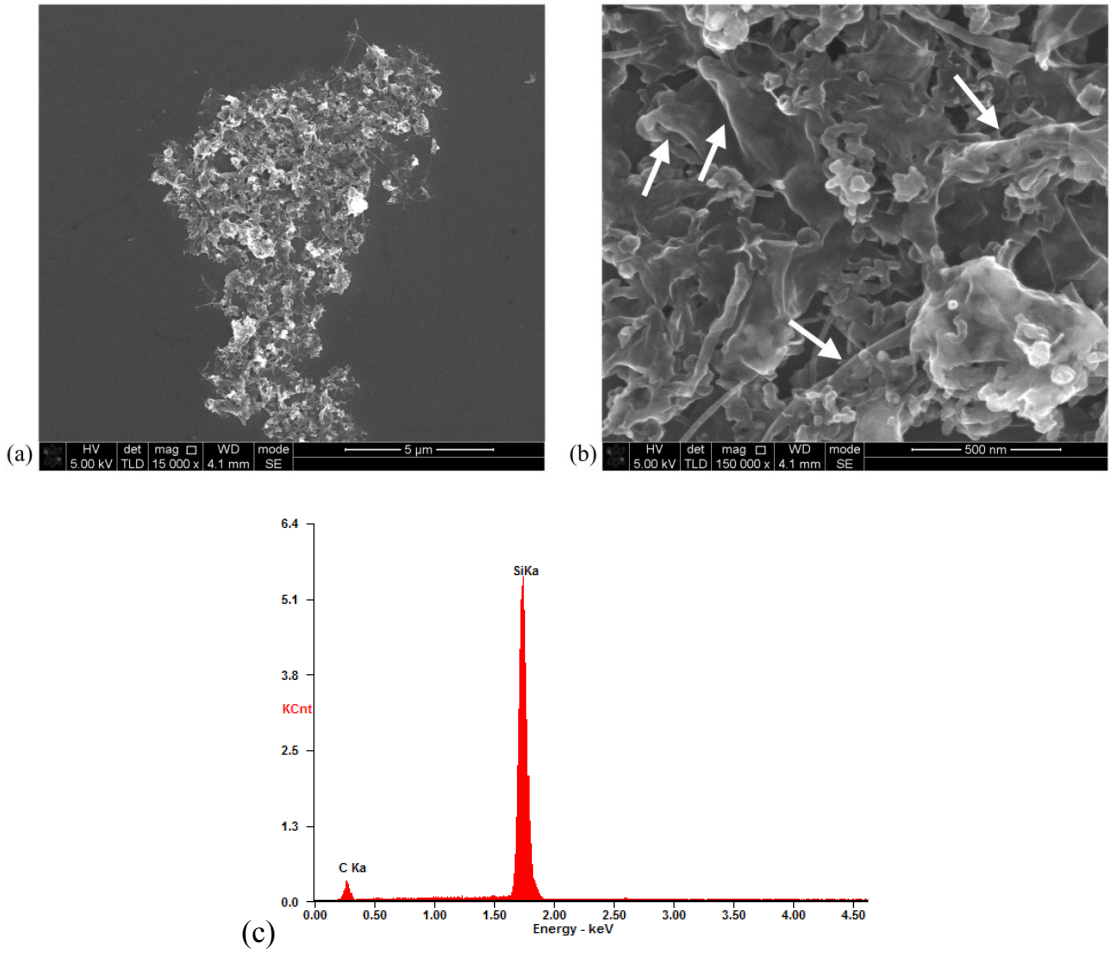

Figure 71 – SEM images of (a) agglomerated carbon, (b) individual sheets (white arrows) and (c) EDX analysis of agglomeration

Similar agglomerations of carbon are observed by TEM (Figure 72), with the free sheets being more visible in transmission. Other CVD methods to produce graphene,

including the plasma decomposition of ethanol[98] and decomposition on sodium ethoxide solvothermal products[110] have produced similar agglomerations. HREM indicates there is evidence of the structuring of the graphene, due to visualization of the individual sheets towards the edge. The individual sheets were observed to be separated by 0.35nm, suggesting the presence of few layer graphene.

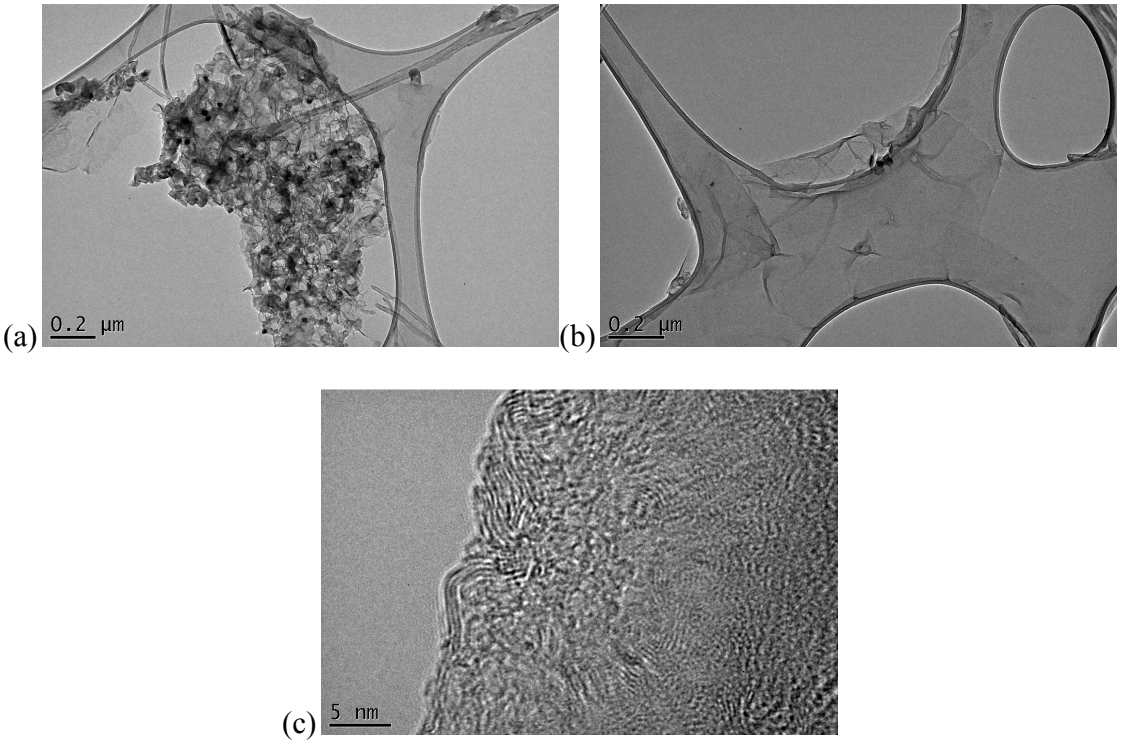

Figure 72 – (a) BF-TEM image showing agglomerations of sheets on grid with SAED as inset (b) BF-TEM showing individual sheet (c) HREM shows a trilayer edge

Analysis of the platelets surface shows the presence of both rings and weak spots in the selected area electron diffraction Due to the thinness of the platelets (shown by images from the AFM) and the appearance of weak spots (in-plane *hki*0 reflections {1100} (2.13Å) and {2110} (1.23Å)) may suggest that the material may be nanocrystalline.

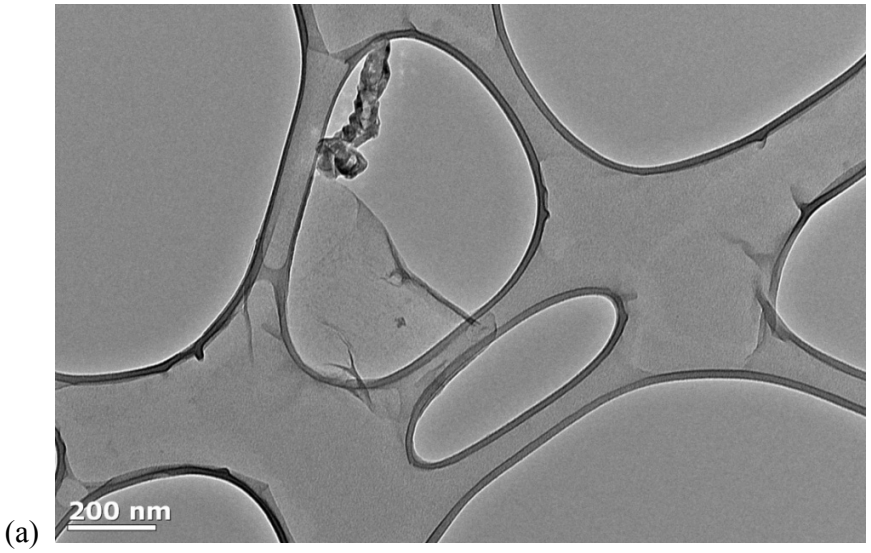

(a)

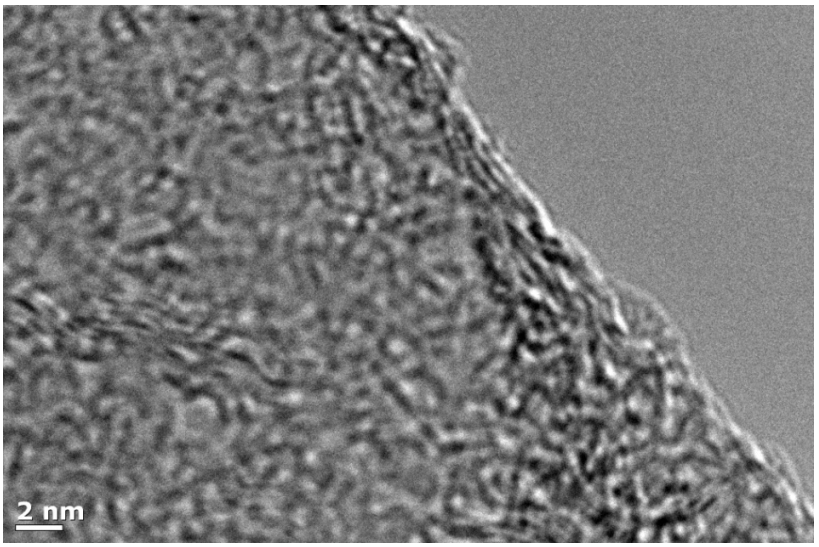

(b)

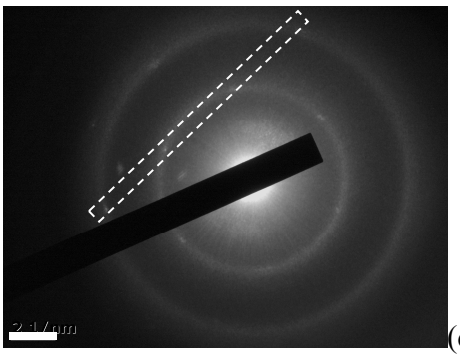

(c)

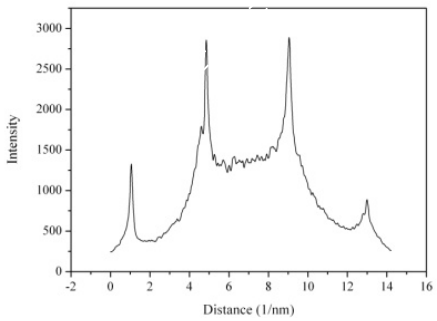

(d)

Figure 73 – (a) Bright field TEM image showing individual few layer graphene platelets on lacey carbon TEM grid (b) HREM image of platelets edge, (c) selected area electron diffraction pattern taken with 100nm aperture (scale bar 2 1/nm) (d) Line profile of boxed area shown in (c)

EELS spectra in the carbon K-edge region were used to probe the structure of the synthesised sheets. Figure 74 displays the EELS spectrum for one of the sheets, combined with that for the amorphous carbon support. The EELS spectrum for the product of this synthesis shows a similar structure to that measured by Dato[98] on graphene, produced by microwave plasma decomposition of ethanol. The increased intensity of the π* (1s – π*, 285 eV) and the appearance of the σ* band (1s – σ*, 291 eV) in comparison to that for the amorphous carbon support, indicate the presence of graphitic carbon.

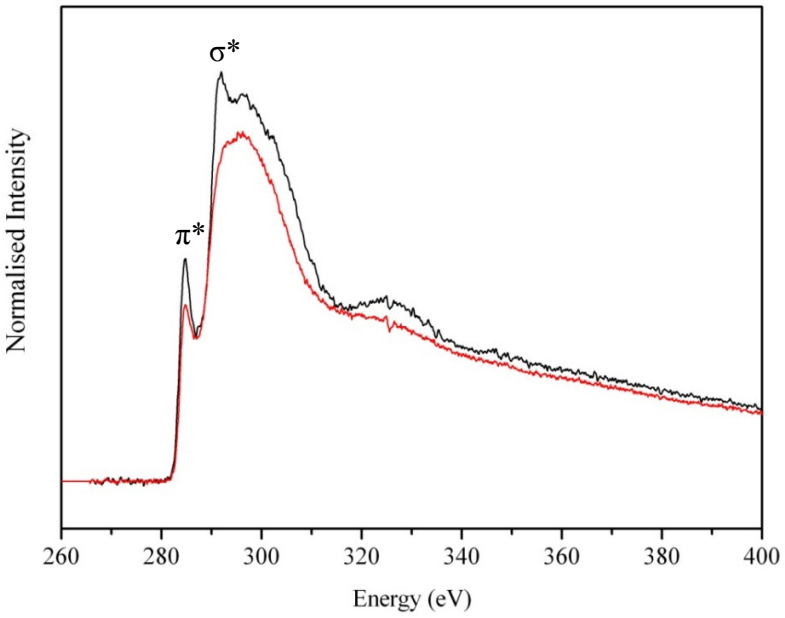

Figure 74 - EELS spectrum of sheet synthesised from ethanol decomposition over cobalt nanosheet/MgO catalyst showing graphene product (black) and amorphous carbon film (red).

As EELS only gives reliable thickness measurements for particles thicker than 10 – 15 nm, AFM was employed to assess the uniformity of the platelets sizes produced. Imaging of graphene platelets, supported on mica, were found to have a thickness between 2 – 5 nm, suggesting the presence of few layer graphene (Figure 75). These platelets

appear slightly thicker than those of the graphene synthesised on the immobilized cobalt platelets on silicon substrates, as observed by TEM. Such a discrepancy is most likely due to the increased time which the alcohol flowed over the supported catalyst (thirty minutes in contrast to two minutes). Upon close observation of Figure 75, surface features can be identified and are described as wrinkles, attributed to the mounting of graphene upon a substrate.[149,268,269]

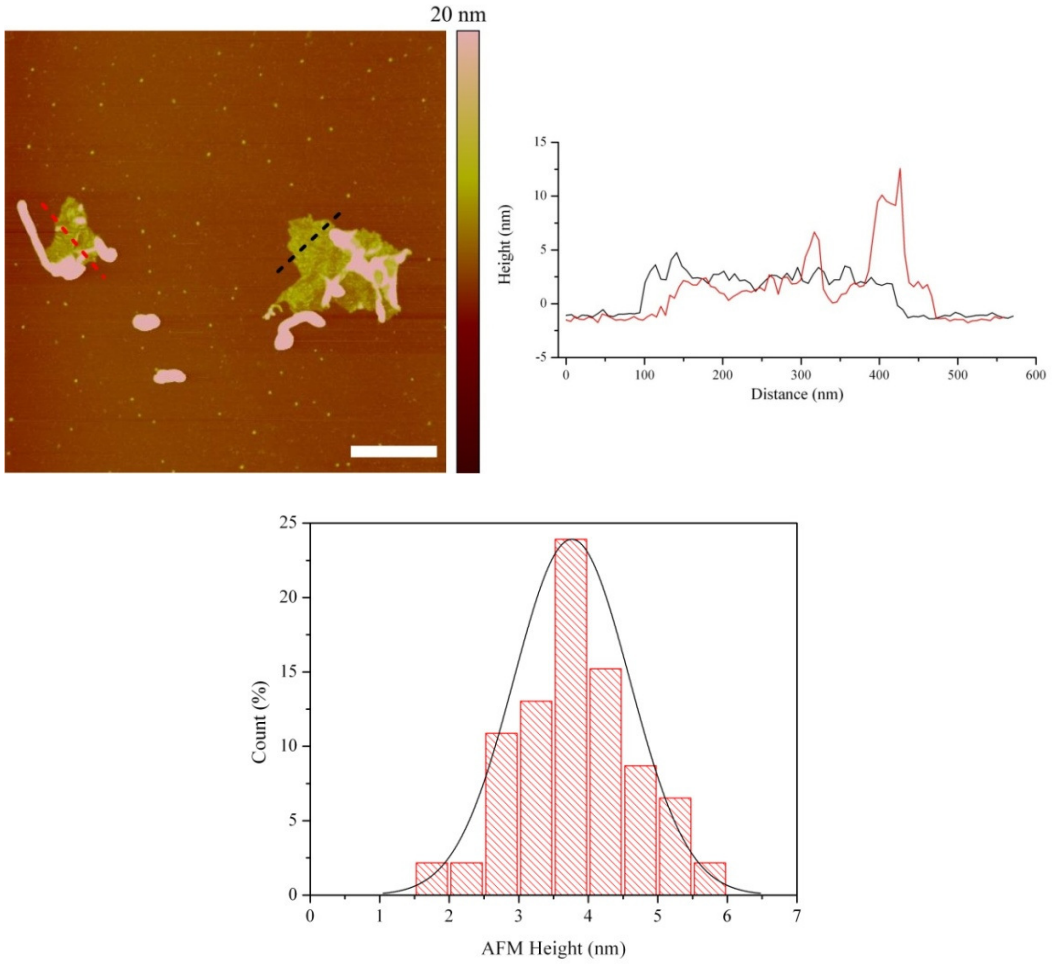

Figure 75 - AFM (2.5 x 2.5µm, scale bar 500nm) analysis of silicon surface spin-coated with carbon product with the corresponding surface cross section analysis (above) and histogram depicting thickness distributions, determined by AFM

6.1.5 Effect of feedstock variation on synthesis

The field of carbon nanotube synthesis provides many methods in the literature corresponding to CVD synthesis on supports.[188,240,270] In the previous sections, ethanol was used as the carbon source for the synthesis of few layer graphene. However, industrial reactors are preferentially set up to work with gas phase carbon sources, commonly: methane, ethane, acetylene and carbon monoxide, which can often be recycled to improve cost and efficiency. By altering the set up of the reaction in 6.1.3 to accept multiple gas phase precursors, the synthesis was carried out under a 10% hydrogen/methane mixture and carbon monoxide.

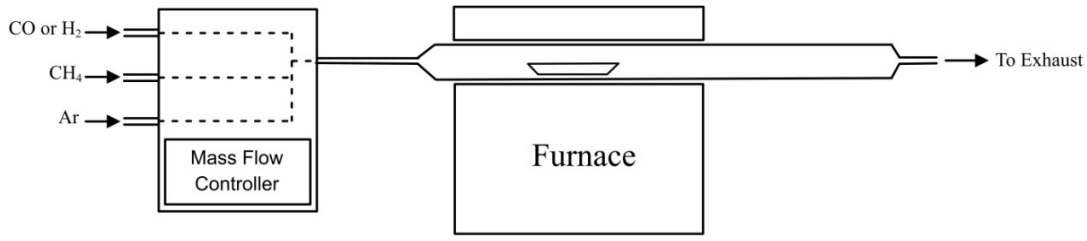

Figure 76 - Apparatus set up for gas phase delivery for CVD reactions

The method that was used for the CH_4:H_2 synthesis was a variation of the method used by Li *et al,*[270] based on the gas phase mixing with argon which has been shown to produce high quality SWNTs on MgO supports. By employing hydrogen prior to the flow of methane, the reduction of cobalt could be ensured, in contrast to an ethanol source, where the platelets are reduced in situ. Carbon monoxide, due to its reducing nature, does not require a pre-reduction step, acts in a similar fashion to ethanol, whereby the nanoparticles are reduced during the procedure. The yield of the carbon product when CO was used as the feedstock was very low, suggesting that total in-situ reduction of the cobalt precursor was not achieved. This is indicated by the presence of the Raman bands

associated with CoO between 500 and 700 cm^{-1} (Figure 77).[271,272] The formation of carbon deposits from the disproportionation of carbon monoxide is known to vary, dependent on temperature.[273] As a result, common CVD nanotube procedures involving CO are carried out in excess of 900°C.[273,274] In relation to the procedure using CH_4:H_2 a similar spectrum is observed to that of CO. However, the Raman bands for cobalt oxide (500 – 700cm^{-1}) are less pronounced indicating more cobalt has been reduced in the procedure. The peak at 1100cm^{-1} has been observed in CVD procedures to make CNTs from hydrocarbon gases[275] and has been attributed to disordered carbon.[276,277]

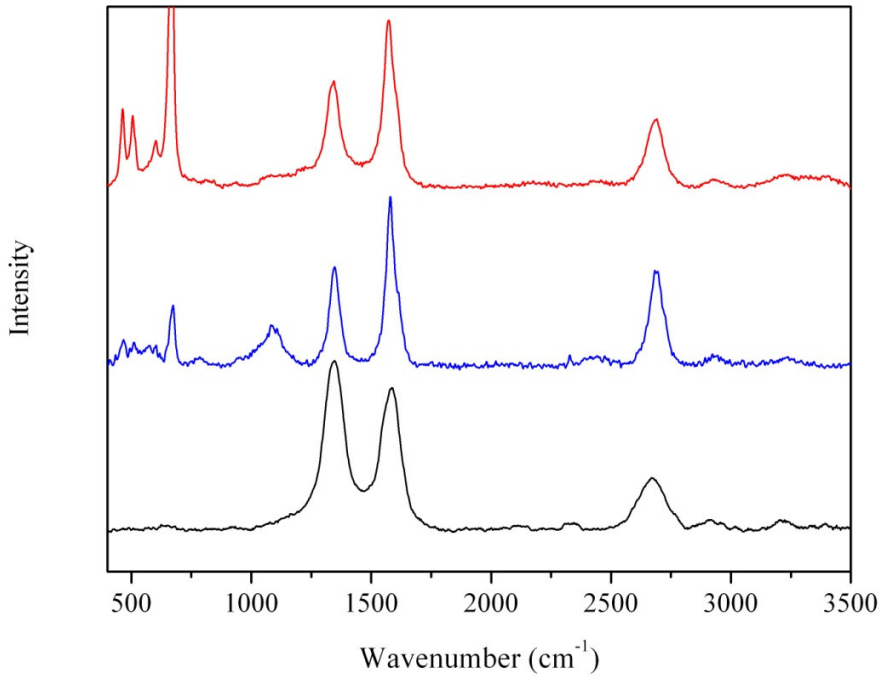

Figure 77 - Raman spectra showing products of the ethanol (black), CO (red) and 10% H_2:CH_4 (blue) over 1% $Co(OH)_2$/MgO

TEM of the products for each using 10% H_2:CH_4 and CO are shown in Figure 78 and Figure 79 respectively. The presence of few layer graphene is shown in the representative HREM images for the methane (Figure 78c, bi-layer edge,) and CO (Figure

79c, few layer) products. The three crystalline diffraction planes are shown in SAED patterns. The presence of the out of plane ring corresponding to the interlayer spacing (0.34nm) is most likely due to the crumpled nature of the sheets exposing vertically lying areas. In addition these areas could lead to diffraction rings in the {1100} and {2110} due to the random orientations of the surface cause by the crumpled nature. However, the sheets could also be nanocrystalline as observed when ethanol was used as the carbon feedstock.

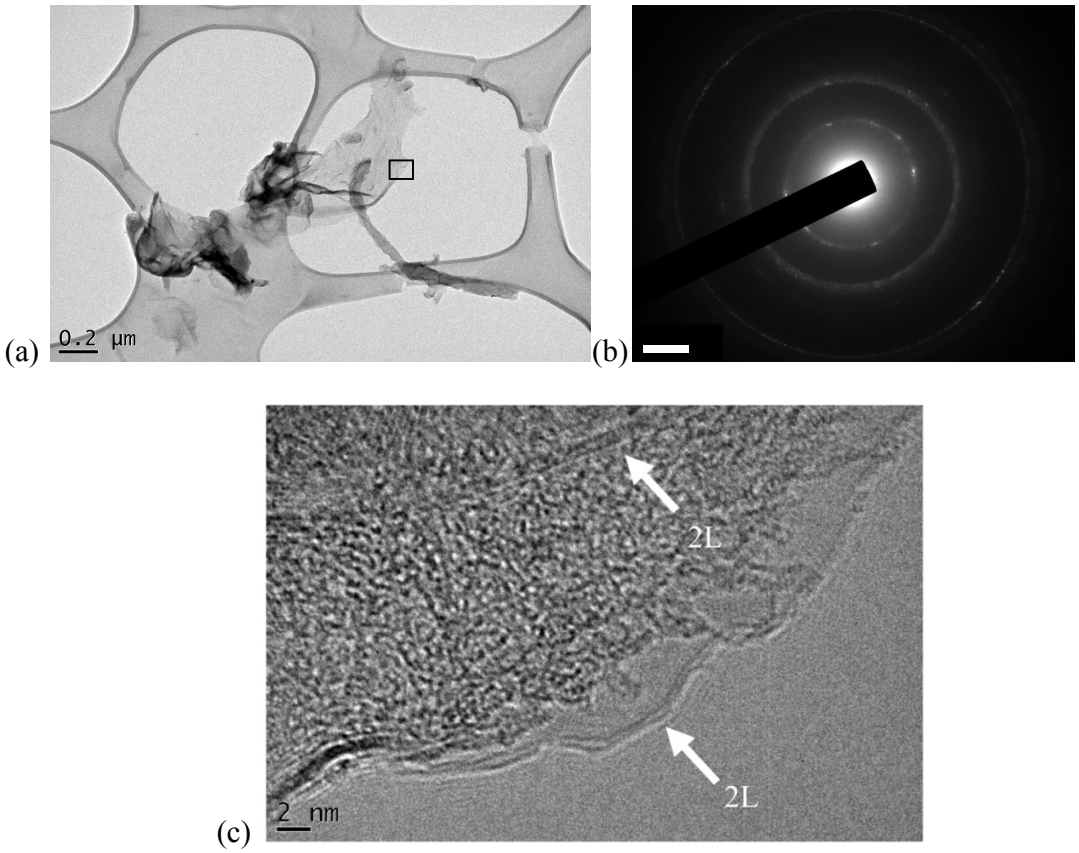

Figure 78 – (a) BF-TEM images showing platelets synthesised from 10% H_2:CH_4 over 1% $Co(OH)_2$/MgO and associated SAED (scale bar 2 1/nm), (b) HREM of edge area in (a) denoted by the black box shows bilayer graphene

TEM of the graphene product using the carbon monoxide method (Figure 79) shows more defined hexagonal spots than the methane product, although this could be rationalised by the presence of amorphous carbon in the methane product (observed by the 1100cm^{-1} peak in its Raman spectrum). The thickness of the graphene platelets were between *ca.* 2 – 6nm (measured at the edges). In addition, FFT of areas of the platelets surface display spots corresponding to the {1100} diffraction planes of graphene. These platelets are of similar thickness to those produced by Kim *et al*[278] from the decomposition of carbon monoxide over aluminium sulphide (α-Al_2S_3) at 1200^oC. HREM at the platelet edges showed an average thickness of 6.5nm increasing when CVD was conducted at higher temperature.

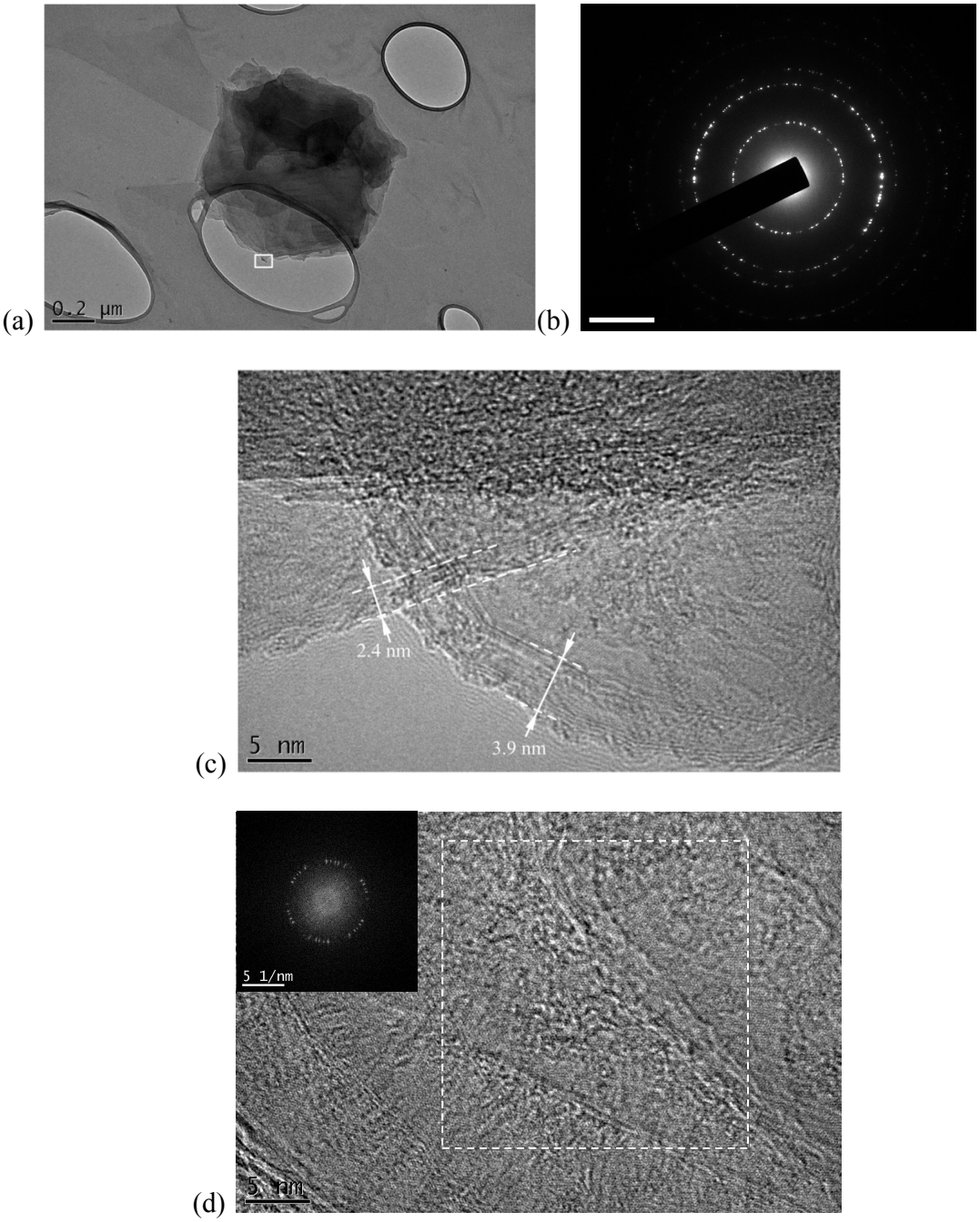

Figure 79 – TEM images showing product of synthesis over 1% $Co(OH)_2$/MgO using CO. (a) bright field, (b) SAED (scale bar 5 1/nm) and (c) HREM of edge, (d) HREM of platelet surface (inset) corresponding FFT of area in white box

The results from the gas phase synthesis for both methane/hydrogen and carbon monoxide show a promising step forward for this type of graphene synthesis adopting this

catalyst system. Raman spectra for the few layer graphene (Figure 77) produced shows similar characteristics to what would be expected for conventional graphene formation on metal foils. The D, G and G' peaks/bands are much sharper than that associated with ethanol indicating an increased product crystallinity. Further investigation of this technique is required to enhance the quality of the few layer graphene that is synthesised.

6.1.6 Comparison to cobalt nitrate doping of MgO

In the previous sections it has been shown how few layer graphene can be grown with a metal nanosheet template. To demonstrate the fundamental importance of the structured platelets to the supported synthesis of graphene, a control reaction using a common cobalt precursor was prepared by wet impregnation in ethanol.

MWNTs and other structures, including a mixture of nano-onions and curled graphifitic cages (Figure 80a-c), were observed using TEM. The results of the microscopy highlight the importance of the initial shape of the particles. When spherical particles are used, the templating effect creates structures with rounded edges as illustrated in the TEM images. Dervishi *et al*[100] have suggested that there is a fine line between the production of CNTs (<1000^{o}C for Co-Fe/MgO bimetallic catalyst) and graphene using spherical nanoparticle doped systems. They propose that at the high reaction temperature the metal nanoparticles melt completely, generating a better wetting property which is more suitable for the formation of graphene.[279] Therefore, this suggests that the initial nanoplatelet morphology used in 6.1.2 and 6.1.3 is important to form graphene at temperatures below 1000^{o}C.

(a)

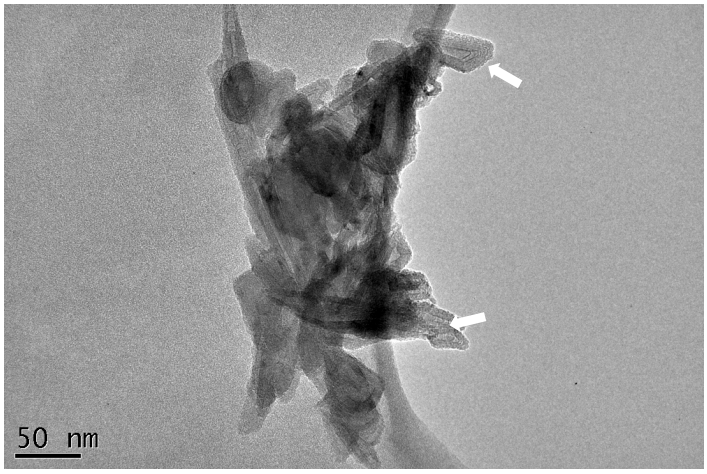

(b)

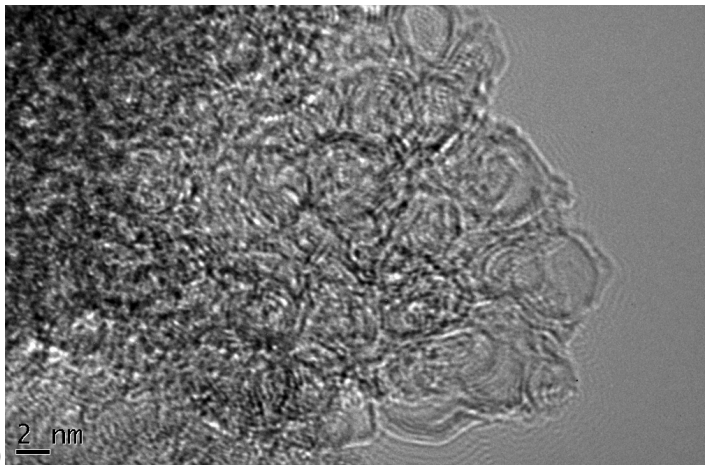

(c)

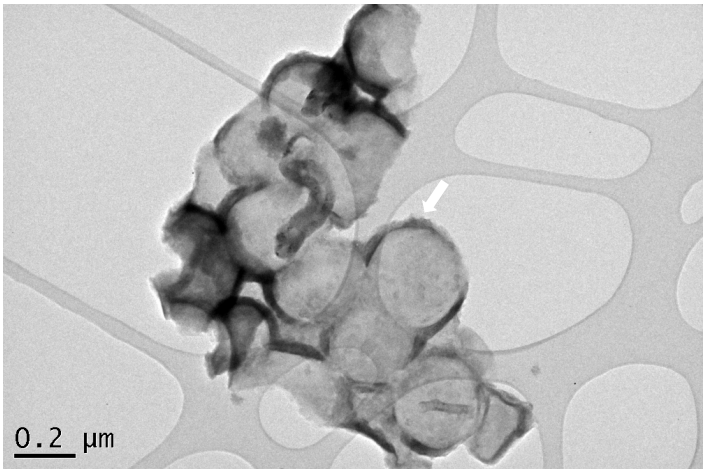

Figure 80 – Example TEM images of graphitic structures from the decomposition of ethanol at 800°C over MgO supports doped with $Co(NO_3)_2$ showing (a) MWNTs, (b) nano-onions and (c) graphitic cages

6.2 Few layer graphene nanoribbons from CVD synthesis using copper nanoparticles

Graphene nanoribbons have recently attracted attention due to the promise of providing building blocks for future generations of carbon based nanoelectronic and spintronic devices. Various methods exist for the production of graphene nanoribbons, ranging from 'bottom up' strategies such as atomic assembly[280,281] and CVD,[191,256] to top down approaches including the 'slicing' of carbon nanotubes[112] and graphene,[282] but are not suitable for scalable synthesis. However there are currently very few methods that are able to produce graphene nanoribbons in bulk quantities. The methods that do exist create a variety of nanoribbon structures which can vary in thickness and the microscopy of these has not shown the presence of single layer nanoribbons.

As stated previously, the use of copper foils has shown reproducible high quality single layer graphene films due to the low solubility of carbon in copper compared to that of nickel, cobalt and iron.[86,283] Therefore, planar copper nanostructures offer an interesting route to the formation of single layer graphene structures on bulk scales in a similar fashion to that shown using the cobalt nanoplatelets. Using the templating methodology employed in the previous section, a method for the formation of single layer graphene nanoribbons is demonstrated using CVD incorporating a magnesium oxide supported copper nanoribbon catalyst.

6.2.1 Synthesis of copper nanoribbons

Nanoribbons of copper are well documented in the literature, whereas the synthesis of sheets is rare and are generally grown hydrothermally.[284-287] To form copper nanoribbons, the hydrothermal synthesis procedure of Xu *et al,*[285] (Scheme 4) was employed using copper chloride dihydrate, sodium dodecyl sulphate (SDS), sodium hydroxide and sodium hypophosphite using a custom built reactor with a glass liner. The red deposit was centrifuged with water and ethanol to remove soluble contaminants.

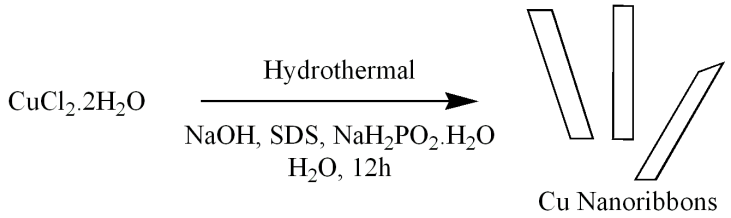

Scheme 4 - Hydrothermal synthesis of copper nanoribbons using sodium hydroxide, sodium dodecyl sulphate and sodium hypophosphite in water[285]

XRD of the product from the hydrothermal reaction shows the characteristic peaks for hexagonally closed packed copper and copper oxides (Figure 81). Similarly to the cobalt hydroxides, the hexagonally closed packed structure allows the production of flat copper/copper oxide nanoparticles of various shapes.[284,285,288] Due to the high surface area of metal nanoparticles, oxidation in air is problematic. The oxidation of the copper nanoparticles was observed by a visual colour change from red to brown after purification. The formation of the oxide was confirmed from the XRD spectrum, Figure 81. The diffraction peaks of copper, cuprous and cupric oxides have been documented for the ribbon morphology.[285,288] XPS was used to further study the degree of oxidation of the copper particles. In the survey scan (Figure 82a), the most intense peaks within the region

0.9 – 1 keV show 2 separate sets of peaks for the copper 2p signal. Due to the difference between the Cu(0) and the Cu(II) environments, the peaks are well separated. The ratio of intensity between the most intense copper $2p_{3/2}$ peak, at *ca.* 932 eV (Figure 82b), and the shifted peak associated with CuO is *ca.* 3:1 (Cu:CuO).

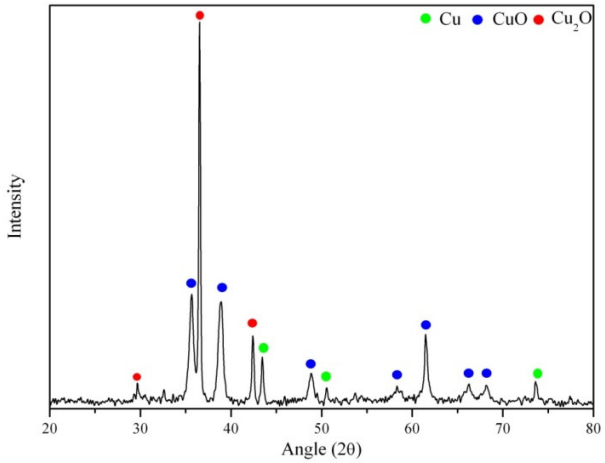

Figure 81 - XRD of the purified copper product after purification. Peaks are labeled as circles depicting the expected diffraction angles for Cu (green), Cu_2O (red) and CuO(blue)

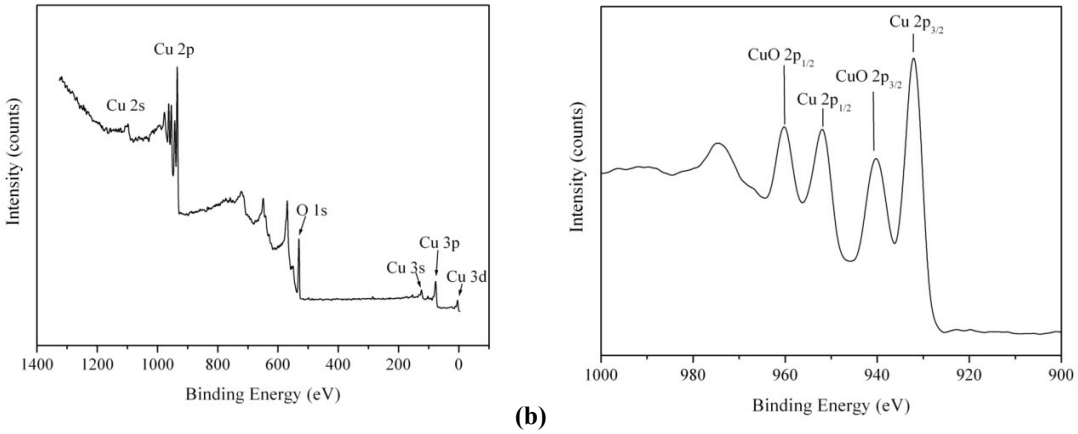

Figure 82 - XPS spectra of copper nanoplatelets showing (a) full survey and (b) Cu 2p region (900 – 1000eV). High resolution scan of Cu 2p displays characteristic $2p_{3/2}$ maxima for Cu and CuO at 932eV and 939eV.

The copper deposits were confirmed as having ribbon morphology by TEM analysis. The ribbon structure dimensions proved largely uniform throughout, the examples typically being 70 – 100nm in width, and an associated thickness of ca 20nm. The structures did however, vary significantly in length. The width and length scales are consistent with those observed by Xu *et al*[285] (ca 100nm and a few hundred nanometres respectively). Under HREM the ribbons appear to have a rough surface which could be due to oxidation observed by XRD and XPS. The intense spots in the SAED were indexed to the ($\bar{1}11$) and (200) diffraction planes at 2.53 Å ($2\theta = 35.4^{o}$) and 1.61 Å ($2\theta = 57.1^{o}$) for copper (II) oxide. However, the presence of copper oxide should not affect the behaviour of the catalyst during the CVD production of graphene due to the natural reducing conditions, presumably resulting in the formation of metallic copper.

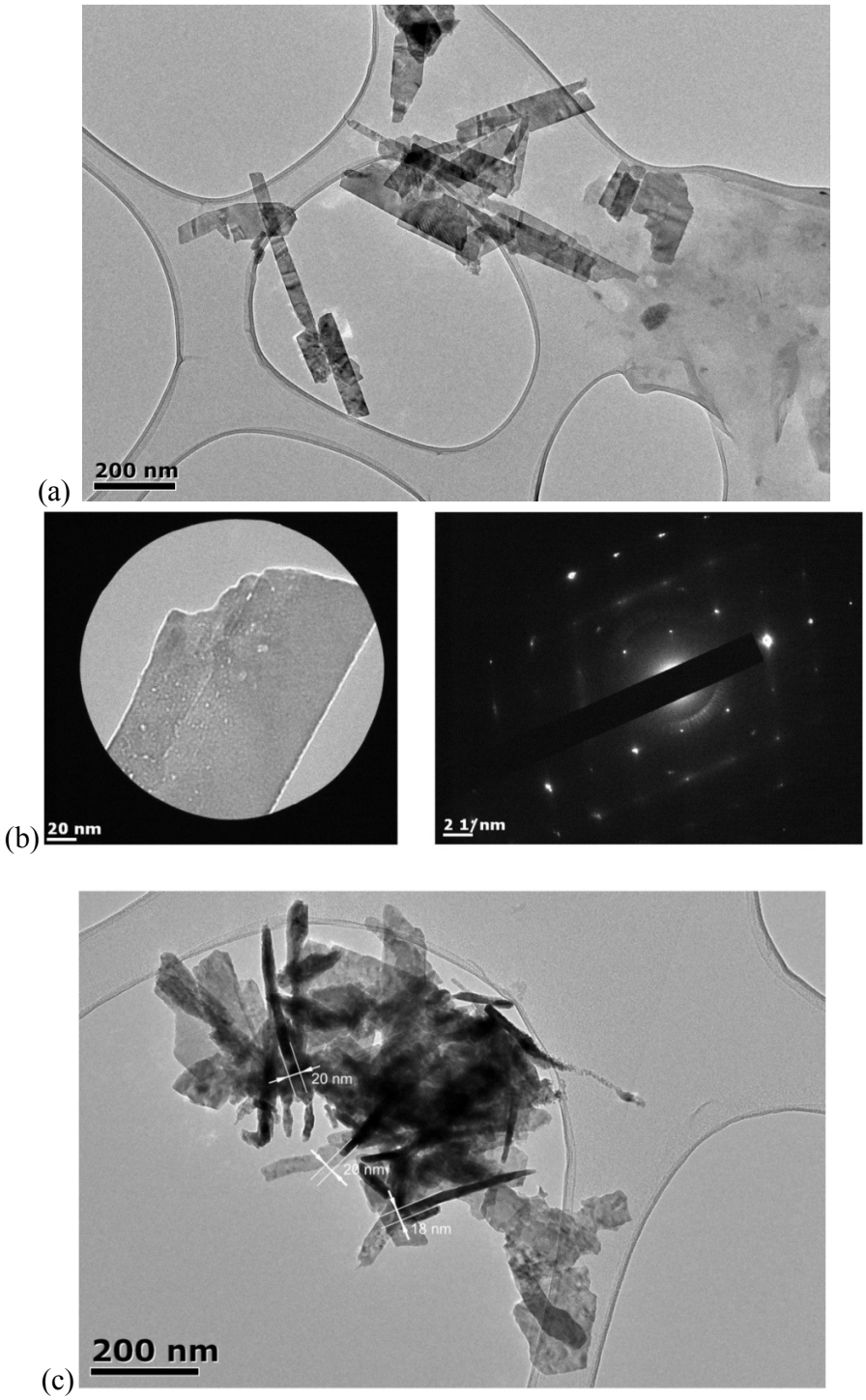

Figure 83 – TEM images of hydrothermally grown nanoribbons with $CuCl_2$, SDS, NaOH and NaH_2PO_3. (a) Bright field image showing nanoribbon morphology (b) shown single ribbon under selected area aperture with the corresponding SAED and(c) bright field image showing consistent thickness ca. 20nm.

6.2.2 Synthesis of graphene nanoribbons using magnesium oxide supported copper nanoribbons

Copper nanoribbons were incorporated into magnesium oxide supports using wet impregnation. To achieve 1 – 5% contents of copper, copper nanoribbons were sonicated in ethanol and mixed with varying amounts of magnesium oxide.. Ethanol was removed under reduced pressure to remove the catalyst. CVD synthesis of graphene was performed at 1000^{o}C, as used in many copper foil based synthesis methods.[22,86,108] Copper and the oxide support were removed with hydrochloric acid and purified with high purity water as in section 6.1.3. This procedure yielded 0.07g of carbon per millimole of copper catalyst used.

The bulk Raman spectrum of the CVD copper product (Figure 84) is comparable to the CVD grown graphene nanoribbons from a liquid phase catalyst/feedstock mixture of ethanol, ferrocene and thiophene (I_D:I_G 1.3).[191] Due to their relatively large aspect ratio, graphene nanoribbons are expected to have more edge carbon and thus a large I_D:I_G ratio (1.1 shown here).[114,191] In addition, π stacking of the nanoribbons can lead to a rippled structure causing strain the sp^2 backbone. These ripples are referred to as additional defect sites and therefore contribute to the size of the D band. Raman studies on "top-down" methods have also shown I_D:I_G ratios greater than one including lithographic patterning of graphene (1.5)[112] and solution phase oxidation (1.1-1.2).[114,289]

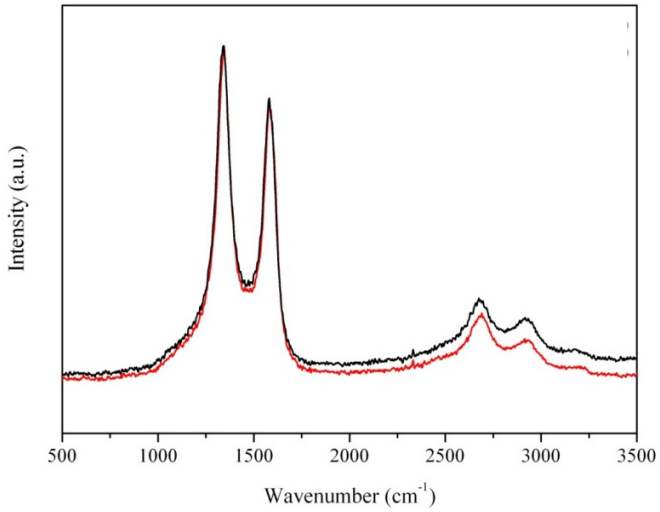

Figure 84 – Raman spectrum of the graphene product resulting from the CVD synthesis of MgO supported catalyst at 1% (black) and 5% (red) Cu content. The D (1340cm^{-1}), G (1575cm^{-1}) and G' (2678cm^{-1}) bands are present with an I_D:I_G ratio of ca. 1.1.

The thermal decomposition of purified graphene ribbons, isolated from the MgO support was followed using TGA in air (Figure 85). The point at which full decomposition of the graphene product occurs is at a similar temperature (620^{o}C) to that of the high purity SWNTs produced via the HiPCO™ process (600^{o}C). This may suggest a similarity in the number of layers produced from this process with respect to that of HiPCO™ single walled nanotubes. In addition, there is no low temperature weight loss that could be attributed to amorphous carbon (observed between 300 – 400^{o}C in HiPCO™ SWNTs). Due to the lack of scalable synthetic methods associated with the production of graphene nanoribbons the thermal stability of these has not been fully documented. The full decomposition temperature of the graphene nanoribbons grown in this study (620^{o}C) is much less than that documented for nanoribbons grown from the spray pyrolysis of ethanol, iron chloride and thiophene, which exhibit a full decomposition *ca.* 700^{o}C.

However, it should be noted that the nanoribbons grown by that method were not single layer (2 – 40) as observed here in the TEM and were very long (20 - 30μm).

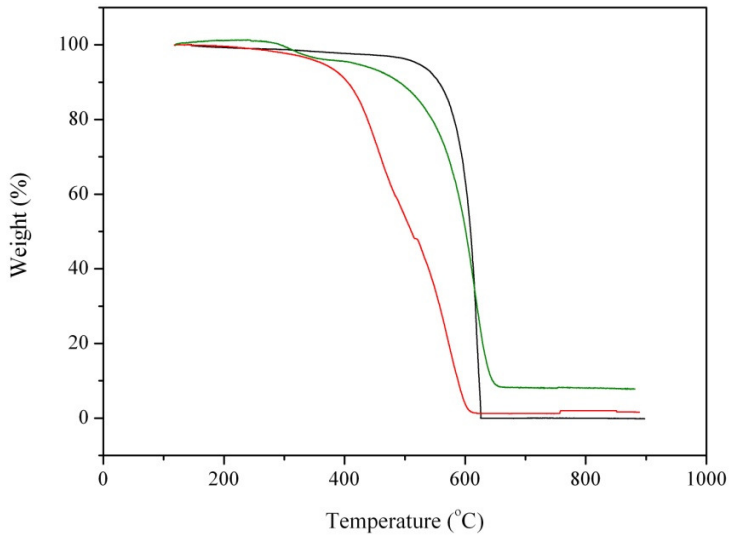

Figure 85 - Thermal decomposition in air of purified product of ethanol over 1% Cu/MgO (black) and its comparison to that of 1% $Co(OH)_2$/MgO (green) and HiPCO™ SWNTs (red)

TEM analysis shows many bundled structures are present, as is seen with nanotube ropes. The boundaries of these agglomerations show the presence of flat lying narrow sheet-like structures, expected for nanoribbons (Figure 86a, white arrow). An example of the nanoribbon geometry in presented in Figure 86b, protruding from an agglomeration. The edges shown by this ribbon measure 65 nm across and are in agreement with the width of some of the observed thinner copper nanoribbons in section 6.2.1. Single layer graphene is expected to form due to the low solubility of carbon in copper in addition to areas of the agglomerates indicating the carbon to be single layer in nature (Figure 86c). Single layer graphene nanoribbons are very rare in the literature and are mainly produced from the "top-down" approaches by lithographic patterning[112] of single layer graphene and the oxidative unzipping of carbon nanotubes.[114] The "bottom-up" CVD methods of

Campos-Delgado[191] and Wei[256] have produced multilayer nanoribbons that vary between 0.6 – 30nm and 4 – 8nm respectively.

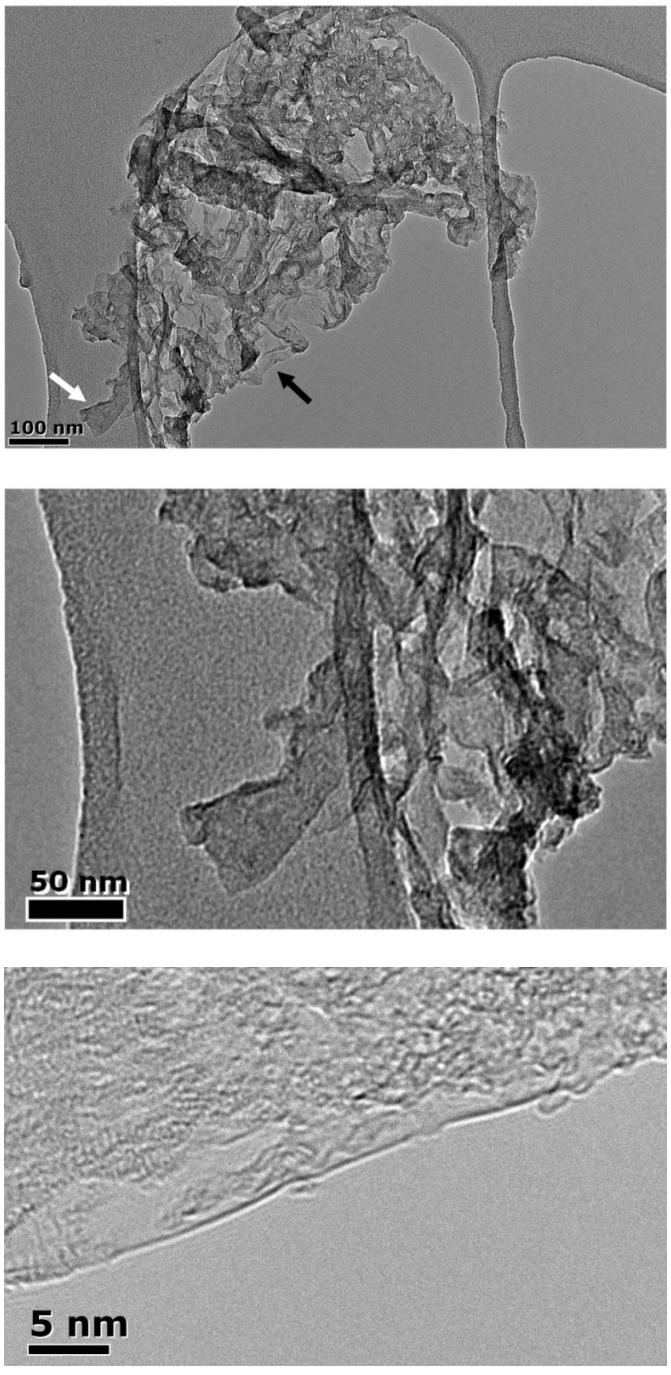

Figure 86 – (a) Bright field TEM image showing agglomerated products from the CVD synthesis using the ethanol 1% Cu/MgO system, (b) magnified area denoted by white arrow in (a), and (c) HREM of edge denoted by black arrow in (a)

Conformation of graphene nanoribbons was obtained by AFM studies (Figure 87). Spin-coated material from DMF on to freshly prepared mica show ribbon-like structures, measured to be just above the background surface noise at *ca.* 0.35nm, denoting the presence of single layer graphitic nanoribbons.

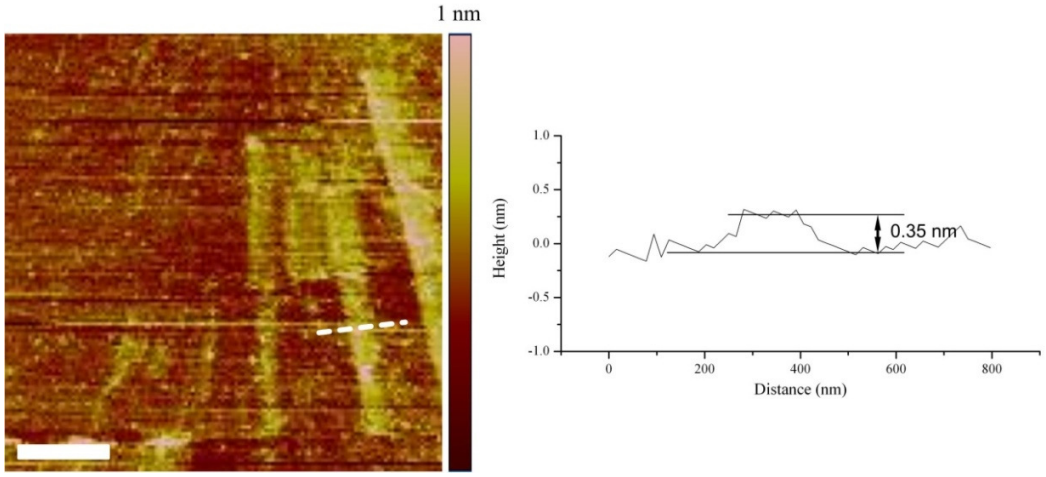

Figure 87 – (left) TappingMode™ AFM image (2.7x2.7µm, 800nm scale bar) of mica surface spin-coated with carbon product of 1% Cu content. (right) Corresponding height trace across white line

Further to the observed agglomerations shown above, other morphologies are distinguished (Figure 88). Equivalently to the graphene, these are not expected to lie flat due to intrinsic ripples and the ability of a single nanoribbon to adhere to itself through pi stacking interactions, wrinkling and twisting into scroll like particles (Figure 88a).[191] Initially, these structures look like bamboo tubes which have been documented in the literature.[290,291] However, closer inspection reveals no capped ends (Figure 88b white arrow, Figure 88c) as expected, but flat ended tubes, lying flat on the carbon support. Structures that could be mistaken for internal caps may be large internal ripples (Figure 88b, black arrow) as they do not span the whole width of the ribbon (Figure 88d) like internal caps observed with bamboo carbon nanotubes. Similar structures have been

discerned in the unzipping of MWNTs, where multiple layers have been cleaved and the pi stacking nature causes the layers to curl up.[292] The widths of these structures are only slightly smaller than that of the copper nanoribbon (70 – 100nm) as expected due to curling at the edges.

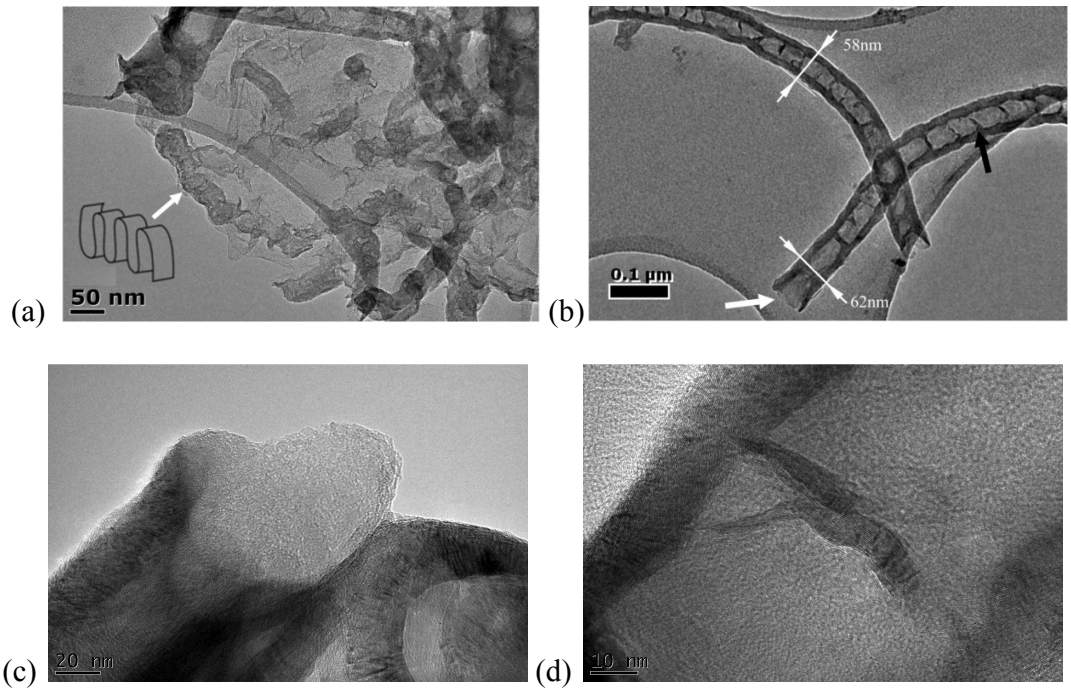

Figure 88 – (a) Bright field image showing rippled nanoribbon, (b) Bright field image shows curled nanoribbon (open end shown by white arrow, internal ripples shown by black arrow) (c) HREM of an open end and (d) HREM example of internal ripples.

6.3 Conclusion

A facile method for the production of single and few layer graphene has been demonstrated, exploiting present bulk carbon nanotube synthesis procedures and the known CVD characteristic growth of graphene on metal surfaces. By using metal nanoplatelet templates, few layer graphene was grown on the flat exterior of the silicon

supported particle surface., Subsequently, the catalyst was etched in a similar way to the documented film syntheses, attaining few layer graphene. The graphitic product had a well crystallised structure, (observed in the TEM) with layer counting at the edges revealing 2 – 10 layers. An extension of this process, utilizing magnesium oxide supports improves the yield *ca.* 30mg of few layer graphene (2 – 5nm in thickness) per 1g of catalyst (0.12g/mmol Co) with conductivity measurements of 100 – 200 Sm^{-1}. Substitution of the cobalt nanoplatelets with copper nanoribbons promotes the formation of single layer graphene nanoribbons (0.07g/mmol Cu). This route is one of the first examples of graphene templating, using CVD conditions and flat transition metal nanoparticles to enable the control of the graphene thickness and morphology by variation of the metal template. In addition, no other procedure that gives single layer graphene nanoribbons, without the need for the sheet patterning or carbon nanotube oxidation is known

This procedure provides various advantages over the existing 'top – down' methods including: small thickness distribution, absence of large graphitic contaminants and inexpensive precursors. Further optimization and scalability studies could potentially offer a source of low cost single and few layer graphene.

7. FUTURE WORK

Much scope remains for the preparation of graphene materials through "bottom-up" CVD techniques described here. CVD is very sensitive to certain parameters and one set of parameters cannot be used to describe the ideal conditions for every synthesis. Morphology and yields can be enhanced by simple variations in the growth parameters.

Preparation of the graphitic platelets from sodium ethoxide is already development at Durham as a scalable process for bulk production. As mentioned in the text, rough outputs at gram per hour scales don't truly give a true estimate of the output. The rate of gas flow has a tendency to take some of the powder out of the exhaust. Investigation into improved collection methods would further increase this and improve production. Examples of both an electronic and mechanical application of the material have been covered here. The MIS device displays potential use in electronic devices, but optimization of the deposition techniques and device architecture is required to enhance the charge retention characteristics. This is currently the basis of further collaborations with Dr Zeze. PMMA is the only material that I have had the chance to work with but there is a much wider variety of polymers which both carbon nanotubes and graphene have been put into to improve various properties. It would be interesting to see if the enhanced mechanical effectiveness is shared when enclosed in other matrices (polystyrene, polyurethanes, polyimides, epoxy resins, silicones, nylons etc) which are more useful for industrial applications.

At present further assessment of the role of sodium is needed in chapter 5. Observation that the precursor material decomposes to cobalt oxide and sodium salts indicates that more control may be achieved by investigating cobalt carbonate with sodium salts added by mechanical or solution methods. Analysis of the yields and carbon products from these catalysts by TEM, XRD etc will provide another avenue of investigation to see whether the Kambaldaite precursor is important or it is just the presence of sodium that influences the primary production of few layer platelets. In addition, the electronic properties of this material have not been investigated and may be suitable for development as vacuum filtered thin films. No attempts were made to exfoliate the materials in good solvents such as N-methylpyrrolidone and dimethylacetamide demonstrated by Hernandez et al using flake graphite.[51] Therefore using their centrifugation procedure, the few layer graphene observed in the TEM may be exfoliated further to thinner sheets.

In my opinion the most exciting part of the thesis is the use of the platelet nanoparticles to create graphene in bulk. This is one of the first support based methods, compatible with industrial reactors, which allows control of thickness and sheet morphology. These platelets can be grown of silicon, on which cleaved samples are sold, and on support used to grow carbon nanotubes. Optimization of the CVD procedure is required to achieve the goal of bulk scale graphene. Here, the change in carbon feedstock was investigated but other parameters, e.g. metal, flow rate, temperature, cooling rate, reactor pressure, calcinations steps and oxide support variation are required, which would form the basis of a very interesting PhD thesis.

8. EXPERIMENTAL DETAILS

8.1 Analytical details

Transmission Electron Microscopy (TEM)

Bright-field TEM images were taken using a JEOL 2100F 200 kV FEG-TEM operated at 80 kV. Samples were prepared by dispersing the material in ethanol/N,N' -dimethylformamide (where appropriate) and pipetting a few drops onto a lacey carbon film supported by a copper grid (300 mesh). Electron Energy Loss Spectroscopy (EELS) was performed using a Tridiem Gatan Imaging Filter, with a 2k x 2k CCD camera.

Scanning Electron Microscopy (SEM)

SEM images were taken using a Hitachi SU70 FEG SEM or FEI Helios Nanolab™ operated in the range 3 – 10 keV using secondary electron detection. Powdered samples were spin coated from sonicated ethanol solutions onto pre-cleaned silicon surfaces.

X-Ray diffraction (XRD)

In house XRD was conducted using a D500 (Cu K_{α}, λ = 1.54 Å) scanned over the 2θ = 5-90 with 0.02 step size, mounted on zero background silicon plates.

High resolution XRD data were recorded at the Diamond Light Source, Didcot, Oxfordshire on the I11 high resolution powder diffraction beamline operating with an X-ray beam energy of 15 keV (0.826 Å). The sample was ground to a fine powder, using a

mortar and pestle, and placed in a glass capillary (id = 0.5 mm) with sample length 50 mm. Data were collected between 2θ = 10–150 degrees.

Atomic Force Microscopy (AFM)

Samples for AFM analysis were produced by drop deposition onto freshly cleaved mica of the corresponding solution of graphene (*ca.* 0.005 $mgmL^{-1}$) in ethanol produced by sonication in an ultrasonic bath (Ultrawave U50, 30–40 kHz) for15 min. Samples were dried in air before imaging in TappingMode™ using a Veeco Multimode AFM with a Nanoscope IV controller. Film thickness on quartz was measured by stripping off part of the film using tape and measuring the height difference using a Veeco Dimension V AFM in TappingMode™ operation. Si AFM probes (model: TESP) with a frequency range: 281 – 348 kHz and a spring constant of 20 – 80 Nm^{-1} were used.

Raman spectroscopy

Raman spectra were recorded using a Jobin Yvon Horiba LabRAM spectrometer in a back scattered confocal configuration using frequency doubled Nd:YAG (532 nm, 2.33 eV) laser excitation. All spectra were recorded on solid samples over several regions and were referenced to the silicon line at 520 cm^{-1}

Fourier Transform Infrared (FTIR) spectroscopy

Infrared spectra were recorded on compressed films using a Perkin Elmer Spectrum 100 equipped with a Pike ATR fitted with a Ge crystal.

X-ray Photoelectron Spectroscopy (XPS)

XPS studies were performed at NCESS, Daresbury laboratory using a Scienta ESCA 300 hemispherical analyzer with a base pressure under 3 x 10^{-9} mbar. The analysis chamber was equipped with a monochromated Al K_α X-ray source ($h\nu$ = 1486.6 eV). The charge compensation was achieved (if required) by supplying low energy (<3 eV) electrons to the samples. Photoelectrons were collected at a 45 degree take-off angle, and the analyzer pass energy was set to 150 eV giving an overall energy resolution of 0.4 eV. Samples were prepared by sonication in propan-2-ol and drop dried onto steel stubs for analysis. All quantification and peak deconvolution processing of XPS data were conducted at NCESS using the CasaXPS software.

Thermogravimetric Analysis (TGA)

TGA data were recorded on 1–3 mg of sample using a Perkin Elmer Pyris I. Data were recorded in flowing air (20 $mLmin^{-1}$) at a ramp rate of 10ºCmin^{-1} to 900ºC after being held at 120ºC for 30 min to remove any residual solvent.

Electrical properties

The bulk electrical transport properties of the graphene powder were measured at room temperature in air on films (2.4 μm thickness) formed by vacuum filtration of ethanol dispersed graphene (1 mg in 10 mL). For the graphene films on quartz the measurements were carried out directly on the film surface. The 4-wire resistances of the samples were measured using the in-line geometry. A sweep current was applied between the two outer terminals and the voltage across the inner terminals was measured.

Dynamic Mechanical Analysis (DMA)

DMA measurements were carried out on a TA DMA Q800 machine with the 3 point bend clamp attachment fitted. Samples suitable for DMA (20 mm x 13 mm x 1 mm) were prepared using a mechanical press equipped with plate heaters in a lined stainless steel mould. Composite powders were pressed at 200^{o}C at 5 tonnes for 5 minutes, released and force reapplied. Samples were allowed to cool to room temperature and removed. All DMA measurements were conducted using the 3 point bend clamp. Controlled force measurements were conducted at a loading of 0.01 N at 30^{o}C, isothermal for 5 minutes, after which force was increased to 18N at 1 Nmin^{-1}. Multifrequncy measurements where conduced at a constant frequency of 1 Hz. Samples were held at 40^{o}C for 5 minutes and heated to 160^{o}C at 3^{o}Cmin^{-1}.

8.2 Materials

All reagents were obtained from commercial sources and used as supplied. Sodium (sticks in mineral oil, 99%), cobalt hydrate hexahydrate ($CoCl_2.6H_2O$, >98%), sodium hypophosphite monohydrate ($NaH_2PO_3.H_2O$, 98%, 12 – 17% water), hexamethylenetetramine ($C_6H_{12}N_4$, 99%) were purchased from Alfa Aesar. Cobalt nitrate hexahydrate ($Co(NO_3)_2.6H_2O$, >98%), copper chloride dihydrate ($CuCl_2.2H_2O$, >98%), sodium dodecylsulphonate ($C_{12}H_{25}SO_4Na$, ≥99.5%), magnesium oxide (MgO, >98%), Sodium chloride (NaCl, ≥99%), sodium hydrogen carbonate ($NaHCO_3$, >99.5%) and poly(methyl methacrylate) (PMMA, M_w = 120,000) was purchased from Aldrich (Gillingham, UK). Sodium hydroxide (NaOH), N, N'-Dimethylformamide (DMF) and ethanol (absolute) were purchased from Fisher Scientific. Sodium carbonate was purchased from BDH industries. High purity water was filtered to a resistivity of 18MΩcm^{-1} using a Purite Neptune Purification System, Purite Ltd, Thame, UK). Si/SiO2 (111) wafers were purchased from Cemat Silicon S.A. (Warsaw, Poland). All gases were purchased from BOC and were of either Pureshield™ grade (argon, hydrogen) or CP™ grade (99.9%, methane, carbon monoxide)

CVD reactions were carried out in a quartz Carbolite tube furnace (12/38/400) controlled by a Eurotherm 2416 GC 8 segment programmer. A multiple input mass flow controller (Brooks® Model 5850E) was used to deliver and mix the gases before delivery to the furnace.

8.3 Synthesis of few layer graphene using sodium ethoxide

8.3.1 Graphene platelet synthesis from sodium ethoxide made by the reaction of sodium with ethanol

Sodium (2.0 g, 87 mmol) was cut into small pieces and washed with hexane. These were added slowly to ethanol (50 mL) and allowed to stir until all had reacted to afford a sodium ethoxide solution in ethanol (1.7 M). The solution was filtered and added to a spray vessel which was then connected to the CVD apparatus. The CVD apparatus consisted of a quartz tube (an internal diameter of 28 mm and a length of 900 mm) positioned in a Carbolite tube furnace with a uniform heating area of approximately 300 mm and electronic mass flow controllers to control gas flow. The furnace was angled at *ca.* 15^{o} to promote recycling of the sodium ethoxide solution. The system was purged with argon (60 $mLmin^{-1}$) while the furnace was heated to temperature (900 ºC at 20 $ºCmin^{-1}$). The sprayer was initialized by increasing the gas flow (*ca.* 200 $mLmin^{-1}$) and allowed to continue until all the solution had been used. The setup was allowed to cool and the black deposit collected from the main furnace tube and collection vessel.

In a typical purification procedure 50 mg of graphene was sonicated (using an ultrasonic probe, Cole-Parmer 750 W Ultrasonic Homogenizer, operating at 20 kHz and 30% amplitude) for 10 min in high purity water (18MΩ, 100 mL) and added to hydrochloric acid to make a 5 M solution and left overnight. The solution was filtered through a polycarbonate membrane (Whatman, 0.2 μm) and the resulting solid material re-dispersed by mild bath sonication (Ultrawave U50, 30–40 kHz) in high purity water for 15 min and filtered once more through a polycarbonate membrane. This was repeated twice

with water and finally ethanol. The solid material was then dried overnight in a vacuum oven at 120^{o}C.

8.3.2 Graphene platelet synthesis from sodium ethoxide made by the reaction of sodium hydroxide with ethanol

Sodium hydroxide (2 g, 50 mmol) added to ethanol (50 mL, 1 M), stirred at 40^{o}C until dissolved and transferred to a spray bottle. The spray pyrolysis and purification steps were carried out in the same manner as in 8.3.1

8.3.3 Graphene platelet synthesis from sodium ethoxide made by the reaction of sodium carbonate with ethanol at high temperature

Sodium carbonate (1 g, 9.4 mmol) was added to an alumina combustion boat and placed in the hot zone of a tube furnace. The carbonate was heated to 800^{o}C under argon atmosphere (60 mLmin^{-1}) at 20^{o}Cmin^{-1}. At 800^{o}C, the argon flow was increased to 180 mLmin^{-1} introducing ethanol to the hot zone. Spraying was continued until all ethanol was consumed; the flow was reduced to 60 mLmin^{-1} and allowed to stand at 800^{o}C for a further 3 hours under argon. After this period the furnace was cooled to room temperature under argon flow, the product removed and stirred in HCl (6 M) overnight. Repeated filtration with water to pH neutral, again with ethanol was used to purify the material, which was then dried under vacuum at 100^{o}C. On average 12 mg of powder was yielded after purification per gram of sodium carbonate used.

8.4 Application of few layer graphene synthesised from sodium/ethanol

8.4.1 Spray pyrolysis film deposition procedure

Silicon surfaces were cleaned using Piranha solution (3:1 H_2SO_4: H_2O_2) at 85^oC for 45 minutes, rinsed with water (high purity, 18 MΩ) and stored in water until required. Before use they were treated with 1:1 H_2O_2: HCl for 15 minutes at room temperature. Quartz microscope slides were washed with water, ethanol and cleaned using a micro-fibre cloth prior to insertion.

Graphitic films were produced on quartz or silicon substrates via a novel chemical vapour deposition, involving spraying a solution of sodium ethoxide (0.056 M) in ethanol (200 mL) into a furnace at 900°C. The furnace was tilted at an angle of *ca.* 15° by inserting a metal tray under the side of the furnace furthest from the sprayer. The 10x10 mm quartz piece was placed on top of the 25x25 mm quartz piece, which was then positioned in the furnace tube 285 mm from the start of furnace. The quartz blockade was positioned 250 mm from the start of the furnace. A heater created by wrapping a 6 ft. heater coil around a 100 mm piece of quart tubing was positioned over the furnace tube directly before the tube entered the furnace. The heater coil was set to *ca.* 90°C. During the initial heating of the furnace (20°Cmin^{-1} to 900°C, 40 minutes) the system was purged with 40 mLmin^{-1} argon. The argon flow rate was increased to *ca.* 125 mLmin^{-1} during spraying of the sodium ethoxide solution for 60 min (*ca.* 20 mL solution sprayed). The system was allowed to cool to room temperature under a 40 mLmin^{-1} flow of argon.

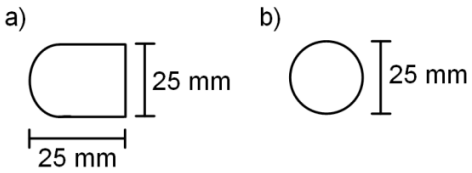

8.4.2 Production for few layer graphene memory device

Anionic surfactant few layer graphene solutions were prepared by sonication of the purified powder in 1% sodium dodecylsulphonate (SDS) solutions for 15min to create a 0.1 $mgmL^{-1}$ solution. P-doped silicon was prepared by sequential cleaning using Piranha solution (1:1, sulphuric acid: hydrogen peroxide) for 30 minutes to remove organic contaminants and washed further with deionised water. Hydrofluoric acid was used to remove the native oxide layer from the silicon surface, washed with deionised water and blown dry with nitrogen gas. An oxide layer was thermally grown on the silicon surface by exposure of the wafers to dry oxygen (3 $Lmin^{-1}$) at 850^{o}C for 10 minutes. A bilayer of poly(ethyleneimine)/poly(acrylic acid) was deposited by sequential dipping of the wafer in aqueous PEI and PAA for 15 minutes each. The active bilayers were deposited by submerging the wafer in PEI for 15 minutes. The substrates were washed with deionised water to remove excess, blown dry with nitrogen and submerged in the few-layer graphene/SDS solution for 15 minutes to produce the bilayers. This was repeated to deposit 2 bilayers. Poly(methyl methacrylate) was deposited as the top insulating layer by spin coating a chloroform solution (8 $mgmL^{-1}$) at 500rpm (10 seconds) and 6000rpm (50 seconds). This was then annealed at 120^{o}C for 20 minutes and aluminium contacts were deposited through thermal evaporation.

8.4.3 Production of few layer graphene/PMMA composites

Composites were generated using shear mixed solution processing. The required weight of few layer graphene was weighed and added to enough DMF to make a 0.25 $mgmL^{-1}$ solution. Graphene/DMF suspensions were produced by sonication (5 minutes, 30%) to which PMMA was added, cooled in ice and shear mixed at 6000rpm for 60 minutes. Composites were coagulated by drop wise addition to water, filtered and dried in a vacuum oven at 100^{o}C overnight.

8.5 Few layer graphene from bimetallic catalysed CVD decomposition of ethanol

8.5.1.1 Synthesis of Kambaldaite analogue sodium cobalt carbonate

Cobalt nitrate hexahydrate (8.73 g, 30 mmol, 50 mL, 0.6 M) was added to an aqueous solution of sodium hydrogen carbonate (12.71 g, 120 mmol, 200 mL, 0.6 M) over a period of 30 mins via a syringe pump and stirred at 50°C for 3 hours. The reaction was completed when the initial purple colour changed to light pink. The product was repeatedly centrifuged in water till the supernatant solution showed neutral pH, washed with ethanol and dried under vacuum at 100^{o}C.

8.5.1.2 CVD procedure using bimetallic catalyst

The dried powder (0.5 g) was ground and added to an alumina combustion boat and heated to 800°C at 20°Cmin^{-1} under argon (40 $mLmin^{-1}$) in a quartz tube. Argon flow

was raised to 180 $mLmin^{-1}$ which introduced ethanol vapour into the furnace via a nebulizer for 1 hour and kept at temperature for a further 3 hours. After cooling to room temperature under argon flow, the remaining powder was stirred overnight in HCl solution (5 M, 100 mL) and filtered through a polycarbonate membrane (0.2 μm pore, Whatman) to remove excess metal salts. Further purification of the material by repeated bath sonication and filtration from water (2 x 100 mL) and ethanol (100 mL) afforded a fine black powder which was dried under vacuum overnight to remove residual solvent.

8.6 Synthesis of single and few layer graphene using transition metal nanoparticles templates

8.6.1 Synthesis of Cobalt Hydroxide Nanosheets

$CoCl_2.6H_2O$ (0.474 g, 10 mmol), NaCl (0.584 g, 10 mmol) and HMT (1.682 g, 12 mmol) dissolved in water/ethanol (200 mL, 9:1) and heated to 90^oC for 1 hour. The green precipitate was filtered from parent solution, centrifuged (3000 rpm, 10 minutes) with water several times, then ethanol and finally dried overnight in a vacuum oven at 100^oC. This procedure generates on average 60 mg (6.5% yield) of α-$Co(OH)_2$.

8.6.2 CVD synthesis of few layer graphene on $Co(OH)_2$ coated silicon/silicon oxide

Silicon surfaces were cleaned as described in 8.4.1 and were spin coated with a suspension of the hydroxide nanosheets in ethanol (5 μgmL^{-1}) at 2000rpm for 1 minute.

Several surfaces were coated and allowed to dry in air at ambient temperature. 3 – 4 coated pieces were placed in a combustion boat (recrystallised alumina, Aldrich) heated to 800^{o}C under Argon flow (60 mLmin^{-1}). Ethanol was flowed into furnace at 1mLmin^{-1} using nebulizer spray bottle using an argon flow rate of 180mLmin^{-1} and flowed for 30 minutes. Upon completion furnace was allowed to cool to room temperature under same argon flow.

8.6.3 CVD synthesis of graphene nanoribbons using cobalt hydroxide doped magnesium oxide supports

Wet impregnation of magnesium oxide support was conducted by sonicating $Co(OH)_2$ (46 mg, 0.5mmol) in 40mL EtOH until dispersed whereby MgO (Aldrich, 2 g, 50 mmol) added and sonicated for 1h. EtOH removed under reduced pressure and catalyst dried overnight at 120^{o}C. The catalyst was added to a combustion boat and treated as in 8.6.2 CVD synthesis of few layer graphene on $Co(OH)_2$ coated silicon/silicon oxide Support and catalyst were removed by stirring in 6 M HCl overnight. Product was filtered, washed with water until neutral pH was achieved, then ethanol and dried in vacuum oven at 100^{o}C overnight.

8.6.4 CVD synthesis using gas phase carbon sources

The syntheses were run using the catalyst described in 8.6.3 using carbon monoxide and methane/hydrogen (10% hydrogen). The furnace was purged with Argon at 100 mLmin^{-1} (1bar) during furnace heating. At 800^{o}C CO was delivered through the mass flow controller at 200 mLmin^{-1} (4bar) for 30 minutes, after which the furnace was cooled to room temperature.

When methane/hydrogen mixtures were used, a reduction step was applied using the addition of hydrogen (20 $mLmin^{-1}$) and ran for 5 minutes. Argon was removed and methane added (200 $mLmin^{-1}$) to create a 10% mixture and ran for 30 min. This was replaced with argon (100 $mLmin^{-1}$) while cooling to room temperature. Catalyst and support were removed with hydrochloric acid as before.

8.6.5 Hydrothermal synthesis of copper nanoribbons

$CuCl_2.2H_2O$ (0.2557 g, 15 mmol), SDS (0.1297 g, 0.45 mmol), NaOH (3.6 g, 90 mmol) added to deionised water so to make a 30 mL solution of 50 mM, 15 mM and 3 M respectively. NaH_2PO_3 (1.272 g, 12 mmol, 0.4 M) was added and vigorously stirred for 30 minutes. Solution was placed in glass lined stainless steel autoclave and maintained at 100^oC for 12 hours. The red precipitate was removed from bottom and centrifuged in water multiple times and finally ethanol and dried under vacuum at 60^oC. The hydrothermal procedure yielded 87 mg (86%) of copper nanoribbons.

8.6.6 CVD synthesis of graphene nanoribbons using copper doped magnesium oxide supports

The catalyst used for the CVD synthesis was prepared using the same procedure as before using 15.9 mg and 79.4 mg (1 mol% and 5 mol%) respectively and run under the same CVD conditions. The CVD procedure was carried out in the same manner as 8.6.3 at 1000^oC for 30 minutes.

Appendix A – Additional figures for chapter III

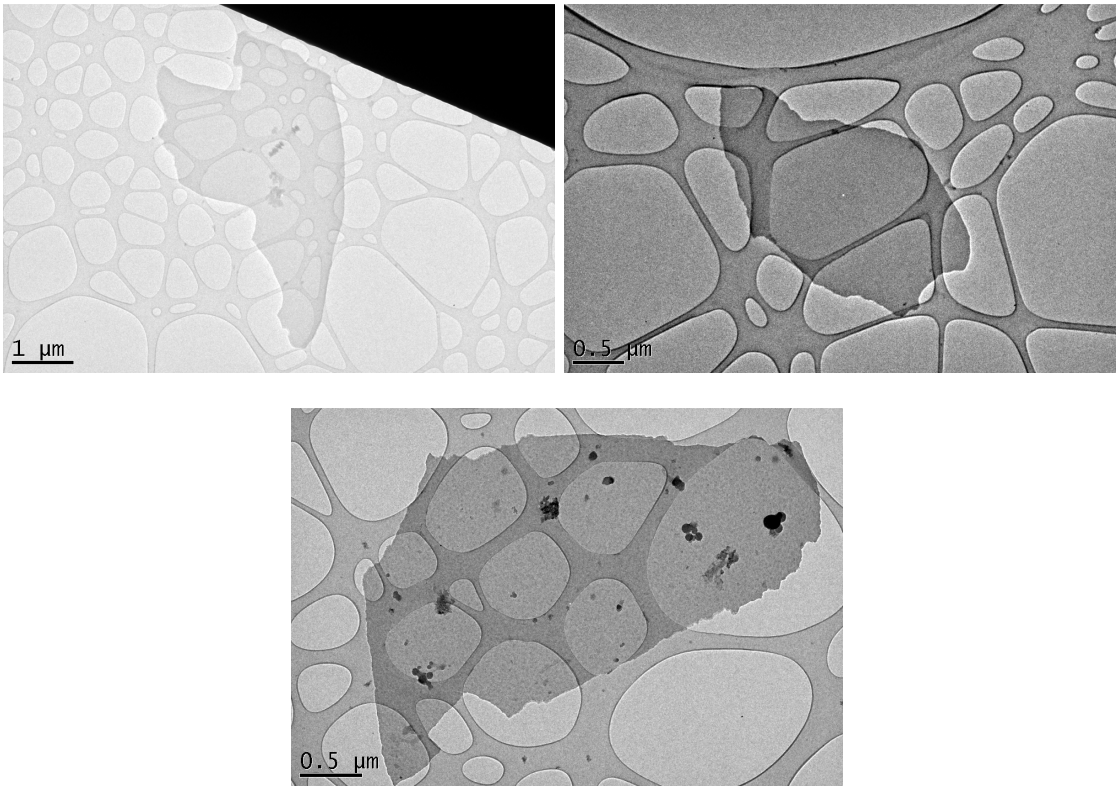

Figure A 1 – BF-TEM images of turbostratic few layer graphene platelets from the spray pyrolysis of sodium/ethanol solutions deposited from ethanol suspension.

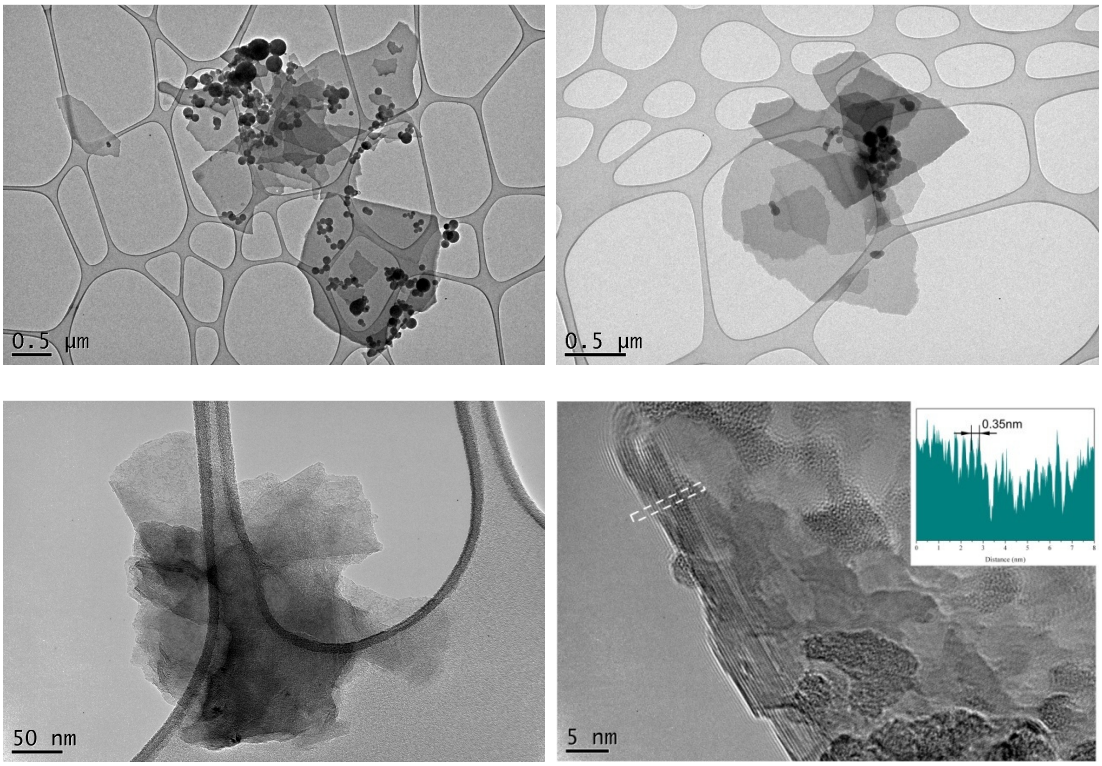

Figure A 2 – BF-TEM of (a,b) Turbostratic and (c) Bernel stacked few layer graphene platelets from sodium hydroxide/ethanol solution, drop dried from an ethanol suspension. (d) folded edge from (c) shows 0.35nm interlayer spacing consistent with graphite (0.34nm)

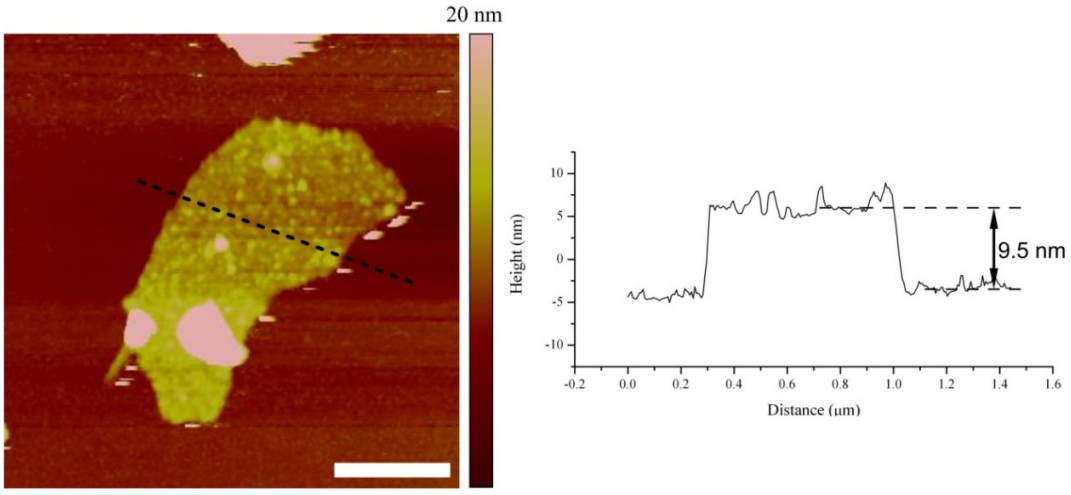

Figure A 3 – AFM image (1.9x1.9µm, 500nm scale bar) of product of sodium hydroxide product spin coated from DMF solution onto mica surface

(a)

(b)

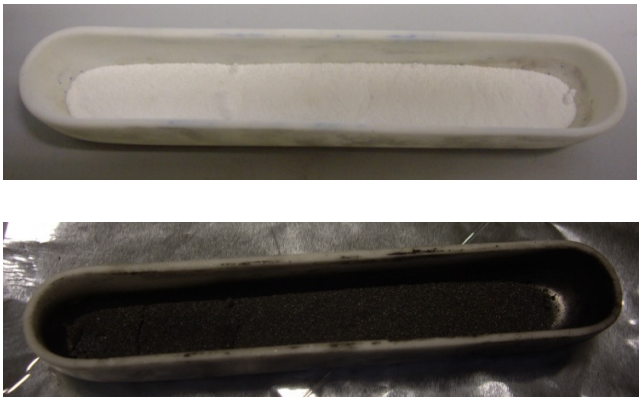

Figure A 4 – Photograph showing sodium carbonate (a) before and (b) after 1 hour in ethanol atmosphere and annealed for a further 3 hours.

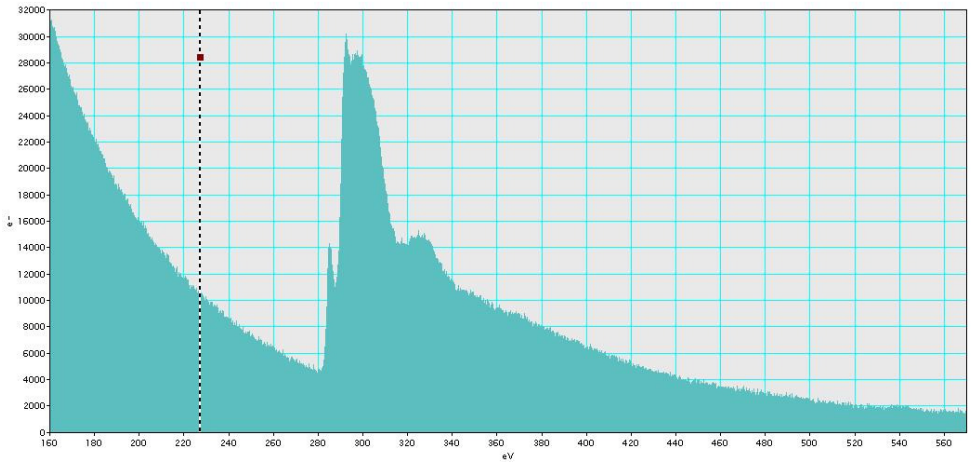

Figure A 5 - EELS spectrum of platelets formed from the high temperature reaction of sodium carbonate with ethanol

Appendix B: Additional figures for Chapter IV

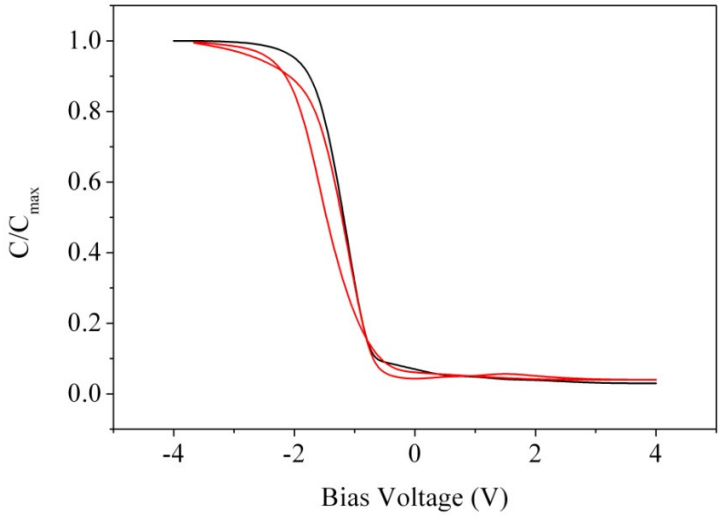

Figure B 1 – C-V characteristics of MIS devices fabricated from Al/SiO2/p-Si (black) and Al/PMMA/SiO2/p-Si (red).

Appendix C – Additional information for chapter VI

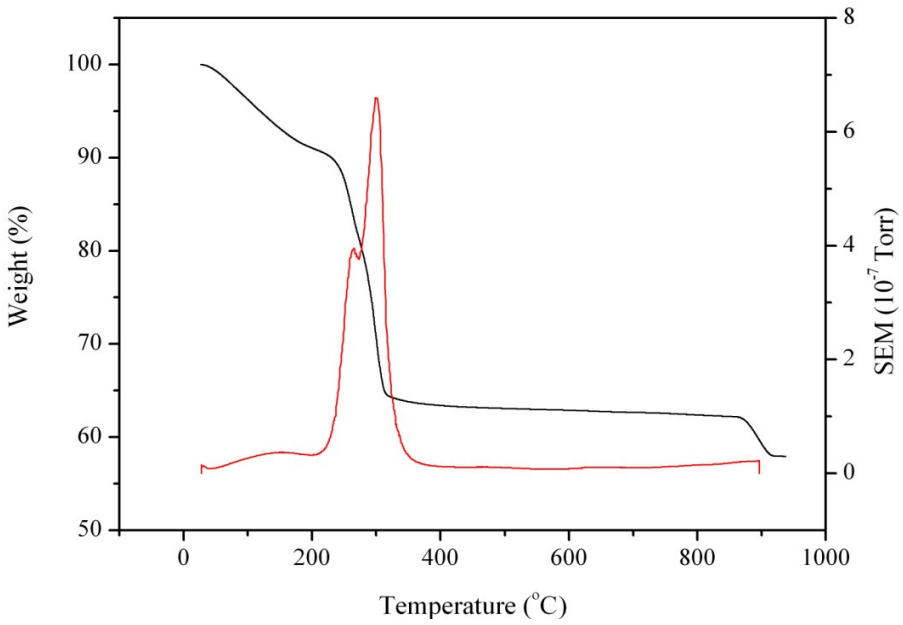

Figure C 1 – TGA-MS of mixed sodium cobalt carbonate precursor showing TGA profile (black) and CO_2 signature (red)

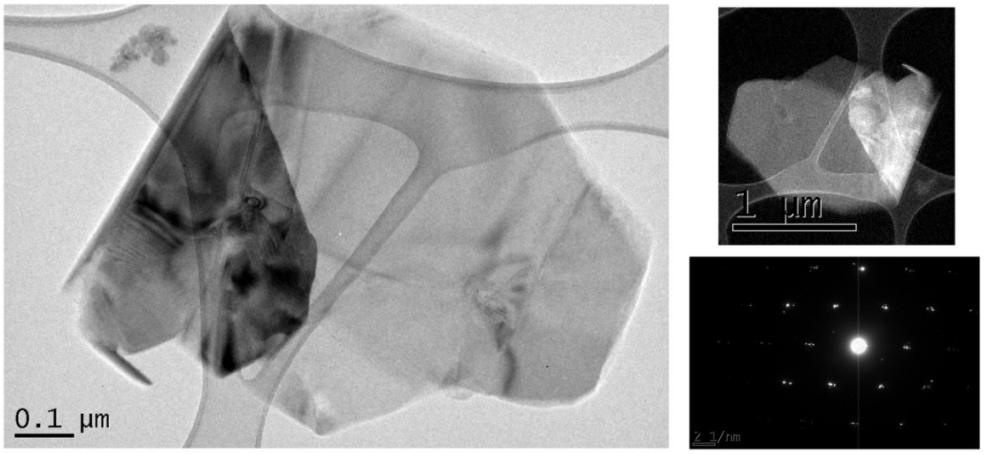

Appendix C

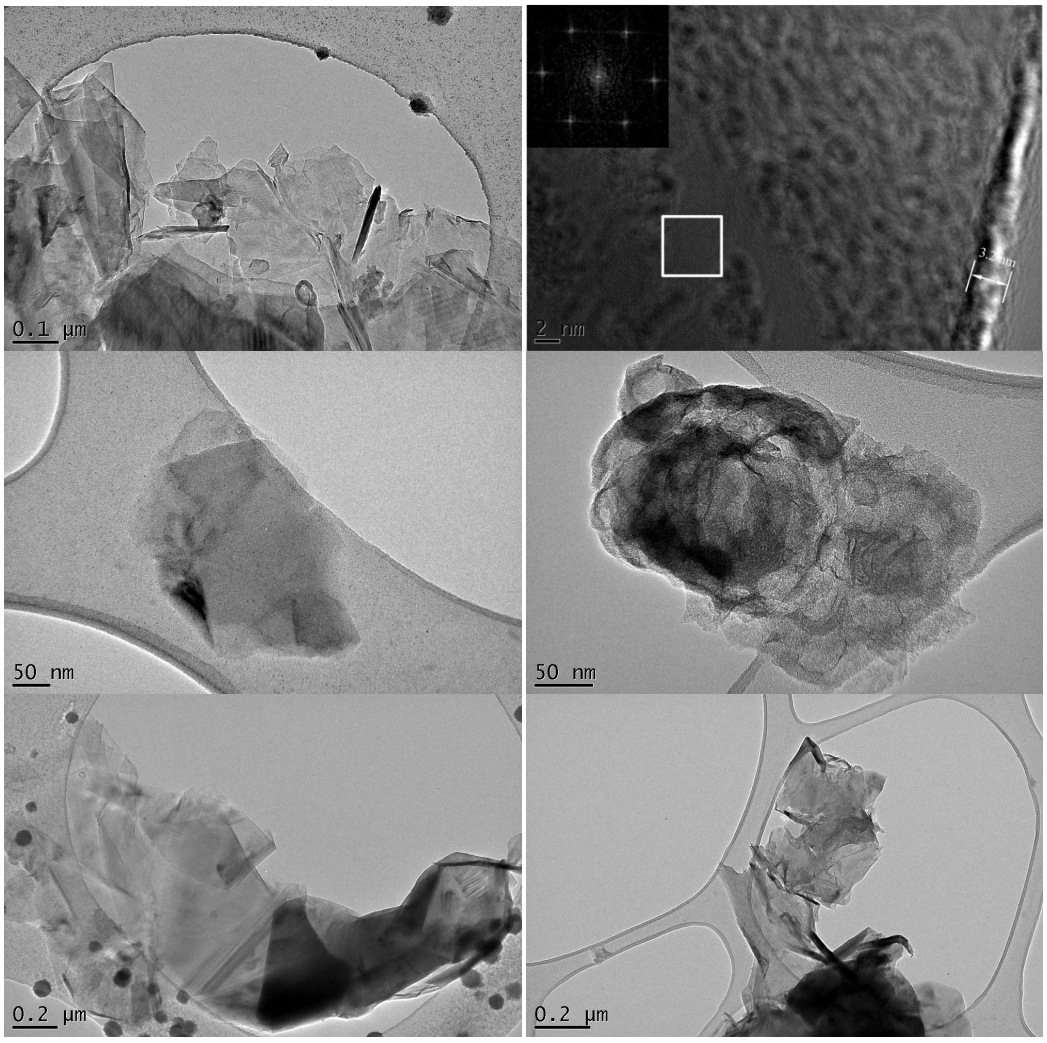

Figure C 2 - TEM images showing instances of thicker platelets observed from samples containing 1.5% sodium

Appendix C

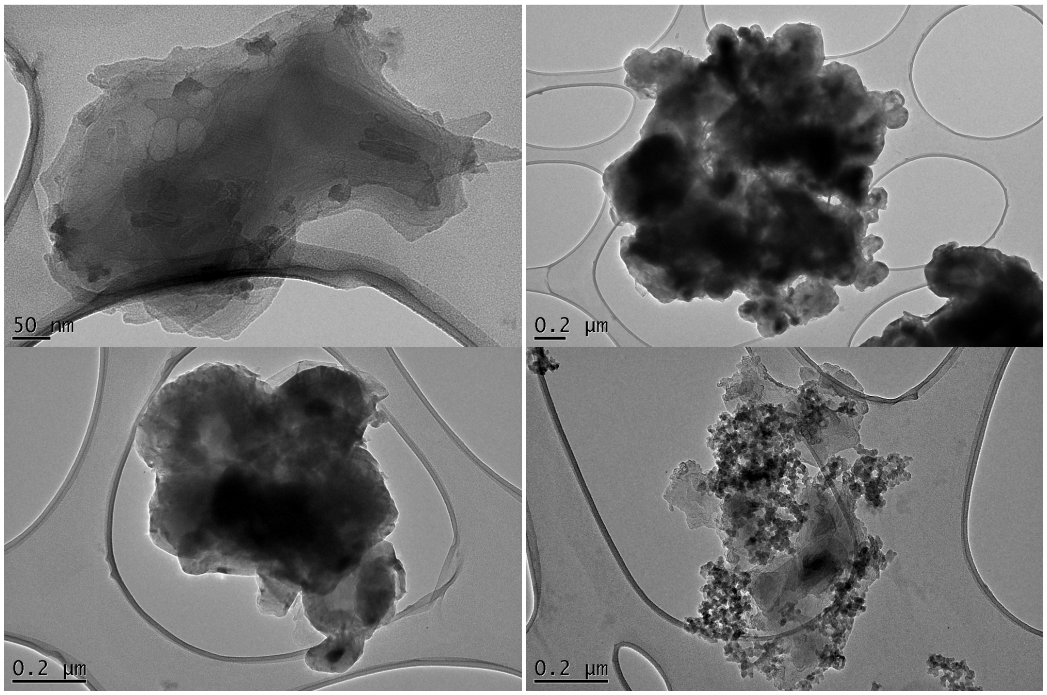

Figure C 3 - Additional images for CVD product of $CoCO_3$

Appendix D – Additional figures from chapter VI

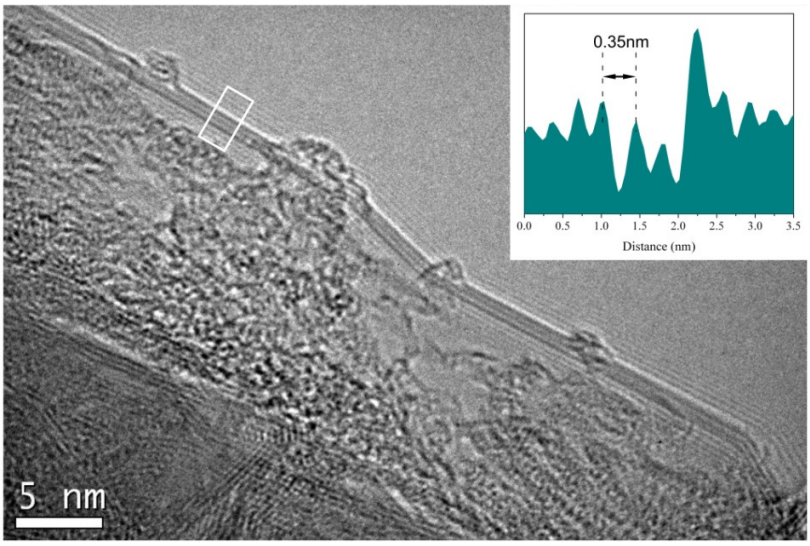

Figure D 1 – TEM image of platelet edge from few layer graphene grown on cobalt nanoplatelets on silicon supports. (insert) Graph shows dark line separation of 0.35nm close to graphite interlayer spacing (0.34nm)

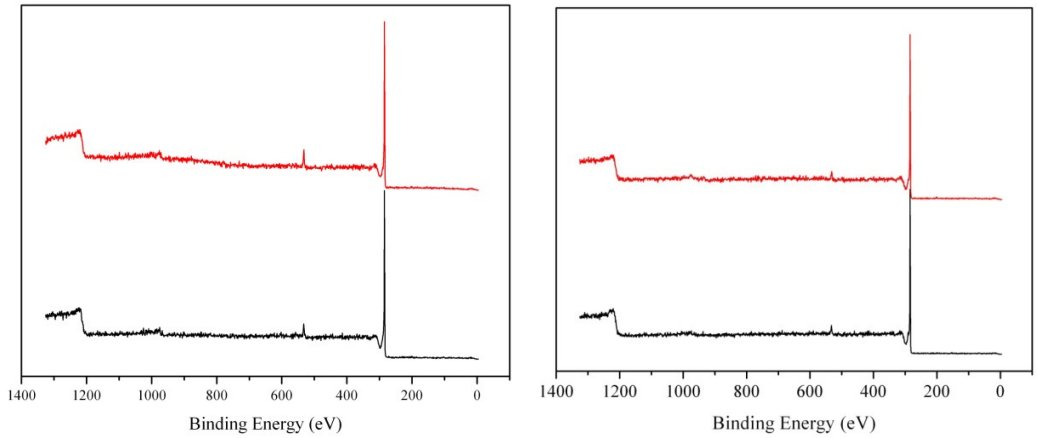

Figure D 2 – (Left) Survey XPS spectra of ethanol decomposition product over 1% (black) and 5% (red) $Co(OH)_2$/MgO catalysts, (Right) Survey XPS spectra of ethanol decomposition product over 1% (black) and 5% (red) Cu/MgO catalysts.

Appendix D

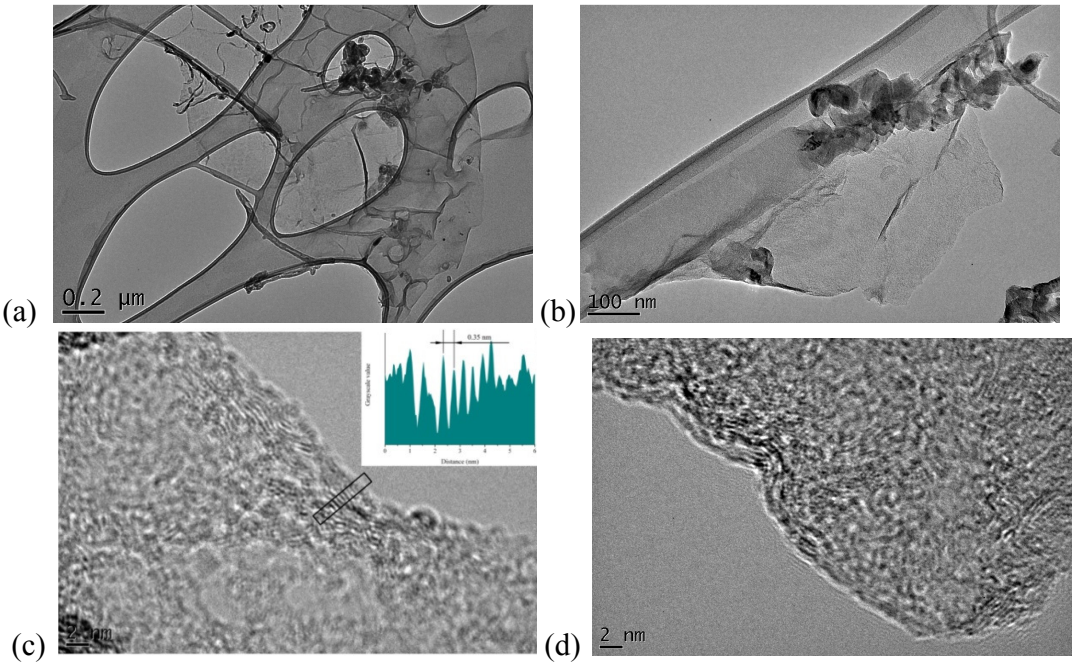

Figure D 3 – BF-TEM images and HREM images of few layer platelets formed by ethanol decomposition over 1% $Co(OH)_2$-MgO

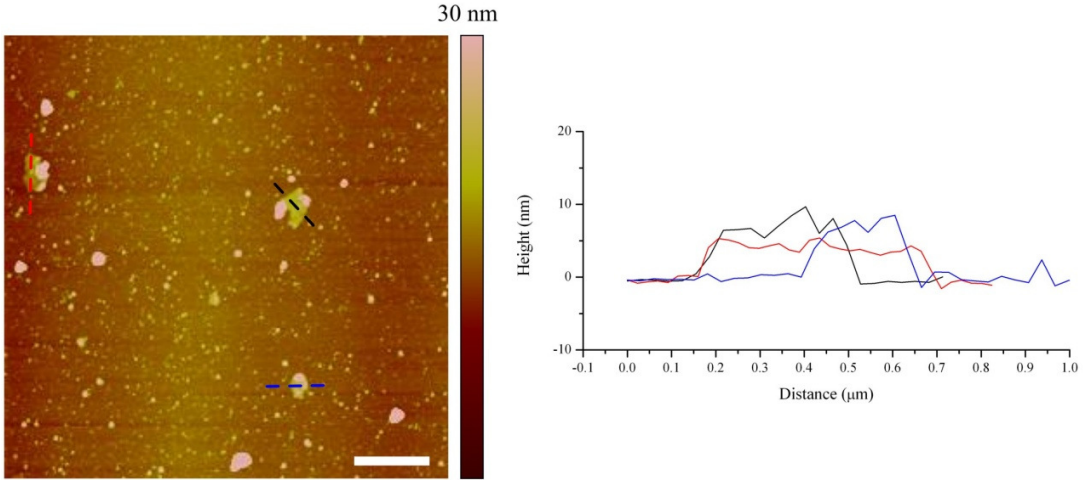

Appendix D

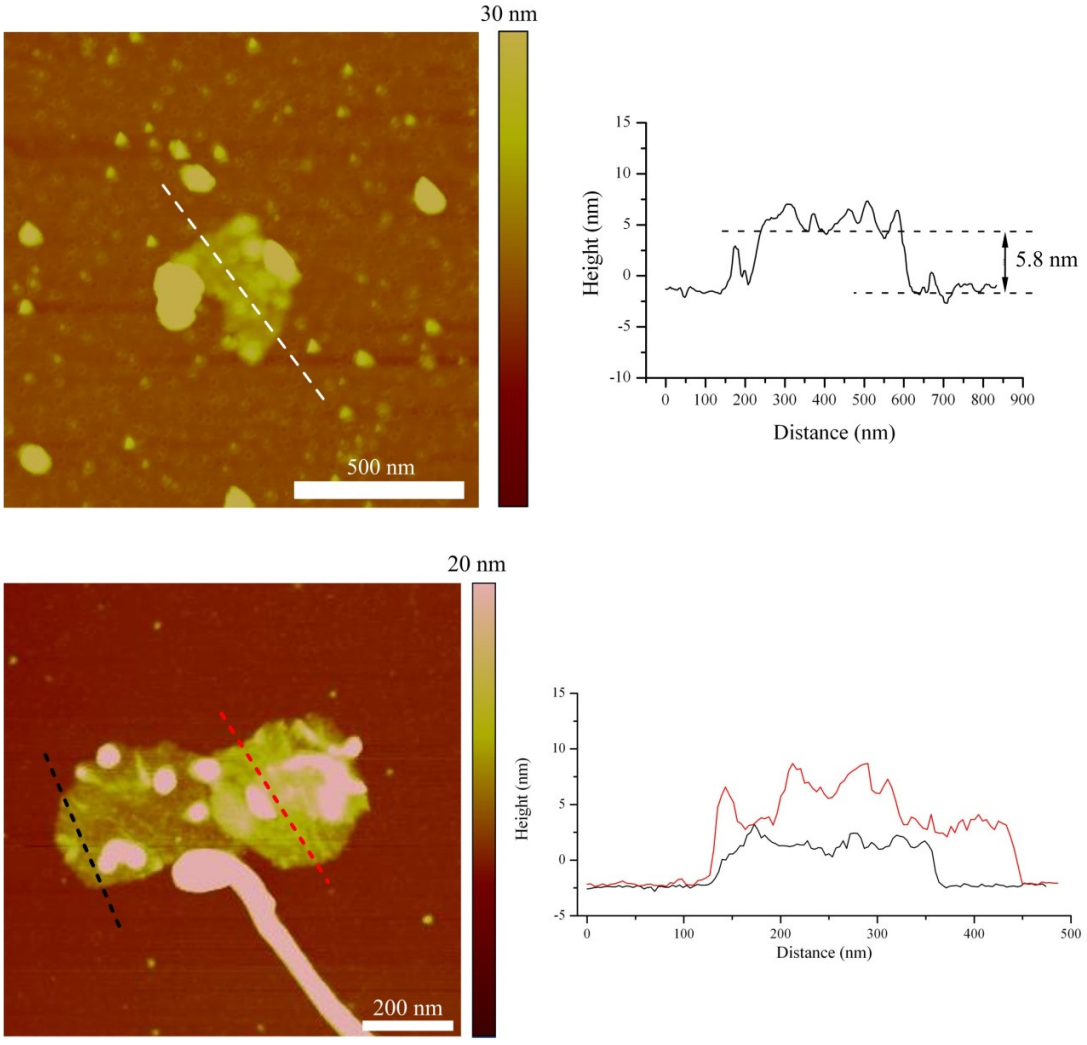

Figure D 4 – TappingMode AFM images and height analysis of few layer graphene platelets formed by ethanol decomposition over 1% $Co(OH)_2$-MgO spin coated onto cleaved mica from DMF

Appendix E. Notable outcomes as result of this work

Further to this work, Durham Graphene Science (DGS) has been set up as a spin-out company of the University of Durham, marketing products developed through the experimentation outlined in this thesis. Following the result of composite studies, these products are in scale development for sale, with focus on the composite industry. The company started trading as of October 2010 becoming one of only 8 companies globally that supply graphene.

Conference Presentations

1. "Simple and scalable route for the 'bottom-up' synthesis of few layer grapheme platelets", 44th Annual Universities of Scotland Inorganic Chemistry Conference in Durham, UK, July 2010

Patents

1. K.S. Coleman, Graphene, GB Patent 0913011, 2009
2. K.S. Coleman, Synthesis of graphene using template transition metal nanoparticles, In preparation for submission April 2011

Journal articles

1. C. R. Herron, K. S. Coleman, R. S. Edwards, B.G. Mendis; Simple and scalable route to the 'bottom-up' synthesis of few layer graphene platelets and thin films, *J. Mater. Chem.* 2011, **21**, 3378-3383

Appendix E

Abstract

Graphene has generated much interest owing to its exceptional electronic properties and high mechanical strength. This has enabled new types of electronic devices and composite materials to be envisaged. The main problem is the availability of the material and the difficulties associated with its synthesis. Here we have used a simple, convenient and scalable chemical vapour deposition method involving sodium ethoxide in ethanol to produce few-layer graphene sheets or platelets. The process has the advantage that it can be used to grow graphene films on non-metal containing substrates such as silicon wafer and quartz glass and that all non-carbon by-products are soluble in water.

(1) Novoselov, K. S.; Geim, A. K.; Morozov, S. V.; Jiang, D.; Zhang, Y.; Dubonos, S. V.; Grigorieva, I. V.; Firsov, A. A. *Science* **2004**, *306*, 666.

(2) Boehm, H. P.; Setton, R.; Stumpp, E. *Pure Appl. Chem.* **1994**, *66*, 1893.

(3) Van Bommel, A. J.; Crombeen, J. E.; Van Tooren, A. *Surf. Sci.* **1975**, *48*, 463.

(4) Kholin, N. A.; Rut'kov, E. V.; Tontegode, A. Y. *Surf. Sci.* **1984**, *139*, 155.

(5) Rosei, R.; De Crescenzi, M.; Sette, F.; Quaresima, C.; Savoia, A.; Perfetti, P. *Physical Review B* **1983**, *28*, 1161.

(6) Mermin, N. D. *Physical Review* **1968**, *176*, 250.

(7) Balandin, A. A.; Ghosh, S.; Bao, W. Z.; Calizo, I.; Teweldebrhan, D.; Miao, F.; Lau, C. N. *Nano Lett.* **2008**, *8*, 902.

(8) Pop, E.; Mann, D.; Wang, Q.; Goodson, K.; Dai, H. *Nano Lett.* **2005**, *6*, 96.

(9) Hammond, C. R. *The Elements, Handbook of Chemistry and Physics*; 81st ed.; CRC Press, 2004.

(10) Avouris, P.; Chen, Z. H.; Perebeinos, V. *Nat. Nanotechnol.* **2007**, *2*, 605.

(11) Geim, A. K.; MacDonald, A. H. *Physics Today* **2007**, *60*, 35.

(12) Lee, C.; Wei, X.; Kysar, J. W.; Hone, J. *Science* **2008**, *321*, 385.

(13) Fowler, J. D.; Allen, M. J.; Tung, V. C.; Yang, Y.; Kaner, R. B.; Weiller, B. H. *ACS Nano* **2009**, *3*, 301.

(14) Bunch, J. S.; van der Zande, A. M.; Verbridge, S. S.; Frank, I. W.; Tanenbaum, D. M.; Parpia, J. M.; Craighead, H. G.; McEuen, P. L. *Science* **2007**, *315*, 490.

(15) Moore, G. E. In *Electron Devices Meeting, 1975 International* 1975; Vol. 21, p 11.

(16) Eda, G.; Fanchini, G.; Chhowalla, M. *Nat Nano* **2008**, *3*, 270.

(17) Ponomarenko, L. A.; Schedin, F.; Katsnelson, M. I.; Yang, R.; Hill, E. W.; Novoselov, K. S.; Geim, A. K. *Science* **2008**, *320*, 356.

(18) Liao, L.; Lin, Y.-C.; Bao, M.; Cheng, R.; Bai, J.; Liu, Y.; Qu, Y.; Wang, K. L.; Huang, Y.; Duan, X. *Nature* **2010**, *467*, 305.

(19) Gomez De Arco, L.; Zhang, Y.; Schlenker, C. W.; Ryu, K.; Thompson, M. E.; Zhou, C. *ACS Nano* **2010**, *4*, 2865.

(20) Wu, J.; Agrawal, M.; Becerril, H. c. A.; Bao, Z.; Liu, Z.; Chen, Y.; Peumans, P. *ACS Nano* **2009**, *4*, 43.

(21) Areshkin, D. A.; White, C. T. *Nano Lett.* **2007**, *7*, 3253.

(22) Bae, S.; Kim, H.; Lee, Y.; Xu, X.; Park, J.-S.; Zheng, Y.; Balakrishnan, J.; Lei, T.; Ri Kim, H.; Song, Y. I.; Kim, Y.-J.; Kim, K. S.; Ozyilmaz, B.; Ahn, J.-H.; Hong, B. H.; Iijima, S. *Nat. Nanotechnol.* **2010**, *5*, 574.

(23) Wang, Y.; Tong, S. W.; Xu, X. F.; Özyilmaz, B.; Loh, K. P. *Adv. Mater.* **2011**, Advance Article.

(24) Matyba, P.; Yamaguchi, H.; Chhowalla, M.; Robinson, N. D.; Edman, L. *ACS Nano* **2010**, *5*, 574.

(25) Lee, D. W.; Hong, T.-K.; Kang, D.; Lee, J.; Heo, M.; Kim, J. Y.; Kim, B.-S.; Shin, H. S. *J. Mater. Chem.* **2011**, Advance Article.

(26) GrapheneIndustries prices correct as of Jan 2011.

(27) Cheaptubes.com prices correct as of Jan 2011.

(28) Ramanathan, T.; Abdala, A. A.; Stankovich, S.; Dikin, D. A.; Herrera-Alonso, M.; Piner, R. D.; Adamson, D. H.; Schniepp, H. C.; Chen, X.; Ruoff, R. S.; Nguyen, S. T.; Aksay, I. A.; Prud'homme, R. K.; Brinson, L. C. *Nat. Nanotechnol.* **2008**, *3*, 327.

(29) Rafiee, M. A.; Rafiee, J.; Yu, Z. Z.; Koratkar, N. *Appl. Phys. Lett.* **2009**, *95*, 223103.

(30) Zhao, X.; Zhang, Q.; Chen, D.; Lu, P. *Macromolecules* **2010**, *43*, 2357.

(31) Stankovich, S.; Dikin, D. A.; Dommett, G. H. B.; Kohlhaas, K. M.; Zimney, E. J.; Stach, E. A.; Piner, R. D.; Nguyen, S. T.; Ruoff, R. S. *Nature* **2006**, *442*, 282.

(32) Choi, K. S.; Liu, F.; Choi, J. S.; Seo, T. S. *Langmuir* **2010**, *26*, 12902.

(33) Chen, C.; Cai, W.; Long, M.; Zhou, B.; Wu, Y.; Wu, D.; Feng, Y. *ACS Nano* **2010**, null.

(34) Watcharotone, S.; Dikin, D. A.; Stankovich, S.; Piner, R.; Jung, I.; Dommett, G. H. B.; Evmenenko, G.; Wu, S.-E.; Chen, S.-F.; Liu, C.-P.; Nguyen, S. T.; Ruoff, R. S. *Nano Lett.* **2007**, *7*, 1888.

(35) Nethravathi, C.; Viswanath, B.; Shivakumara, C.; Mahadevaiah, N.; Rajamathi, M. *Carbon* **2008**, *46*, 1773.

(36) Nethravathi, C.; Rajamathi, J. T.; Ravishankar, N.; Shivakumara, C.; Rajamathi, M. *Langmuir* **2008**, *24*, 8240.

(37) Rao, C. N. R.; Sood, A. K.; Subrahmanyam, K. S.; Govindaraj, A. *Angewandte Chemie-International Edition* **2009**, *48*, 7752.

(38) Taghioskoui, M. *Materials Today* **2009**, *12*, 34.

(39) Roddaro, S.; Pingue, P.; Piazza, V.; Pellegrini, V.; Beltram, F. *Nano Lett.* **2007**, *7*, 2707.

(40) Blake, P.; Hill, E. W.; Neto, A. H. C.; Novoselov, K. S.; Jiang, D.; Yang, R.; Booth, T. J.; Geim, A. K. *Appl. Phys. Lett.* **2007**, *91*.

(41) Kim, J.; Cote, L. J.; Kim, F.; Huang, J. *J. Am. Chem. Soc.* **2009**, *132*, 260.

(42) Treossi, E.; Melucci, M.; Liscio, A.; Gazzano, M.; Samorilè€, P.; Palermo, V. *J. Am. Chem. Soc.* **2009**, *131*, 15576.

(43) Novoselov, K. S.; Geim, A. K.; Morozov, S. V.; Jiang, D.; Katsnelson, M. I.; Grigorieva, I. V.; Dubonos, S. V.; Firsov, A. A. *Nature* **2005**, *438*, 197.

(44) Zhang, Y.; Tan, Y.-W.; Stormer, H. L.; Kim, P. *Nature* **2005**, *438*, 201.

(45) Viculis, L. M.; Mack, J. J.; Mayer, O. M.; Hahn, H. T.; Kaner, R. B. *J. Mater. Chem.* **2005**, *15*, 974.

(46) Valles, C.; Drummond, C.; Saadaoui, H.; Furtado, C. A.; He, M.; Roubeau, O.; Ortolani, L.; Monthioux, M.; Penicaud, A. *J. Am. Chem. Soc.* **2008**, *130*, 15802.

(47) Kim, H.; Thomas Hahn, H.; Viculis, L. M.; Gilje, S.; Kaner, R. B. *Carbon* **2007**, *45*, 1578.

(48) Li, D.; Muller, M. B.; Gilje, S.; Kaner, R. B.; Wallace, G. G. *Nat. Nanotechnol.* **2008**, *3*, 101.

(49) Pu, N. W.; Wang, C. A.; Sung, Y.; Liu, Y. M.; Ger, M. D. *Mater. Lett.* **2009**, *63*, 1987.

(50) Hernandez, Y.; Lotya, M.; Rickard, D.; Bergin, S. D.; Coleman, J. N. *Langmuir* **2010**, *26*, 3208.

(51) Hernandez, Y.; Nicolosi, V.; Lotya, M.; Blighe, F. M.; Sun, Z. Y.; De, S.; McGovern, I. T.; Holland, B.; Byrne, M.; Gun'ko, Y. K.; Boland, J. J.; Niraj, P.; Duesberg, G.; Krishnamurthy, S.; Goodhue, R.; Hutchison, J.; Scardaci, V.; Ferrari, A. C.; Coleman, J. N. *Nat. Nanotechnol.* **2008**, *3*, 563.

(52) Lotya, M.; Hernandez, Y.; King, P. J.; Smith, R. J.; Nicolosi, V.; Karlsson, L. S.; Blighe, F. M.; De, S.; Wang, Z. M.; McGovern, I. T.; Duesberg, G. S.; Coleman, J. N. *J. Am. Chem. Soc.* **2009**, *131*, 3611.

(53) Hummers, W. S.; Offeman, R. E. *J. Am. Chem. Soc.* **1958**, *80*, 1339.

(54) Brodie, B. C. *Philosophical Transactions of the Royal Society of London* **1859**, *149*, 249.

(55) Staudenmaier, L. *Ber. Deut. Chem. Ges.* **1898**, *2*, 1481.

(56) Park, S.; Ruoff, R. S. *Nat Nano* **2009**, *4*, 217.

(57) Dreyer, D. R.; Park, S.; Bielawski, C. W.; Ruoff, R. S. *Chem. Soc. Rev.* **2010**, *39*, 228.

(58) Lerf, A.; He, H. Y.; Forster, M.; Klinowski, J. *J. Phys. Chem. B* **1998**, *102*, 4477.

(59) He, H. Y.; Klinowski, J.; Forster, M.; Lerf, A. *Chem. Phys. Lett.* **1998**, *287*, 53.

(60) Buchsteiner, A.; Lerf, A.; Pieper, J. *J. Phys. Chem. B* **2006**, *110*, 22328.

(61) Ju, H. M.; Huh, S. H.; Choi, S. H.; Lee, H. L. *Mater. Lett.* **2010**, *64*, 357.

(62) Subrahmanyam, K. S.; Vivekchand, S. R. C.; Govindaraj, A.; Rao, C. N. R. *J. Mater. Chem.* **2008**, *18*, 1517.

(63) Tung, V. C.; Allen, M. J.; Yang, Y.; Kaner, R. B. *Nat. Nanotechnol.* **2009**, *4*, 25.

(64) Stankovich, S.; Dikin, D. A.; Piner, R. D.; Kohlhaas, K. A.; Kleinhammes, A.; Jia, Y.; Wu, Y.; Nguyen, S. T.; Ruoff, R. S. *Carbon* **2007**, *45*, 1558.

(65) Shin, H. J.; Kim, K. K.; Benayad, A.; Yoon, S. M.; Park, H. K.; Jung, I. S.; Jin, M. H.; Jeong, H. K.; Kim, J. M.; Choi, J. Y.; Lee, Y. H. *Adv. Funct. Mater.* **2009**, *19*, 1987.

(66) Wang, G. X.; Yang, J.; Park, J.; Gou, X. L.; Wang, B.; Liu, H.; Yao, J. *J. Phys. Chem. C* **2008**, *112*, 8192.

(67) Stankovich, S.; Piner, R. D.; Nguyen, S. T.; Ruoff, R. S. *Carbon* **2006**, *44*, 3342.

(68) Wang, G. X.; Wang, B.; Park, J.; Yang, J.; Shen, X. P.; Yao, J. *Carbon* **2009**, *47*, 68.

(69) Wei, T.; Luo, G.; Fan, Z.; Zheng, C.; Yan, J.; Yao, C.; Li, W.; Zhang, C. *Carbon* **2009**, *47*, 2296.

(70) Wu, Z.-S.; Ren, W.; Gao, L.; Liu, B.; Jiang, C.; Cheng, H.-M. *Carbon* **2009**, *47*, 493.

(71) Segal, M. *Nat Nano* **2009**, *4*, 612.

(72) Becerril, H. c. A.; Mao, J.; Liu, Z.; Stoltenberg, R. M.; Bao, Z.; Chen, Y. *ACS Nano* **2008**, *2*, 463.

(73) Ohta, T.; Bostwick, A.; Seyller, T.; Horn, K.; Rotenberg, E. *Science* **2006**, *313*, 951.

(74) Berger, C.; Song, Z. M.; Li, X. B.; Wu, X. S.; Brown, N.; Naud, C.; Mayou, D.; Li, T. B.; Hass, J.; Marchenkov, A. N.; Conrad, E. H.; First, P. N.; de Heer, W. A. *Science* **2006**, *312*, 1191.

(75) de Heer, W. A.; Berger, C.; Wu, X. S.; First, P. N.; Conrad, E. H.; Li, X. B.; Li, T. B.; Sprinkle, M.; Hass, J.; Sadowski, M. L.; Potemski, M.; Martinez, G. *Solid State Commun.* **2007**, *143*, 92.

(76) Berger, C.; Song, Z.; Li, T.; Li, X.; Ogbazghi, A. Y.; Feng, R.; Dai, Z.; Marchenkov, A. N.; Conrad, E. H.; First, P. N.; de Heer, W. A. *J. Phys. Chem. B* **2004**, *108*, 19912.

(77) Tapaszto, L.; Dobrik, G.; Lambin, P.; Biro, L. P. *Nat Nano* **2008**, *3*, 397.

(78) de Heer, W. A. Patterned thin film graphite devices and method for making same, U.S. Patent 7015142, 2006.

(79) Kedzierski, J.; Pei-Lan, H.; Healey, P.; Wyatt, P. W.; Keast, C. L.; Sprinkle, M.; Berger, C.; de Heer, W. A. *IEEE Trans. Electron Devices* **2008**, *55*, 2078.

(80) Moon, J. S.; Curtis, D.; Hu, M.; Wong, D.; McGuire, C.; Campbell, P. M.; Jernigan, G.; Tedesco, J. L.; VanMil, B.; Myers-Ward, R.; Eddy, C.; Gaskill, D. K. *IEEE Electron Device Lett.* **2009**, *30*, 650.

(81) Juang, Z.-Y.; Wu, C.-Y.; Lo, C.-W.; Chen, W.-Y.; Huang, C.-F.; Hwang, J.-C.; Chen, F.-R.; Leou, K.-C.; Tsai, C.-H. *Carbon* **2009**, *47*, 2026.

(82) Liu, W.; Chung, C.-H.; Miao, C.-Q.; Wang, Y.-J.; Li, B.-Y.; Ruan, L.-Y.; Patel, K.; Park, Y.-J.; Woo, J.; Xie, Y.-H. *Thin Solid Films* **2010**, *518*, S128.

(83) Somani, P. R.; Somani, S. P.; Umeno, M. *Chem. Phys. Lett.* **2006**, *430*, 56.

(84) Thiele, S.; Reina, A.; Healey, P.; Kedzierski, J.; Wyatt, P.; Hsu, P. L.; Keast, C.; Schaefer, J.; Kong, J. *Nanotechnology* **2010**, *21*, 015601.

(85) Reina, A.; Jia, X. T.; Ho, J.; Nezich, D.; Son, H. B.; Bulovic, V.; Dresselhaus, M. S.; Kong, J. *Nano Lett.* **2009**, *9*, 30.

(86) Li, X.; Cai, W.; An, J.; Kim, S.; Nah, J.; Yang, D.; Piner, R.; Velamakanni, A.; Jung, I.; Tutuc, E.; Banerjee, S. K.; Colombo, L.; Ruoff, R. S. *Science* **2009**, *324*, 1312.

(87) Ago, H.; Ito, Y.; Mizuta, N.; Yoshida, K.; Hu, B.; Orofeo, C. M.; Tsuji, M.; Ikeda, K.-i.; Mizuno, S. *ACS Nano* **2010**, *4*, 7407.

(88) Ueta, H.; Saida, M.; Nakai, C.; Yamada, Y.; Sasaki, M.; Yamamoto, S. *Surf. Sci.* **2004**, *560*, 183.

(89) Coraux, J. *New Journal of Physics* **2009**, *11*, 023006.

(90) Pletikosicacute, I.; Kralj, M.; Pervan, P.; Brako, R.; Coraux, J.; N'Diaye, A. T.; Busse, C.; Michely, T. *Phys. Rev. Lett.* **2009**, *102*, 056808.

(91) Sutter, P. W.; Flege, J.-I.; Sutter, E. A. *Nat. Mater.* **2008**, *7*, 406.

(92) Li, X.; Cai, W.; Colombo, L.; Ruoff, R. S. *Nano Lett.* **2009**, *9*, 4268.

(93) *ASM handbook*; ASM International, 2002; Vol. 3 - Alloy Phase Diagrams.

(94) Rasool, H. I.; Song, E. B.; Allen, M. J.; Wassei, J. K.; Kaner, R. B.; Wang, K. L.; Weiller, B. H.; Gimzewski, J. K. *Nano Lett.* **2011**, *11*, 251.

(95) Kim, K. S.; Zhao, Y.; Jang, H.; Lee, S. Y.; Kim, J. M.; Ahn, J. H.; Kim, P.; Choi, J. Y.; Hong, B. H. *Nature* **2009**, *457*, 706.

(96) Bolotin, K. I.; Sikes, K. J.; Jiang, Z.; Klima, M.; Fudenberg, G.; Hone, J.; Kim, P.; Stormer, H. L. *Solid State Commun.* **2008**, *146*, 351.

(97) Du, X.; Skachko, I.; Barker, A.; Andrei, E. Y. *Nat. Nanotechnol.* **2008**, *3*, 491.

(98) Dato, A.; Radmilovic, V.; Lee, Z. H.; Phillips, J.; Frenklach, M. *Nano Lett.* **2008**, *8*, 2012.

(99) Wang, X.; You, H.; Liu, F.; Li, M.; Wan, L.; Li, S.; Li, Q.; Xu, Y.; Tian, R.; Yu, Z.; Xiang, D.; Cheng, J. *Chem. Vap. Deposition* **2009**, *15*, 53.

(100) Dervishi, E.; Li, Z.; Watanabe, F.; Courte, A.; Biswas, A.; Biris, A. R.; Saini, V.; Xu, Y.; Biris, A. S. *Chem. Mater.* **2009**, *21*, 5491.

(101) Parker, D. H.; Wurz, P.; Chatterjee, K.; Lykke, K. R.; Hunt, J. E.; Pellin, M. J.; Hemminger, J. C.; Gruen, D. M.; Stock, L. M. *J. Am. Chem. Soc.* **1991**, *113*, 7499.

(102) Scrivens, W. A.; Tour, J. M. *The Journal of Organic Chemistry* **1992**, *57*, 6932.

(103) Journet, C.; Maser, W.; Bernier, P.; Loiseau, A.; Lamy de la Chapelle, M.; Lefrant, S.; Deniard, P.; Lee, R.; Fischer, J. *Nature* **1997**, *388*, 756.

(104) Subrahmanyam, K. S.; Panchakarla, L. S.; Govindaraj, A.; Rao, C. N. R. *The Journal of Physical Chemistry C* **2009**, *113*, 4257.

(105) Zhiyong, W.; et al. *Nanotechnology* **2010**, *21*, 175602.

(106) Li, N.; Wang, Z.; Zhao, K.; Shi, Z.; Gu, Z.; Xu, S. *Carbon* **2010**, *48*, 255.

(107) Amini, S.; Garay, J.; Liu, G. X.; Balandin, A. A.; Abbaschian, R. *J. Appl. Phys.* **2010**, *108*.

(108) Sun, Z.; Yan, Z.; Yao, J.; Beitler, E.; Zhu, Y.; Tour, J. M. *Nature* **2010**, *advance online publication*.

(109) Zheng, M.; Takei, K.; Hsia, B.; Fang, H.; Zhang, X. B.; Ferralis, N.; Ko, H.; Chueh, Y. L.; Zhang, Y. G.; Maboudian, R.; Javey, A. *Appl. Phys. Lett.* **2010**, *96*, 063110.

(110) Choucair, M.; Thordarson, P.; Stride, J. A. *Nat. Nanotechnol.* **2009**, *4*, 30.

(111) Xu, Z.; Li, H.; Li, W.; Cao, G.; Zhang, Q.; Li, K.; Fu, Q.; Wang, J. *Chemical Communications* **2011**, *47*, 1166.

(112) Jiao, L.; Zhang, L.; Wang, X.; Diankov, G.; Dai, H. *Nature* **2009**, *458*, 877.

(113) Elías, A. L.; Botello-Méndez, A. s. R.; Meneses-Rodríguez, D.; Jehová González, V.; Ramírez-González, D.; Ci, L.; Muñoz-Sandoval, E.; Ajayan, P. M.; Terrones, H.; Terrones, M. *Nano Lett.* **2009**, *10*, 366.

(114) Kosynkin, D. V.; Higginbotham, A. L.; Sinitskii, A.; Lomeda, J. R.; Dimiev, A.; Price, B. K.; Tour, J. M. *Nature* **2009**, *458*, 872.

(115) Biró, L. P.; Lambin, P. *Carbon* **2010**, *48*, 2677.

(116) Janowska, I.; Ersen, O.; Jacob, T.; Vennégues, P.; Bégin, D.; Ledoux, M.-J.; Pham-Huu, C. *Appl. Catal., A* **2009**, *371*, 22.

(117) Andersson, O. E.; Prasad, B. L. V.; Sato, H.; Enoki, T.; Hishiyama, Y.; Kaburagi, Y.; Yoshikawa, M.; Bandow, S. *Physical Review B* **1998**, *58*, 16387.

(118) Affoune, A. M.; Prasad, B. L. V.; Sato, H.; Enoki, T.; Kaburagi, Y.; Hishiyama, Y. *Chem. Phys. Lett.* **2001**, *348*, 17.

(119) Wu, J. S.; Tomovic, Z.; Enkelmann, V.; Mullen, Y. *J. Org. Chem.* **2004**, *69*, 5179.

(120) Simpson, C. D.; Brand, J. D.; Berresheim, A. J.; Przybilla, L.; Rader, H. J.; Mullen, K. *Chemistry-a European Journal* **2002**, *8*, 1424.

(121) Yang, X. Y.; Dou, X.; Rouhanipour, A.; Zhi, L. J.; Rader, H. J.; Mullen, K. *J. Am. Chem. Soc.* **2008**, *130*, 4216.

(122) Cai, J. M.; Ruffieux, P.; Jaafar, R.; Bieri, M.; Braun, T.; Blankenburg, S.; Muoth, M.; Seitsonen, A. P.; Saleh, M.; Feng, X. L.; Mullen, K.; Fasel, R. *Nature* **2010**, *466*, 470.

(123) Dresselhaus, M. S.; Dresselhaus, G.; Sugihara, K.; Spain, I. L.; Goldberg, H. A. *Graphite Fibers and Filaments*; Springer-Verlag: Berlin, 1988; Vol. 5.

(124) Cancado, L. G.; Pimenta, M. A.; Neves, B. R. A.; Medeiros-Ribeiro, G.; Enoki, T.; Kobayashi, Y.; Takai, K.; Fukui, K.; Dresselhaus, M. S.; Saito, R.; Jorio, A. *Phys. Rev. Lett.* **2004**, *93*.

(125) Dresselhaus, M. S.; Dresselhaus, G. *Science of Fullerenes and Carbon Nanotubes*; Academic Press: San Diego: San Diego, C.A., 1996.

(126) Dresselhaus, M. S.; Dresselhaus, G.; Saito, R.; Jorio, A. *Phys. Rep.* **2005**, *409*, 47.

(127) Malard, L. M.; Pimenta, M. A.; Dresselhaus, G.; Dresselhaus, M. S. *Phys. Rep.* **2009**, *473*, 51.

(128) Ferrari, A. C.; Robertson, J. *Philos. Trans. R. Soc. London, A* **2004**, *362*, 2477.

(129) Briggs, D.; Seah, M. P. *Practical Surface Analysis by Auger and X-ray Photoelectron Spectroscopy*; 2nd ed.; John Wiley & Sons, 1996; Vol. 1.

(130) Beamson, G.; Briggs, D. *High Resolution XPS of Organic Polymers*; Wiley: London, U.K., 1992.

(131) Taylor, J. A.; Lancaster, G. M.; Rabalais, J. W. *Appl. Surf. Sci.* **1978**, *1*, 503.

(132) Suri, A.; Chakraborty, A. K.; Coleman, K. S. *Chem. Mater.* **2008**, *20*, 1705.

(133) Valdes, L. B. *Proceedings of the Institute of Radio Engineers* **1954**, *42*, 420.

(134) Smits, F. M. *Bell Sys. Tech. J.* **1958**, *37*, 711.

(135) Li, Z.; Dharap, P.; Nagarajaiah, S.; Barrera, E. V.; Kim, J. D. *Adv. Mater.* **2004**, *16*, 640.

(136) Pang, S. P.; Tsao, H. N.; Feng, X. L.; Mullen, K. *Adv. Mater.* **2009**, *21*, 3488.

(137) Verma, V. P.; Das, S.; Lahiri, I.; Choi, W. *Appl. Phys. Lett.* **2010**, *96*.

(138) Suk, J. W.; Piner, R. D.; An, J.; Ruoff, R. S. *ACS Nano* **2010**, *4*, 6557.

(139) Giesbers, A. J. M.; Zeitler, U.; Neubeck, S.; Freitag, F.; Novoselov, K. S.; Maan, J. C. *Solid State Commun.* **2008**, *147*, 366.

(140) Wei, Z.; Wang, D.; Kim, S.; Kim, S.-Y.; Hu, Y.; Yakes, M. K.; Laracuente, A. R.; Dai, Z.; Marder, S. R.; Berger, C.; King, W. P.; de Heer, W. A.; Sheehan, P. E.; Riedo, E. *Science* **2010**, *328*, 1373.

(141) Sidorov, A. N.; Yazdanpanah, M. M.; Jalilian, R.; Ouseph, P. J.; Cohn, R. W.; Sumanasekera, G. U. *Nanotechnology* **2007**, *18*, 135301.

(142) Li, X.; Wang, X.; Zhang, L.; Lee, S.; Dai, H. *Science* **2008**, *319*, 1229.

(143) Nemes-Incze, P.; Osvath, Z.; Kamaras, K.; Biro, L. P. *Carbon* **2008**, *46*, 1435.

(144) Warner, J. H.; Schäffel, F.; Zhong, G.; Rümmeli, M. H.; Büchner, B.; Robertson, J.; Briggs, G. A. D. *ACS Nano* **2009**, *3*, 1557.

(145) Doytcheva, M.; Kaiser, M.; de Jonge, N. *Nanotechnology* **2006**, *17*, 3226.

(146) Wang, M. S.; Wang, J. Y.; Jin, C. H.; Chen, Q.; Peng, L. M. *Mater. Sci. Forum* **2005**, *475-479*, 4071.

(147) Smith, B. W.; Luzzi, D. E. *J. Appl. Phys.* **2001**, *90*, 3509.

(148) Warner, J. H.; Rummeli, M. H.; Gemming, T.; Buchner, B.; Briggs, G. A. D. *Nano Lett.* **2009**, *9*, 102.

(149) Meyer, J. C.; Geim, A. K.; Katsnelson, M. I.; Novoselov, K. S.; Booth, T. J.; Roth, S. *Nature* **2007**, *446*, 60.

(150) Silva, S. R. P. *Properties of Amorphous Carbon*; INSPEC: London, UK, 2003.

(151) El-Barbary, A. A.; et al. *J. Phys. Conf. Ser.* **2006**, *26*, 149.

(152) Reed, J. P.; Uchoa, B.; Joe, Y. I.; Gan, Y.; Casa, D.; Fradkin, E.; Abbamonte, P. *Science* **2010**, *330*, 805.

(153) Menard, K. P. *Dynamic Mechanical Analysis: A Practical Introduction*; CRC Press, 1999.

(154) Ramanathan, T.; Liu, H.; Brinson, L. C. *Journal of Polymer Science, Part B: Polymer Physics* **2005**, *43*, 2269.

(155) Ogasawara, T.; Ishida, Y.; Ishikawa, T.; Yokota, R. *Compos. Part A - Appl. S* **2004**, *35*, 67.

(156) Kumar, S.; Li, B.; Caceres, S.; Maguire, R. G.; Zhong, W. H. *Nanotechnology* **2009**, *20*.

(157) Awad, W. H.; Beyer, G.; Benderly, D.; Ijdo, W. L.; Songtipya, P.; Jimenez-Gasco, M. D.; Manias, E.; Wilkie, C. A. *Polymer* **2009**, *50*, 1857.

(158) Kashiwagi, T.; Harris, R. H.; Zhang, X.; Briber, R. M.; Cipriano, B. H.; Raghavan, S. R.; Awad, W. H.; Shields, J. R. *Polymer* **2004**, *45*, 881.

(159) Dodiuk, H.; Belinski, I.; Dotan, A.; Kenig, S. *J. Adhes. Sci. Technol.* **2006**, *20*, 1345.

(160) Cai, D. Y.; Yusoh, K.; Song, M. *Nanotechnology* **2009**, *20*, 315708

(161) Bragg, W. L. *Proceedings of the Cambridge Philosophical Society* **1913**, *17*, 43.

(162) Li, Z. Q.; Lu, C. J.; Xia, Z. P.; Zhou, Y.; Luo, Z. *Carbon* **2007**, *45*, 1686.

(163) Wang, G.; Yang, J.; Park, J.; Gou, X.; Wang, B.; Liu, H.; Yao, J. *The Journal of Physical Chemistry C* **2008**, *112*, 8192.

(164) Park, S.; An, J.; Jung, I.; Piner, R.; An, S.; Li, X.; Velamakanni, A.; Ruoff, R. *Nano Lett.* **2009**, *9*, 1593.

(165) Patil, P. S. *Mater. Chem. Phys.* **1999**, *59*, 185.

(166) Xu, Z. J.; Chu, R. Q.; Li, G. R.; Yin, Q. R. *Journal of Inorganic Materials* **2004**, *19*, 1240.

(167) Palchan, I.; Crespin, M.; Estradeszwarckopf, H.; Rousseau, B. *Chem. Phys. Lett.* **1989**, *157*, 321.

(168) Hammond, J. S.; Holubka, J. W.; Devries, J. E.; Dickie, R. A. *Corros. Sci.* **1981**, *21*, 239.

(169) Stankovich, S.; Piner, R. D.; Chen, X.; Wu, N.; Nguyen, S. T.; Ruoff, R. S. *J. Mater. Chem.* **2006**, *16*, 155.

(170) Castle, J. E.; Salvi, A. M. *J. Vac. Sci. Technol., A* **2001**, *19*, 1170.

(171) Retzko, I.; Unger, W. E. S. *Advanced Engineering Materials* **2003**, *5*, 519.

(172) Filik, J.; May, P. W.; Pearce, S. R. J.; Wild, R. K.; Hallam, K. R. *Diamond Relat. Mater.* **2003**, *12*, 974.

(173) Taki, Y.; Takai, O. *Thin Solid Films* **1998**, *316*, 45.

(174) Ferrari, A. C.; Meyer, J. C.; Scardaci, V.; Casiraghi, C.; Lazzeri, M.; Mauri, F.; Piscanec, S.; Jiang, D.; Novoselov, K. S.; Roth, S.; Geim, A. K. *Phys. Rev. Lett.* **2006**, *97*, 187401.

(175) Si, Y.; Samulski, E. T. *Nano Lett.* **2008**, *8*, 1679.

(176) Drouin, D.; Couture, A.; Joly, D.; Tastet, X.; Aimez, V.; Gauvin, R. *Scanning* **2007**, *29*, 92.

(177) Ertl, G.; Knözinger, H.; Weitkamp, J. *Preparation of Solid Catalysts*; Wiley - VCH: Wienhiem, 1999.

(178) Singh, M. K.; Titus, E.; Goncalves, G.; Marques, P. A. A. P.; Bdikin, I.; Kholkin, A. L.; Gracio, J. J. A. *Nanoscale* **2010**, *2*, 700.

(179) Orlita, M.; Faugeras, C.; Plochocka, P.; Neugebauer, P.; Martinez, G.; Maude, D. K.; Barra, A. L.; Sprinkle, M.; Berger, C.; de Heer, W. A.; Potemski, M. *Phys. Rev. Lett.* **2008**, *101*, 267601.

(180) Hass, J.; de Heer, W. A.; Conrad, E. H. *J. Phys.: Condens. Matter* **2008**, *20*, 323202.

(181) Sprinkle, M.; Soukiassian, P.; de Heer, W. A.; Berger, C.; Conrad, E. H. *physica status solidi (RRL) – Rapid Research Letters* **2009**, *3*, A91.

(182) Talyzin, A. V.; Szaboì□, T. s.; Deì□kaì□ny, I.; Langenhorst, F.; Sokolov, P. S.; Solozhenko, V. L. *The Journal of Physical Chemistry C* **2009**, *113*, 11279.

(183) Yoshizawa, K.; Kato, T.; Yamabe, T. *J. Chem. Phys.* **1996**, *105*, 2099.

(184) Caldin, E. F.; Long, G. *Nature* **1953**, *172*, 583.

(185) Yang, D.; Velamakanni, A.; Bozoklu, G.; Park, S.; Stoller, M.; Piner, R. D.; Stankovich, S.; Jung, I.; Field, D. A.; Ventrice Jr, C. A.; Ruoff, R. S. *Carbon* **2009**, *47*, 145.

(186) Salzmann, C. G.; Nicolosi, V.; Green, M. L. H. *J. Mater. Chem.* **2010**, *20*, 314.

(187) Evdokimov, A. N.; Kurzin, A. V.; Majorova, E. D.; Platonov, A. J. U.; Sivakov, A. A.; Chistokleto, V. V. Russia, 2002; Vol. RU2178402 (C1)

(188) Dupuis, A.-C. *Prog. Mat. Sci* **2005**, *50*, 929.

(189) Wu, J.; Zheng, H. *Chem. Geol.* **2010**, *273*, 267.

(190) Chandran, K.; Kamruddin, M.; Ajikumar, P. K.; Gopalan, A.; Ganesan, V. *J. Nucl. Mater.* **2006**, *358*, 111.

(191) Campos-Delgado, J.; Romo-Herrera, J. M.; Jia, X.; Cullen, D. A.; Muramatsu, H.; Kim, Y. A.; Hayashi, T.; Ren, Z.; Smith, D. J.; Okuno, Y.; Ohba, T.; Kanoh, H.; Kaneko, K.; Endo, M.; Terrones, H.; Dresselhaus, M. S.; Terrones, M. *Nano Lett.* **2008**, *8*, 2773.

(192) Wang, S. J.; Geng, Y.; Zheng, Q.; Kim, J.-K. *Carbon* **2010**, *48*, 1815.

(193) Su, C.-Y.; Xu, Y.; Zhang, W.; Zhao, J.; Tang, X.; Tsai, C.-H.; Li, L.-J. *Chem. Mater.* **2009**, *21*, 5674.

(194) Yu, A. P.; Roes, I.; Davies, A.; Chen, Z. W. *Appl. Phys. Lett.* **2010**, *96*.

(195) Ni, Z. H.; Wang, H. M.; Kasim, J.; Fan, H. M.; Yu, T.; Wu, Y. H.; Feng, Y. P.; Shen, Z. X. *Nano Lett.* **2007**, *7*, 2758.

(196) Dua, V.; Surwade, S.; Ammu, S.; Agnihotra, S.; Jain, S.; Roberts, K.; Park, S.; Ruoff, R.; Manohar, S. *Angew. Chem., Int. Ed.* **2010**, *49*, 2154.

(197) Cheung, C. L.; Kurtz, A.; Park, H.; Lieber, C. M. *J. Phys. Chem. B* **2002**, *106*, 2429.

(198) Biswas, S.; Drzal, L. T. *Nano Lett.* **2009**, *9*, 167.

(199) Dai, H.; Rinzler, A. G.; Nikolaev, P.; Thess, A.; Colbert, D. T.; Smalley, R. E. *Chem. Phys. Lett.* **1996**, *260*, 471.

(200) D'Andrade, B. W.; Forrest, S. R. *Adv. Mater.* **2004**, *16*, 1585.

(201) Hoppe, H.; Sariciftci, N. S. *J. Mater. Res.* **2004**, *19*, 1924.

(202) Kamtekar, K. T.; Monkman, A. P.; Bryce, M. R. *Adv. Mater.* **2010**, *22*, 572.

(203) Mabrook, M. F.; Yun, Y. J.; Pearson, C.; Zeze, D. A.; Petty, M. C. *Appl. Phys. Lett.* **2009**, *94*.

(204) Reese, C.; Roberts, M.; Ling, M.-m.; Bao, Z. *Materials Today* **2004**, *7*, 20.

(205) Werner, J. H.; Dassow, R.; Rinke, T. J.; Köhler, J. R.; Bergmann, R. B. *Thin Solid Films* **2001**, *383*, 95.

(206) Paul, S.; Kanwal, A.; Chhowalla, M. *Nanotechnology* **2006**, *17*, 145.

(207) Lu, X. B.; Dai, J. Y. *Appl. Phys. Lett.* **2006**, *88*.

(208) Sargentis, C.; Giannakopoulos, K.; Travlos, A.; Tsamakis, D. *Physica E-Low-Dimensional Systems & Nanostructures* **2007**, *38*, 85.

(209) Yang, Y.; Ouyang, J.; Ma, L. P.; Tseng, R. J. H.; Chu, C. W. *Adv. Funct. Mater.* **2006**, *16*, 1001.

(210) Park, B.; Cho, K.; Moon, B. M.; Kim, S. *Microelectron. Eng.* **2007**, *84*, 1627.

(211) Duguay, S.; Burignat, S.; Kern, P.; Grob, J. J.; Souifi, A.; Slaoui, A. *Semicond. Sci. Technol.* **2007**, *22*, 837.

(212) Guan, W. H.; Long, S. B.; Liu, M.; Li, Z. G.; Hu, Y.; Liu, Q. *J. Phys. D: Appl. Phys.* **2007**, *40*, 2754.

(213) Mabrook, M. F.; Jombert, A. S.; Machin, S. E.; Pearson, C.; Kolb, D.; Coleman, K. S.; Zeze, D. A.; Petty, M. C. *Mater. Sci. Eng., B* **2009**, *159-60*, 14.

(214) Wang, S.; Pu, J.; Chan, D. S. H.; Cho, B. J.; Loh, K. P. *Appl. Phys. Lett.* **2010**, *96*, 143109.

(215) Park, C. I.; Choi, W. M.; Kim, M. H.; Park, O. O. *J. Polym. Sci., Part B: Polym. Phys.* **2004**, *42*, 1685.

(216) Wu, T. M.; Hsu, S. F.; Wu, J. Y. *Journal of Polymer Science, Part B: Polymer Physics* **2003**, *41*, 1730.

(217) Zheng, W.; Lu, X. H.; Wong, S. C. *J. Appl. Polym. Sci.* **2004**, *91*, 2781.

(218) Mack, J. J.; Viculis, L. M.; Ali, A.; Luoh, R.; Yang, G. L.; Hahn, H. T.; Ko, F. K.; Kaner, R. B. *Adv. Mater.* **2005**, *17*, 77.

(219) He, F. A.; Fan, J. T.; Lau, S. T. *Polym. Test.* **2008**, *27*, 964.

(220) Rafiee, M. A.; Rafiee, J.; Wang, Z.; Song, H.; Yu, Z.-Z.; Koratkar, N. *ACS Nano* **2009**, *3*, 3884.

(221) Xu, Y. X.; Hong, W. J.; Bai, H.; Li, C.; Shi, G. Q. *Carbon* **2009**, *47*, 3538.

(222) Kai, W. H.; Hirota, Y.; Hua, L.; Inoue, Y. *J. Appl. Polym. Sci.* **2008**, *107*, 1395.

(223) Zhang, H. B.; Zheng, W. G.; Yan, Q.; Yang, Y.; Wang, J. W.; Lu, Z. H.; Ji, G. Y.; Yu, Z. Z. *Polymer* **2010**, *51*, 1191.

(224) Du, F.; Fischer, J. E.; Winey, K. I. *J. Polym. Sci., Part B: Polym. Phys.* **2003**, *41*, 3333.

(225) Zhao, X.; Zhang, Q. H.; Chen, D. J.; Lu, P. *Macromolecules* **2010**, *43*, 2357.

(226) Fang, M.; Wang, K. G.; Lu, H. B.; Yang, Y. L.; Nutt, S. *J. Mater. Chem.* **2009**, *19*, 7098.

(227) Prud'homme, R. K.; Ozbas, B.; Aksay, I. A.; Register, R. A.; Adamson, D. H. US Patent 2008045778, 2008.

(228) Velasco-Santos, C.; Martinez-Hernandez, A. L.; Fisher, F. T.; Ruoff, R.; Castano, V. M. *Chem. Mater.* **2003**, *15*, 4470.

(229) Viswanathan, G.; Chakrapani, N.; Yang, H. C.; Wei, B. Q.; Chung, H. S.; Cho, K. W.; Ryu, C. Y.; Ajayan, P. M. *J. Am. Chem. Soc.* **2003**, *125*, 9258.

(230) Gong, X.; Liu, J.; Baskaran, S.; Voise, R. D.; Young, J. S. *Chem. Mater.* **2000**, *12*, 1049.

(231) Sreekumar, T. V.; Liu, T.; Min, B. G.; Guo, H.; Kumar, S.; Hauge, R. H.; Smalley, R. E. *Adv. Mater.* **2004**, *16*, 58.

(232) Pramoda, K. P.; Hussain, H.; Koh, H. M.; Tan, H. R.; He, C. B. *Journal of Polymer Science Part A: Polymer Chemistry* **2010**, *48*, 4262.

(233) Ma, W.; Liu, L.; Zhang, Z.; Yang, R.; Liu, G.; Zhang, T.; An, X.; Yi, X.; Ren, Y.; Niu, Z.; Li, J.; Dong, H.; Zhou, W.; Ajayan, P. M.; Xie, S. *Nano Lett.* **2009**, *9*, 2855.

(234) Grady, B. P.; Paul, A.; Peters, J. E.; Ford, W. T. *Macromolecules* **2009**, *42*, 6152.

(235) Yang, S.; Rafael Castilleja, J.; Barrera, E. V.; Lozano, K. *Polym. Degrad. Stab.* **2004**, *83*, 383.

(236) Moon, T. G.; Kim, J. H.; Choi, C. H. *Polymer (Korea)* **1983**, *7*, 380.

(237) Gupta, S.; Mantena, P. R.; Al-Ostaz, A. *J. Reinf. Plast. Compos.* **2010**, *29*, 2037.

(238) Manchado, M. A. L.; Valentini, L.; Biagiotti, J.; Kenny, J. M. *Carbon* **2005**, *43*, 1499.

(239) Zheng, W.; Wong, S.-C. *Composites Science and Technology* **2003**, *63*, 225.

(240) Kitiyanan, B.; Alvarez, W. E.; Harwell, J. H.; Resasco, D. E. *Chem. Phys. Lett.* **2000**, *317*, 497.

(241) Huang, L. M.; Cui, X. D.; White, B.; O'Brien, S. P. *J. Phys. Chem. B* **2004**, *108*, 16451.

(242) Shajahan, M.; Mo, Y. H.; Nahm, K. S. *Korean J. Chem. Eng.* **2003**, *20*, 566.

(243) Cassell, A. M.; Raymakers, J. A.; Kong, J.; Dai, H. J. *J. Phys. Chem. B* **1999**, *103*, 6484.

(244) Wang, X.; Yue, W. B.; He, M. S.; Liu, M. H.; Zhang, J.; Liu, Z. F. *Chem. Mater.* **2004**, *16*, 799.

(245) Liu, B. H.; Ding, J.; Zhong, Z. Y.; Dong, Z. L.; White, T.; Lin, J. Y. *Chem. Phys. Lett.* **2002**, *358*, 96.

(246) Forrest, G. A.; Alexander, A. J. *Carbon* **2008**, *46*, 818.

(247) Petrov, K.; Mirtcheva, E.; Devidales, J. L. M.; Rojas, R.; Garciamartinez, O. *Polyhedron* **1994**, *13*, 3269.

(248) Ohnishi, C. H.; Asano, K.; Jeon, H.-J.; Hosokawa, S.; Iwamoto, S.; Inoue, M. *Polyhedron* **2009**, *28*, 1295.

(249) Zhao, Z.; Geng, F.; Bai, J.; Cheng, H.-M. *The Journal of Physical Chemistry C* **2007**, *111*, 3848.

(250) Cong, H.-P.; Yu, S.-H. *Cryst. Growth Des.* **2008**, *9*, 210.

(251) Gupta, A.; Chen, G.; Joshi, P.; Tadigadapa, S.; Eklund *Nano Lett.* **2006**, *6*, 2667.

(252) Lespade, P.; Marchand, A.; Couzi, M.; Cruege, F. *Carbon* **1984**, *22*, 375.

(253) Bulavchenko O.A.; Cherepanova S.V.; Tsybulya S.V. *Z. Kristallogr.* **2009**, *30*, 329.

(254) Sun, G.; Li, X.; Qu, Y.; Wang, X.; Yan, H.; Zhang, Y. *Mater. Lett.* **2008**, *62*, 703.

(255) Wang, R.; Hao, Y.; Wang, Z.; Gong, H.; Thong, J. T. L. *Nano Lett.* **2010**, *10*, 4844.

(256) Wei, D.; Liu, Y.; Zhang, H.; Huang, L.; Wu, B.; Chen, J.; Yu, G. *J. Am. Chem. Soc.* **2009**, *131*, 11147.

(257) Yu, Q. K.; Lian, J.; Siriponglert, S.; Li, H.; Chen, Y. P.; Pei, S. S. *Appl. Phys. Lett.* **2008**, *93*.

(258) Yang, J.; Liu, H.; Martens, W. N.; Frost, R. L. *The Journal of Physical Chemistry C* **2009**, *114*, 111.

(259) Liu, X. H.; Yi, R.; Zhang, N.; Shi, R. R.; Li, X. G.; Qiu, G. Z. *Chem. Asian J.* **2008**, *3*, 732.

(260) Hou, Y.; Kondoh, H.; Shimojo, M.; Kogure, T.; Ohta, T. *J. Phys. Chem. B* **2005**, *109*, 19094.

(261) Zhan, P. *J. Alloys Compd.* **2009**, *478*, 823.

(262) Altuntasoglu, O.; Matsuda, Y.; Ida, S.; Matsumoto, Y. *Chem. Mater.* **2010**, *22*, 3158.

(263) Liu, Z.; Ma, R.; Osada, M.; Takada, K.; Sasaki, T. *J. Am. Chem. Soc.* **2005**, *127*, 13869.

(264) Obraztsov, A. N.; Obraztsova, E. A.; Tyurnina, A. V.; Zolotukhin, A. A. *Carbon* **2007**, *45*, 2017.

(265) Chae, S. J.; Güneş, F.; Kim, K. K.; Kim, E. S.; Han, G. H.; Kim, S. M.; Shin, H.-J.; Yoon, S.-M.; Choi, J.-Y.; Park, M. H.; Yang, C. W.; Pribat, D.; Lee, Y. H. *Adv. Mater.* **2009**, *21*, 2328.

(266) Reina, A.; Jia, X.; Ho, J.; Nezich, D.; Son, H.; Bulovic, V.; Dresselhaus, M. S.; Kong, J. *Nano Letters* **2008**, *9*, 30.

(267) Kim, K. S.; Imris, M.; Shahverdi, A.; Alinejad, Y.; Soucy, G. *J. Phys. Chem. C* **2009**, *113*, 4340.

(268) Pandey, D.; Prakash, G.; Yu, Q.; Cao, H.; Jauregui, L. A.; Pei, S. S.; Chen, Y. P. In *Graphene and Emerging Materials for Post-Cmos Applications*; Obeng, Y., DeGendt, S., Srinivasan, P., Misra, D., Iwai, H., Karim, Z., Hess, D. W., Grebel, H., Eds.; Electrochemical Society Inc: Pennington, 2009; Vol. 19, p 75.

(269) Cuong, T. V.; Pham, V. H.; Tran, Q. T.; Chung, J. S.; Shin, E. W.; Kim, J. S.; Kim, E. J. *Mater. Lett.* **2010**, *64*, 765.

(270) Li, Q. W.; Yan, H.; Cheng, Y.; Zhang, J.; Liu, Z. F. *J. Mater. Chem.* **2002**, *12*, 1179.

(271) Gallant, D.; Pézolet, M.; Simard, S. *J. Phys. Chem. B* **2006**, *110*, 6871.

(272) Tyczkowski, J.; Kapica, R.; Lojewska, J. *Thin Solid Films* **2007**, *515*, 6590.

(273) Bronikowski, M. J.; Willis, P. A.; Colbert, D. T.; Smith, K. A.; Smalley, R. E. *J. Vac. Sci. Technol., A* **2001**, *19*, 1800.

(274) Zheng, B.; Lu, C. G.; Gu, G.; Makarovski, A.; Finkelstein, G.; Liu, J. *Nano Lett.* **2002**, *2*, 895.

(275) Li, W. Z.; Zhang, H.; Wang, C. Y.; Zhang, Y.; Xu, L. W.; Zhu, K.; Xie, S. S. *Appl. Phys. Lett.* **1997**, *70*, 2684.

(276) Ferrari, A.; Robertson, J. *Phys. Rev. B: Condens. Matter Mater. Phys.* **2000**, *61*, 14095.

(277) Paillard, V. *EPL (Europhysics Letters)* **2001**, *54*, 194.

(278) Kim, C. D.; Min, B. K.; Jung, W. S. *Carbon* **2009**, *47*, 1610.

(279) Little, R. B. *J. Cluster Sci.* **2003**, *14*, 135.

(280) Yang, X.; Dou, X.; Rouhanipour, A.; Zhi, L.; Räder, H. J.; Müllen, K. *J. Am. Chem. Soc.* **2008**, *130*, 4216.

(281) Cai, J.; Ruffieux, P.; Jaafar, R.; Bieri, M.; Braun, T.; Blankenburg, S.; Muoth, M.; Seitsonen, A. P.; Saleh, M.; Feng, X.; Mullen, K.; Fasel, R. *Nature* **2010**, *466*, 470.

(282) Wu, Z.-S.; Ren, W.; Gao, L.; Liu, B.; Zhao, J.; Cheng, H.-M. *Nano Research* **2010**, *3*, 16.

(283) Kulikov, I. S. *Thermodynamics of Carbides and Nitrides*; Metallurgiya, Chelyabinsk, 1988.

(284) Gou, X.; Wang, G.; Yang, J.; Park, J.; Wexler, D. *J. Mater. Chem.* **2008**, *18*, 965.

(285) Xu, R.; Xie, T.; Zhao, Y.; Li, Y. *Cryst. Growth Des.* **2007**, *7*, 1904.

(286) Zarate, R. A.; Hevia, F.; Fuentes, S.; Fuenzalida, V. M.; Zúñiga, A. *J. Solid State Chem.* **2007**, *180*, 1464.

(287) Zou, G. F.; Li, H.; Zhang, D. W.; Xiong, K.; Dong, C.; Qian, Y. T. *J. Phys. Chem. B* **2006**, *110*, 1632.

(288) Luo, Y.; Tu, Y.; Ren, Q.; Dai, X.; Xing, L.; Li, J. *J. Solid State Chem.* **2009**, *182*, 182.

(289) Zhang, Z.; Sun, Z.; Yao, J.; Kosynkin, D. V.; Tour, J. M. *J. Am. Chem. Soc.* **2009**, *131*, 13460.

(290) Lee, C. J.; Park, J. *Appl. Phys. Lett.* **2000**, *77*, 3397.

(291) Lee, C. J.; Park, J. H.; Park, J. *Chem. Phys. Lett.* **2000**, *323*, 560.

(292) Higginbotham, A. L.; Kosynkin, D. V.; Sinitskii, A.; Sun, Z.; Tour, J. M. *ACS Nano* **2010**, *4*, 2059.